SODIUM POTASSIUM NIOBATE–BASED THICK FILMS BY ELECTROPHORETIC DEPOSITION FOR PIEZOELECTRIC ENERGY HARVESTING

Hugo Mercier

Doctoral Dissertation
Jožef Stefan International Postgraduate School
Ljubljana, Slovenia

Supervisors: Assoc. Prof. Dr. Danjela Kuščer Hrovatin, Jožef Stefan Institute, Ljubljana, Slovenia
Prof. Dr. Franck Levassort, University of Tours, Tours, France

Evaluation Board:
Prof. Dr. Barbara Malič, Chair, Jožef Stefan Institute, Ljubljana, Slovenia
Assoc. Prof. Dr. Pascal Marchet, Member, University of Limoges, Limoges, France
Prof. Dr. Marc Lethiecq, Member, INSA Centre Val de Loire, Blois, France
Prof. Dr. Dragan Damjanovic, Member, Ecole Polytechnique Fédérale de Lausanne (EPFL), Lausanne, Switzerland

MEDNARODNA PODIPLOMSKA ŠOLA JOŽEFA STEFANA
JOŽEF STEFAN INTERNATIONAL POSTGRADUATE SCHOOL

Hugo Mercier

SODIUM POTASSIUM NIOBATE–BASED THICK FILMS BY ELECTROPHORETIC DEPOSITION FOR PIEZOELECTRIC ENERGY HARVESTING

Doctoral Dissertation

DEBELE PLASTI NA OSNOVI KALIJEVEGA NATRIJEVEGA NIOBATA, PRIPRAVLJENE Z ELEKTROFORETSKIM NANOSOM ZA PIEZOELEKTRIČNO ZBIRANJE ENERGIJE

Doktorska disertacija

Supervisors: Assoc. Prof. Dr. Danjela Kuščer Hrovatin

Prof. Dr. Franck Levassort

Ljubljana, Slovenia, July 2020

Acknowledgments

I would like to thank Prof. Dr. Dragan Damjanovic and Assoc. Prof. Dr. Pascal Marchet for agreeing to review and evaluate this thesis.

I would like to acknowledge Prof. Dr. Barbara Malič, Head of the Electronic Ceramics Department (K5) and Prof. Dr. Marc Lethiecq former Head of the GREMAN laboratory, for welcoming me to their laboratories, their support and useful suggestions, for reviewing and evaluating this work.

I would like to express my deepest thanks to my supervisors Assoc. Prof. Dr. Danjela Kuščer Hrovatin and Prof. Dr. Franck Levassort for their support, patience, and guidance in the research work. I am also grateful that they offered me this opportunity of a co-directed PhD between the Electronic Ceramics Department (K5) of the Jožef Stefan Institute and the University of Tours.

I would like to express my appreciation to colleagues in the K5 department for fruitful discussions and their help. Dr. Jitka Hreščak for the powder synthesis and answering my questions concerning its preparation. Asst. Prof. Dr. Hana Uršič for the piezo-response force microscopy experiments and her help with measuring the dielectric and ferroelectric properties of the thick films. Dr. Tina Bakarič for sharing her experience with suspensions' preparation and characterization. Assoc. Prof. Dr. Tadej Rojac and Prof. Dr. Vid Bobnar for discussions about the dielectric properties of the thick films. I would like to show my gratitude to Jana Cilenšek, Silvo Drnovšek and Brigita Kmet for sharing their experiences and helping me with the lab work. I also express my thanks to the students Maja Majcen, Hafsa Znibrat and Grégoire Levavasseur, for their assistance with the lab work.

I would like to thank Dr. Marina Santo Zarnik for her help with the finite-element analysis, Prof. Anton Meden for discussions about the XRD patterns and Maja Koblar for introducing me to scanning electron microscopy.

I would also like to express my gratitude to my co-workers from GREMAN for their help in the realisation of this work. Asst. Prof. Dr. Rémi Rouffaud for the determination of the database of the material and the calculation of the theoretical influence of the porosity on the material properties using the matrix method. Asst. Prof. Dr. Kevin Nadaud for discussions about additional measurements of the dielectric properties of ferroelectric materials. Assoc. Prof. Dr. Guylaine Poulin-Vittrant and Asst. Prof. Dr. Maxime Bavencoffe for discussions and answering my questions about piezoelectric energy harvesting. Prof. Dr. Isabelle Monot-Laffez for discussions about sodium potassium niobate and sintering thick films in an inert atmosphere. Dr. Micka Bah and Asst. Prof. Dr. Quentin Simon for discussions about lead-free piezoelectric materials. I wish to extend my thanks to Laurent Colin, Dr. Damien Valente, Dr. Virginie Grimal, David Chouteau and Marie Perroteau for their help with laboratory work.

I wish to acknowledge Claire Bantignies, Dr. Guillaume Férin, Dr. Thien Hoang, Dr. Bogdan Rosinski and Maxime Cheppe from VERMON SA for the conception and preparation of the new electrophoretic deposition setup and for fruitful discussions about energy harvesting.

I would like to thank Magali Leger, Tina Ručigaj Korošec and Tamara Matevc, who helped me with administrative issues and arranging the travel/accommodation.

I would like to express my appreciation to coworkers from both K5 and GREMAN: Dr. Andraž Bradeško, Maja Makarovič, Dr. Lovro Fulanović, Dr. Aleksander Matavž, Uroš Prah, Dr. Marko Vrabelj, Dr. Tanja Vrabelj, Jaweb Ben Messaoud, Clément Mauduit, Clément Berger, Flavien Barcella, Dr. Camille Justeau, Camille Compère, Dr. Maxime Hery, Dr. Antoine Bale, Sylvain Audière, Dr. Taoufik Slimani, for discussions, breaks, laughing (from time to time) at my jokes and all the good times we spent together.

I acknowledge the Slovenian Research Agency (research core funding No. P2-0105 and the project L2-8180) and French Research Agency LabCOM Lab-TMEMS (ANR 14-LAB5-0004) for the financial support of this work. This work was also supported by the bilateral projects (BI-FR-16-17-PROTEUS-009/PHC PROTEUS 2016 and BI-FR-19-20-PROTEUS-08, 41658ZM) and the Erasmus + programme). In addition, I would like to thank the Centre of Excellence NAMASTE and the Jožef Stefan Institute for the use of laboratory equipment.

Finally, I am grateful to my family, girlfriend and friends for their support and motivation during my studies.

Abstract

Autonomous electronic devices require a long-term, sustainable power supply. One possible solution is the transduction of mechanical energy, available in the sensor's environment, into electrical energy by piezoelectric layers integrated on a flexible substrate. A-few-tens-of-micrometres-thick piezoelectric layers can be processed on a substrate using electrophoretic deposition (EPD). EPD is based on the mobility of charged particles in a solvent and their deposition on a conductive substrate upon the application of an electric field. After the EPD, the layers are sintered. Most piezoelectric energy harvesters (PEHs) integrate lead-based piezoelectric materials. However, due to governmental regulations, alternative lead-free materials have been investigated. Thus, a lead-free piezoelectric based on potassium sodium niobate ($(K_{0.5}Na_{0.5})_{0.99}Sr_{0.005}NbO_3$, KNNSr) was selected for this work.

In the first part we studied the stabilisation of KNNSr particles in ethanol using poly(acrylic acid-co-maleic acid) (PAM) and an organic base: n-butylamine (BA). By optimising the PAM amount and the PAM/BA ratio, we stabilized the particles, with a zeta-potential (ZP) of around -45 mV and tailored the conductivity of the suspensions in the range 9–30 μS/cm. The deposition of KNNSr particles on a 640-μm-thick platinised alumina substrate (RAO), demonstrated that the conductivity of the suspensions influences the deposited masses, the homogeneity and the thickness uniformity of the layers. The thickness uniformity of the layers depends on the geometry of the deposition setup. Using a finite-element analysis (FEA) we predicted and optimised the electric field strength in the setup by varying the interelectrode distance and the counter electrode diameter. The FEA results were well correlated with the experimental thickness profiles of the layers.

In the second part the thick films deposited on the RAO substrate were sintered. The thick films sintered at 1075 °C were porous, whereas the ones sintered at 1120 °C delaminated from the substrate. To avoid the delamination, we first deposited a ~10-μm-thick layer and fired it at 1000 °C, followed by the deposition of a second, thicker layer. We sintered the layers at 1090, 1100 and 1110 °C, both in air and oxygen, to understand the microstructure evolution of the KNN thick films. The microstructure, X-ray-diffraction patterns and local ferroelectric domain structure were correlated with the electromechanical properties. The KNNSr thick films sintered at 1100 °C for 2 hours had a homogenous microstructure, a relative density of ~ 81 % and a thickness-coupling factor of ~ 40 %.

In the third part we focus on the processing of a bimorph structure on flexible, 110-μm-thick platinised alumina (DFAO) substrates. For this purpose we modified the EPD setup. The sintering of KNNSr layers on one side of the DFAO substrate results in the bending of the structure. To minimise this spurious effect, the ~ 65-μm-thick layers were deposited on both sides of the DFAO substrate. After sintering at 1100 °C for 2 h in oxygen we obtained a thick film with a homogeneous microstructure, a thickness of ~ 40 μm and a relative density of ~85 %. We theoretically estimated and showed the influence of the porosity on the figure of merit (FOM) for a KNNSr-based PEH operating in the 31-mode. We found that the FOM at resonance was more impacted by the porosity than the FOM in off-resonance conditions. This work demonstrated that EPD is a suitable method for the preparation of bimorph cantilevers made of lead-free thick films for PEHs.

Povzetek

Z razvojem avtonomnih elektronskih naprav se je povečalo povpraševanje po napravah, ki lahko pretvorijo energijo, razpoložljivo v okolju, v električno energijo. Mehansko energijo lahko pretvorimo v električno s piezoelektričnimi zbiralniki energije (PZE). Naprava ima največkrat obliko konzole, na katero je integriran piezoelektrik debeline nekaj deset mikrometrov. Takšne plasti lahko izdelamo z metodo elektroforetskega nanosa (EN), ki temelji na mobilnosti nabitih delcev v topilu pod vplivom električnega polja. Na elektrodi nastaja nanos, ki ga je potrebno ustrezno termično obdelati. V PZE se najpogosteje uporabljajo piezoelektriki, ki vsebujejo svinec. Uporabo teh materialov omejujejo zaradi okoljskih in zdravstvenih pomislekov, kar je spodbudilo raziskave alternativnih materialov. V doktorski disertaciji smo preiskovali materiale na osnovi kalijevih natrijevih niobatov z nominalno sestavo $(K_{0.5}Na_{0.5})_{0.99}\,Sr_{0.005}NbO_3$ (KNNSr).

V prvem delu doktorske disertacije smo raziskali stabilizacijo delcev KNNSr v etanolu z dodatkom poliakrilne-maleinske kisline (PAM) ter organske baze n-butilamin (BA). Z optimizacijo razmerja PAM/BA smo pripravili stabilno suspenzijo delcev z zeta potencialom -45 mV ter električno prevodnostjo od 9 do 30 μS/cm. Delce smo nanesli na platinizirano podlago Al_2O_3 debeline 640 µm (RAO). Proučevali smo vpliv električne prevodnosti suspenzije na maso, homogenost in enakomernost debeline nanosa. Z metodo končnih elementov smo proučevali električno poljsko jakost v celici. Ugotovili smo, da razdalja med elektrodama in premer referenčne elektrode vplivata na porazdelitev električne poljske jakosti med elektrodama ter posledično na enakomernost debeline nanosa. Rezultate analize smo primerjali z izmerjenimi debelinami nanosa pri izbranih pogojih ter potrdili dobro ujemanje rezultatov obeh analiz.

V drugem delu doktorske disertacije smo plasti, ki smo jih nanesli na RAO z dobro ponovljivostjo, sintrali. Plasti, sintrane pri 1075 °C, so bile porozne, plasti, sintrane pri 1120 °C, pa so imele slabo oprijemljivost s podlago. Da bi izboljšali oprijemljivost, smo na podlago najprej nanesli plast debeline ~ 10 µm in jo žgali pri 1000 °C. Na to plast smo nanesli debelejšo past. Strukture smo sintrali pri 1090, 1100 in 1110 °C na zraku in v kisiku, da bi raziskali povezavo med strukturo, mikrostrukturo, domensko strukturo in elektromehanskimi lastnostmi plasti. Po sintranju pri 1100 °C so imele plasti homogeno mikrostrukturo, relativno gostoto 81 % ter sklopitveni faktor 40 %.

V tretjem delu doktorske disertacije smo se osredotočili na pripravo bimorfne strukture na fleksibilni, 110 µm debeli platinizirani podlagi Al_2O_3 s prilagojeno eksperimentalno celico. Struktura s plastjo KNNSr na eni strani se je po sintranju ukrivila, medtem ko je ostala bimorfna struktura ravna. Po sintranju pri 1100 °C 2 h v kisiku sta bili plasti KNNSr na obeh straneh enakomerne debeline ~ 40 μm, brez defektov, s homogeno mikrostrukturo in relativno gostoto 85 %. S teoretičnim pristopom smo ocenili vpliv poroznosti KNNSr na delovanje PZE v načinu 3-1. Ugotovili smo, da ima poroznost večji vpliv na delovanje PZE pri resonančnih pogojih, medtem ko na delovanje izven resonance vpliva nekoliko manj. Rezultati so pokazali, da je EN primerna metoda za pripravo bimorfne strukture PZE, pripravljene iz KNNSr.

Contents

List of Figures

List of Tables

Abbreviations

AO ... alumina (α-Al_2O_3)
AO-0.11 ... 110-μm-thick alumina substrate
AO-0.64 ... 640-μm-thick alumina substrate
AR ... aspect ratio, assess the thickness uniformity of the layers
AR_E ... aspect ratio, assess the electric-field-strength uniformity in the EPD setup
BA ... n-butylamine
BSE ... backscattered electron
CE ... counter electrode
CMOS ... complementary metal oxide semiconductor
CN ... coordination number
CSD ... chemical solution deposition
DFAO ... 110-μm both-sides-platinised alumina
EDL ... electrical double layer
EDXS ... energy-dispersive X-ray spectroscopy
EH ... energy harvester
EPD ... electrophoretic deposition
EtOH ... absolute ethanol
FEA ... finite-element analysis
FOM ... figure of merit
KLM ... Krimholtz-Leedom-Matthaei
KN ... potassium niobate, $KNbO_3$
KNN ... sodium potassium niobate, $K_{0.5}Na_{0.5}NbO_3$
KNNSr ... strontium-modified sodium potassium niobate, $(K_{0.5}Na_{0.5})_{0.99}Sr_{0.005}NbO_3$
LF ... Lotgering factor
MAD ... normalised median absolute deviation
MEMS ... micro-electromechanical systems
MO ... metal oxide
NN ... sodium niobate, $NaNbO_3$
PAM ... poly(acrylic acid-co-maleic acid)
PEH ... piezoelectric energy harvester
PFM ... piezo-response force microscopy
PSD ... particle size distribution
PZT ... lead zirconate titanate, $Pb(Zr_{0.52}Ti_{0.48})O_3$
Pt ... platinum
RAO ... 640-μm-thick platinised alumina
SD ... standard deviation
SE ... secondary electron
SEM ... scanning electron microscopy
SiC ... silicon carbide
TB ... tungsten bronze
ThickFT ... thick-film technology

WE ... working electrode
XRD ... X-ray powder diffraction
YSZ3 ... yttria-stabilised zirconia balls with diameter 3 mm
YSZ10 ... yttria-stabilised zirconia balls with diameter 10 mm
ZP ... zeta-potential

Symbols

$A_{A,10}$ ... 10 % of the total pore area lies below this pore area [m²]
$A_{A,50}$ ... median pore area (area distribution) [m²]
$A_{A,90}$ ... 90 % of the total pore area lies below this pore area [m²]
C ... capacitance [F]
C_0 ... static capacitance [F]
C' ... motional capacitance [F]
C_s ... particle concentration in the suspension [kg/m³]
D_e ... counter electrode diameter [m]
D ... electric displacement [C/m²]
E ... electric field strength [V/m]
E_C ... coercive electric field [V/m]
$\underline{E_Z}$ ... electric field strength along the z direction [V/m]
$\overline{E_Z}$ ... mean value of the electric field strength along the z direction [V/m]
$\widetilde{E_Z}$ ... median value of the electric field strength along the z direction [V/m]
$E_{Z,i}$ ... electric field strength along the z direction at the point "i" [V/m]
$\overrightarrow{F_1}$ ... force applied to the front face [N]
$\overrightarrow{F_2}$ ... force applied to the rear face [N]
G ... conductance [S/m]
I ... electrical current [A]
J ... electrical current density [A/m²]
L ... inductance [H/m]
L_{WE} ... length of the side of squared working electrode [m]
M ... global transfer matrix (KLM model)
N_{Au} ... transfer matrix of the gold electrode (KLM model)
N_C ... transfer matrix of the motional and static capacitance in series (KLM model)
N_R ... transfer matrix of the rear face (KLM model)
N_Φ ... transfer matrix of the ideal electromechanical transformer (KLM model)
P ... polarisation [C/m²]
P_r ... remanent polarisation [C/m²]
Q_m ... mechanical quality factor [/]
R ... resistance [Ω]
S ... strain tensor [/]
S_{elec} ... surface of the electrode [m²]
T ... Stress tensor [N/m²]
T_C ... Curie temperature [°C]
U_e ... electric voltage at the surface of a piezoelectric plate [V]
U_g ... electric voltage of the external electrical generator [V]
V ... electric potential [V]
V_A ... attractive potential between the particles [V]
V_L ... longitudinal wave velocity [m/s]

V_R ... repulsive potential between the particles [V]
V_T ... total potential between two particles [V]
X_i ... position of the point "i" along the A-A line [mm]
Y ... yield: mass deposited per working area [kg/m^2]
Y_e ... electric admittance of the piezoelectric layer [S]
Z ... acoustic impedance [MRa]
Z_e ... electric impedance of the piezoelectric plate [Ω]
Z_q ... internal electric impedance of the external generator [Ω]
Z_m ... mechanical impedance of the media [N.s/m]
Z_P ... mechanical impedance of the piezoelectric plate [N.s/m]

c^D ... elastic stiffness tensor at constant electric displacement [N/m^2]
c_{33}^D, c_{33}^{D*} ... elastic constant and complex elastic constant, respectively, at constant electric displacement along the polarisation direction [N/m^2]
c^E ... elastic stiffness tensor at constant electric field [N/m^2]
dm/dt ... deposition rate [kg/s]
dY/dt ... deposition rate per working electrode area [kg/(m^2.s)]
d ... piezoelectric tensor [C/N]
d_{31}, d_{33} ... 31- and 33-mode piezoelectric coefficients, respectively [C/N]
$d_{33,\mathrm{f}}$ ... 33-mode piezoelectric coefficient of a clamped thick film [C/N]
$d_{v,50}$ ... median particle size (volume distribution) [m]
e ... piezoelectric tensors [C/m^2]
e_{33} ... piezoelectric coefficient [C/m^2]
f ... frequency [Hz]
f_a ... anti-resonant frequency [Hz]
f_H ... Henry constant [/]
f_r ... resonance frequency [Hz]
g ... piezoelectric tensor [V.m/N]
g_{31} ... piezoelectric strain voltage coefficient of the 31 mode [V.m/N]
h ... piezoelectric tensor [V/m]
h_i ... interelectrode distance [m]
k_B ... Boltzmann constant (1.381×10^{-23} J/K)
k ... electromechanical coupling factor [/]
k_{31} ... 31-mode electromechanical coupling factor [/]
k_p ... planar-mode electromechanical coupling factor [/]
k_t ... thickness-mode electromechanical coupling factor [/]
l_i ... initial length (at room temperature) [m]
m ... deposited mass [kg]
$\vec{n}$ ... unit vector normal to the surface [/]
n_i^0 ... bulk concentration of the ion i [mol/m^3]
p ... intensity of the (hkl) preferential orientation in the thick film divided by all other hkl intensity [/]
p_0 ... normalised intensity of the (hkl) plane in the randomly oriented sample divided by all other hkl intensity [/]
q_e ... elementary charge (1.602×10^{-19} C)
r ... radius of a particle [m]
t ... time [s]
t_{edges} ... thickness at the edges of the as-deposited KNNSr layer [m]
t_{centre} ... thickness at the centre of the as-deposited KNNSr layer [m]
t_M ... thickness of the material [m]
t_S ... thickness of the substrate [m]

t_L ... thickness of the as-deposited layer[m]
$\tan\delta$ ... dielectric losses measured on unpoled material [/]
$\tan\delta_e$ ... dielectric losses measured on poled material [/]
v_e ... electrophoretic velocity [m/s]
v_1 ... displacement velocity at the front face [m/s]
v_2 ... displacement velocity at the rear face [m/s]
s^D ... elastic compliance at constant electric displacement [m^2/N]
s^E ... elastic compliance at constant electric field [m^2/N]
s^E_{11},s^E_{12} ... elastic compliance at constant electric field components [m^2/N]
z_i ... valence of ions i [/]

α ... acoustic attenuation coefficient [dB/m/Hz]
α_{TF} ... linear thermal expansion coefficient of the thick film [K^{-1}]
α_S ... linear thermal expansion coefficient of the substrate [K^{-1}]
β^S ... reciprocal of the dielectric tensor at constant strain [m/F]
β^T ... reciprocal of the dielectric tensor at constant stress [m/F]
δ_m ... mechanical losses [/]
$\Delta l/l$ ... relative shrinkage [/]
$\Delta V(t)$ ... experimentally measured voltage during the deposition [V]
$\Delta V_{0,EXP}$ ... voltage experimentally delivered at time zero of the deposition [V]
$\Delta V_{0,FEA}$ ... voltage theoretically predicted at time zero of the deposition [V]
ε_0 ... dielectric permittivity of the vacuum (8.854×10^{-12} F/m)
ε_r ... relative dielectric permittivity of the media [/]
ε_{33} .. dielectric permittivity of unpoled material [F/m]
$\varepsilon_{r,33}$ ... relative dielectric permittivity of unpoled material [/]
ε^{S*}_{33} ... complex dielectric permittivity at constant strain along the polarisation direction [F/m]
ε^S_{33}, ε^T_{33} ... dielectric permittivity at constant strain and constant stress, respectively, along the polarisation direction [F/m]
$\varepsilon^S_{r,33}$, $\varepsilon^T_{r,33}$ ... relative dielectric permittivity at constant strain and constant stress, respectively, along the polarisation direction [/]
Φ ... transformer ratio [/]
γ_P ... propagation constant of the piezoelectric element [/]
κ ... inverse of the Debye-Hückel length [m^{-1}]
λ ... wavelength [m]
ω ... pulsation [rad/s]
η ... dynamic viscosity of the media [Pa.s]
ρ ... density [kg/m^3]
ρ_s ... resistivity of the suspension [Ω.m]
$\sigma_{r,S}$ ... in-plane stress in the substrate [N/m^2]
$\sigma_{r,L}$ ... in-plane stress in the thick film [N/m^2]
σ_{susp} ... conductivity of the suspension [S/m]
μ_e ... electrophoretic mobility [m^2/(V.s)]

Chapter 1

Introduction

In this chapter piezoelectric energy harvesters (PEHs), with an emphasis on the bimorph cantilever structure, are described. In the second part, the synthesis, sintering, and properties of piezoelectric lead-free sodium potassium niobate materials are reviewed. The third part focuses on the processing of piezoelectric thick films by electrophoretic deposition. The last part reviews existing KNN-based PEHs.

1.1 Piezoelectric Energy Harvesters (PEHs)

An energy harvester (EH) scavenges the ambient environmental energy, such as mechanical energy, heat or light, to produce electrical energy [1], [2]. An EH allows the powering of self-sustained devices, such as sensors or transmitters, which required power in the μW-to-mW range [3]. These devices have the potential to be incorporated into devices used for various applications, such as structural health monitoring [4] or implantable devices in medicine [5]. Among the energy sources, the mechanical energy is readily generated indoors and outdoors from human motion, industrial machinery, vehicles, etc. [6]. Piezoelectric energy harvesters (PEHs) allow the conversion of the mechanical energy in the form, for example, of vibrations or shocks into electrical energy using the direct piezoelectric effect, which is the linear relationship between the stress applied to the material and the resulting charge density [7]. A general and brief description of the piezoelectric and ferroelectric materials with the corresponding notation used in this manuscript is given in Appendix A.

PEHs have received much attention due to the large energy density and the relatively simple architecture of the devices in comparison to EHs based on electrostatic and electromagnetic effects [8]. The vibration PEHs use a structure designed to resonate at a frequency matching the excitation vibration of the source [9]. Its power output is related to the vibration amplitude and the excitation frequency of the source. The typical dependence of the output power versus excitation frequency of a vibrating PEH is characterised by a resonant frequency (f_r) and a bandwidth, as illustrated in Figure 1.1.

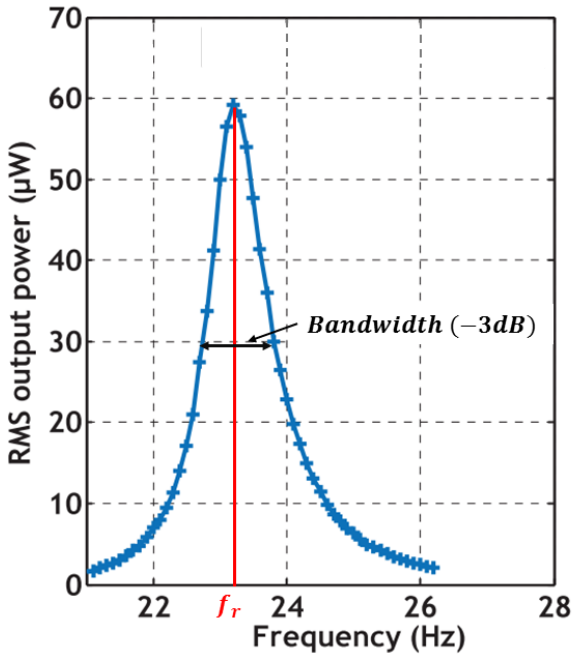

Figure 1.1: Root mean square (RMS) output power of a piezoelectric energy harvester as a function of the excitation frequency [10]. f_r is the resonance frequency.

1.1.1 Bimorph cantilever PEH

Typical PEH resonant structures are the unimorph and bimorph cantilevers. A unimorph cantilever consists of a piezoelectric layer attached to a conductive shim (Figure 1.2a, Figure 1.2b). The bimorph cantilevers consist of piezoelectric layers attached on two sides of a shim (Figure 1.3a, Figure 1.3b). One end of the cantilever is clamped, whereas the other end is kept mechanically free. The cantilever operates in the bending mode with the layers being alternatively in extension and in compression (see, for example, the unimorph in tension in Figure 1.2a). The unimorph and bimorph structures take the advantages of the large mechanical strain within the material at resonance and of the low frequency of the fundamental flexural mode [3]. Usually, a cantilever integrates a proof mass at its free-end, which is used to decrease the resonance frequency of the structure, it also amplifies the mechanical energy stored and consequently increases the power output of the PEH [2].

The PEH can operate either in 33- or 31-mode, as schematically shown in Figure 1.2 [3] (see Appendix A for notation). In 33-mode the polarisation direction of the piezoelectric material is parallel to the applied strain/stress (Figure 1.2b). PEHs operating in 33-mode use interdigitated electrodes, and the output power depends on the electrode's design [11]. In devices operated in 31-mode the polarisation direction of the piezoelectric material is perpendicular to the applied strain/stress (Figure 1.2a, Figure 1.3a, Figure 1.3b). In this case the top and bottom surfaces of the piezoelectric material are fully covered by electrodes. When the substrate is conductive (shim) it serves as a bottom electrode.

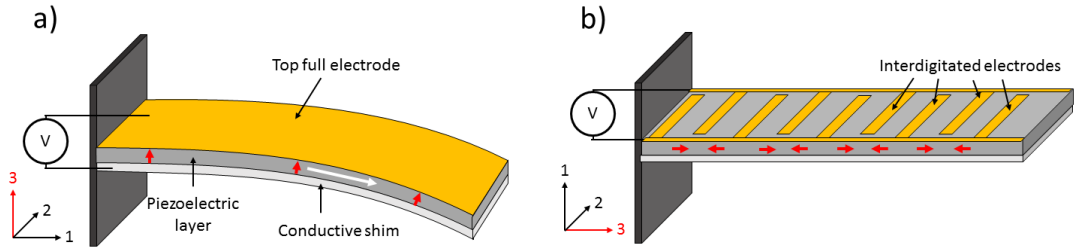

Figure 1.2: Schematic representations of unimorph cantilevers in a) 31-mode configuration (working condition), b) 33-mode configuration with interdigitated electrodes. Red arrows indicate the poling direction in the piezoelectric material, the white arrow indicates the tensile strain in the piezoelectric layer.

Focusing on 31-mode, the two piezoelectric layers of a bimorph can be either poled in the same (Figure 1.3a) or opposite directions (Figure 1.3b), which are specified as parallel and series connections, respectively. A parallel connection leads to a larger current output, and a lower electrical impedance and voltage output of the structure, in comparison to the series connection [12].

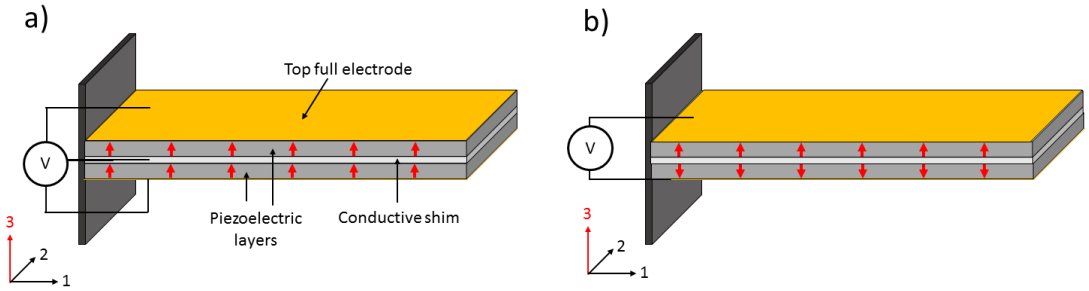

Figure 1.3: Schematic representations of bimorph cantilevers working in 31-mode connected a) in parallel and b) in series. Red arrows indicate the poling direction in the piezoelectric material.

A PEH bimorph operated in the 31-mode, with the piezoelectric material's layers having a thickness of a few tens/hundreds of micrometres, has been conventionally processed by machining bulk ceramics [10], [13], [14]. Ferin *et al.* [10] manufactured a bimorph cantilever from commercial lead zirconate titanate–based bulk ceramics. A schematic representation of the process is presented in Figure 1.4a. First, the bulk ceramics were glued on both sides of a conductive substrate, termed a shim (steps 1, 2 and 3, in Figure 1.4a), and then grinded and polished to achieve the desired thickness (steps 4, 5). Finally, the top and bottom electrodes were deposited (step 6). The images and cross-section of the bimorph PEH are presented in Figure 1.4b and Figure 1.4c, respectively. Similar manufacturing processes have been used to prepare unimorph structures in the literature, where, for example, the piezoelectric material was thinned before being integrated onto the substrate [13], [14].

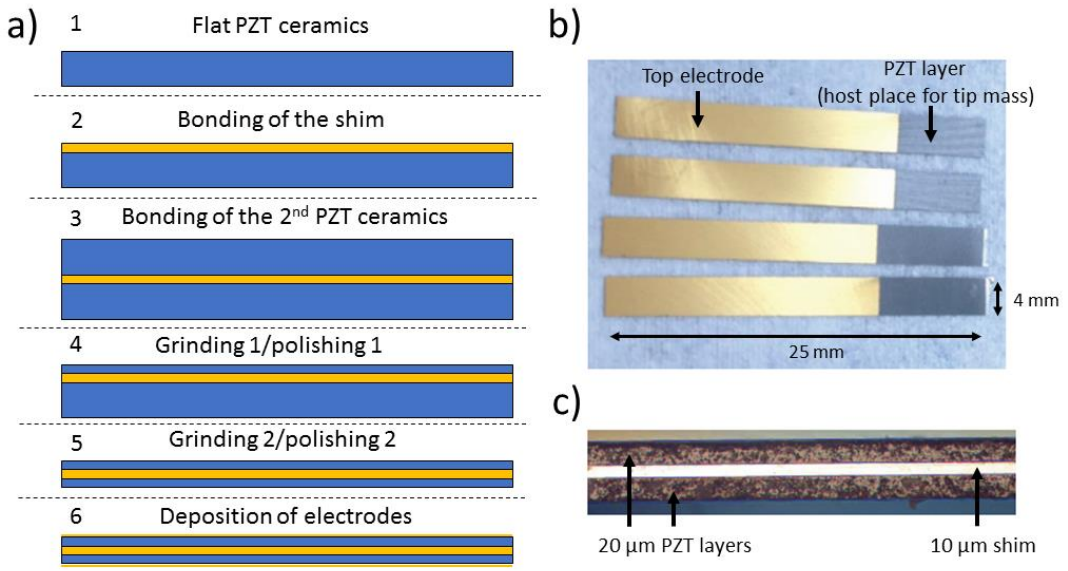

Figure 1.4: a) Schematic representation in cross-section of the processing steps for the fabrication of a bimorph cantilever PEH from lead zirconate titanate–based (PZT) bulk ceramics. Processed bimorph: b) top view and c) cross-section (optical microscope) [10].

1.1.2 Cantilever PEH figure of merit

The efficiency of the PEH strongly depends on the electromechanical properties of the piezoelectric material. The latter are related to the material's chemical composition, microstructure and phase composition. For cantilever structures operating in 31-mode, Priya [15] proposed a figure of merit (FOM) based on the material properties. The FOM of a 31-mode PEH, valid in off-resonance conditions ($FOM_{off-resonance}$), i.e., for a frequency far from the resonance frequency of the device, is given by:

$$FOM_{off-resonance} = \frac{\mathrm{d}_{31}^2}{\varepsilon_{33}^T \tan\delta_e} = \frac{d_{31} g_{31}}{\tan\delta_e} \tag{1.1}$$

with d_{31} and g_{31} the piezoelectric strain-charge and strain-voltage coefficients of the 31-mode, respectively, ε_{33}^T is the dielectric permittivity at constant stress along the poling direction and $\tan\delta_e$ the dielectric losses of the poled piezoelectric layer (introduced in Appendix A) [15].

In the case of a PEH that operates at its resonant frequency, the $FOM_{on-resonance}$ of a PEH operating in 31-mode is given by [15]:

$$FOM_{on-resonance} = \frac{k_{31}^2 Q_m}{s_{11}^E} \tag{1.2}$$

with k_{31} the 31-mode electromechanical coupling factor that represents the ratio of the mechanical to electrical energy conversion, Q_m the mechanical quality factor, and s_{11}^E the elastic compliance at constant electric field component of the piezoelectric layer (Appendix A).

We calculated the $FOM_{off-resonance}$ and $FOM_{on-resonance}$ for selected piezoelectric ceramics: two commercial lead zirconate titanate–based (PZT) ceramics [16] and one lead-free ceramic, namely, sodium potassium niobate ($K_{0.5}Na_{0.5}NbO_3$, KNN) [7]. A "soft" PZT composition (Pz29, MEGGITT Ferroperm) characterised by large dielectric permittivity,

piezoelectric coefficient, and dielectric losses but low mechanical quality factor and a "hard" PZT composition (Pz24, MEGITT Ferroperm) which exhibits a large mechanical quality factor but low piezoelectric charge constant [16] were selected. The electromechanical properties and corresponding FOMs are listed in Table 1.1.

Table 1.1: $FOM_{off-resonance}$ and $FOM_{on-resonance}$ calculated for Pz29, Pz24 and KNN ceramics based on d_{31}, g_{31}, $\varepsilon^{T}_{r,33}$, $\tan\delta_e$, Q_m, $k_{31}$and s^{E}_{11} the value were taken from [7], [16].

Properties \ Materials	Pz29 (soft)	Pz24 (hard)	KNN
d_{31} (pC/N)	-243	-58	-51
g_{31} (x 10^{-3} V.m/N)	-9.6	-15.4	-11.6
$\varepsilon^{T}_{r,33}$	2870	425	496
$tan\,\delta_e$	0.016	0.002	0.02
$FOM_{off-resonance}$ (x 10^{-12} m^2/N)	145	447	30
Q_m	76	1662	240
k_{31}(%)	37	29	27
s^{E}_{11} (x 10^{-12} m^2/N)	17	10.5	8.2
$FOM_{on-resonance}$ (x 10^{12} N/m^2)	0.6	13.3	2.1

d_{31} and g_{31}: 31-mode piezoelectric coefficient, $\varepsilon^{T}_{r,33}$: relative dielectric permittivity at constant stress, $\tan\delta_e$: the dielectric losses of the poled ceramic, Q_m: mechanical quality factor (measured on planar mode), k_{31}: 31-mode electromechanical coupling factor and s^{E}_{11} elastic compliance at constant electric field component.

The results revealed that the largest $FOM_{off-resonance}$ and $FOM_{on-resonance}$ were achieved for the hard PZT (Pz24) material, thanks to the low dielectric losses and high mechanical quality factor. In comparison, the KNN material exhibits moderate piezoelectric coefficients, mechanical quality factor and larger dielectric losses. Thus, the $FOM_{on-resonance}$ of the KNN material was larger than that of the soft PZT material, but one order of magnitude lower than that of hard PZT material.

The FOMs proposed by Priya [15] are based on the linear constitutive piezoelectric equations, and neglect the electroelastic non-linearities when the acceleration magnitude become large, which can result, for example, in softening [17], [18]. Moreover, the calculation of the $FOM_{off-resoncance}$ is performed without an electrical load connected, i.e., in open-circuit conditions whereas the power output depends on the connected electrical load [13]. The $FOM_{on-resonance}$ is calculated by considering the PEH excited with an applied acceleration matching the resonant frequency of the device.

Thus, the FOMs values for the 31- cantilever PEH are calculated based solely on the material properties and serve as a guideline in the evaluation of a piezoelectric material's performance for PEH applications. However, the power output of the PEH also depends on the electric and mechanical environments.

The PEH device usually consists of the harvester, which provides an AC electrical signal, the power-conditioning electronics and the energy-storage system [19]. The impedance matching and voltage regulation are performed with the power conditioning circuit to make compatible the output power with the electronic load.

Moreover, the harvested power also depends on the vibration sources, i.e., the acceleration level and the excitation frequencies. For example, a linear analytic model shows that for a harmonic excitation the power output is proportional to the cube of the frequency and the square of the acceleration amplitude [20]. Moreover, in operating conditions, the acceleration usually covers frequency bands [21], and the vibrations can have a stochastic and time-dependent magnitude and frequencies [19]. For PEH integrating a high Q_m piezoelectric material, which results in a narrow resonance bandwidth, if the excitation frequency does not match the frequency of the PEH, the harvested energy decreases [22]. For example, in Figure 1.1, the maximum output power of ~60 μW is reached at a frequency of ~23 Hz. However, if the vibration frequency shifts to ~ 24 Hz the output power drops to ~ 20 μW.

The most-often used materials for PEH have been lead-based piezoelectric materials, such as lead zirconate titanate ($Pb(Zr_{0.52}Ti_{0.48})O_3$, PZT) due to their high piezoelectric performance. However, the European regulation "Restriction of Hazardous Substances" (RoHS) directive has placed lead-based piezoelectric materials on the list of hazardous materials. These materials should be replaced by environmentally benign materials, which triggered the research on lead-free substitutes [23]. Among the potential lead-free candidates, the sodium potassium niobate–based compositions have attracted significant interest due to their high Curie temperatures and relatively high piezoelectric constants [24].

1.2 Sodium Potassium Niobate ($K_{1-x}Na_xNbO_3$)

1.2.1 Phase diagram and structure

Sodium potassium niobate ($K_{1-x}Na_xNbO_3$, $0 \leq x \leq 1$) is a solid solution of sodium niobate (NN, $NaNbO_3$) and potassium niobate (KN, $KNbO_3$). The NN-KN solid solution was reported in 1954 by Shirane *et al.* [25].

The KN-NN phase diagram is presented in Figure 1.5. At room temperature the NN is antiferroelectric with an orthorhombic unit cell. The KN and compositions with x smaller than 0.994 are ferroelectric with different orthorhombic unit cells [26].

The composition $K_{0.5}Na_{0.5}NbO_3$, referred to as KNN (red line in Figure 1.5), has been widely studied, as it exhibits the highest planar-mode electromechanical coupling factor (k_p) of 36–45 %, a remanent polarisation (P_r of ~30 μC/cm²) and the lowest coercive field (E_c of ~1 kV/mm) [27]–[29]. The typical dielectric, piezoelectric and electromechanical properties of the KNN are d_{33} of 80–160 pC/N [27], [28], thickness-mode electromechanical coupling factor k_t of 45 % [30], k_{31} of 22–27 % [27], [28], [30], relative dielectric permittivity of 290–420 (at 100 kHz) [27], [28] and Curie temperature T_C ~410-420 °C (see the Appendix A for definition of the parameters).

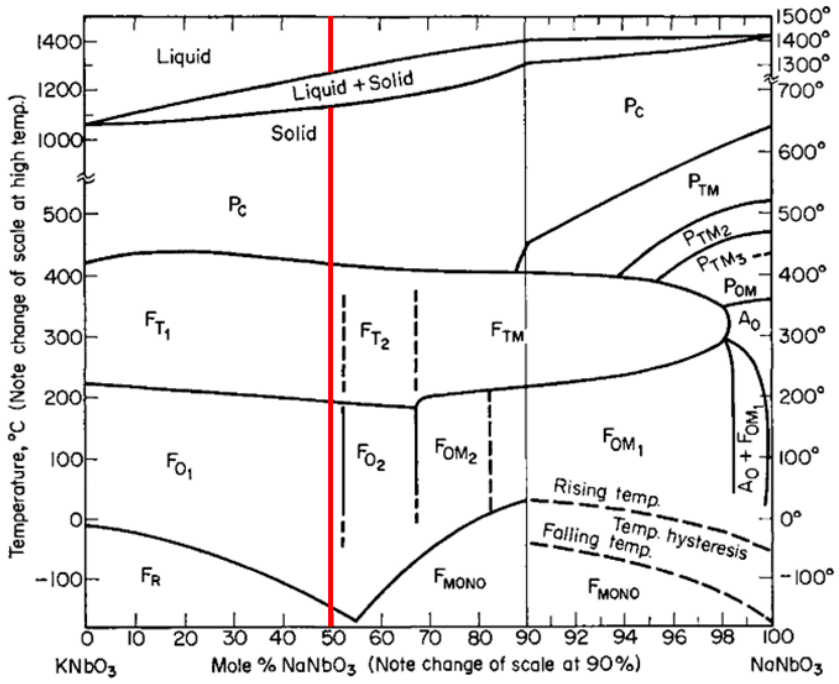

Figure 1.5: Phase diagram $KNbO_3$-$NaNbO_3$ [7]. The red line represents the $K_{0.5}Na_{0.5}NbO_3$ composition (KNN).

KNN possesses a perovskite structure with the general formula ABO_3, where K and Na occupy the A-site and Nb occupies the B-site. The Nb atom is located in the centre of the cube, coordinated with 6 oxygen atoms, and the K and Na atoms are located in the corners of the cube, coordinated with 12 oxygen atoms.

Above the Curie temperature the unit cell of KNN is a face-centred-cubic perovskite cell, schematically presented in Figure 1.6. Upon cooling, KNN shows phase transitions from the cubic phase to the tetragonal phase at ~410 °C, from the tetragonal phase to the monoclinic phase at ~200 °C (Figure 1.6) and from monoclinic to rhombohedral at -130 °C [7]. At room temperature the KNN is frequently described with an orthorhombic unit cell. However, it was shown that the ABO_3 cell is monoclinic with a β angle slightly larger than 90° [31], [32]. Phase transitions are accompanied with an expansion of the material upon cooling [33], namely, a linear expansion of ~0.04 % for the cubic-to-tetragonal transition and of ~0.01 % for the tetragonal to monoclinic phase transition.

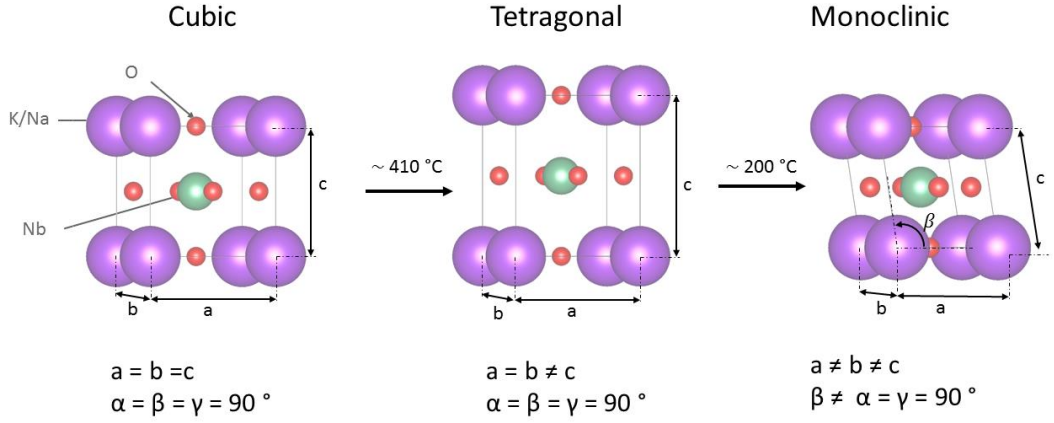

Figure 1.6: Schematic representations of the cubic, tetragonal and monoclinic KNN phases [7], [32].

1.2.2 Processing of bulk $K_{0.5}Na_{0.5}NbO_3$ (KNN)

KNN is commonly produced by solid-state synthesis via the reaction of potassium- and sodium carbonate and niobium pentoxide (Figure 1.7). The reaction is given by equation (1.3).

$$K_2CO_3(s) + Na_2CO_3(s) + 2Nb_2O_5(s) \rightarrow\ 4\ K_{0.5}Na_{0.5}NbO_3(s) + 2\ CO_2(g) \tag{1.3}$$

According to the literature, the synthesis of KNN takes place in two steps at temperatures between 600 and 950 °C [34], [35]. In the first step, the sodium, potassium and oxygen ions diffuse onto the Nb_2O_5 and an intermediate polyniobate phase ($(K,Na)_2Nb_4O_{11}$) is formed at the interface between the carbonates and the niobium pentoxide. In the second step the KNN perovskite is formed at the interface between the intermediate phase and the carbonates as a result of the diffusion of potassium and sodium ions through the intermediate layer towards the niobium pentoxide [34].The process is diffusion-controlled and the reaction rate is determined by the diffusion of the slowest species, i.e., the potassium ions [36].

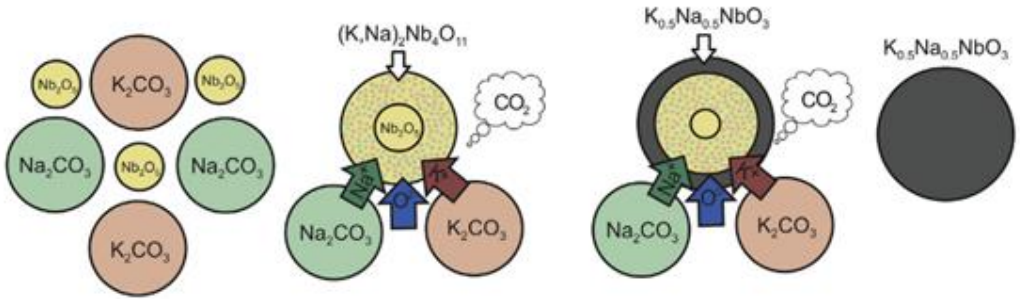

Figure 1.7: Schematic presentation of the reactions during the solid-state synthesis of KNN from K_2CO_3, Na_2CO_3 and Nb_2O_5 raw materials [37].

It is reported that it is challenging to prepare single-phase KNN ceramics with a homogeneous microstructure and high density by conventional sintering [38]–[40]. The difficulty in reaching a high density for the KNN is related to the diffusion mechanisms during the processing of KNN. It was reported that the sintering of KNN is similar to $NaNbO_3$ (NN). For NN, the surface diffusion is active in the temperature range 500–600 °C, due to its low activation energy (~50-60 kJ/mol) [41]. The surface diffusion causes coarsening of the microstructure and grain growth during the initial stage of the sintering, thus reducing the curvature of the neck and the driving force for sintering.

KNN densifies in a very narrow temperature range only a few tens of degrees below the KNN solidus temperature (~1140 °C) [42]. However, despite the careful selection of sintering conditions (temperature, time, atmosphere), the ceramic frequently has a low density and the microstructure exhibits a bimodal particle size distribution [43], [44] consisting of a matrix with fine grains in between larger grains containing entrapped pores (see yellow arrow in Figure 1.8c).

It is also challenging to control the stoichiometry of the KNN during the processing. The stoichiometry of KNN can vary due to the hygroscopicity of the raw materials, namely, carbonates. Thus, the synthesis requires drying of the raw material and weighing the reagents in a dry atmosphere [45].

The stoichiometry of KNN could also vary due to the volatility of alkalis at elevated temperatures. The vapour pressure of potassium is an order of magnitude larger than that

of the sodium above KNN ceramics in the temperature range 900–1030 °C [46]. Due to the volatilisation of alkalis the stoichiometry of KNN is altered, for example, it shifts towards a Na-rich composition during the sintering of KNN material [47].

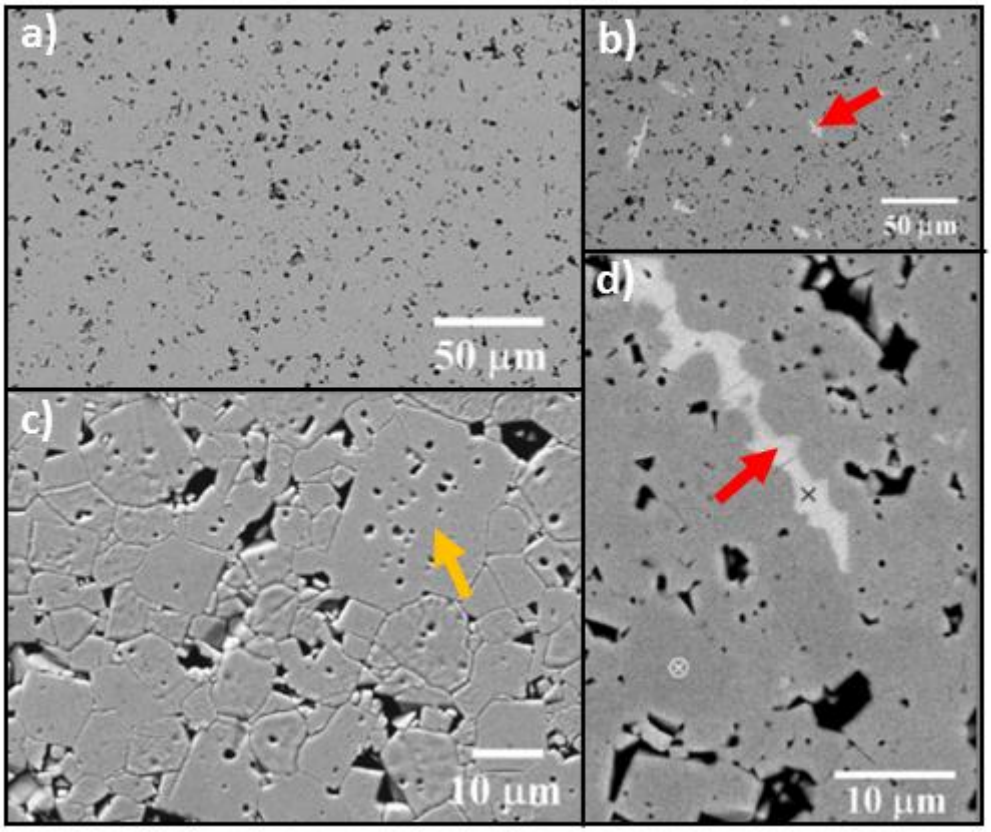

Figure 1.8: SEM images of KNN ceramic sintered at 1100 °C for 2 h (a) polished and c) thermally etched) and for 24 h (b) and d) polished). The yellow arrow illustrates an abnormally grown grain with internal pores. d) Polished surface matrix phase - KNN and a brighter phase (marked by red arrows) tungsten bronze (TB) [43].

The formation of a polyniobate phase has been frequently reported in KNN ceramics (see red arrows in Figure 1.8b and d) [38], [47]. The polyniobate phase has the tungsten-bronze crystal structure (TB) and a composition similar to $K_{5.75}Nb_{10.85}O_{30}$ with a small amount of sodium [48].

A lot of efforts have been put into increasing the density of KNN and thus improving the functional properties of the KNN material. The relative density can be tailored by varying the sintering conditions [39], [49]–[51]. The literature reports the following:

1. Zuo *et al.* [52] found that increasing the sintering temperature from 1020 °C to 1100 °C increases the density and that the density of the ceramics decreases when the sintering temperature was further increased above the threshold temperature. A similar trend was observed by other authors with different threshold temperatures of 1080 °C [49] and 1130 °C [53] and showed that the optimal piezoelectric properties do not necessarily correspond to the sample with optimal density [49]. Sintering of the KNN ceramics at high temperature could lead to the formation of the TB phase [39], [44], [49] and the volatilisation of the alkalis shifts the material composition which could results in the presence of a liquid phase during the sintering that promoted the grain growth [38], [54].

2. Fisher *et al.* [55] found that increasing the sintering dwell time at 1040 °C from 30 min to 1 h and 10 h in an oxygen atmosphere promoted the densification of the material. Similarly, it was found by Bah [56] that for KNN ceramics sintered at 1090, 1100 and 1110 °C, increasing the dwell time from 2 h to 48 h resulted in an increase of the relative density. However, Acker *et al.* [44] found that it yielded an increase of the relative density of stoichiometric KNN when the dwell time was increased from 3 min to 30 min, but then the density decrease when the sintering dwell time was increased to 8 h at 1105 °C. An increased sintering dwell time was also reported to lead to the formation of the TB phase [43], [51]
3. The sintering of KNN in a reducing atmosphere leads to the formation of oxygen vacancies, which resulted in grain-boundary roughening, reducing the abnormal grain growth, increases in the relative density [51], [55], [57] and a partial reduction of the Nb^{5+} ions to Nb^{4+} [58]. The samples were electrically conductive, i.e., n-type conductivity was observed, whereas the conductivity of the KNN was reported to be of p-type in oxygen-sintered KNN ceramics [59]. After sintering KNN in a reducing atmosphere, a post annealing in oxygen atmosphere was necessary to reduce the conductivity of the material [58]. Some authors found that the sintering of KNN in oxygen in comparison to air slightly increased the relative density of the KNN from 92.3 % to 93.1 % [57]. The increase in the relative density was associated with the lower formation energy of A-site vacancies in an oxygen-rich atmosphere [57], which favours the atomic diffusion and improves the densification [42]. Sintering of KNN-based material in a high oxygen partial pressure was reported by some authors to increase the P_r, d_{33} and k_p and lower the E_C of the ceramics [59], [60]. Other authors found that the piezoelectric coefficient d_{33} and dielectric properties of their KNN-based ceramics were independent of the oxygen partial pressure during the sintering [61].

Another approach to tailor the microstructure and functional properties of KNN material is the modification of its chemical compositions [52], [62]. It was shown that the chemical modification of KNN with Sr ($(K_{0.5}Na_{0.5})_{1-2x}Sr_xNbO_3$) inhibited the grain growth and resulted in a slight increase of the relative density of the material from 94.4 % for unmodified KNN to 95.8 % for $(K_{0.5}Na_{0.5})_{1-2x}Sr_xNbO_3$with the 0.5 % Sr [62]. The grain size of the ceramics decreased from 6.15 ± 4.01 μm for pure KNN to 1.76 ± 1.26 μm for 0.5 % Sr modified KNN [63]. At a Sr concentration over 2 % the relative density decreases [64] and the formation of a polyniobate phase was observed [48]. The 0.5 % Sr modified KNN ceramic exhibited a permittivity of 500, a d_{33} of 95 pC/N and a dielectric loss of 0.04 [64]. The 0.5 % Sr-modified $(K_{0.5}Na_{0.5})_{0.99}Sr_{0.005}NbO_3$ (KNNSr) composition was selected for this work.

1.3 Processing of Thick Films using Thick-Film Technology

In Subchapter 1.1.1 we show that bimorph PEH can be produced from bulk ceramics. A more appropriate procedure to produce ceramic layers with a thicknesses ranging from 1 μm to a few hundreds of micrometres directly onto a substrate is thick-film technology (ThickFT) [65], [66]. For applications requiring layers in this range of thickness, ThickFT allows the patterning of the films directly onto the substrates, which simplifies the process and requires fewer processing steps, avoiding, for example, grinding and polishing of the bulk material [65], [66] and consequently lowering the production cost. The main processing steps of ThickFT are schematically presented in Figure 1.9. The process starts from the

synthesised powder and the preparation of a suspension by dispersing the powder in a solvent [67]. The suspension should have the required properties for the patterning technology. Such properties are, for example, the stability [67], [68], the viscosity [69] or the conductivity [70] of the suspension. Then, the suspension is used to pattern the as-deposited layer onto the substrate using technologies such as screen-printing [71], pad-printing [72] or electrophoretic depositions [73]. The as-deposited layers are then fired (sintered) at elevated temperatures to impart mechanical and functional properties to the thick films.

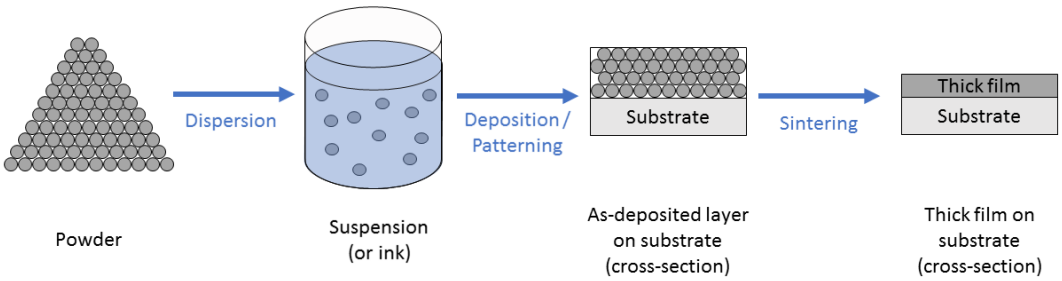

Figure 1.9: Processing of thick films on a substrate using thick-film technology.

A thick film is associated with various challenges during the sintering at elevated temperature. It is frequently deposited on a rigid substrate such as alumina. During the sintering the layer tends to shrink; however, it is constrained by the substrate and thus shrinks predominantly in the thickness direction. The sintering of the layers in constrained conditions may lead to the formation of defects in the thick films and/or delamination of the layer from the substrate. An additional challenge is the compatibility of chemically different materials (substrate, thick film, electrodes) at elevated temperatures, which could lead to the formation of undesirable phases at the interfaces. Also, the large area-to-volume ratio could lead to the loss of volatile oxides, which may change the stoichiometry of the thick film [65].

In this work we processed the thick films by electrophoretic deposition (EPD). We selected EPD because it allows the simultaneous deposition of layers on two sides of a substrate, which reduces the numbers of processing steps in the course of the preparation of KNNSr bimorph cantilevers.

1.3.1 Electrophoretic deposition (EPD)

EPD is based on the mobility of charged particles dispersed in a solvent under an external applied electric field (E) between the working and counter electrode (WE and CE, respectively) immersed in a suspension. This is followed by the deposition, i.e., the formation of a layer of particles at the surface of the oppositely charged electrode (WE) [74]. Thus, EPD requires a conductive or metallised ceramic substrate. EPD has been successfully used for the preparation of coatings, free-standing objects, laminated and functionally graded structures [75]. An EPD setup, illustrating the deposition of particles with a negative zeta-potential (ZP) on the positively charged WE, is schematically presented in Figure 1.10.

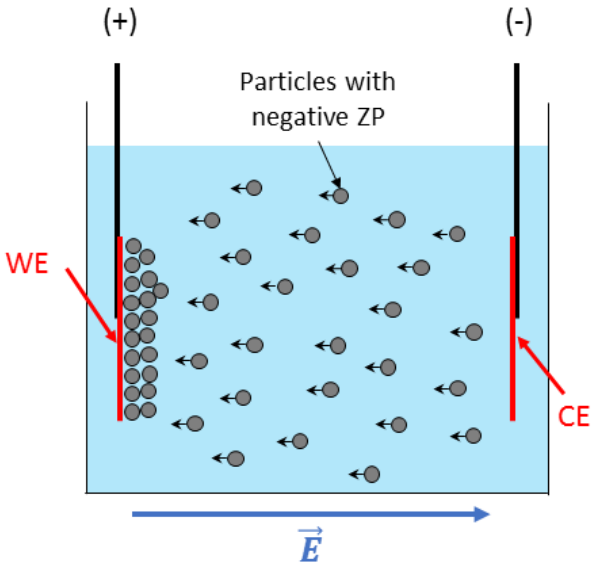

Figure 1.10: Schematic illustration of the EPD setup. Particles exhibiting a negative ZP move towards and deposit on the working electrode (WE), CE is the counter electrode.

The kinetics of the deposition have been described by the formula proposed by Hamaker [76]:

$$\frac{dm}{dt} = \mu_e \, C_s \, E \, \mathrm{S}_{elec} \tag{1.4}$$

where m is the deposited mass, t is the time, C_s is the concentration of particles in suspension, E is the electric field between the electrodes, S_{elec} is the area of the WE, and μ_e is the electrophoretic mobility. This formula indicates that the deposition rate (noted dm/dt, in kg/s) during EPD depends both on **the suspension properties**, (μ_e, C_s) and **the deposition conditions** (E, S_{elec}).

1.3.1.1 Influence of the properties of the suspension on EPD

EPD requires the preparation of a stable suspension of charged particles homogenously distributed in a solvent, which can be water [77] or an organic solvent such as isopropanol, ethanol or acetone [78], [79]. The particles dispersed in a solvent are characterised by their ZP. An absolute value of ZP of a few tens of mV ensures the stability of the suspension and ensures the mobility of the particles towards WE by the application of the external electric field. A detailed description of the electrostatic stabilisation of metal oxide (MO) particles in water can be found in Appendix B. The ZP is given for a non-conducting particle in the Smoluchowski approximation as [80]:

$$ZP = \frac{\eta v_e}{\varepsilon_r \varepsilon_0 E} \tag{1.5}$$

where η is the dynamic viscosity of the solvent, v_e is the electrophoretic velocity, E is the applied electric field strength, ε_r is the relative permittivity of the solvent, ε_0 is the permittivity of the vacuum. The electrophoretic mobility is:

$$\mu_e = \frac{v_e}{E} \tag{1.6}$$

Thus, for a given solvent, the electrophoretic mobility is proportional to the ZP (Equation (1.5)). A high absolute value of the ZP (typically > 20 mV) and a low ionic strength ensure the electrostatic stabilisation of MO in water-based systems [81].

In EPD, organic solvents are frequently used and in such solvents the particles are often stabilised using electrosteric stabilisation. Electrosteric stabilisation uses polyelectrolytes, which are polymers combining the steric effect of the long macromolecule chains and the electrostatic effect of the dissociated functional groups. For the stabilisation of KNNSr particles, we selected a polyelectrolyte containing carboxyl groups (R-COOH). This kind of polyelectrolytes have already been reported in the literature to be effective for the stabilisation of different MO particles in ethanol (EtOH) [82]–[85]. The effectiveness of the stabilisation of the particles in the selected solvent depends on the type of functional groups of the polyelectrolyte, their degree of dissociation, the conformation of the polyelectrolyte, the concentration of the adsorbed and free polyelectrolyte and the ionic strength of the suspension [86], [87].

Polyacrylic acid $(C_3H_4O_2)_n$, PAA, Figure 1.11a) is a weak acid and its dissociation in water is pH dependent. For PAA, it was shown that in water at pH below 3 the carboxyl groups of the PAA are not dissociated (R-COOH), and the polymer is in a coil configuration (Figure 1.11b) [88], [89]. When the pH is larger than 3, the carboxyl groups partly dissociate into carboxylate ions ($R\text{-}COO^-$). The electrostatic repulsions between the carboxylate groups uncoil the polymer chains (Figure 1.11b). When the pH is higher than 11, the polymer is totally dissociated and in a train configuration (see Figure 1.11b) [90].

The use of other carboxylic-containing polyelectrolyte such as poly(acrylic acid-co-maleic acid) $((C_4H_4O_4)_Y\text{-}(C_3H_4O_2)_X$, PAM, see Figure 1.11c) has also been reported to be effective for the stabilisation of MO particles. PAM which presented a larger charge density than PAA was shown to be effective for $BaTiO_3$ (BT) particles dispersed in water at pH 10 [91], [92] and for the stabilisation of PZT particles in aqueous dispersion at alkaline pH [93].

The stabilisation of MO particles in ethanol is more challenging, since PAA does not dissolve in ethanol. Thus, an organic base such as n-butylamine (BA) was used to deprotonate the carboxylic groups of the PAA [82]–[84], [90]. The deprotonated carboxyl group interacts with the positively charged site at the surface of the MO particle and contributes to their stabilisation in ethanol [90]. Similarly, we expect that PAM could be used for stabilisation of KNNSr particles in ethanol with the addition of n-butylamine.

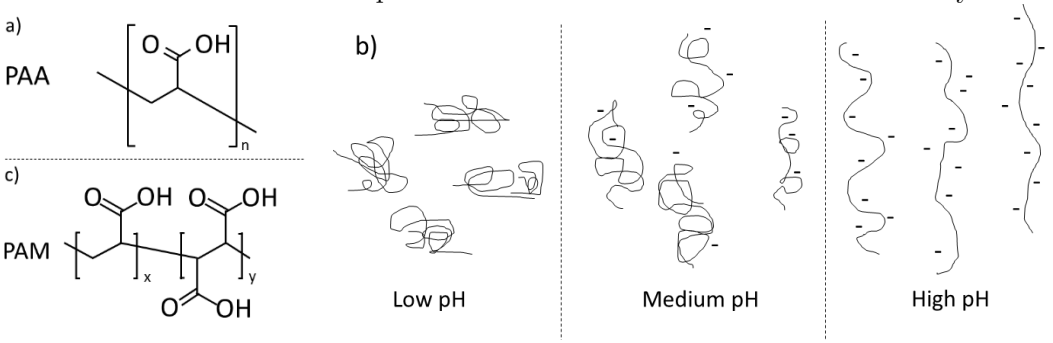

Figure 1.11: a) Structural formula of one unit of polyacrylic acid (PAA), b) Schematic representation of conformation of PAA: coil at low pH, partly uncoiled at medium pH, uncoiled at high pH and c) Structural formula of one unit of poly(acrylic acid-co-maleic acid) (PAM).

Parameters that also influence the EPD are the concentration of particles (C_S) and the conductivity of the suspension (σ_{susp}). Increasing the concentration of the particles while

keeping electrophoretic mobility, electrode surface and electric field strength constant cause the deposited mass to increase according to Equation (1.4). This was verified experimentally for a range of concentrations of the particles [76], [94].

Increasing the conductivity of the suspension is associated with an increase of the ionic strength [95], and consequently the Debye-Hückel length is reduced (see Appendix B). This effect lowers the ZP and the stability of the suspension [96]. In an electrosterically stabilised suspension, the ionic strength influences the conformation of the polyelectrolyte and the amount of adsorbed polyelectrolyte on charged surfaces [87]. Thus, in order to achieve the deposition of particles on a selected substrate by EPD, the σ_{susp} has to be typically in the range of a few tens of μS/cm [70], [90], [97]. The optimal conductivity range for EPD must be optimised for each individual system, since it depends on the many factors including solvent, particles and type of additives [74].

1.3.1.2 Influence of the deposition conditions on EPD

The time evolution of the deposited mass onto a selected substrate during EPD is based on the equation proposed by Hamaker (Equation (1.4)). The electric field strength and current density in the suspension between two infinite plane parallel electrodes are related by the formula [98]:

$$E = J/\sigma_{susp} \tag{1.7}$$

with J is the current density and σ_{susp} the conductivity of the suspension.

Assuming that the concentration of particles, the conductivity of the suspension and the electrophoretic mobility of the particles do not vary during the deposition, then for a deposition performed at a constant current density (J), the deposited mass (m) increases linearly with the deposition time, with a constant deposition rate (dm/dt) [99], [100]. However, during the EPD the concentration of particles in suspension decreases, thus the dm/dt decreases with increasing deposition time [100]. When the deposition times are sufficiently short, typically one or two minutes, the concentration of particles in the suspension does not vary significantly and the relationship between the deposited mass and the deposition time is linear [101].

Since the deposited mass is proportional to the electric field, it increases with the increasing applied voltage and current, which was verified experimentally [97], [102], [103]. For a deposition performed at constant current, the electric field in the suspension is inversely proportional to the conductivity of the suspension (Equation (1.7)), thus the deposited mass decreases with increasing conductivity of the suspension [94], [104].

It was reported that the morphology of the deposits depends on the dm/dt. A low dm/dt leads to the more homogeneous deposition of the particles in comparison to a higher dm/dt [95], [104]. For example, lead zirconate titanate as-deposited layers processed at constant current and identical conditions from the suspension with a conductivity of 20 ± 0.5 μS/cm, exhibited a more homogenous distribution of the particles (Figure 1.12a) than the as-deposited layers processed from the suspension with a lower conductivity of 17 ± 0.5 μS/cm and a larger dm/dt (Figure 1.12b) [104].

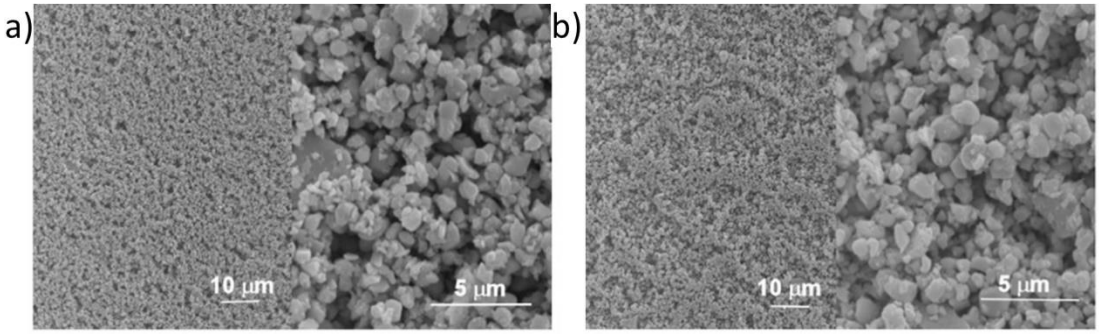

Figure 1.12: SEM images of lead zirconate titanate particles deposited by EPD at a constant current density from two suspensions with conductivities of a) 20 ± 0.5 μS/cm and b) 17 ± 0.5 μS/cm [104].

It is reported that a low dm/dt, which can be achieved at a low electric field (Eq. (1.4)), results in a larger green density of the as-deposited layer [95] and smaller pores [105]. However, another publication [106] proposed that the high electric field strength (larger dm/dt) enhanced the electro-osmotic flow around the particles. As a result, the particles rearrange and could be pulled together near the substrate, which enables the formation of deposits with a larger green density [106]. Similarly, the theoretical model showed that with increasing electric field the particles were less ordered, but resulted in layers with a larger green density [107].

The uniformity of the deposits in term of their thickness is closely related to the uniformity of the electric field between the WE and CE. It was shown that the edges of the layers deposited in a setup consisting of two plane parallel electrodes with finite dimensions were regularly thicker than in its centre for a short deposition time [108], [109]. This feature was explained by the singularity of the electric field [110], which was a few times stronger at the electrode edges than in the centre of the electrode. With increasing deposition time, the thickness uniformity of the as-deposited layers was found to improve [104], [108]. Moreover, the thickness uniformity of the as-deposited layers could be tailored by the conductivity of the suspensions [104], [108], [111] and the setup geometrical parameters such as the interelectrode distance [112].

1.3.2 Densification of thick films

The as-deposited MO layers on a selected substrate need to be sintered to develop microstructure, mechanical strength and suitable functional properties [113]. During the sintering, a bulk ceramic shrinks along all the directions (see Figure 1.13a). In contrast, the thick film clamped on a rigid substrate can only shrink along the thickness direction (denotes z direction, Figure 1.13b) [114].

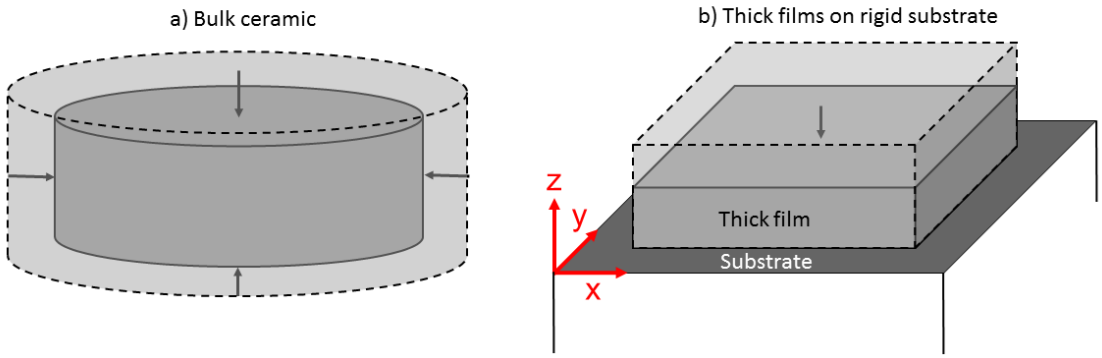

Figure 1.13: Schematic representations of the sintering of a) bulk ceramics and b) thick films clamped on a rigid substrate. Black arrows represent the shrinkage direction. Dashed line: before sintering, solid line after the sintering.

The inability of the layer to shrink in the x and y directions results in in-plane tensile stresses in the layer. Due to these in-plane tensile stresses, the densification rate and final density of thick films processed on rigid substrate are reduced in comparison to freely sintered compacts [115], [116]. The slower densification rates and lower sintered densities were frequently experimentally verified for MO thick films [117]–[119]. It was observed that the sintering in constrained conditions impacted the final microstructure of the thick films [120], [121]. Moreover, if the tensile stresses do not relax during the high-temperature processing, this can lead to the formation of processing defects (cracks, delamination) [122].

For a selected MO material, substrate and sintering conditions, there is a critical as-deposited thickness above which defects would grow during the sintering in constrained conditions [123], [124]. Thus, defects are more prone to happen in thicker films. To minimise the formation of defects we should either reduce the densification rate, i.e., using larger particles, decrease the sintering temperature, decrease the density of the as-deposited layer, and/or improve the homogeneity of the green body [124], [125].

Since the sintering of MO material requires high temperature (> 800 °C), the thick film and the substrate should be chemically inert. For example, processing of PZT-based materials on a platinised alumina substrate (Pt/AO) leads to the formation of β-aluminate at the interface, which results in delamination of the Pt/PZT from the substrate [126]. To minimise the chemical interactions between the materials, the substrate should withstand the sintering temperature, and the diffusion between the chemically different materials (thick film, electrode, substrate) should be as low as possible.

1.3.3 Sodium potassium niobate–based thick films

The majority of KNN-based thick films have been processed by the conventional method. To the best of our knowledge, there are only a few studies describing the processing of KNN by EPD.

$K_{0.5}Na_{0.5}NbO_3$ thick films were processed by EPD from acetone-based [127] and water-based suspensions [128]. The cross-section of the thick film processed from a water-based suspension and sintered at 1100 °C is shown in Figure 1.14. The 13-μm-thick film consisted of micrometre-sized particles. A relative density, calculated from the mass and the thickness of the KNN thick films, was ~85 %. The relative dielectric permittivity of those thick films was 495 and the tan δ was 0.08 measured at 1 MHz and room temperature. The film poled at 12 kV and 80 °C for 8 h had a d_{33} of 69 pC/N.

The KNN thick films processed from an acetone-based suspension were ~45 μm thick and exhibited a relative dielectric permittivity of 397 and dielectric loss of 0.07. The density of the film was not given. After poling under the same conditions for a shorter time (2 h), the piezoelectric coefficient d_{33} was 40 pC/N. Based on these data it is challenging to conclude about the influence of the solvent on the functional properties of KNN thick films.

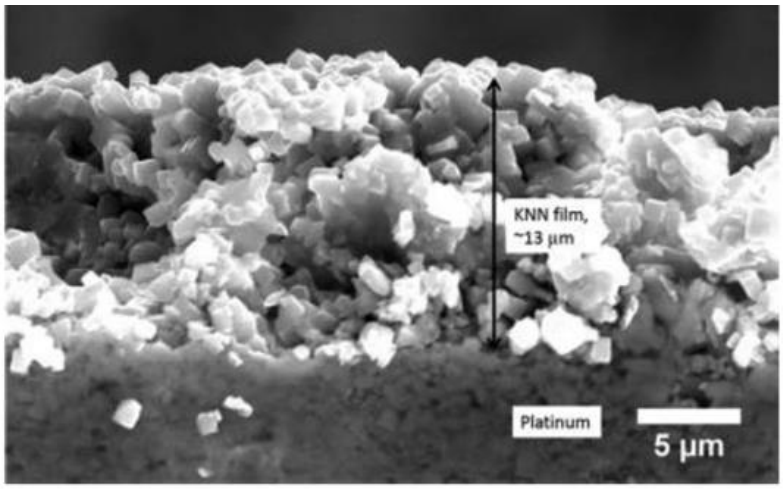

Figure 1.14: Fracture cross-section SEM images of the KNN thick film deposited on a platinum electrode by EPD from a water-based suspension sintered at 1100 °C for 2 h [128].

The KNN thick films processed by EPD have similar properties to KNN-based thick films processed by screen-[72], [129], [130], or pad-printing [72]. The reported dielectric and piezoelectric properties of the KNN thick films scattered, i.e., d_{33} in the range 40–69 pC/N, dielectric permittivity in the range 300–500, dielectric losses in the range 0.01–0.08, [72], [127]–[129]. However, a direct comparison of the properties of the thick films is difficult due to the different nominal compositions, processing conditions, microstructures and lack of data, such as the thickness, density and grain size.

1.4 Sodium Potassium Niobate–Based Material Integrated in a Cantilever PEH

KNN-based ceramics and films were integrated in a unimorph cantilever PEH configuration. Since the dimensions of the PEHs vary, the devices are compared using the power density, i.e., the power normalized by the volume. However, the various architectures of the PEHs, the eventual addition of a proof mass, and the difference in the measurement conditions (acceleration, resonance frequency, etc.) make it challenging to directly compare the power densities harvested at the resonance with an optimal electrical load. Typical power densities from the literature for various unimorph PEH integrating KNN-based layers prepared with various process and dimensions are presented in Table 1.2.

Table 1.2: The power densities of unimorph KNN-based PEH measured at the given acceleration and resonance frequency on the specified resistive. The thickness, relative density of KNN-based layers, the substrate material and substrate's thickness are also given.

Material	Thickness μm	Processing	Substrate	Proof mass	Relative Density %	Acceleration m/s^2	Resonance frequency Hz	Resistive load kΩ	Power density mW/cm^3	Literature
KNN	300	Bulk	350 μm stainless steel	No	95	/	10	680	0.05	[131]
KNN	500	Bulk	800 μm spring steel	No	97	9.8	84	450	9.8	[14]
KNN + CuO	500	Bulk	800 μm spring steel	No	97	9.8	93	250	12	[14]
KNN	400	Bulk	1600 μm fibre reinforced plastic	No	93*	**	57	470	0.008	[13]
KNN + 0.25 mol % Fe_2O_3	400	Bulk	1600 μm fibre reinforced plastic	No	94	**	57	470	0.38	[13]
1 % Mn doped KNN	500	Bulk	900 μm stainless steel	No	98	10.0	90	380	0.32	[132]
$K_{0.45}Na_{0.55}NbO_3$	2.2	Sputtering	30 μm stainless steel	Yes	/	10.0	393	5	0.41	[133]
$K_{0.45}Na_{0.55}NbO_3$	1.0	Sputtering	22 μm silicon	Yes	/	9.9	1510	90	2.3	[134]
0.5 % Mn doped KNN	2.0	CSD	22 μm stainless steel	Yes	/	9.8	132	9.6	1.8	[135]

CSD: chemical solution deposition, Sputtering: RF magnetron sputtering, Bulk: cut and thinned starting from bulk ceramics, *: calculated assuming a theoretical density of 4.51 g/cm^3 for KNN, **: in this article the acceleration is not given, but the power density is given for a displacement of 2 mm.

The KNN layers in the thickness range of a few hundreds of micrometres have been processed from bulk ceramics. The unimorph PEHs were processed by thinning the bulk ceramics to the desired thickness and then gluing them to the substrates [13], [14], [131], [132]. Depending on the relative density, microstructure, and measuring conditions, the power density ranged from 0.008 mW/cm^3 to 9.8 mW/cm^3 for unmodified KNN. The power output at the resonance of the PEHs was increased by the chemical modification of the KNN composition with Fe_2O_3 [13] and CuO [14], which increased the Q_m and thus the on-resonance harvested power density.

A relatively high power density has been achieved from PEH consisting of few-micrometres-thick KNN layers processed by physical methods, such as sputtering or from chemical solution deposition (CSD) [133]–[135]. The power density of RF magnetron sputtered $K_{0.45}Na_{0.55}NbO_3$ films ranged from 0.41 mW/cm^3 to 2.3 mW/cm^3. The difference is presumably related to the variation in the geometry of the device, the substrate and resulting variation of the resonance frequency. The piezoelectric films realised using sputtering or CSD can be micromachined and integrated as functional materials into micro-electromechanical systems (MEMS). The compatibility with CMOS (complementary metal oxide semiconductor) technology offers the possibility to integrate the micro-PEH into microdevices and microsystems [19]. Nevertheless, the sputtering and CSD methods are limited to relatively thin layers (typically below 3 μm), which restricts the power output of the PEH [71].

The thickFT has already been successfully used for the processing of PEHs that integrated lead-based piezoelectric layers [71], [136], [137]. To the best of our knowledge, KNN-based layers with thicknesses of a few tens of micrometres processed by thick-film technology have not yet been processed for integration in a bimorph PEH.

1.5 Summary

Piezoelectric energy harvesters (PEHs) offer the possibility to convert mechanical energy into electrical energy using the piezoelectric effect. The most common structures are the unimorph and bimorph cantilevers with a few-tens-of-micrometres-thick piezoelectric layers integrated on a substrate. Lead-based materials are generally used in PEH. However, due to the environmental and health concerns the European regulations triggered the research on lead-free piezoelectric materials for integration in PEH.

One of the candidates is potassium sodium niobate with the composition $K_{0.5}Na_{0.5}NbO_3$ (KNN). The processing of KNN is challenging due to the difficulty in densifying the material, which sinters in a narrow temperature range close to the solidus temperature, and due to difficulty of stoichiometry control, due to the volatility of the alkalis and the formation of a tungsten bronze phase during the processing.

Electrophoretic deposition is a method that allows for the processing of a few-tens-of-micrometres-thick layers directly onto both sides of a substrate. This method based on the dispersion of particles in a solvent, the mobility of charged particles towards a conductive substrate by the application of DC electric field and their deposition on the substrate. The particle size and morphology, the suspension properties and the deposition conditions impact the quality of the as-deposited layers. The literature shows that the conductivity of the suspension and the geometry of the EPD setup impact the thickness uniformity of the as-deposited layer.

A sintering step is required to consolidate the as-deposited layers. Clamping of the thick films on the rigid substrates results in in-plane tensile stresses in the thick films during the sintering, which lowers the densification rate and the relative density of the thick films in comparison to bulk ceramics sintered under identical conditions. The stresses may also

promote the formation of defects and/or the delamination of the thick films from the substrate. Sintering conditions have to be optimised to obtain a single-phase, dense microstructure and the appropriate piezoelectric properties of the thick films, required for a high PEH power output.

KNN-based materials have been integrated in unimorph PEHs. The piezoelectric layers with a thickness a few hundreds of micrometres have been processed from bulk ceramics, and up to 2.2 μm by RF magnetron sputtering and chemical solution deposition. The ThickFT offers the possibility to integrate a few-tens-of-micrometres-thick KNN layers directly onto a substrate and was used in this work for the preparation of KNN-based layers integrated in a bimorph structure.

.

Chapter 2

Aims and Hypothesis

2.1 Aims

The aims of the dissertation are:

- To optimise the properties of the suspension, deposition and sintering conditions for processing $(K_{0.5}Na_{0.5})_{0.99}Sr_{0.005}NbO_3$ (KNNSr) layers on a rigid 640-μm-thick platinised alumina substrate by electrophoretic deposition (EPD). The goal is to understand the processing-properties relationship and to reproducibly process defect-free 20–40-μm-thick KNNSr films with a uniform thickness and homogeneous microstructure, and with a thickness-mode electromechanical coupling factor $k_t \approx 40$ %.

- To adjust the experimental set-up and processing conditions to prepare the bimorph structure of KNNSr thick films on a flexible platinised 110-μm-thick alumina substrate and to characterise it in terms of microstructure and electromechanical properties. The goal is to evaluate whether the KNNSr thick films integrated onto this substrate can be used for piezoelectric energy harvesting (PEH) applications and to address the limitations.

2.2 Hypothesis

The hypotheses of the dissertation are as follows:

- EPD requires charged particles well dispersed in a solvent. To achieve this, KNNSr particles will be dispersed in ethanol using poly(acrylic acid-co-maleic acid) and will have a high absolute value of the zeta-potential suitable for EPD.
- The layers as-deposited by EPD frequently have a non-uniform thickness with thicker edges. With the optimisation of the deposition conditions, namely interelectrode distance and counter electrode diameter, we will process the layers with controlled and uniform thicknesses on rigid substrates.
- The sintering of KNNSr layers on an alumina substrate is difficult due to the sintering in constrained conditions, volatilisation of the alkalis and the formation of secondary phases. We hypothesise that by optimising the sintering temperature and atmosphere we will process the layers with a perovskite structure, homogeneous microstructure, density over 85 %, and thickness-mode electromechanical coupling factor k_t of $\sim$ 40 %.
- The bimorph piezoelectric energy harvester requires the integration of piezoelectric layers on both sides of a flexible substrate. We hypothesise that such structure will be realised by EPD with a specifically designed setup. We assume that the deposition and sintering conditions optimised for KNNSr on rigid substrates will allow processing of

KNNSr thick films onto flexible substrates and that the sintered KNNSr thick films on flexible substrates will have similar properties as KNNSr thick films on rigid substrates.

Chapter 3

Materials and Methods

3.1 Chemicals

The chemicals used for the processing and characterisation of the powder, the suspensions and the thick films are collected in the Table 3.1.

Table 3.1: List of chemicals used in this work.

Name	Chemical formula [abbreviation]	Specifications and supplier
potassium carbonate	K_2CO_3	Anhydrous, 99.9+ %, ChemPur, Germany
sodium carbonate	Na_2CO_3	Anhydrous, 99.9+ %, ChemPur, Germany
Niobium (V) oxide	Nb_2O_5	99.9 %, Sigma Aldrich, Germany
Strontium carbonate	$SrCO_3$	99.994%, Alfa Aesar, Germany
2-propanol	C_3H_8O	99.8 %, pure for analysis, Sigma Aldrich, Germany
acetone	C_3H_6O	Carlo Erba Reagents, Italy
absolute ethanol	C_2H_6O [EtOH]	Anhydrous, Carlo Erba Reagents, Italy
n-butylamine	C_4H_9-NH_2 [BA]	99 %, Alfa Aesar, Germany
poly(acrylic acid-co-maleic acid)	$(C_4H_4O_4)_Y$- $(C_3H_4O_2)_X$ [PAM]	50 wt. % water solution, M=3.000 g/mol, Sigma Aldrich, Germany
platinum paste	Pt [Pt]	E1192, Ferro Corp., USA
alumina substrates	α-Al_2O_3 [AO-0.64]	12.7 mm x 12.7 mm x 0.64 mm, A493, Kyocera, Japan
	α-Al_2O_3 [AO-0.11]	12.7 mm x 12.7 mm x 0.11 mm, A493, Kyocera, Japan
platinised alumina substrate	[RAO]	Pt on one side of AO-0.64
	[DFAO]	Pt on top and bottom sides of AO-
yttria stabilised zirconia balls	94.7 wt. % ZrO_2 + 5.3 wt. % Y_2O_3 [YSZ3]	⌀ 3 mm, Tosoh Corporation, Tokyo, Japan
	94.7 wt. % ZrO_2 + 5.3 wt. % Y_2O_3 [YSZ10]	⌀ 10 mm, Tosoh Corporation, Tokyo, Japan

3.2 Sample Preparation

3.2.1 Synthesis of $(K_{0.5}Na_{0.5})_{0.99}Sr_{0.005}NbO_3$ (KNNSr) powder

The powder with the nominal composition $(K_{0.5}Na_{0.5})_{0.99}Sr_{0.005}NbO_3$ (KNNSr) was prepared by solid-state synthesis from the starting powders K_2CO_3, Na_2CO_3, $SrCO_3$ and Nb_2O_5 according to the procedure detailed by Hreščak *et al.* [138].

A total of 50 g of K_2CO_3, 50 g of Na_2CO_3 and 10 g of $SrCO_3$ were dried at 200 °C for 6 h and subsequently separately milled for 4 h at 175 min^{-1} in acetone, using a 250 mL polyethylene (PE) vial filled with YSZ10 and YSZ3. The mass ratios YSZ10:YSZ3 were 1:5 and 1:3 for milling K_2CO_3/Na_2CO_3 and $SrCO_3$, respectively. The mass ratios powder:acetone:YSZ were 1:1:9 and 2:1:13 for milling K_2CO_3/Na_2CO_3 and $SrCO_3$, respectively. Some 75 g of Nb_2O_5 was attritor milled in a 290 mL PE vial using YSZ3 milling balls at 800 min^{-1} for 3 h in 2-propanol. The mass ratio powder:2-propanol:milling balls was 1:1:2. After milling, the powders were dried at 200 °C for at least 2 h.

The K_2CO_3, Na_2CO_3, $SrCO_3$ and Nb_2O_5 milled powders were weighed in the molar ratio 0.2475:0.2475:0.005:0.5, respectively, in a protective argon atmosphere. A batch of 70 g of the powder mixture was homogenised in a planetary mill in acetone for 4 h at 175 min^{-1} in an YSZ milling vial with YSZ3. The mass ratio powder:acetone:YSZ3 was 1:1:2. After homogenisation, the mixture was dried at 105 °C for 1 h, sieved and dried at 200 °C for at least 2 h.

The powder was put into a cylindrical mould with a diameter of 20 mm and compacted by applying a uniaxial pressure of 50 MPa (PW10, Paul-Otto Weber Laborpresstechnik, Germany). The powder compacts were calcined on platinum foil in a covered alumina crucible in a chamber furnace at 800 °C for 4 h with the heating/cooling rates of 5 °C/min and re-calcined at 750 °C for 4 h. After each calcination step, the samples were crushed into powder and milled using the same conditions as for the homogenisation. Finally, the powder was dried, sieved and stored in a dry box.

3.2.2 Preparation of KNNSr suspensions

KNNSr powder was stabilised in EtOH using PAM and BA. To determine the optimal amount of additives, we first prepared the EtOH solutions with the concentrations of PAM of 1.13, 2.26 and 3.38 µmol/mL and the PAM:BA molar ratios of 1:0.5, 1:1, 1:1.5, 1:2, 1:3, 1:4 and 1:5 as follows. We mixed PAM with EtOH and into the clear solution we added BA. Additionally, we also prepared a solution of EtOH and BA (reference solution). In the reference solution we added 1.13, 2.26, 3.38, 4.52, 6.78, 9.04 and 11.3 μmol/mL of BA which corresponded to the PAM:BA molar ratios of 1:0.5, 1:1, 1:1.5, 1:2, 1:3, 1:4 and 1:5 for the solution with 2.26 μmol/mL PAM. Solutions were stirred with a magnetic stirrer for 10 minutes before characterisation.

The 50 mL suspensions were prepared as follows. 1 vol % of the KNNSr powder was added to an ethanol solution with a PAM:BA molar ratio of 1:2 and PAM concentration of 1.13, 2.26 and 3.38 µmol/mL which correspond to 25, 50 and 75 µmol PAM per gram of the powder, respectively. The corresponding suspensions are referred to as S25, S50 and S75. The suspensions were mixed with a magnetic stirrer for 1 h and subsequently homogenised in a planetary ball mill in a PE vial with seven YSZ10 at 150 min^{-1} for 1 h. Prior to the characterisation and EPD, the suspensions were rested overnight.

3.2.3 Substrates for the processing of thick films

A platinum paste was screen-printed onto 8 mm × 8 mm (L_{WE} x $L_{WE} = S_{elec}$) area of the substrates, namely on one side of the substrate AO-0.64 and on two sides of the substrate AO-0.11. The paste was fired at 1200 °C for 1 h in air using heating and cooling rates of 5 °C/min. The substrates with a platinum electrode on AO-0.64 and AO-0.11 are referred as the RAO substrate and the DFAO substrate, respectively, and are shown in Figure 3.1.

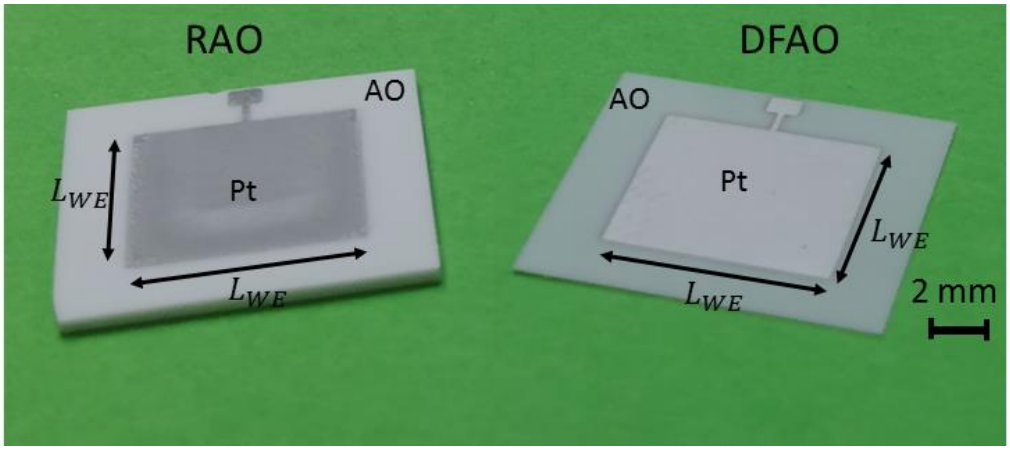

Figure 3.1: Side views of the platinised α-Al_2O_3 (AO) substrates with thickness of 0.64 mm (RAO) and 0.11 mm (DFAO). Pt: platinum, L_{WE}: length of the working electrode.

3.2.4 Electrophoretic deposition of KNNSr

KNNSr thick films were processed by EPD using custom-made setups.

The Setup 1 (Figure 3.2) was used to process KNNSr as-deposited layers onto RAO substrates. It is composed of a 50-mL glass beaker, counter electrode (CE) and working electrode (WE) supported with polymer. The counter electrode was a disc made of platinum with a thickness of 0.1 mm and diameters (D_e) of 4, 8 or 35 mm. The RAO substrate acted as the WE. The distance between WE and CE (h_i) can vary between 3 mm and 14 mm.

All the depositions were performed at a constant-current density of 1.56 mA/cm² ($J = I/S_{elec}$) controlled by a Keithley 2400 source meter (Keithley Instruments Inc., Cleveland, USA). The current density and the deposition times were controlled by Labview software (National Instruments, Austin, USA). The supplied voltage during the deposition ($\Delta V(t)$) was recorded.

In the first set of experiments, we study the effect of the suspension conductivity on the deposition of KNNSr as-deposited layers. We performed the deposition from suspensions, namely, S25, S50 and S75 with different conductivities. We processed KNNSr thick films on RAO substrate under the following deposition conditions:

1) h_i = 14 mm, D_e = 35 mm and the deposition times were 30, 60, 90, 120 and 150 s,
2) h_i = 3 mm, D_e = 8 mm and deposition time of 60 s.

In the next step, we studied the influence of the setup geometry, i.e., interelectrode distance and counter-electrode diameter, on the thickness uniformity of the as-deposited layers. We performed depositions onto RAO substrates from the suspension S50 and a deposition time of 60 s under the following conditions:

3) D_e of 4 mm for h_i of 3, 8 and 14 mm,
4) h_i of 3 mm and D_e of 8 and 35 mm.

Finally, for the preparation of KNNSr thick films, EPDs were performed on RAO substrates using suspension S50, h_i of 3 mm, D_e of 8 mm and deposition times of 30 s and 90 s. The prepared samples were denoted by the name of the suspension, followed by the deposition time. For example, S25-30 represents the samples deposited from the suspension S50 for 30 s.

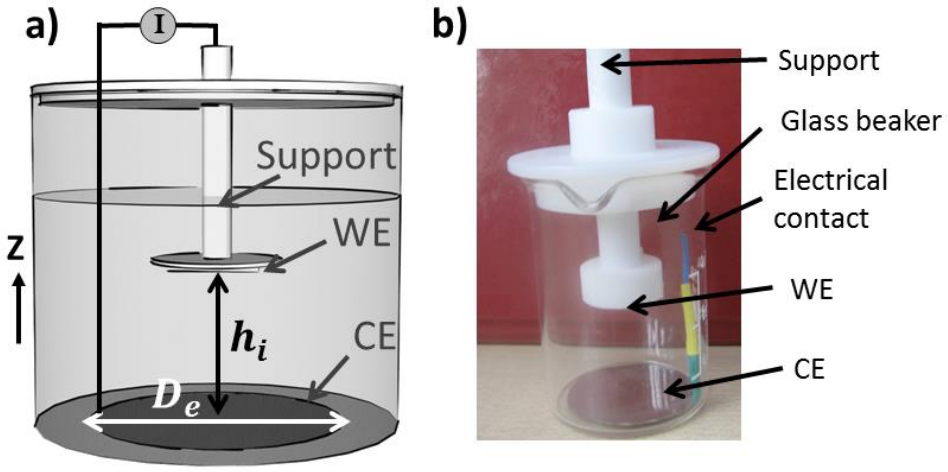

Figure 3.2: a) Schematic representation of the EPD Setup 1 and b) Picture of the Setup 1. WE: working electrode, CE: counter electrode, h_i: interelectrode distance and D_e: counter electrode diameter, Z: direction normal to the electrode's surfaces.

Setup 2 was used for the processing of the KNNSr layers onto the DFAO substrates (Figure 3.3a). The DFAO substrate, acting as WE, was sandwiched between two printed circuit boards (PCBs) and fastened in a polymer support, ensuring the electrical contacts with the current source (Figure 3.3b). The counter electrodes were circular copper electrodes with diameter of 8 mm on PCBs which were integrated into the polymer support. The isolated copper conducting tracks allowed the connection with the current source (see Figure 3.3c). The WE were inserted into the holder and the two CEs were placed left and right from the WE support at the identical distance of $h_i = 3$ mm, as illustrated in Figure 3.3a. Later, the support was placed in the beaker.

The depositions were performed using suspension S50 and the deposition times of 30 s or 90 s at a constant-current density of 1.56 mA/cm^2 controlled by a Keithley 2400 source meter and Labview software. We deposited the KNNSr layer on one side (WE1) by contacting WE1 and the CE1, and subsequently on the second side (WE2), by contacting WE2 and CE2 (Figure 3.3a).

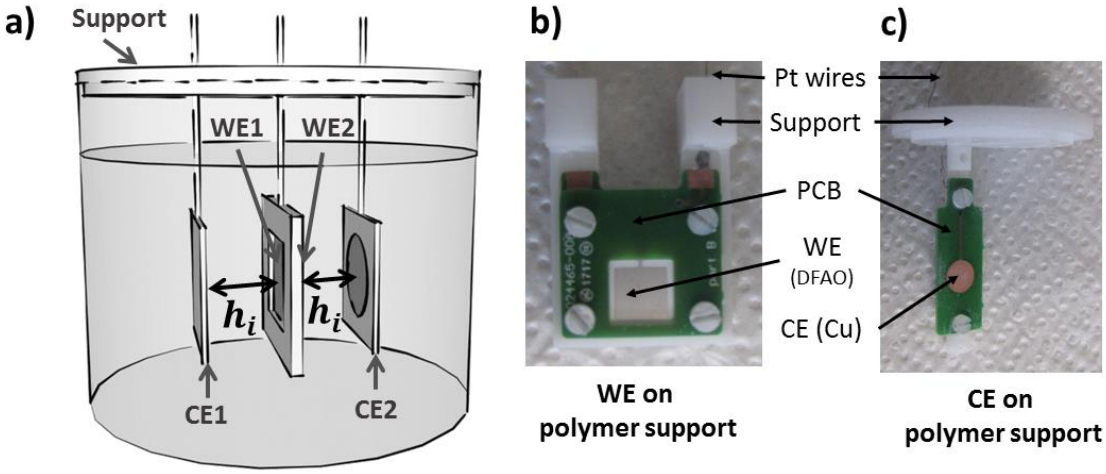

Figure 3.3: a) Schematic representation of the EPD Setup 2, b) Picture of the working electrode between PCBs and c) Picture of one counter electrode on PCB. WE: working electrode, CE: Counter electrode, h_i: interelectrode distance and PCB: printed circuit boards.

After the deposition of the KNNSr layer(s) on the substrate, the substrate was removed from the EPD Setup 1 or Setup 2 and placed in a Petri dish in an ethanol-rich atmosphere at a temperature of 20 ± 2 °C to dry for at least 2 h.

3.2.5 KNNSr thick films

KNNSr thick films deposited onto RAO and DFAO substrates from suspension S50 with an interelectrode distance h_i of 3 mm and a counter electrode of diameter D_e of 8 mm were sintered. Two procedures were used for the processing of KNNSr thick films, namely, the one-step and two-step deposition-sintering procedures. Both procedures are schematically presented in Figure 3.4 and Figure 3.5.

3.2.5.1 One-step deposition-sintering procedure

In the one-step procedure, the KNNSr was deposited onto RAO substrates for 90 s using Setup 1 (Figure 3.4). After drying, the as-deposited layers were heated in a tube furnace to 500 °C for 1 h and subsequently fired at 1075, 1100 and 1120 °C for 2 h in air with heating and cooling rates of 2 °C/min. The thick films are denoted as T-1075-A, T-1100-A and T-1120-A, respectively.

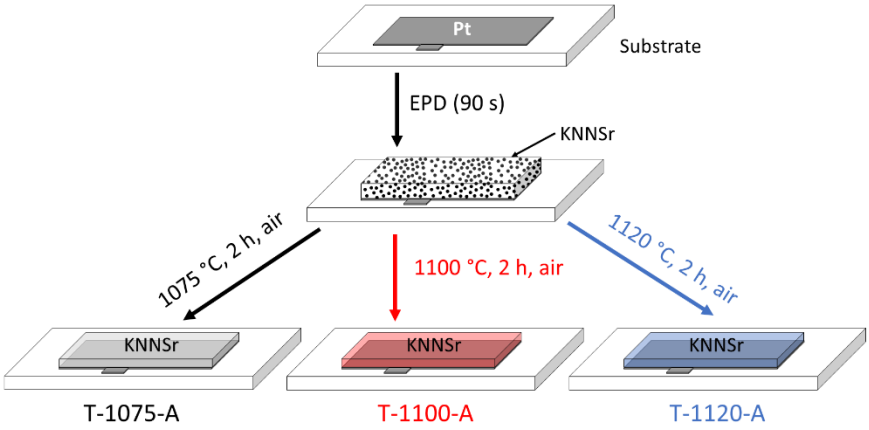

Figure 3.4: Schematic representation of one-step deposition-sintering procedure for KNNSr on platinised alumina substrate.

3.2.5.2 Two-step deposition-sintering procedure

In the two-step deposition-sintering procedure, a first KNNSr layer was deposited onto the RAO substrate for 30 s with Setup 1 (Figure 3.5). After drying, the layer was heated in a tube furnace at 500 °C for 1 h and then fired at 1000 °C for 2 h with heating and cooling rates of 2 °C/min. This layer is denoted as F-1000-A. The second layer was deposited onto F-1000-A under identical deposition conditions, but for a longer deposition time of 90 s. After drying, the samples were heated at 500 °C for 1 h and then fired at 1090, 1100 and 1110 °C for 2 h in a flow of synthetic air or oxygen. The heating and cooling rates were 2 °C/min. KNNSr thick films fired at selected temperatures in air are denoted 1090-A, 1100-A, 1110-A and the ones fired in oxygen are denoted as 1090-O, 1100-O and 1110-O.

The two-step deposition-sintering procedure was also used for the sintering of KNNSr thick films on DFAO substrates. In this case, the EPD was performed with Setup 2. The films were processed under identical conditions as on RAO substrates, except the firing after the deposition of the second layer, which was only fired at 1100 °C for 2 h in oxygen. The samples processed on only one side of the DFAO substrates are denoted OF-1100-O and the ones processed on both sides of the DFAO substrates are denoted as DF-1100-O.

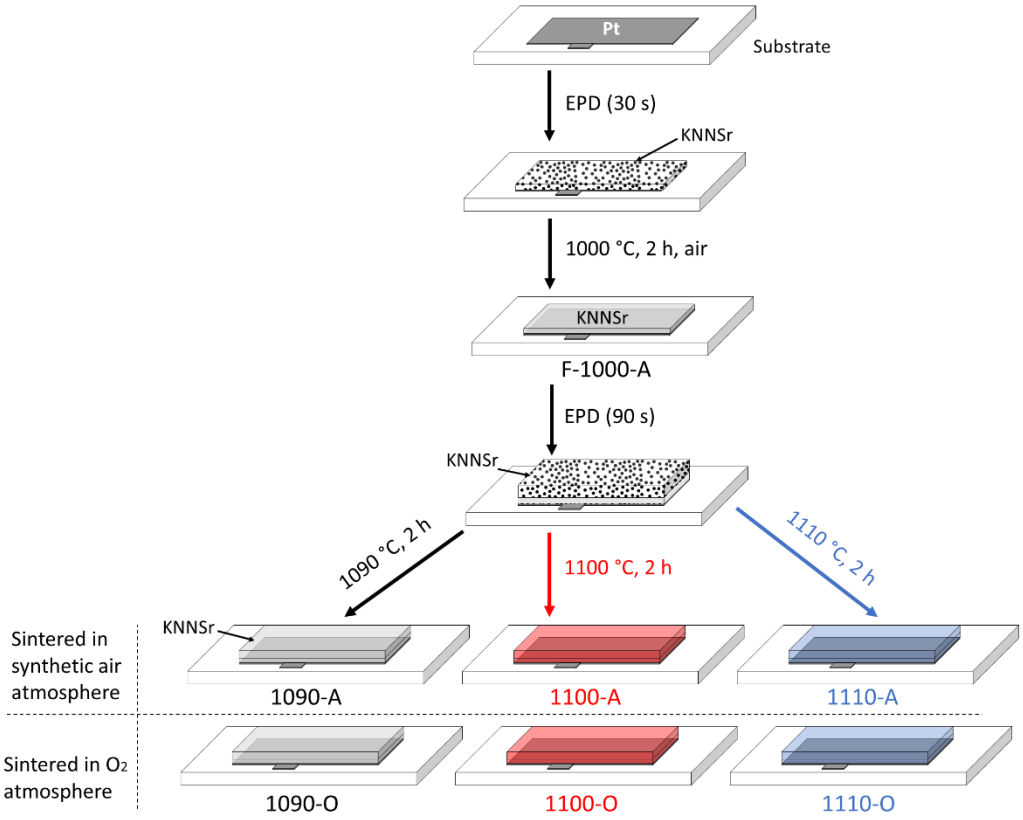

Figure 3.5: Schematic representation of two-step deposition-sintering procedure on platinised alumina substrate.

A list of KNNSr thick films processed by the one-step and two-step deposition-sintering procedures is given in Table 3.2. For each condition at least two samples were processed and characterised.

Table 3.2: A list of KNNSr thick films and their processing conditions.

Sample Name	substrate	Deposition conditions	Sintering conditions		
			Temperature (°C)	Time (h)	Atmosphere
T-1075-A	RAO	One-step	1075	2	Air
T-1100-A	RAO	One-step	1100	2	Air
T-1120-A	RAO	One-step	1120	2	Air
1090-A	RAO	Two-step	1090	2	Air
1100-A	RAO	Two-step	1100	2	Air
1110-A	RAO	Two-step	1110	2	Air
1090-O	RAO	Two-step	1090	2	Oxygen
1100-O	RAO	Two-step	1100	2	Oxygen
1110-O	RAO	Two-step	1110	2	Oxygen
OF-1100-O	DFAO	Two-step	1100	2	Oxygen
DF-1100-O	DFAO	Two-step	1100	2	Oxygen

3.2.6 KNNSr bulk ceramics

Bulk ceramics were prepared with 0.6 g of the KNNSr powder inserted into a cylindrical mould with a diameter of 8 mm and pressed with a uniaxial pressure of 100 MPa. The powder compacts were then isostatically pressed at 200 MPa (401C-0063, Autoclave Engineers, USA). Samples were placed onto a platinum foil and sintered in a closed alumina crucible in a tube furnace. The powder compacts were heated at 200 °C for 2 h with a heating rate of 10 °C/min and then sintered at 1120 °C for 2 h in a flow of oxygen or synthetic air with a heating and cooling rate of 5 °C/min. KNNSr ceramics sintered in air and oxygen are denoted as C-1120-A and C-1120-O, respectively.

3.3 Characterisation

3.3.1 Laser granulometry

The particle size and particle-size distribution of the powders were measured using a static light-scattering particle-size analyser (Microtrac S3500 Particle Size Analyser, PA, USA).

The measurements were performed in 2-propanol. The results were derived from the volume particle-size distribution (d_v).

3.3.2 Zeta-potential and conductivity

The zeta-potential (ZP) of the KNNSr particles in ethanol was measured at room temperature using a zeta-potential analyser (ZetaPALS Brookhaven, USA). Prior to the measurement, 10 μL of a suspension was diluted in 10 mL of the corresponding solution.

The conductivities of the solutions and suspensions were measured at 25 °C using a conductivity meter (inoLab Cond 730, WTW, Germany).

3.3.3 X-Ray diffraction (XRD)

The X-ray diffraction (XRD) patterns were collected on sintered thick films, while the bulk ceramics were crushed into powder before analysis. The X-ray diffraction patterns of the powder and thick films were collected with a diffractometer (PANalytical X'Pert PRO MPD, The Netherlands) with Cu–Kα radiation. The data were collected in the 2θ range from 20° to 70° with steps of 0.017°, and an integration time of 200 s for thick films and 100 s for the powder. The phases were identified using the X'pert HighScore program and the PDF-2 database [139].

The relative intensities of the diffraction peaks and the unit-cell parameters were obtained by fitting the XRD patterns using the Le Bail method and Topas R software (Bruker AXS, Karlsruhe, Germany). For the analysis, we used the structural model having a monoclinic unit cell with the space group Pm [32]. The preferential crystallographic orientation of the thick films was assessed with the Lotgering factor [140]:

$$LF(hkl) = \frac{p - p_0}{1 - p_0} \tag{3.1}$$

p is the intensities of the (hkl) diffraction peaks with preferential orientation in the thick films divided by the sum of the intensities of all the other diffraction peaks. p_0 is the same ratio calculated in a randomly oriented sample, i.e., KNNSr ceramic with the identical nominal composition.

3.3.4 Scanning electron microscopy (SEM)

The samples were analysed using a JEOL-7600F field-emission SEM (Jeol, Tokyo, Japan) equipped with an energy-dispersive X-ray spectrometer (Oxford INCA energy 350, Oxford instruments, United Kingdom) with a secondary-electron detector (SE) and backscattered-electron detector (BSE).

Prior to the analysis, the powder was dispersed in ethanol and a drop of suspension was placed on a conductive carbon tape. For the analysis of the surface of the as-deposited and sintered thick films the samples were placed onto a conductive carbon tape. The samples were then coated with ~ 5 nm of gold using a Precision Etching Coating System (PECS, model 682, Gatan). The cross-sections of the ceramics and thick films were prepared by cutting the samples with a diamond saw, embedding in epoxy resin, grinding using SiC papers and polishing with diamond pastes with 3-μm and 0.25-μm particles. Prior to the SEM investigations, the samples were coated with carbon.

The relative densities and pore sizes of the thick films were obtained from polished cross-section SEM images using ImageJ software (National Institutes of Health, USA). The images were converted into binary images. The black pixels areas were considered as individual pores and the white pixels as a KNNSr ceramic. The ratio of black and white

pixels to the total number of pixels was used to calculate the porosity and relative density of the thick films, respectively. The black pixel areas were used to calculate the pore-area distribution. A threshold for the pore area of 0.2 μm^2 was used to avoid counting individual pixels as pores. The pore area distribution was calculated based on the area distribution (median pore area $A_{A,50}$, 10 % of the total pore areas lies below the pore area $A_{A,10}$, 90 % of the total pores area lies below the pore area $A_{A,90}$). The data for the relative density and pore size were averaged over at least three different images. An experimental error was calculated from the standard deviation of the density and the number of pores per area estimated from the SEM images.

3.3.5 Heating-stage microscopy

To record the dynamic sintering curves, 0.2 g of the KNNSr powder was uniaxially pressed at 100 MPa in a cylindrical mould with a diameter of 6 mm. The dimensional change of the compact was recorded with an optical dilatometer (Leitz Version 1A, Leitz, Germany) from room temperature to 1200 °C with a heating rate of 10 °C/min. The dimensional change of the pellet ($\Delta l/l$) was monitored through the recorded images of the sample. The shrinkage (in percent) was calculated from the following equation:

$$\frac{\Delta l}{l}(T) = \frac{l(T) - l_i}{l_i} \times 100 \tag{3.2}$$

where $l(T)$ is the length of the sample at the temperature T and l_i is the initial length of the sample at room temperature.

3.3.6 Profilometry

The thickness profiles of the as-deposited and sintered layers were measured along the line A-A (Figure 3.7) with a non-contact optical profilometer (Viking Micro 60, Solarius Development Inc, USA). The samples were analysed at a constant scan speed of 50 μm/s with a sampling frequency of 100 Hz. Thickness profiles of selected sintered thick films were measured with a contact profilometer (P16+, KLA Tencor, USA).

The measured thickness profile is a sum of the thickness of the KNNSr layers and the Pt electrode. If not stated otherwise, the thickness profiles of the KNNSr layers were calculated by subtracting the thickness of the platinum electrode. The mean thickness of the as-deposited layer was the average thickness of the KNNSr as-deposited layer or thick film between the two edges of the platinum electrode. The thicknesses at the electrode edges was the average of the thicknesses measured at the two electrode edges. The thicknesses in the centre of the electrode were calculated as the average thickness at $\pm$ 1 mm from the centre of the electrode.

3.3.7 Piezo-response force microscopy (PFM)

The domain-structure analysis was performed on polished thick films (1090-O, 1100-O, 1110-O and 1100-A) using an atomic force microscope (AFM; Asylum Research, MFP-3D) equipped with a piezo-response force microscope (PFM). Prior to the analysis the samples were grinded with SiC, polished with a diamond paste and fine polished for 1.5 h using an OPS silica colloidal suspension. An electric field was applied between the conductive AFM tip and the film's bottom electrode. A Pt-coated Si tip with a radius of curvature ~ 10 nm (OMCL-AC240TM-R3, Olympus, Japan) was used. The out-of-plane piezoresponse amplitude images were recorded in Dual ac resonance tracking (DART) mode at an ac

amplitude signal of 2 V and ~ 260 kHz. The PFM amplitude and phase hysteresis loops were measured in the switching spectroscopy (SS) off-loop mode with the pulse dc step signal and overlapped drive ac signal. The waveform parameters were: the sequence of increasing dc electric field steps was 20 Hz with a maximum amplitude of 30 V; the frequency of the triangle envelope was 200 mHz; and an overlapping ac sinusoidal signal of amplitude 2 V and a frequency of 300 kHz.

3.3.8 Piezoelectric and dielectric properties

On the surface of the sintered thick films four gold electrodes with a diameter of 2 or 3 mm and a thickness of ~ 100 nm were sputtered using 5 Pascal, Italy.

Bulk ceramics were cut to a thickness of ~ 500 μm, polished, cleaned in an ultrasound bath and afterwards annealed at 600 °C using heating and cooling rates of 5 and 1 °C/min, respectively. The gold electrodes with a diameter of 5 mm and a thickness of ~ 100 nm were sputtered on the top and bottom sides of the bulk ceramics.

The capacitance (C) and dielectric losses ($\tan\delta$) were measured on non-poled samples with a precision LCR meter (HP4284A, Hewlett Packard, USA) (see Figure 3.6). Measurements were performed in vacuum as a function of frequency from 10^3 to 10^5 Hz. The relative dielectric permittivity ($\varepsilon_{r,33}$) was calculated using Equation (3.3).

$$\varepsilon_{r,33} = \frac{C.S_{elec}}{t_M\ \varepsilon_0} \tag{3.3}$$

with C the capacitance, S_{elec} the area of the top electrode, t_M the thickness of the sample and ε_0 the permittivity of the vacuum.

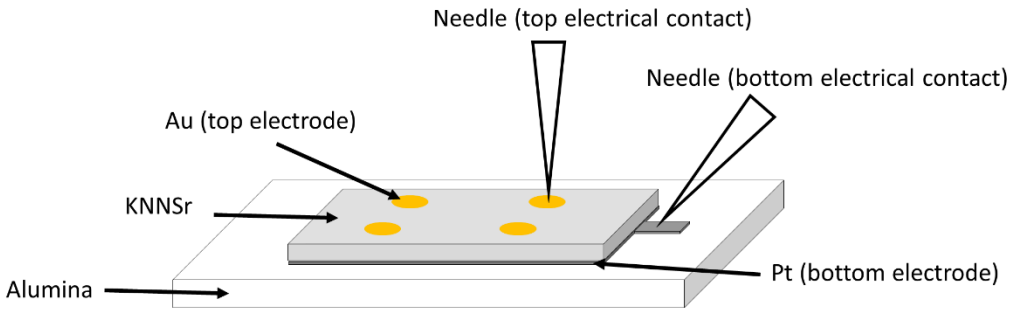

Figure 3.6: Schematic representation of the dielectric measurement of the KNNSr thick films with electrical contacts on a platinised alumina substrate in the Metal (Platinum, Pt)-Insulator (KNNSr)-Metal (Au) configuration.

The samples were poled at 120 °C for 2 h in a silicone bath at 3 kV/mm, supplied by an external dc generator (248 high-voltage supply, Keithley Instruments Inc, USA). The samples were cooled to room temperature under the applied external field. The piezoelectric coefficients d_{33} of the bulk ceramics and $d_{33,f}$ of the thick films were measured after 24 h with a Berlincourt piezometer (Take Control PM10, UK).

3.3.9 Electromechanical characterisation

The complex electrical impedance around the fundamental resonance frequency of the ceramics and thick films was measured with an HP4395 vector analyser and its impedance test kit. The theoretical complex electrical impedance as a function of the frequency was

calculated using the Krimholtz-Leedom-Matthaei (KLM) equivalent electrical circuit [141], [142]. A description of the KLM equivalent circuit can be found in Appendix C. The following parameters were stepwise refined in order to obtain the best agreement between the experimental and calculated impedance: the longitudinal wave velocity (V_L) the relative dielectric permittivity at constant strain ($\varepsilon^S_{r,33}$), the thickness-mode electromechanical coupling factor (k_t) and the electrical and mechanical losses (δ_e and δ_m, respectively, see Appendix A). From the refined data we also obtained the elastic stiffness at a constant electric displacement (c^D_{33}) and the piezoelectric coefficient (e_{33}).

We assumed the thickness, area (of the top electrode) and density of the thick films and ceramics to be non-refined parameters. For the bulk ceramics, a resonance in free mechanical conditions was assumed. For the thick films, we considered a coupled system and accounted for three inert layers: the bottom and top electrodes and the alumina substrate (Figure 3.6). The properties of the latter were taken from the literature [142], [143] and are given in Table 3.3.

Table 3.3: Properties of the three inert layers in the thick-film structures on a platinised alumina substrate [142], [143]. thickness (t_M), longitudinal wave velocity (V_L), density (ρ), acoustical impedance ($Z = \rho V_L$) and acoustic attenuation coefficient (α).

Layer	Material	t_M (μm)	V_L (m/s)	ρ (g/cm^3)	Z (MRa)	α (dB/mm/MHz)
Top electrode	Au	0.1	3240	19.7	63.8	Negligible
Bottom electrode	Pt	6	3260	21.4	69.8	Negligible
AO-0.64 substrate	Al_2O_3	640	10500	3.9	41.0*	0.006

*calculated from the data in [142]

For the electromechanical characterisation of the KNNSr layers processed on DFAO substrates we assumed, in addition, a second platinum electrode. For the theoretical calculation, we also accounted for an inert KNNSr layer (i.e., considered unpoled and thus non-piezoelectric) on the rear face of the alumina substrate.

3.4 Numerical Calculation of the Electric Field in a Suspension Between Two Electrodes

A finite-element analysis (FEA) was implemented using COMSOL® Multiphysics software to simulate the 3D spatial distribution of the electric field between the CE and WE. The model was based on the work of Kuscer *et al.* [104]. In the model, the suspension was considered as an electrically neutral and homogenous medium, the ionic concentration gradient was neglected, and the electric field was not perturbated by the presence of the particles. The stationary solution of the spatial electric potential distribution for a constant-current deposition is given by Laplace equation [144]:

$$\nabla^2 \mathrm{V} = 0 \tag{3.4}$$

where ∇ is the divergence operator and V is the electric potential.

The electric field in the suspension is given by:

$$\mathrm{E} = -\nabla \mathrm{V} \tag{3.5}$$

To match our experimental conditions, the model was built with the geometry presented in Figure 3.2. The following boundary conditions were used:

- A constant-current density of 1.56 mA/cm^2 was applied at the WE;
- CE was grounded and the potential at the Pt electrode surface was zero;
- The outer boundaries of the system (walls of the beaker) were considered as a perfect electrical insulator where $\vec{n} \cdot \vec{J} = 0$, with $\vec{n}$ the normal to the surface.
- The CE was a disc of diameter D_e and the WE electrode was a 12.7 mm × 12.7 mm square of alumina with an 8 mm × 8 mm platinum electrode. The centre of the WE and CE were aligned and the distance between the electrodes was h_i.

The material properties were taken from the COMSOL® built-in library. For the material properties of the suspension we used the properties of ethanol, except its conductivity. We used the experimentally measured conductivity of the suspensions S25, S50 and S75. Domains were discretized using free-tetrahedral mesh with predefined "physics-based" meshing. The model was built in a parametric form and allows the finite-element analysis to vary the following parameters: the conductivity of the suspension, the counter-electrode′s diameter (D_e) and the interelectrode distance (h_i).

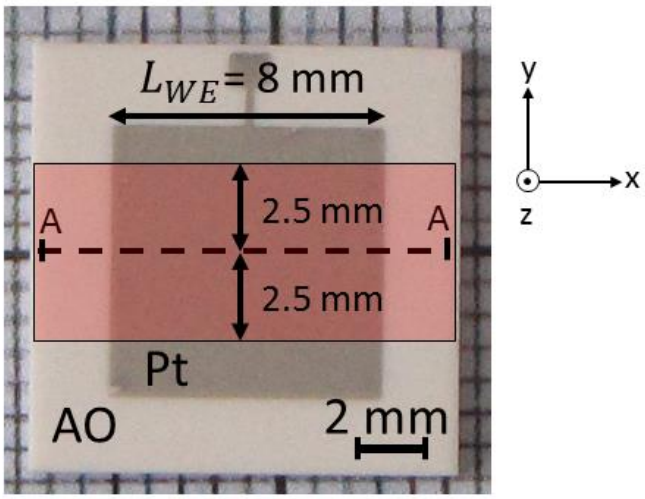

Figure 3.7: Top view of the WE with the line A-A (dashed line on the figure) and the red area considered in the analysis for averaging the electric field strength results.

We deduced from the model: the electrical potential at the WE ($\Delta V_{0,FEA}$, averaged on the whole surface of the electrode) and the absolute value of the E_Z component of the electric field at a distance of 100 μm from the WE (referred later on as close vicinity). The E_Z component of the electric field was represented along the line A-A (presented in Figure 3.7). The $E_{Z,i}$ i.e., at a particular abscissae X_i, was calculated by averaging all the values of E_Z at the abscissae X_i and ordinate Y_i within ± 2.5 mm from the centre of the working electrode (red area marked on Figure 3.7).

Chapter 4

Results and Discussion

4.1 Electrophoretic Deposition of $(K_{0.5}Na_{0.5})_{0.99}Sr_{0.005}NbO_3$ (KNNSr)

In the thesis we studied the processing of thick films with the nominal composition $(K_{0.5}Na_{0.5})_{0.99}Sr_{0.005}NbO_3$ (KNNSr) on platinised alumina substrates by electrophoretic deposition (EPD) for piezoelectric energy harvesting. In this first subchapter the properties of the KNNSr powder and the processing of ethanol-based suspensions suitable for EPD are described. To reproducibly process KNNSr thick films with a thicknesses of 20 to 40 μm, the effects of the conductivity of the suspension, deposition time, interelectrode distance and counter-electrode diameter on the deposited mass, thickness uniformity and morphology of as-deposited layers are discussed.

4.1.1 KNNSr powder

The powder with the nominal composition $(K_{0.5}Na_{0.5})_{0.99}Sr_{0.005}NbO_3$ (KNNSr) was prepared by solid-state synthesis. The SEM image and the particle size distribution (PSD) of the KNNSr powder are presented in Figure 4.1a and Figure 4.1b, respectively. The powder consisted of particles with a log-normal PSD. The median particle size ($d_{v,50}$) was 0.64 μm.

The XRD pattern of the KNNSr powder is shown in Figure 4.1c. The diffraction peaks corresponded to the perovskite structure indexed with a monoclinic phase (PDF: 77-0038).

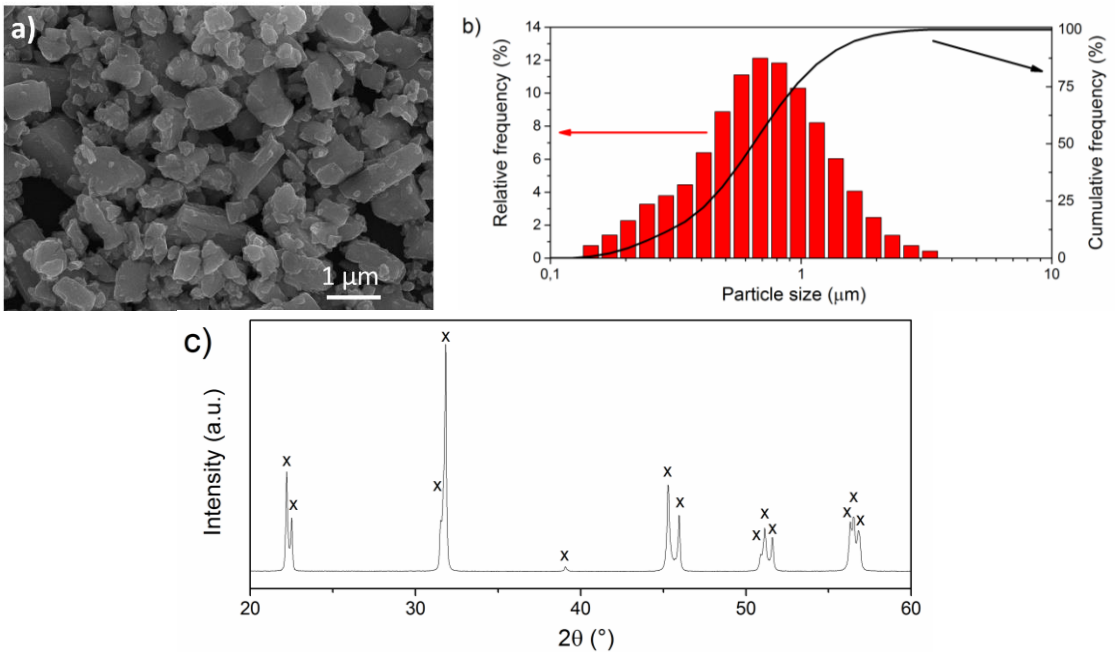

Figure 4.1: KNNSr powder a) SEM image, b) Particle size distribution and c) XRD pattern. x: $K_{0.65}Na_{0.35}NbO_3$ (PDF: 77-0038).

The shrinkage-temperature curve of the KNNSr powder is presented in Figure 4.2. The KNNSr powder compact shrank in a narrow temperature range between ~1040 and ~1140 °C. It shrank up to 12 % at 1140 °C, where it melted. The melting temperature of the KNNSr powder was similar to the values reported for pure KNN, i.e., 1130 ± 10 °C [145] and 1140 °C [7].

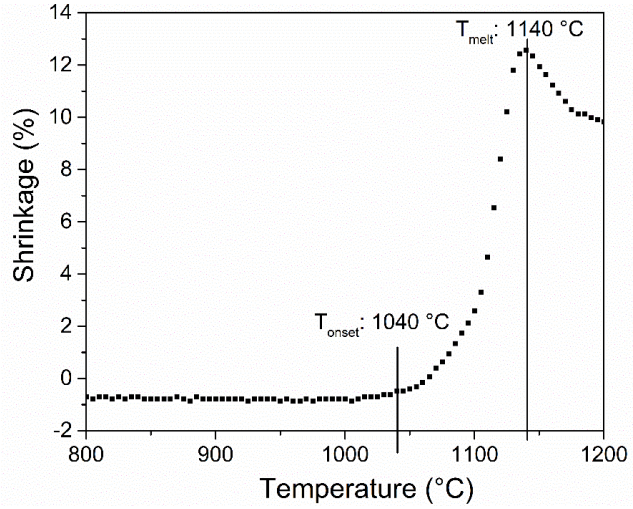

Figure 4.2: Shrinkage-temperature curve for KNNSr powder.

4.1.2 KNNSr suspensions for EPD

To prepare the suspension for EPD the KNNSr particles must be charged and well dispersed in ethanol, while the electrical conductivity of the suspension must be in the range of a few to a few tens of μS/cm [90].

For the stabilisation of the KNNSr particles in ethanol, poly(acrylic acid-co-maleic acid) (PAM) and n-butylamine (BA) were used. To optimise the amount of PAM and the amount of BA, we prepared ethanol solutions with different PAM concentrations and different PAM:BA molar ratios and measured the conductivities of the solutions (Figure 4.3). The conductivity of the solutions increased with an increasing concentration of PAM and PAM:BA ratio. It increases up to PAM:BA ratios of 1:2, reaching values of 15, 24 and 33 μS/cm for the concentration of PAM being 1.13, 2.26, 3.38 μmol/mL, respectively. For a PAM:BA ratio larger than 1:2, conductivity did not vary significantly. Note that the conductivity of the reference solution (denoted (R)), i.e., ethanol with BA only steadily increased from 0.5 to 9.5 μS/cm with an increasing concentration of BA. This can be attributed to the increasing concentration of ions in the solution. The pK_a for the BA is 10.60 at 25 °C [146], meaning that the amino group in BA partly deprotonates in ethanol solution, which results in an increase of the conductivity of the reference solution (R) with the increasing concentration of BA. The pK_a for PAA is 4.25 and for the maleic acid (containing 2 carboxyl groups) the two pK_a are 1.92 and 6.23 at 25 °C [146]. Thus, the carboxyl groups deprotonate and the deprotonation is larger in the higher pH range, i.e., upon addition of BA, because of its basic character [90]. Consequently, the conductivity of the solution increased with an increasing PAM:BA ratio, as well as with an increasing concentration of PAM for an equal PAM:BA ratio.

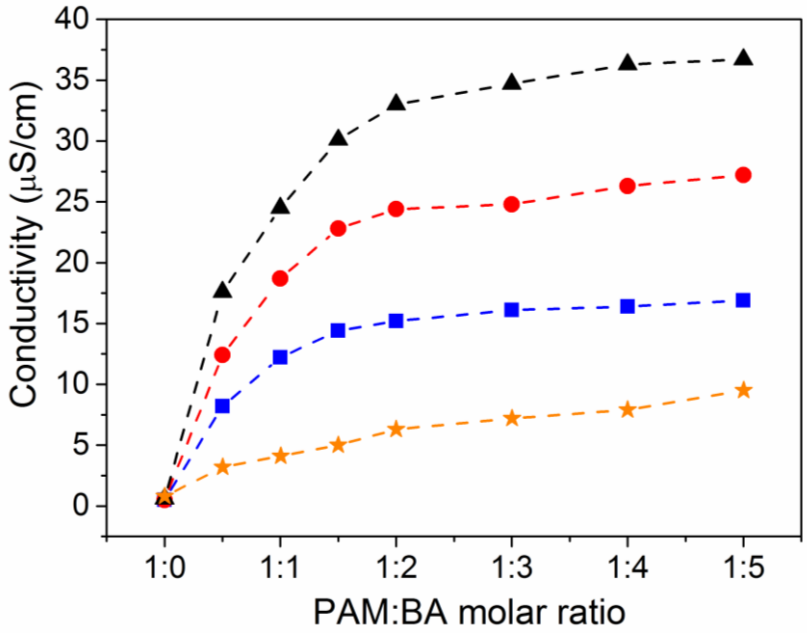

Figure 4.3: Conductivity of the PAM–BA-EtOH solution for PAM concentrations of 0 (★, (R)), 1.13 (■), 2.26 (●) and 3.38 (▲) μmol/mL as a function of the PAM:BA molar ratio.

For our further experiments, we processed the 1 vol.% of KNNSr suspensions with a PAM:BA molar ratio of 1:2. For this ratio, we varied the concentrations of PAM, namely, 1.13 μmol/mL, 2.26 μmol/mL and 3.38 μmol/mL, which represented 25, 50 and 75 μmol PAM per gram of KNNSr powder, respectively. The corresponding suspensions were denoted S25, S50 and S75. The median particle size of the KNNSr powder, the zeta-potential (ZP) and the electrical conductivity of the suspensions (σ_{susp}) are listed in Table 4.1.

The particle size distributions (PSD) presented in Figure 4.4 are log-normal with particles ranging from 0.1 to 4 μm and no agglomerates were observed. The PSD and the $d_{v,50}$ (Table 4.1) of the particles in the suspensions were close to the values of the as-prepared KNNSr powder (Figure 4.1b). The high absolute value of the ZP of the particles, larger than 46 $\pm$ 5 mV, showed that particles were electrosterically stabilised in the suspension and ensured that they could move towards the oppositely charged electrode by applying a DC electric field between the two electrodes. The main difference between the suspensions was their conductivities. The conductivity of the suspensions increased with the increasing amount of PAM, similar to that observed for the solutions (Figure 4.3).

Table 4.1: Median particle size ($d_{v,50}$), zeta-potential (ZP) and conductivity (σ_{susp}) of the KNNSr suspensions.

Suspension name	$d_{v,50}$ (μm)	ZP (mV)	σ_{susp} (μS/cm)
S25	0.62	-46 $\pm$ 5	9.2 $\pm$ 0.1
S50	0.52	-48 $\pm$ 5	21.2 $\pm$ 0.1
S75	0.56	-47 $\pm$ 5	29.1 $\pm$ 0.1

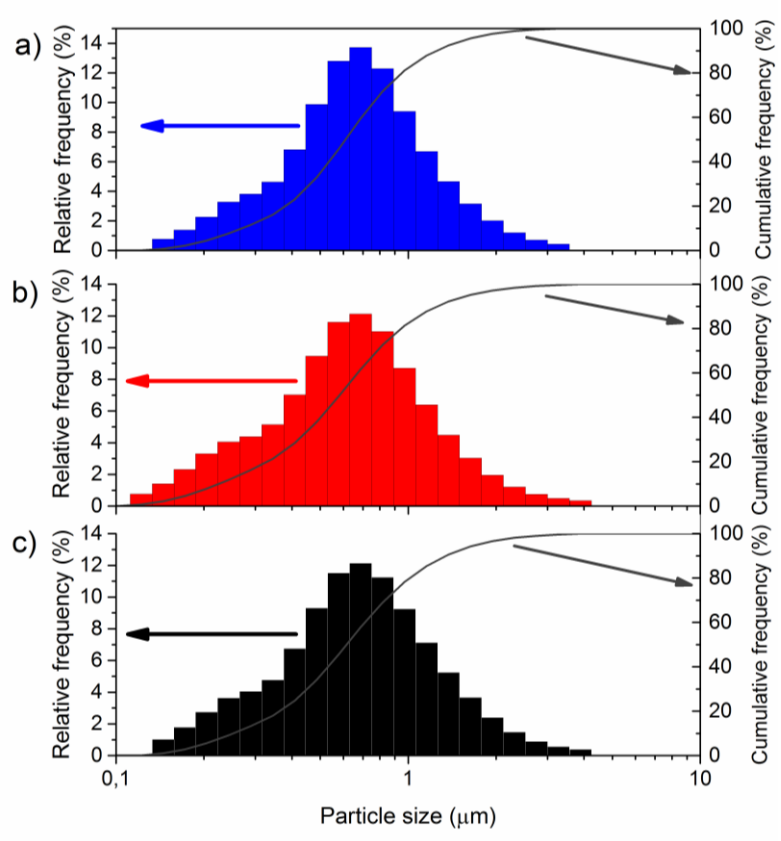

Figure 4.4: Particle size distribution of the KNNSr powder dispersed in suspensions a) S25 (blue), b) S50 (red) and c) S75 (black).

In the next step, we investigated the effect of the PAM concentration on the deposition mass of the KNNSr deposited onto 640-μm-thick platinised alumina (RAO) substrates using Setup 1. The deposited mass is reported in this thesis as the yield (Y), i.e., the mass

deposited (m) per working electrode (WE) area (S_{elec}) ($Y = m/(S_{elec})$, see 3.2.3). The yields of as-deposited layers processed from S25, S50 and S75 as a function of the deposition time is depicted in Figure 4.5. The yield increased linearly with the increasing deposition time. For a given time, the largest yields were obtained from S25, followed by S50 and S75.

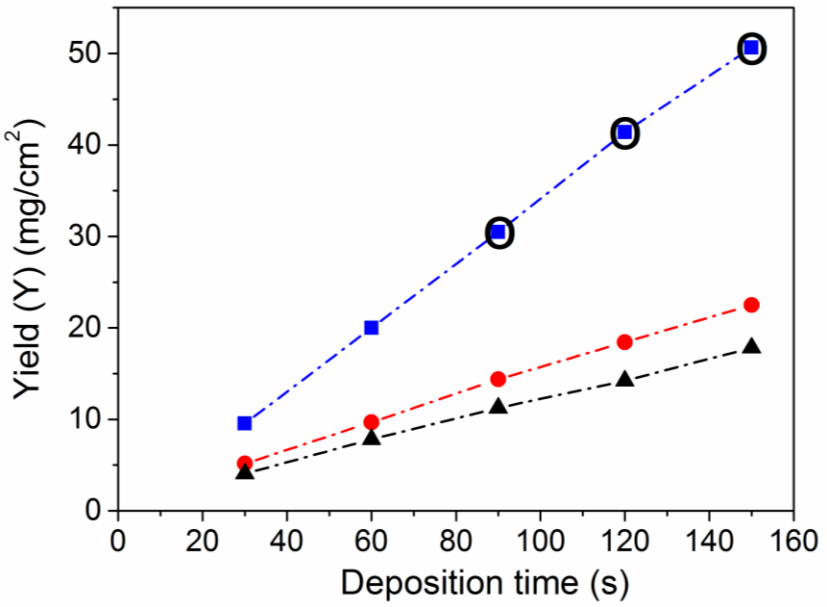

Figure 4.5: Yield (Y) versus the deposition time for the deposition from the suspensions S25 (■), S50 (●) and S75 (▲).

The thickness profiles of the as-deposited layers from S25, S50 and S75 as a function of deposition time are given in Figure 4.6. The profiles were measured along the line A-A represented in Figure 3.7. The mean thicknesses (see 3.3.6) of the samples increased linearly with increasing deposition time and were the largest for the suspension with the lowest conductivity, i.e., S25 followed by S50 and S75 (Figure 4.6.d). With increasing deposition time from 30 to 150 s, the mean thickness increased from 37 to 180 ± 8 μm for S25, from 28 to 100 ± 8 μm for S50 and from 28 to 79 ± 8 μm for S75. The as-deposited layers' thicknesses as a function of the deposition times and suspension conductivities followed the same trends that were observed for the yield as a function of the deposition time in Figure 4.5.

Figure 4.5 and Figure 4.6d illustrate a linear dependence of the yield and mean thickness versus deposition time. If the variation of conductivity is negligible during constant current deposition, the electric field strength in the suspension can be assumed to be constant (Equation (1.7)). Additionally, if the variation of the concentration of particles in the suspension is negligible, then the linear increase of the yield versus deposition time is expected from Equation (1.4), which can be rewritten as:

$$Y = \mu_e . C_s . E . t \tag{4.1}$$

The surface of the as-deposited layers was investigated with an optical microscope. We observed macro-defects in the samples with yields larger than ~25 mg/cm² (points circled on Figure 4.5). We assumed that the formation of defects was associated with the large yield and large thickness of the samples deposited from suspension S25 [147], [148]. Yields and thicknesses of the as-deposited layers from S50 and S75 were smaller than 25 mg/cm² and 105 μm, respectively, for a deposition time of 150 s. In these samples, we have not observed any defects with the optical microscope. Also, the layers from S50 and S75 were

obtained from a suspension that contained a higher concentration of PAM, which may act as a binder in the as-deposited layers and may prevent the formation of defects.

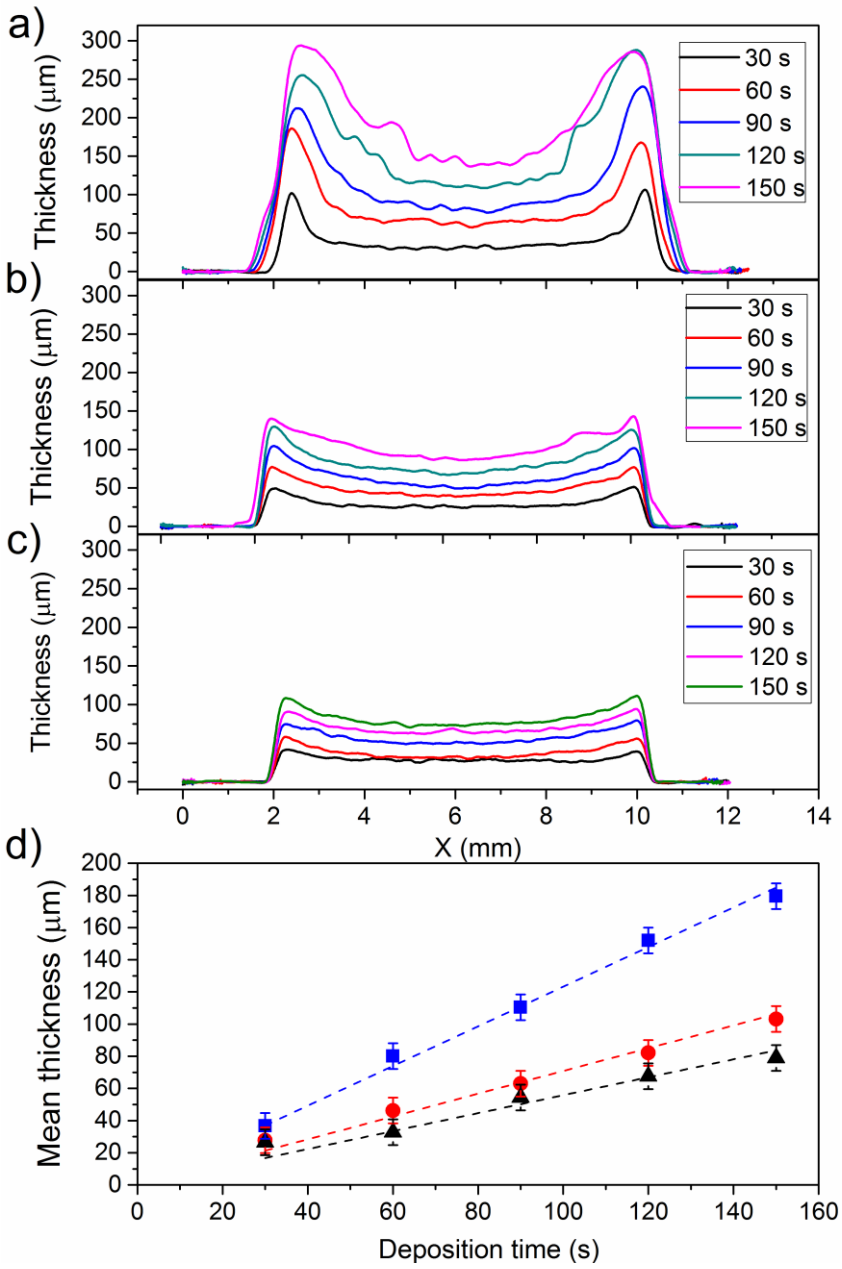

Figure 4.6: Thickness profiles of the as-deposited KNNSr layers from suspensions a) S25, b) S50 and c) S75 for deposition times of 30, 60, 90, 120 and 150 s, d) Mean thickness of the layers as a function of deposition time for the deposition from suspensions S25 (■), S50 (●) and S75 (▲). The dashed lines are linear regressions of the data.

The deposition rate (dY/dt) was calculated from a linear regression of the curve of the yield as a function of the deposition time (Figure 4.5). The dY/dt values were 20.3, 9.2 and 7.3 mg/(cm^2.min) for S25, S50 and S75, respectively.

We observed that the deposition rate increased linearly with the inverse of the conductivity ($1/\sigma_{susp}$) (Figure 4.7). This is consistent with Equation (4.1) showing that the deposition rate is proportional to the electric field strength between the electrode and

Equation (1.7) which illustrate that the electric field strength between the electrode is inversely proportional to the conductivity of the suspension.

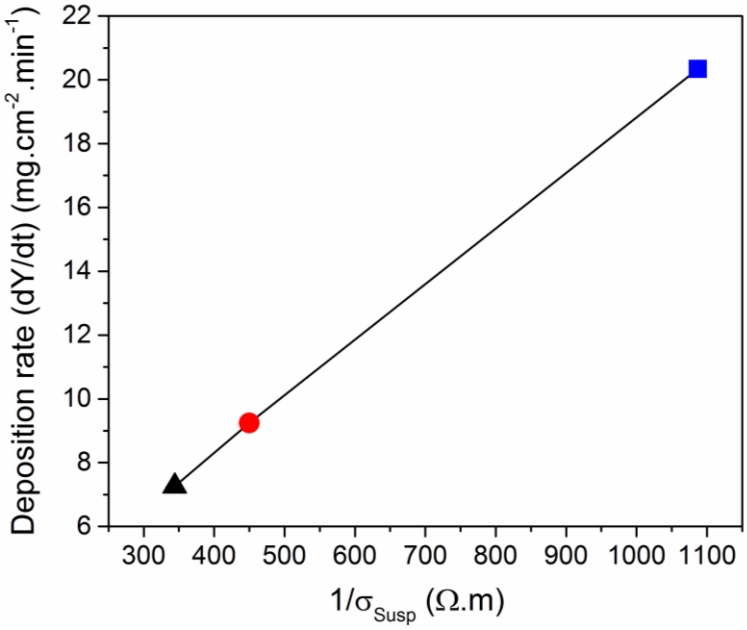

Figure 4.7: Deposition rate (dY/dt) as a function of the inverse of the conductivity $(1/\sigma_{susp})$ of the suspensions for deposition from suspensions S25 (■), S50 (●) and S75 (▲).

We observed that the deposits at the edges of the electrode were thicker compared to the centre (Figure 4.6). For example, for S75-150 (Figure 4.6.c) the thickness of the as-deposited layer at the electrode edge was ~110 μm, while the thickness in the electrode centre was ~75 μm. To evaluate the uniformity of the as-deposited layers we calculated the aspect ratio (AR) [104]:

$$\mathrm{AR} = \frac{t_{edges}}{t_{centre}} \tag{4.2}$$

where t_{edges} is the thickness of the deposit at the edges and t_{centre} is the thickness of the deposit at the centre. We estimated an error of ± 0.2 for the ARs, based on three samples processed for 90 s from S25 (S25-90).

The ARs of the deposits from S25, S50 and S75 are presented as a function of the deposition time in Figure 4.8. The ARs of the as-deposited layers decreased with increasing deposition time for a suspension with the lowest conductivity, i.e., S25, while it did not vary significantly for the suspensions S50 and S75 with larger conductivities. For example, the ARs decreased from 3.4 to 2.0 for S25-30 and S25-150, respectively, and from 1.9 to 1.8 for S50-30 and S50-150, respectively. The ARs for S75-30 and S75-150 were similar, i.e., 1.4. The layers deposited for 30 s had the largest ARs, i.e., 3.4, for S25-30, followed by 1.9 and 1.4 for S50-30 and S75-30, respectively.

Thicker edges were frequently observed in the EPD-derived as-deposited layer, in particular for a short deposition time [104], [109], [149] and are related to the non-uniform distribution of the electric field strength at the surface of the electrode. Pascall *et al.* [110] showed that the electric field strength is stronger at the edges of the electrode and thus the deposit is thicker at the edges than in the centre during the initial stage of the

deposition. We cannot avoid the singularity of the electric field, but by optimising the properties of the suspension and deposition conditions the AR can be minimised.

We correlated the high AR values for the deposits from suspension S25 with the lower conductivity of the suspension, in addition to the singularity of the electric field. In the early stage of the deposition, the particles from suspension S25 deposit on the entire electrode; however, predominantly and with the largest deposition rate at the regions with the strongest electric field strength, i.e., at the edges of the WE. As the deposition time increases, the thickness of the layer at the edges increases [110]. Consequently, the deposition rate at the edges of the electrode decreases compared to the centre of the electrode since the electric field strength at the edges become weaker [110]. Thus, with the increasing deposition time the AR values decreased, which is consistent with the literature [111], [150]. The ARs of the deposits from the suspensions S50 and S75 were lower and the variation of the AR as a function of the deposition time in the 30–150 s range is less pronounced.

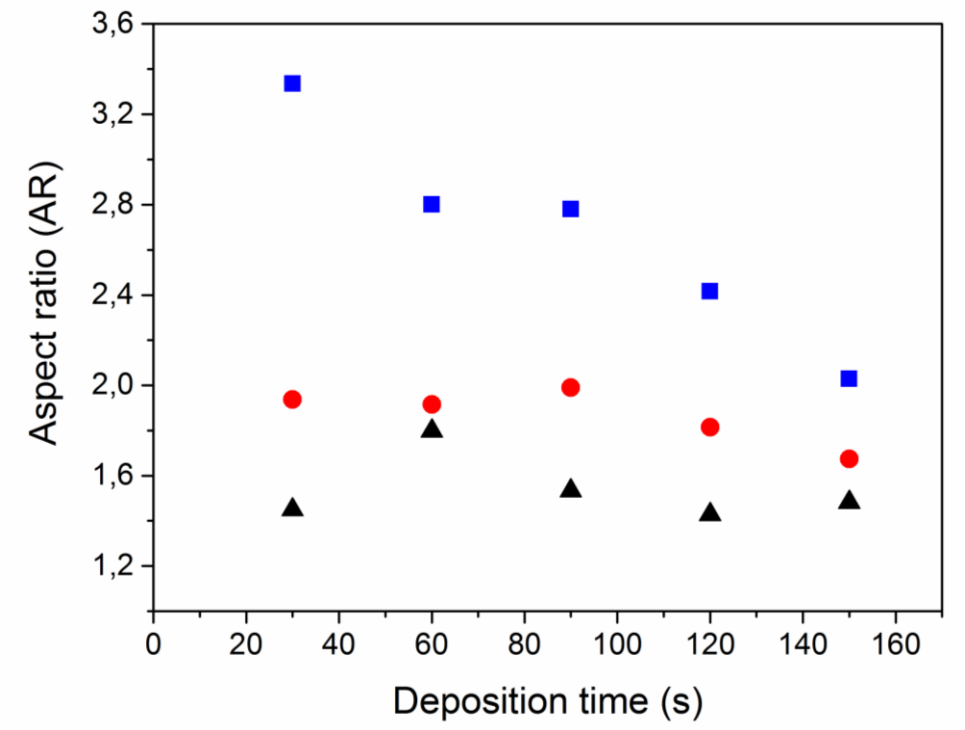

Figure 4.8: Aspect ratio AR as a function of the deposition time for deposition from suspensions S25 (■), S50 (●) and S75 (▲).

During the EPD a potential drop across the deposit can occur [99]. If we assume no polarisation at the electrodes the situation can be represented by an equivalent electrical circuit consisting of two resistances in series: the resistance of the suspension and a resistance associated with the voltage drop across the deposit, which will be called the deposit resistance [111], [151]. Literature reports that the most uniform thickness deposits were obtained from the suspension forming deposits with higher potential drops across the deposits [108], [111], [152].

During the deposition at constant current I ($= J \times S_{elec}$), the voltage delivered by the source ΔV(t) varied with time. If we assume that the variations of the resistance of the suspension (R_{susp}) are negligible, then the measurement of ΔV(t) allowed us to calculate the deposit resistance (R_{dep}) as [108]:

$$R_{dep}\ (t) = \frac{\Delta V(t)}{I} - R_{susp} = \frac{\Delta V(t) - \Delta V_{0,EXP}}{I} \tag{4.3}$$

with $\Delta V_{0,EXP}$ the voltage of the EPD cell at $t = 0$ s. We calculated the resistance of the suspension from $\Delta V_{0,EXP}$ (at t=0) and the deposit resistance from $\Delta V(t)$ recorded during the deposition. The resistances of the suspensions (R_{susp}) were 49.8 $k\Omega$, 22.7 $k\Omega$ and 17.4 $k\Omega$ for S25, S50 and S75, respectively. The differences in the R_{susp} agree with the conductivity measurement (Table 4.1), i.e., the largest resistance was observed for the suspension that exhibited the lowest conductivity. The calculated R_{dep} are presented in Figure 4.9. We observe that the R_{dep} increases with the increasing deposition time and at a fixed deposition time, in the 30-90 s range, it increases with the conductivity of the suspension between S25 and S50 whereas values were similar for S50 and S75.

These results indicated that deposit processed from S25 was more conductive than the one processed from S50 and S75. Thus, at a given time, at the edges of the deposit the electric field strength was stronger for S25 in comparison to S50 and S75. The stronger electric field strength resulted in a higher deposition rate at the edges of deposit for S25 and consequently the highest ARs (Figure 4.8). For the deposition performed from S50 and S75, the less conductive edges of the deposits resulted in weaker electric field strength at the edges and consequently lower ARs (Figure 4.8). This observation qualitatively agreed with the literature [108], [111], [152]. For example, Bernardo *et al.* [108] observed that the difference in thickness between the edges and the centre of PZT-based deposits was more pronounced for suspension that led to a R_{dep} of 3.2 $k\Omega$ than for the suspension that resulted in a R_{dep} of 9.6 $k\Omega$.

After a prolonged deposition time the R_{dep} for S25 increases. Thus, the edges of the deposit became less conductive. Consequently, the deposition rate at the edges of the electrode decreased compared to the centre of the electrode, which caused a decrease of the ARs with the deposition time (Figure 4.8).

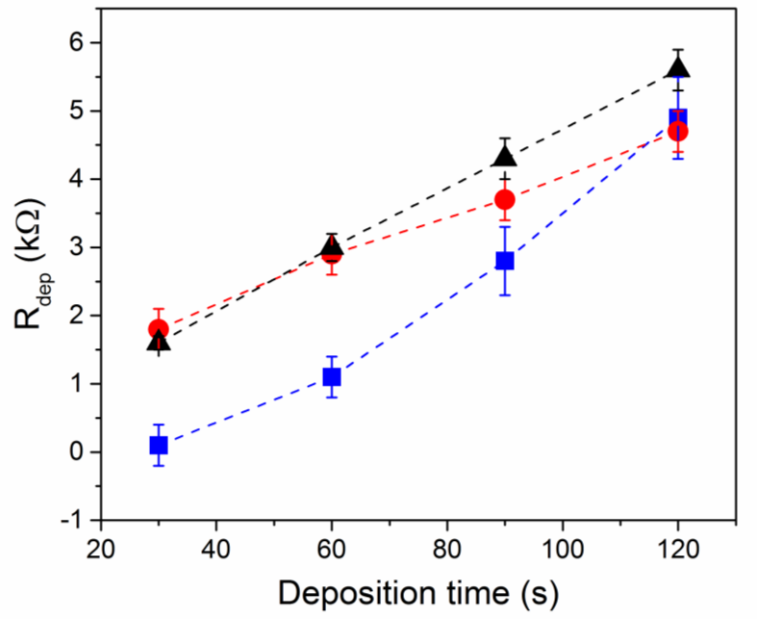

Figure 4.9: Deposit resistance (R_{dep}) as a function of deposition time for depositions performed from suspensions S25 (■), S50 (●) and S75 (▲). Dashed lines are guides to the eyes.

We investigated the thickness profile of the as-deposited layers with a similar yield of ~ 10 mg/cm^2 from suspensions S25, S50 and S75. To reach the similar yield the deposition time was longer for the suspensions with larger conductivity and lower deposition rate, i.e., 90 s for S75, 60 s for S50 and 30 s for S25 (Figure 4.5). The selected samples were S25-30, S50-60 and S75-90. From Figure 4.10, it is evident that the thickness profiles of the layers differ, although the yields were similar. The thicknesses at the edges were ~105, ~80 and ~75 μm for S25, S50 and S75, respectively whereas the thickness at the centres were ~30, ~40 and ~50 μm for S25, S50 and S75, respectively. The corresponding ARs were 3.3, 1.9 and 1.5 $\pm$ 0.2 for S25, S50 and S75, respectively.

We relate the differences in the ARs to the values of the resistance of the deposit, i.e., 0.1 $\pm$ 0.3 $k\Omega$, 2.9 $\pm$ 0.3 $k\Omega$ and 4.3 $\pm$ 0.3 $k\Omega$ for the as-deposited layers S25-30, S50-60 and S75-90 (Figure 4.9). The deposit resistance of S75-90 in comparison to S50-60 and S25-30 contributed to the lower AR values [108], [111] and S75-90 was the most uniform thickness as-deposited layers compared to S50-60 and S25-30.

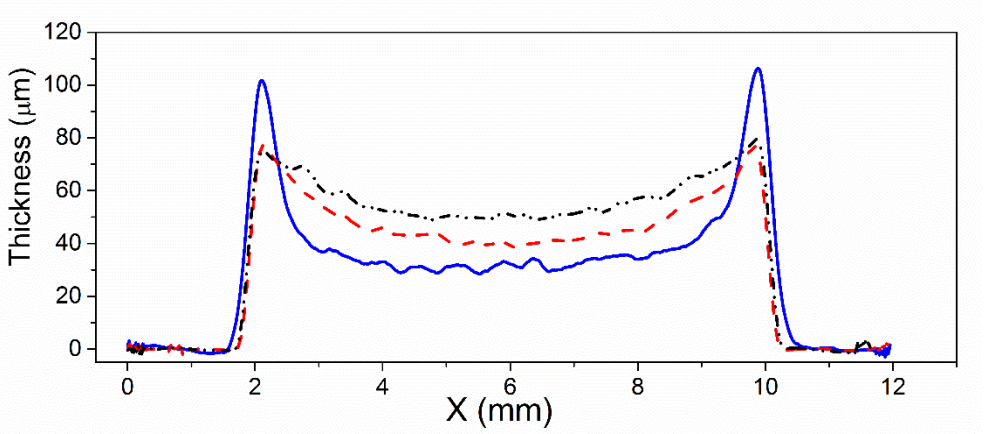

Figure 4.10: Thickness profile of the as-deposited KNNSr layers S25-30 (solid blue line), S50-60 (dashed red line) and S75-90 (dashed dotted line).

We investigated the surfaces of the as-deposited KNNSr layers S25-30, S50-60 and S75-90 by SEM (Figure 4.11). The as-deposited layers consisted of micrometre-sized particles. We did not observe any agglomerates. From the SEM images it is evident that the morphologies of the S50-60 and S75-90 samples were similar, with uniform surfaces. The as-deposited layers S25-30 exhibited a less homogeneous distribution of the particles on its surface, which we relate to the rapid deposition rate (dY/dt). The dY/dt value of the suspension S25, i.e., 20.3 mg/(cm^2.min), was more than two times larger than those from S50 and S75, i.e., 9.2 and 7.3 mg/(cm^2.min), respectively. Due to the rapid deposition, the KNNSr particles from the S25 suspension could not efficiently rearrange on the surface of the electrode and consequently formed less uniform as-deposited layers. Similar phenomena were reported in the literature [104].

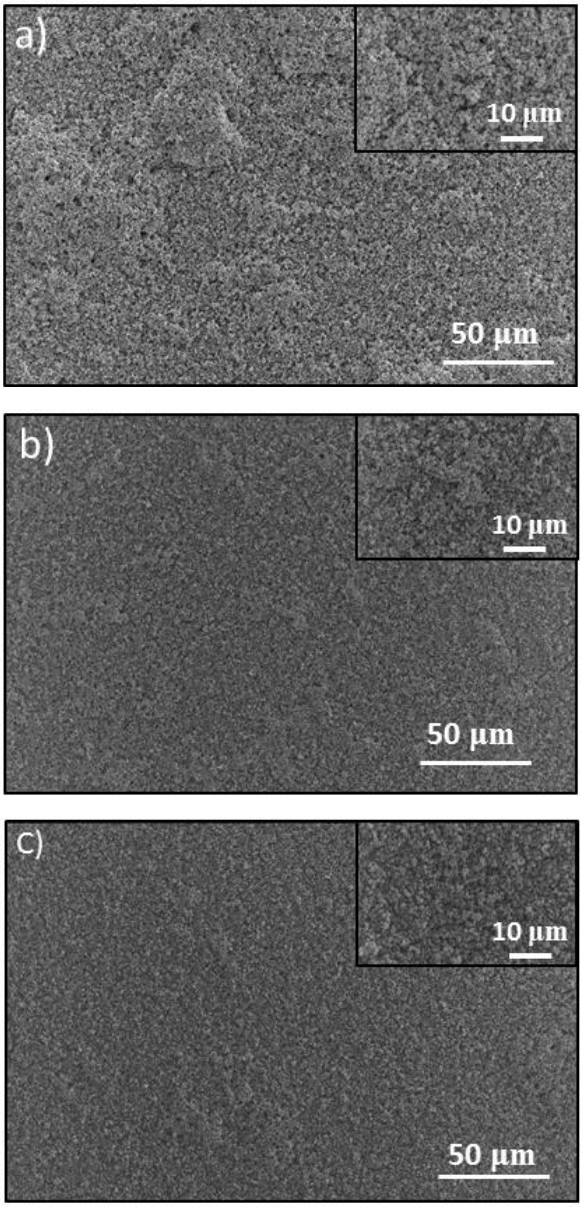

Figure 4.11: SEM images of the surface of as-deposited KNNSr layers a) S25-30, b) S50-60 and c) S75-90. The insets show the corresponding surfaces at higher magnification.

4.1.3 Impact of the EPD setup geometry on the thickness uniformity of the as-deposited layers

We have shown in the previous subchapter that the conductivity of the suspension has an impact on the yield, morphology and thickness-uniformity of as-deposited layers. The thickness profiles of the as-deposited KNNSr layers were related to the higher electric field strength at the edges of the electrode in comparison to its central part [110]. A finite-element analysis (FEA), based on the study presented in [104], was used to assess the voltage and the electric field strength in the suspension between the electrodes at the initial stage (t=0 s) of the deposition. The FEA-predicted voltages ($\Delta V_{0,FEA}$) and electric field strength distributions normal to the electrode surface (E_Z) in close vicinity of the WE

were compared to the experimental voltage at the beginning of the deposition ($\Delta V_{0,EXP}$) and thickness profiles.

First, the parametric analysis of the EPD process under constant-current conditions (1.56 mA/cm²) was carried out for the conductivities of the suspensions S25, S50 and S75, i.e., 9.2, 21.2, 29.1 μS/cm (Table 4.1), respectively, for Setup 1 with the inter-electrode distance (h_i) of 14 mm and counter-electrode diameter (D_e) of 35 mm.

The E_Z component is presented in Figure 4.12a and Figure 4.12b. Figure 4.12a shows a top view of E_Z in close vicinity to the working electrode. E_Z is the largest at the electrode edges and more particularly at its corners. When representing the E_Z along a line A-A (Figure 4.12b, see 3.4 for details), we confirmed that it was the largest at the edges of the WE, which is in accordance with the thickness profiles (see Figure 4.6). These results qualitatively agree with the results of a larger electric field magnitude and current density at the electrode edges reported by Pascall *et al.* [110] and Kuscer *et al.* [104].

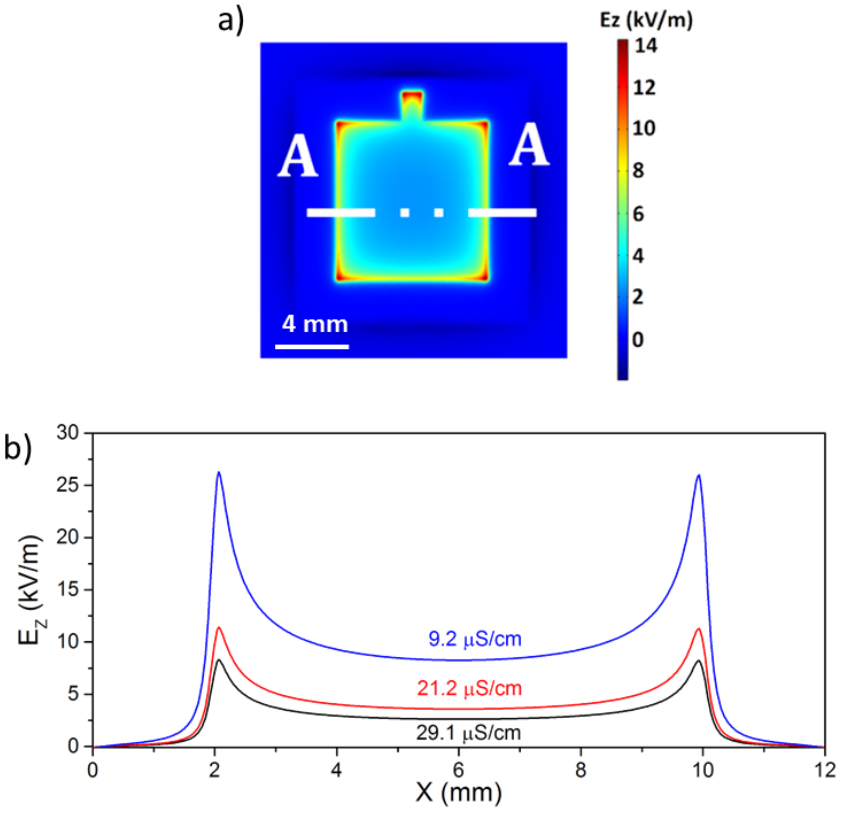

Figure 4.12: a) E_Z in close vicinity to the surface of the WE (top view, same dimension as RAO substrate), the E_Z profiles show thereafter are extracted along the marked A-A line, b) E_Z along the line A-A for suspensions with conductivities of 9.2 μS/cm (S25, solid blue line), 21.2 μS/cm (S50, dashed red line) and 29.1 μS/cm (S75, dashed dotted line) predicted close to the surface of the working electrode.The characteristics of the EPD cell is h_i= 14 mm, D_e= 35 mm (Setup 1) and deposition at constant current density of 1.56 mA/cm².

Table 4.2 showed that the FEA-predicted voltages were close to the experimentally measured voltages at the initial stage of the deposition. The similar values for the predicted and experimental voltages suggested that the proposed FEA was suitable to describe the electric field strength distribution in the suspension during the initial stage of deposition with Setup 1.

The electric field strength E_Z at a given position in close vicinity to the electrode was inversely proportional to the electrical conductivity of the suspension (Figure 4.12, Equation (1.7)) and confirmed the reason for the increased deposition rate with decreasing conductivity of the suspension (Figure 4.7). The MAD (normalised Median Absolute Deviation, Equation (4.4)), which quantified the statistical dispersion, was selected to assess the uniformity of the electric field strength profiles. A comparison of MAD with normalised standard deviation and an aspect ratio defined for the electric field strength (AR_E), is presented in Appendix E.

$$\text{MAD} = \text{median}\left(\left|E_{Z,i} - \widetilde{E_{Z,i}}\right|\right)/\widetilde{E_{Z,i}} \tag{4.4}$$

In the relation (4.4), $E_{z,i}$ is the electric field strength along the z direction at the point with abscissa X_i and $\widetilde{E_{Z,i}}$ is the value of the median of the dataset. The point X_i are taken to account only for the $E_{z,i}$ above the WE, i.e., 2.35 mm $< X_i <$ 10.35 mm along the line A-A (Figure 4.12b), which represent n points ($n \approx 160$ points).

For the electric field strength distribution calculated for different suspension conductivities, (Figure 4.12), the MAD value was 10.5 %, regardless of the conductivity of the suspensions. Thus, before any deposition the electric field strength uniformity in the suspensions S25, S50 and S75 was similar. This agrees with the fact that E_Z are inversely proportional to the conductivity, and thus the three E_Z profiles are proportional. We choose one of the conductivities of the suspensions as an example and we selected 21.2 μS/cm (S50) for the following analysis.

Table 4.2: Finite-element-analysis predicted voltage ($\Delta V_{0,FEA}$) and experimental voltage ($\Delta V_{0,EXP}$) and MAD values.

Suspension	$\Delta V_{0,FEA}$ (V)	$\Delta V_{0,EXP}$ (V)	*MAD* %
S25	47.3	49.8	10.5
S50	20.5	22.7	10.5
S75	15.0	17.4	10.5

We performed a FEA for eleven inter-electrode distances (h_i between 1 and 20 mm) and ten counter-electrode diameters (D_e between 0.4 and 35 mm). A 2D representation of the calculated MAD as a function of (h_i) and (D_e) is given in Figure 4.13. The results showed that the MAD values depended on the EPD setup geometry.

The MAD was equal or larger than 7.3 % for h_i larger than 9 mm, regardless of the D_e value. The MAD was less than 0.24 % only for the smallest $h_i = 1$ mm and for $D_e > 8$ mm. When $h_i < 4$ mm and $D_e < 6$ mm, the MAD was larger than 3.1 %. For $2 < h_i < 4$ mm and $8 < D_e < 10$ mm, we found MAD in the range 0.5–3.1 %. However, for those h_i values ($2 < h_i < 4$ mm), when $D_e > 10$ mm and $D_e < 8$ mm the MADs were larger than 3.1 %.

The model predicts that the optimal conditions (minimal MAD values) were obtained for $h_i = 1$ mm with $D_e \geq 8$ mm (horizontal dark-blue area, MAD$<$ 0.24 %). However, with the current EPD setup (Setup 1) the interelectrode distance cannot be smaller than 3 mm. According to the model, the smallest MAD parameter, for the $h_i = 3$ mm, is expected for $7.5 < D_e < 9$ mm, with MAD values in the range 0.24–0.56 %, which is close to the lowest calculated value. Thus, the most uniform E_Z profile along line A-A that could be experimentally realised with Setup 1 was predicted for the conditions $h_i = 3$ mm

and D_e = 8 mm (see red cross in Figure 4.13), for which the ratio (R_e) between the dimension of the CE (= D_e) and WE (= L_{WE}) ($R_e = D_e/L_{WE}$) was one.

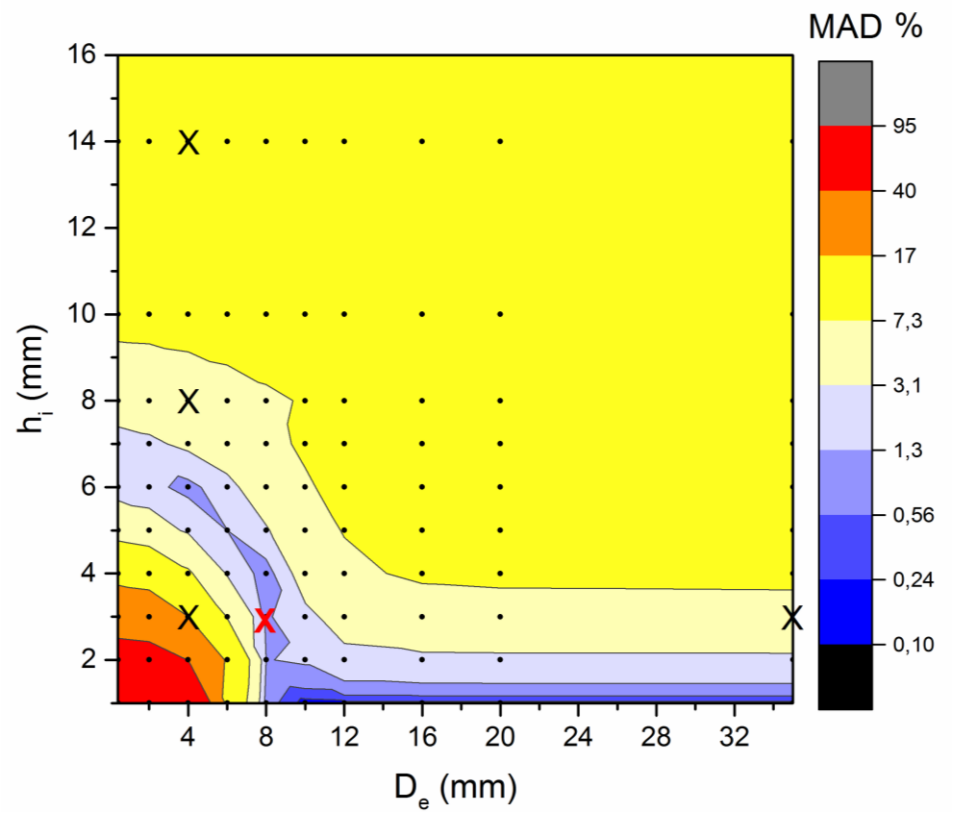

Figure 4.13: 2D representation of the MAD value as a function of the interelectrode distance (h_i) and CE diameter (D_e). The points (·) were calculated by FEA. The (X) corresponds to the conditions that were experimentally performed and (**X**) correspond to the theoretical optimal conditions achieved with Setup 1.

To study and compare the variations of the E_Z component along the line A-A with various h_i and D_e values, we selected the conditions marked with a cross in Figure 4.13. The E_Z component profiles were compared to the experimental thickness profiles of the as-deposited layers with the same EPD cell geometry. The aim was to validate that the influences of h_i and D_e observed on the E_Z profiles were also experimentally detected on the thickness profiles. First, the results at a constant diameter of the CE (D_e = 4 mm, R_e = 0.5) and three different inter-electrode distances (h_i = 3, 8, 14 mm) are shown in Figure 4.14.

For h_i values of 14 and 8 mm, the E_Z component along line A-A exhibit the largest values near the edges of the electrode and the lowest values at its centre (Figure 4.14a). At a smaller inter-electrode distance, i.e., h_i = 3 mm, the E_Z values increased in the centre of the electrode but were slightly lower at the edges of the electrode compared to those of the two previous cases. The experimental thickness profiles of the as-deposited layers (Figure 4.14b) showed a similar behaviour to those obtained with the FEA: the as-deposited thickness profiles for h_i = 14 and 8 mm were similar, with a concave shape in the centre of the as-deposited layers, while for h_i = 3 mm the thickness of the as-deposited layer is higher at the centre, corresponding to a convex shape in the centre of the as-deposited layers. The thicknesses of the as-deposited layers at the edges were comparable for the three cases.

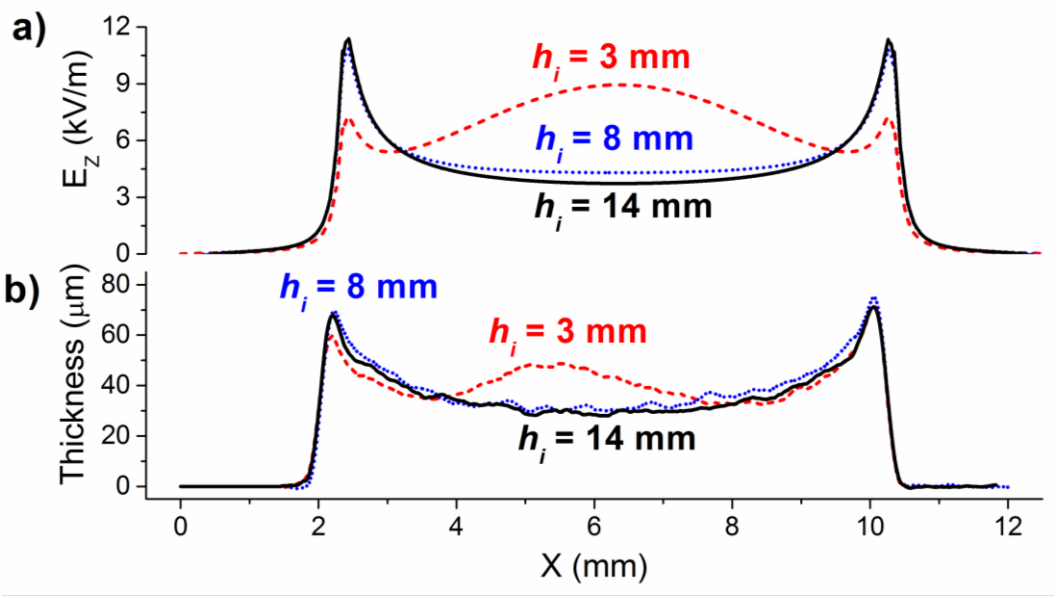

Figure 4.14: a) Finite-element-analysis-predicted electric field strengths along line A-A in close vicinity to the WE for $R_e = 0.5$ (CE diameter D_e of 4 mm) and $h_i = 3$, 8 or 14 mm, b) Experimentally measured thickness profiles along line A-A of KNNSr as-deposited layers obtained under identical conditions. The axes are not to scale.

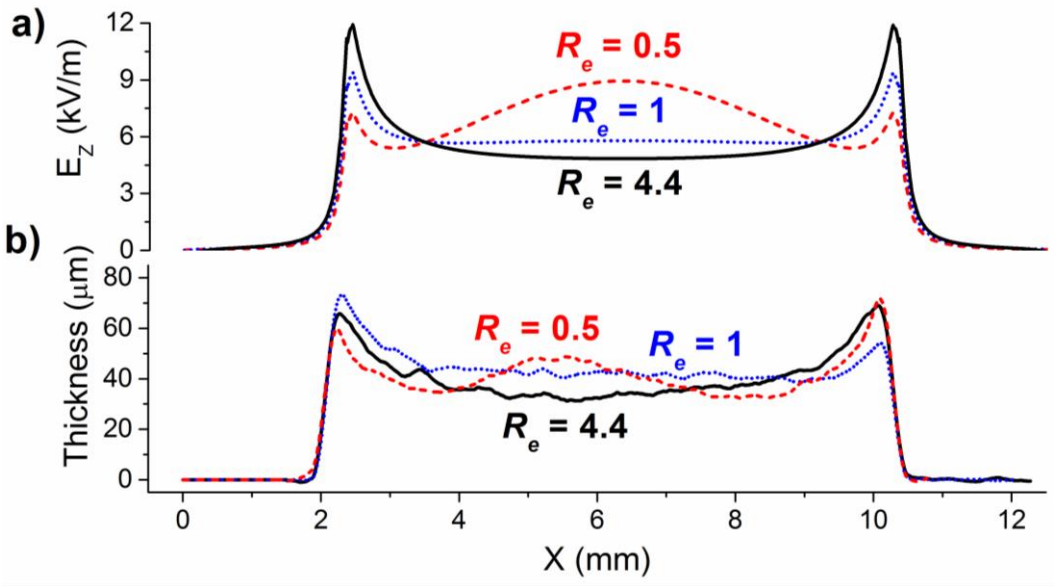

Figure 4.15: a) Finite-element-analysis-predicted electric field strengths along line A-A in close vicinity to the WE for $h_i = 3$ mm and $R_e = 0.5$, 1 or 4.4, b) Experimentally measured thickness profiles along line A-A for as-deposited KNNSr layers prepared under identical conditions. The axes are not to scale.

We also checked the influence of the diameter D_e (4, 8, 35 mm, corresponding to $R_e = 0.5$, 1, 4.4, respectively) of the CE on the E_Z distribution and thickness profiles at a constant inter-electrode distance ($h_i = 3$ mm). The results are presented in Figure 4.15.

For $R_e = 4.4$, the E_Z component exhibited larger values at the edges of the electrode. As the R_e value decreased from 4.4, 1 and 0.5, E_Z values increased in the centre of the

electrode and became slightly lower at the edges. For $R_e = 1$ the most uniform E_Z value was obtained on a large part of the lateral dimension of the electrode. The experimentally obtained thickness profiles of the as-deposited layers presented in Figure 4.15b showed similar trends to the E_Z values: it was observed that at the inter-electrode distance $h_i = 3$ mm the thickness in the centre of the deposit increased when R_e decreased from 4.4 to 1 and 0.5. The thicknesses of the as-deposited layers at the edges were similar for the three R_e values (4.4, 1 and 0.5). These results showed that the most thickness-uniform as-deposited layers were obtained for $h_i = 3$ mm and $R_e = 1$, corresponding to a similar lateral dimension between the two electrodes.

These results confirmed the strong correlation between the thickness profile of the as-deposited layers and the theoretical E_Z profiles.

We compared the thickness profiles of the samples S25-30, S50-60 and S75-90 presented in Figure 4.10, deposited under initial conditions ($h_i = 14$ mm and $R_e = 4.4$), to those from the same suspensions and deposition times during optimised conditions ($h_i = 3$ mm and $R_e = 1$). The comparisons of the thickness profiles are presented in Figure 4.16. An improvement of the thickness uniformity was observed for the as-deposited layer processed in optimised conditions, i.e., we observed a decrease of the thickness at the edges for all the samples and an increase of the thickness at the centre of the as-deposited layer for S25-30.

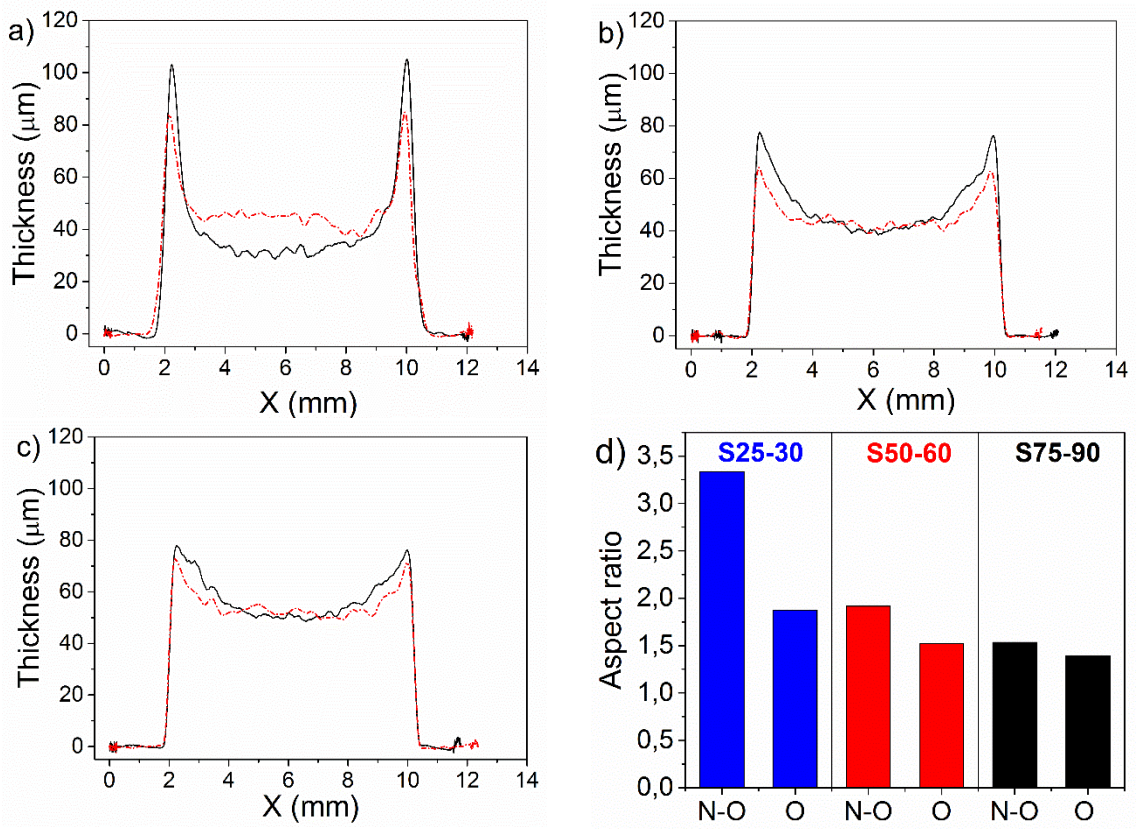

Figure 4.16: Thickness profile of as-deposited layers deposited at initial conditions ($h_i = 14$ mm and $R_e = 4.4$, solid black lines) and at optimised conditions ($h_i = 3$ mm and $R_e = 1$, dashed red lines) a) S25-30, b) S50-60 and c) S75-90. d) Aspect ratio (AR) calculated for the KNNSr as-deposited layers S25-30, S50-60 and S75-90 at initial conditions (NO) and at optimised conditions (O).

This was highlighted from the decrease of the ARs from 3.2, 1.9 and 1.5, to 1.9, 1.5 and 1.4 for S25-30, S50-60 and S75-90, respectively (Figure 4.16d). The largest decrease in AR values was observed for the low-conductivity suspension, i.e., suspension S25. The effect was less prominent for the deposition performed from S75, which already exhibited low ARs in initial deposition conditions due to the high conductivity of the suspension (Figure 4.8).

Thickness uniform as-deposited layers, with AR in the range 1.4–1.5 can be processed by deposition under optimal geometric conditions using the suspension S50 or S75. From the suspension S50 with the conductivity 21.2 μS/cm, we obtained a homogenous particle distribution at the surface of the electrodes (Figure 4.11) and thus we selected the suspension S50 for further experiments.

4.1.4 Reproducibility of the EPD process

We investigated the reproducibility of EPD by measuring the yield from 50 mL of the S50 suspension. We performed 15 consecutive depositions at a constant current density of 1.56 mA/cm^2 for 30 s. We measured the yield for each as-deposited layer and the conductivity of the suspension after every 5 deposits. The results are presented in Figure 4.17. We observed that the yield was 4.3 $\pm$ 0.3 mg/cm^2 and it did not vary significantly with the number of depositions. We calculated the concentration of the particles in the suspension after 15 depositions. We found that the particles' concentration decreased from 45.1 to 44.5 g/L, which represented a 2 % relative decrease in particle concentration after 15 depositions. We observed that the conductivity of the suspension increased from 25.0 to 25.5 $\pm$ 0.1 μS/cm after 13 depositions.

These results indicated the high reproducibility of the process. Moreover, they showed that the decrease of the solid load and the increase of the electrical conductivity of the suspension after 15 depositions under selected conditions had a negligible influence on the yield.

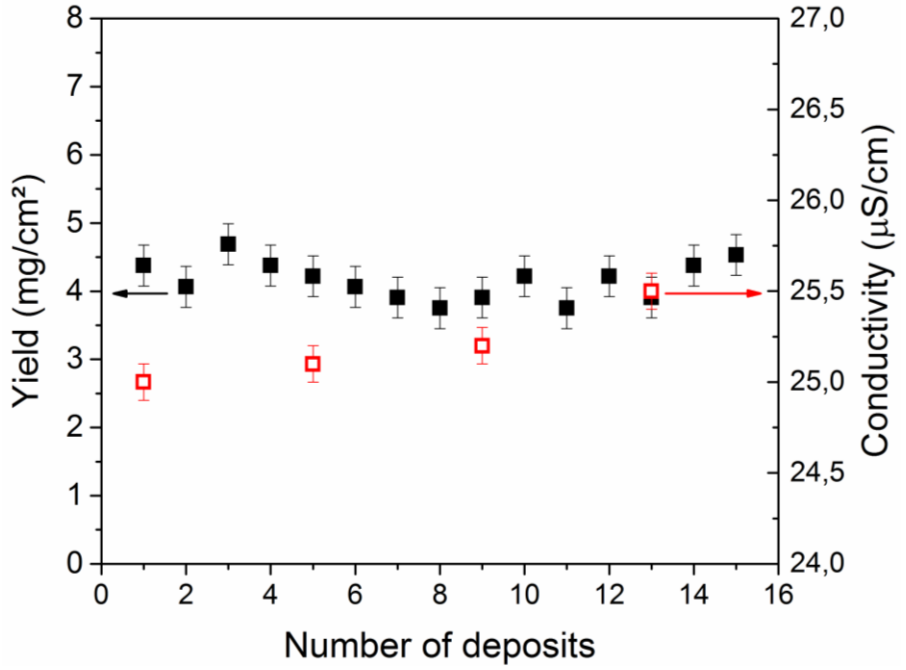

Figure 4.17: Yield as a function of the number of deposits for depositions performed at 1.56 mA/cm^2 for 30 s from suspension S50 at optimised conditions (h_i = 3 mm and D_e = 8 mm).

4.1.5 Summary

1 vol. % of KNNSr powder with a micrometre particle size was dispersed in ethanol with the addition of poly(acrylic acid-co-maleic acid) (PAM) and n-butylamine (BA). We have shown that the suspensions were stable with a ZP of - 45 mV.

The deposition yield depends on the conductivity of the suspension and the deposition time. With decreasing conductivity of the suspension and increasing deposition time the deposition yield and the as-deposited thickness of the layers increase.

The as-deposited layers exhibit thicker edges due to the stronger electric field strength in close vicinity to the edges of the electrode. The thickness uniformity of the as-deposited layers depended on the resistance of the deposit, which varied with the conductivity of the suspension. The most thickness-uniform as-deposited layers were obtained from the suspensions with the largest conductivity.

To improve the thickness uniformity of the as-deposited layer, the distribution of the electric field strength in close vicinity to the working electrode was studied by finite-element analysis. The interelectrode distance and counter-electrode diameter were varied to obtain optimal conditions for the processing of thickness-uniform KNNSr layers. The FEA predicted optimal conditions were compared to the experimental thickness profiles. The use of a small interelectrode distance (3 mm) and counter electrode of same dimensions as the working electrode (8 mm) allow the processing of thickness uniform KNNSr layers. Under optimal geometric conditions, the thickness uniformity of the as-deposited KNNSr layers processed from suspensions with a conductivity in the range 21–30 $\mu S/cm$ was similar and suspension S50 was selected.

Finally, we showed that the yield of KNNSr as-deposited layers could be obtained reproducibly from subsequent deposition from PAM/BA/EtOH-based suspensions.

4.2 Sintering and Characterisation of KNNSr Thick Films

The as-deposited KNNSr layers processed by EPD with a thickness of ~ 45 µm on platinised 640-µm-thick alumina (RAO) substrates were sintered between 1075 and 1120 °C. There, the samples often contain defects. To address this issue a modified deposition procedure was proposed: a ~ 10 µm initial KNNSr layer is deposited and fired, subsequently a second thicker KNNSr layer is deposited on top of the first KNNSr layer and subsequently sintered. With the aim to obtain dense and single-phase thick films, we optimised the sintering conditions in terms of temperature and atmosphere. We relate the sintering conditions to the microstructure, structure and electromechanical properties of the KNNSr thick films.

4.2.1 Preliminary sintering of KNNSr thick films

The preliminary sintering experiments were performed after we deposited 45 ± 4 μm thick KNNSr layers onto the RAO substrate. The approach is referred to as one-step deposition-sintering. The KNNSr layers with the yield of 10.9 ± 0.6 mg/cm^2 were obtained from the suspension with a conductivity of 22.0 μS/cm. The sintering was performed in air at temperatures of 1075, 1100 and 1120 °C.

In these preliminary sintering experiments, we frequently observed defects at the surface of the thick films and sometimes also delamination of the KNNSr from the substrate. These features were more pronounced when the layers were sintered at higher temperatures. For example, the thick films sintered at 1120 °C (T-1120-A) frequently delaminated from the substrate (Figure 4.18a) and the non-delaminated layers exhibited cracks at its surface (Figure 4.18b). Both issues prevented the electrical characterisation of the samples.

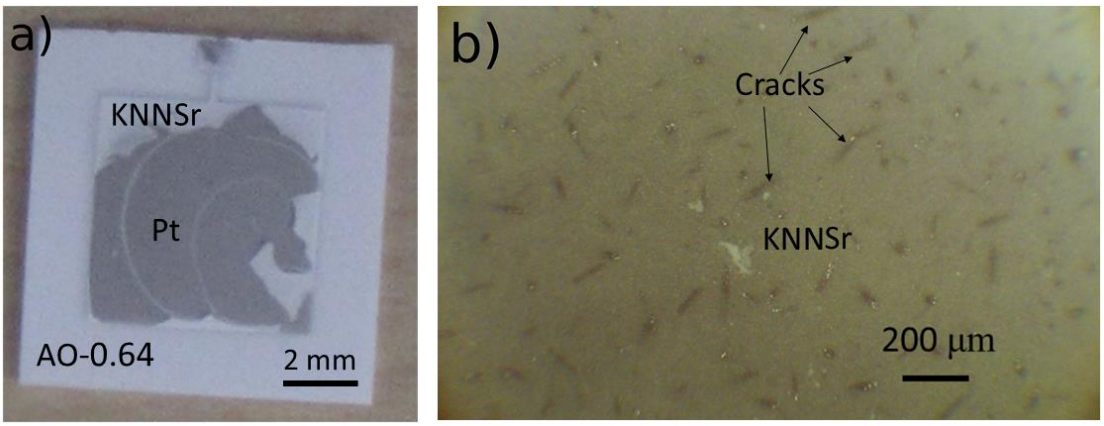

Figure 4.18: a) Top view of T-1120-A, where delamination can be observed after sintering, b) Optical image of cracks on the non-delaminated surface of T-1120-A after sintering. KNNSr: $(K_{0.5}Na_{0.5})_{0.99}Sr_{0.005}NbO_3$, Pt: platinum bottom electrode, AO-0.64; 640 μm alumina.

For the further analysis, we selected the samples and regions of the thick films that were well adhered to the substrate and exhibited a minimal number of defects.

The XRD patterns of the thick films are presented in Figure 4.19. In all the samples we identified the diffraction peaks corresponding to the perovskite phase with a monoclinic unit cell (PDF 77-0038, $K_{0.65}Na_{0.35}NbO_3$). In addition to the perovskite phase we observed diffraction peaks with low intensities at 25.5° and 29.4 ° indexed as a tungsten-bronze phase (TB, $K_{5.75}Nb_{10.85}O_{30}$, PDF 38-0297). The intensity of the peak at ~29.4 ° increased slightly with increasing temperature (Figure 4.19b), which may indicate a larger amount

of the TB phase formed at higher temperature. The diffraction peaks at 39.9° and 46.4° were indexed as platinum (PDF: 04-0802) and originated from the bottom electrode.

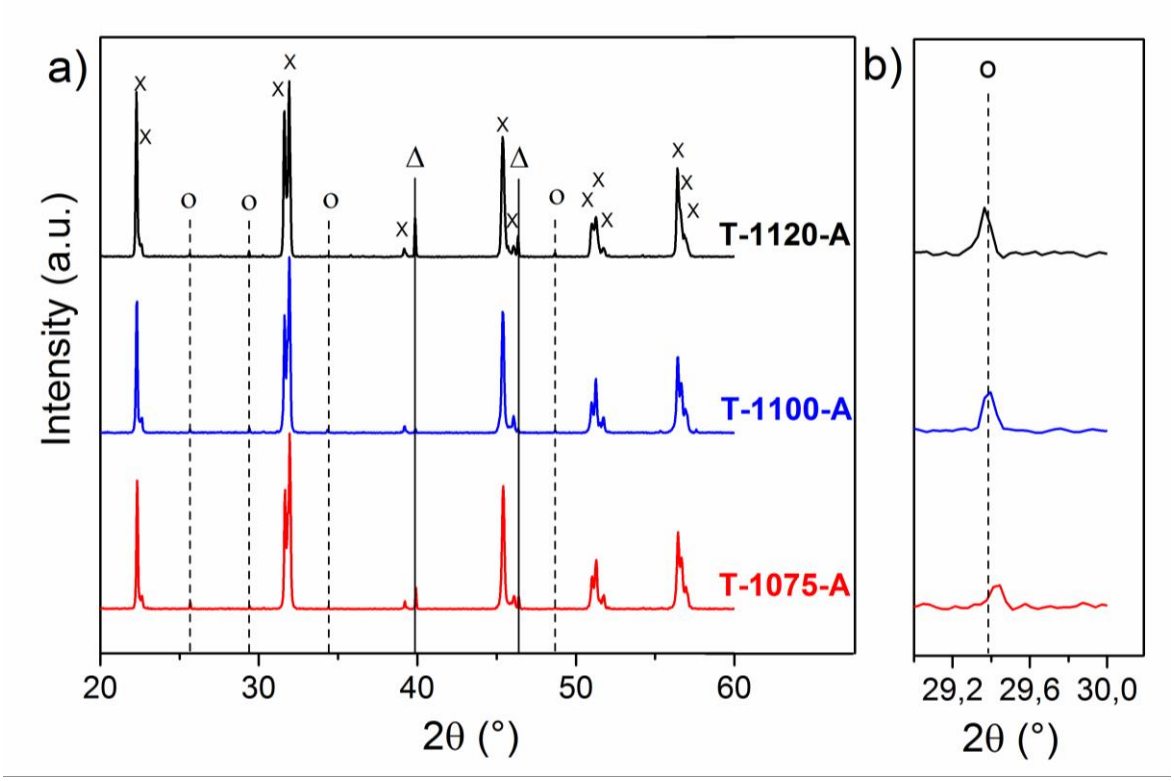

Figure 4.19: a) XRD pattern of the thick films sintered at 1075 °C (T-1075-A), 1100 °C (T-1100-A) and 1120 °C (T-1120-A) for 2 hours in air. x: $K_{0.65}Na_{0.35}NbO_3$ (PDF:77-0038); o: $K_{5.75}Nb_{10.85}O_{30}$ (PDF: 38-0297) and Δ: Pt (PDF: 04-0802), b) Enlarged view of the diffraction peak at ~29.4 ° corresponding to TB phase.

The polished cross-section SEM images of T-1075-A, T-1100-A and T-1120-A are presented in Figure 4.20. The samples sintered at 1075 and 1100 °C exhibited a homogeneous microstructure consisting of KNNSr grains with randomly distributed pores. The thick films sintered at 1075 °C exhibited shrinkage (along the thickness) of 28 ± 12 % and their relative density was 70 ± 5 % (Figure 4.20a). The thick films sintered at 1100 °C had a shrinkage of 37 ± 10 % and a relative density of 77 ± 4 % (Figure 4.20b). A further increase of the sintering temperature to 1120 °C resulted in shrinkage of 46 ± 9 % and thick films with a relative density of 86 ± 4 % (Figure 4.20c). In the microstructure of the thick films sintered at 1120 °C, we detected large bright grains (denoted TB in Figure 4.20d). According to the EDXS analyses, this phase corresponds to the TB, which agrees well with the XRD patterns. The TB phase had been reported previously in the KNN system for both ceramics and thick films and corresponded well to a TB phase of the type $K_{5.75}Nb_{10.85}O_{30}$ which contains, in addition to K and Nb, also a minor amount of sodium ions [48].

The formation of TB in the thick films may be related to the volatilisation of the alkalis from the KNNSr thick films. At elevated temperatures, the volatilisation of alkalis from the thick films is likely due to the larger area-to-volume ratio of the thick film in comparison to bulk ceramics. Also, the volatilisation is more pronounced at higher temperature [46], [153].

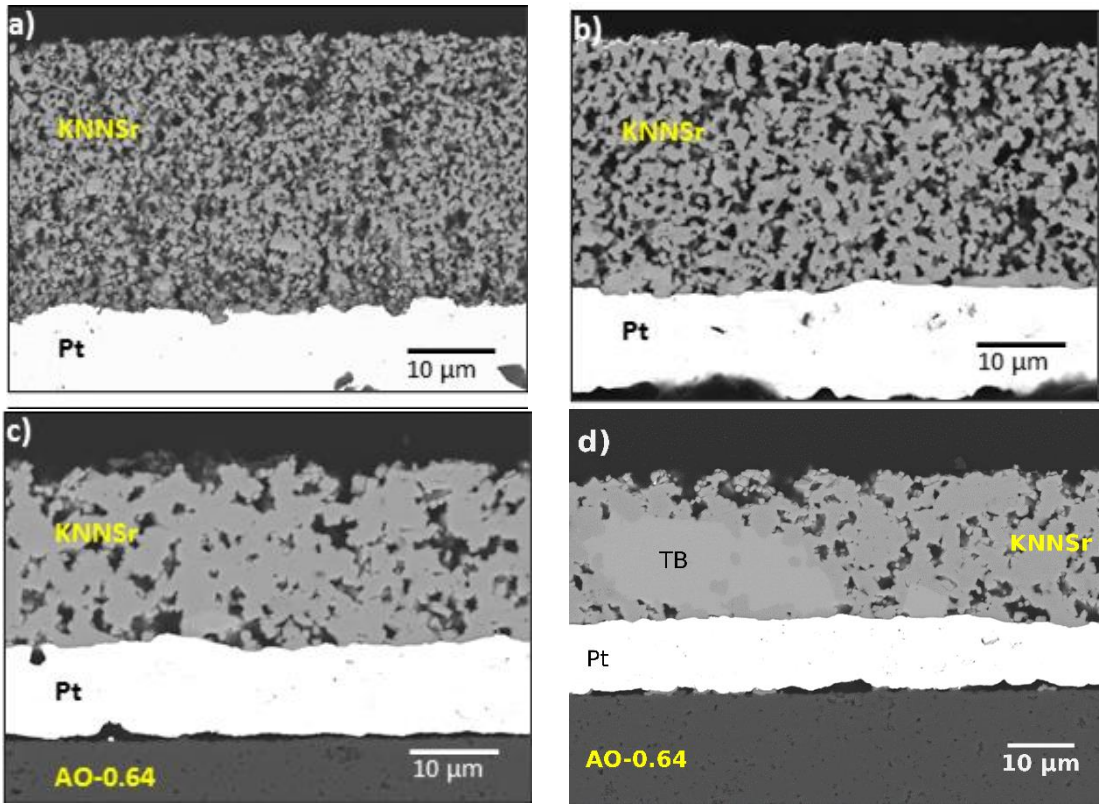

Figure 4.20: Polished cross-section SEM images of the samples a) T-1075-A, b) T-1100-A and c) and d) T-1120-A. KNNSr: $(K_{0.5}Na_{0.5})_{0.99}Sr_{0.005}NbO_3$, Pt: platinum, AO-0.64: alumina substrate and TB: tungsten bronze.

The thickness profiles measured before and after sintering of T-1100-A are presented in Figure 4.21. We observed that the KNNSr layers shrank predominantly along the thickness direction. The linear shrinkage along this direction was of ~ 35 ± 5 %. The KNNSr thick film is clamped on a rigid substrate and sintered in constrained conditions. We assume that the formation of defects in the thick films (Figure 4.18b) and/or the delamination (Figure 4.18a) of the thick films from the substrate was related to the in-plane tensile stresses that develop in the layer during the sintering [123], [154].

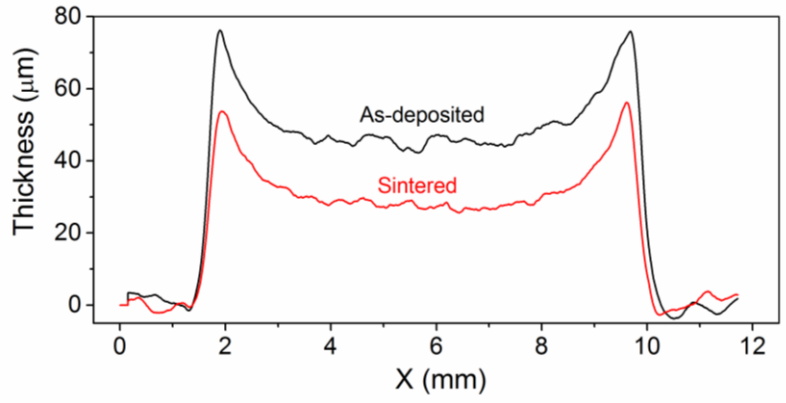

Figure 4.21: Thickness profiles of as-deposited and 1100 °C-sintered KNNSr thick films (T-1100-A).

With the aim to process dense, defect-free KNNSr thick films with a minimal amount of TB phase, we modified the process and sintering conditions.

4.2.2 KNNSr thick films by a two-step deposition-sintering procedure

The two-step deposition-sintering procedure was reported to reduce the tendency of crack formation in PZT-based thick films sintered on a rigid substrate [155]. This procedure was implemented for the sintering of KNNSr thick films.

4.2.2.1 Processing of the KNNSr thick films

The first KNNSr layer, denoted as F-1000-A, was deposited onto the RAO substrate for 30 s from the suspension with a conductivity of 29.8 μS/cm. After drying, we have not observed any defects in the layer by optical microscope. The yield was 2.5 $\pm$ 0.4 mg/cm^2. The layer was well adhered to the substrate after firing at 1000 °C. As seen in Figure 4.22a the thickness profiles of the as-deposited and fired layers are similar with thicknesses of about 9 $\pm$ 3 μm in the centre. Thus, no shrinkage was observed, either laterally or along the thickness directions. The relative density of the layer, calculated from the SEM images, was ~ 55 %. The absence of shrinkage and low density indicated that the densification was poor, which agreed well with the shrinkage-temperature curve (Figure 4.2), where we did not detect any shrinkage below ~1040 °C. This was also evident from the microstructure of F-1000-A (Figure 4.22b), which was porous.

The XRD pattern of F-1000-A is presented in Figure 4.22c. The diffraction peaks belong to the monoclinic perovskite phase (PDF: 77-0038). Two diffraction peaks at 39.9° and 46.4° which originate from the platinum bottom electrode (PDF: 04-0802) were also identified.

Onto the F-1000-A, we deposited a second layer for 90 s (see Appendix F). The samples exhibited a whole thickness of 44 $\pm$ 3 μm and a yield of 11.8 $\pm$ 0.5 mg/cm^2. Using an optical microscope, we did not observe any macroscopic defects at the surface of the layers.

The layer prepared by one-step deposition-sintering for an identical deposition time, i.e., 120 s from suspension S50 (see Figure 4.5), had a larger yield and it was thicker, i.e., 18.5 mg/cm^2 and ~ 60 μm, respectively, which we relate to the lower conductivity of the suspension. The conductivity of the suspension for the one-step deposition-sintering procedure was 21.2 μS/cm and for the two-step deposition-sintering procedure it was 29.8 μS/cm.

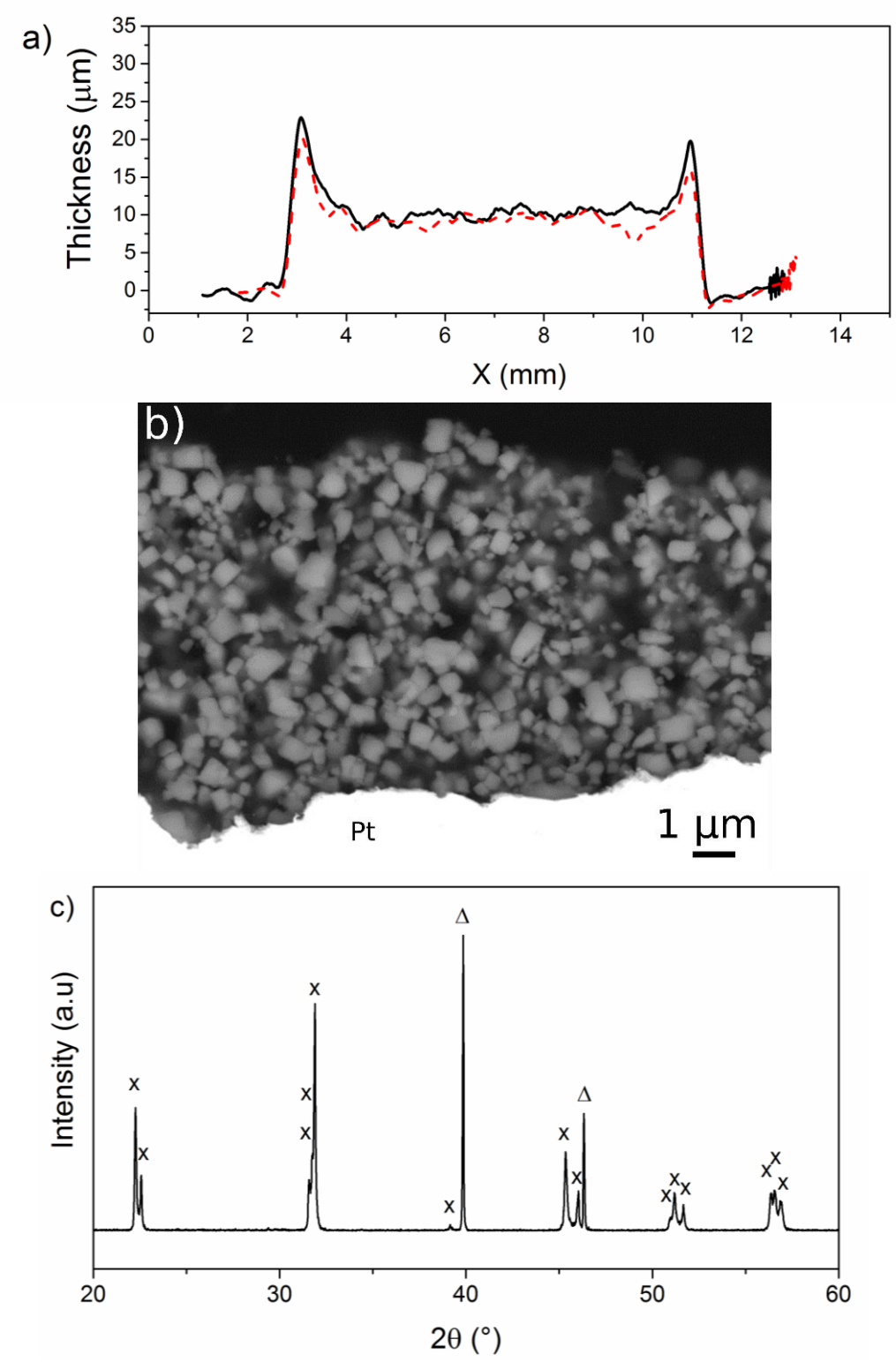

Figure 4.22: a) Thickness profile for the as-deposited layer (S50-30, black solid line) and for the fired layer at 1000 °C for 2 hour in air (F-1000-A, dashed red line), b) Cross-section SEM image of F-1000-A and c) XRD pattern of F-1000-A. x: $K_{0.65}Na_{0.35}NbO_3$ (PDF:77-0038); Δ: Pt (PDF: 04-0802).

4.2.2.2 Microstructure of KNNSr thick films

From the preliminary sintering results, we observed that at a low sintering temperature, i.e., 1075 °C, the microstructure was porous with a density of 70 %, while at 1120 °C the density increases to 86 %, but we also observed the formation of the TB phase. These results indicate that it is very challenging to obtain dense, single-phase KNNSr thick films, particularly due to a very narrow sintering temperature range of KNNSr (Figure 4.2) and alkali volatilisation at elevated temperature [46]. Thus, we investigated the sintering of KNNSr thick films in a temperature range 1090–1110 °C.

The samples were sintered at 1090, 1100 and 1110 °C in air and oxygen. According to the cross-section SEM images, all the sintered KNNSr thick films were well adhered to the substrate and exhibited a uniform thickness (Figure 4.23 and Figure 4.24).

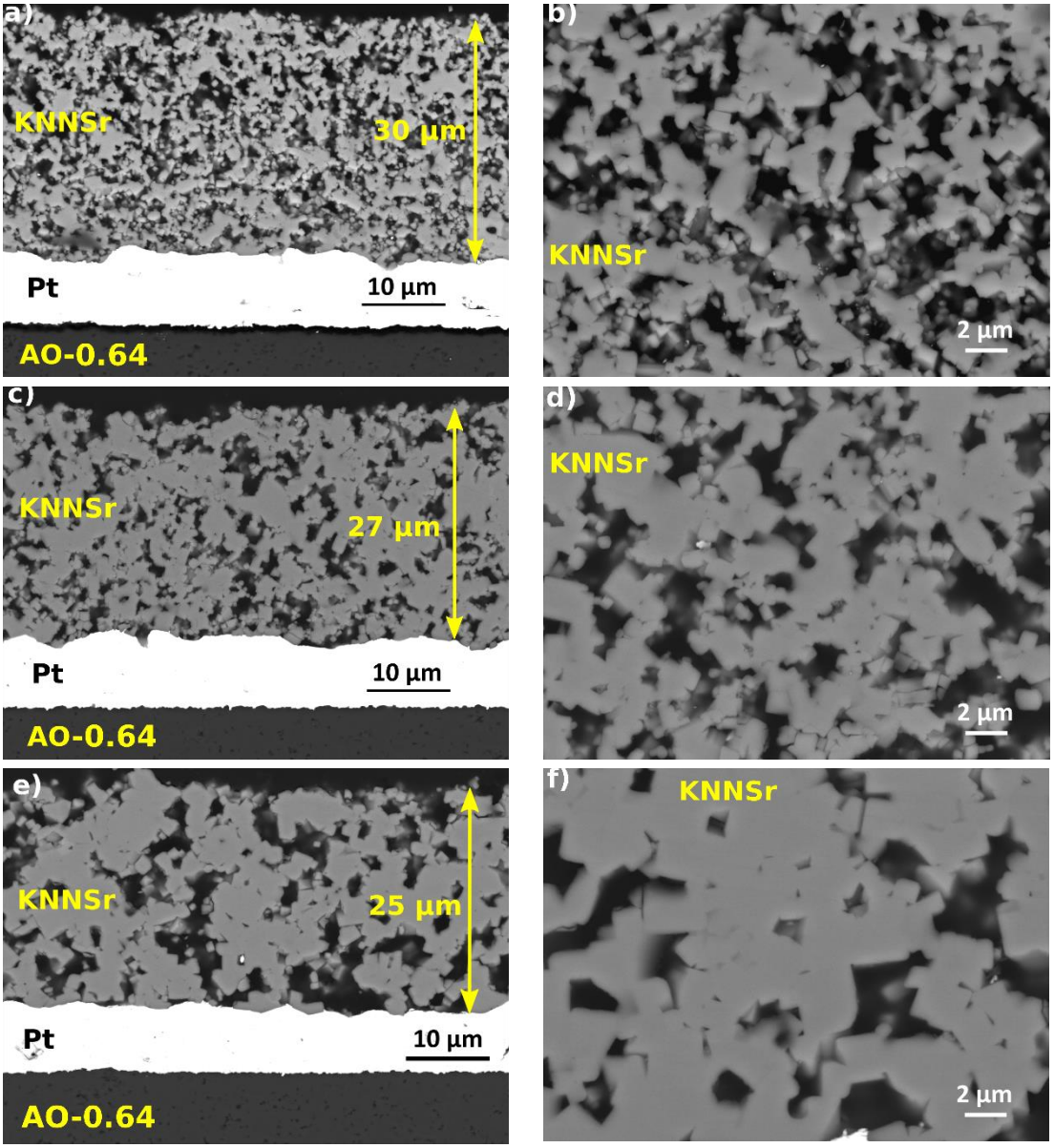

Figure 4.23: Polished cross-section SEM images of KNNSr thick films sintered in air for 2 hours a), b) 1090-A, c), d) 1100-A and e), f) 1110-A. KNNSr: $(K_{0.5}Na_{0.5})_{0.99}Sr_{0.005}NbO_3$, Pt: platinum, AO-0.64: alumina substrate.

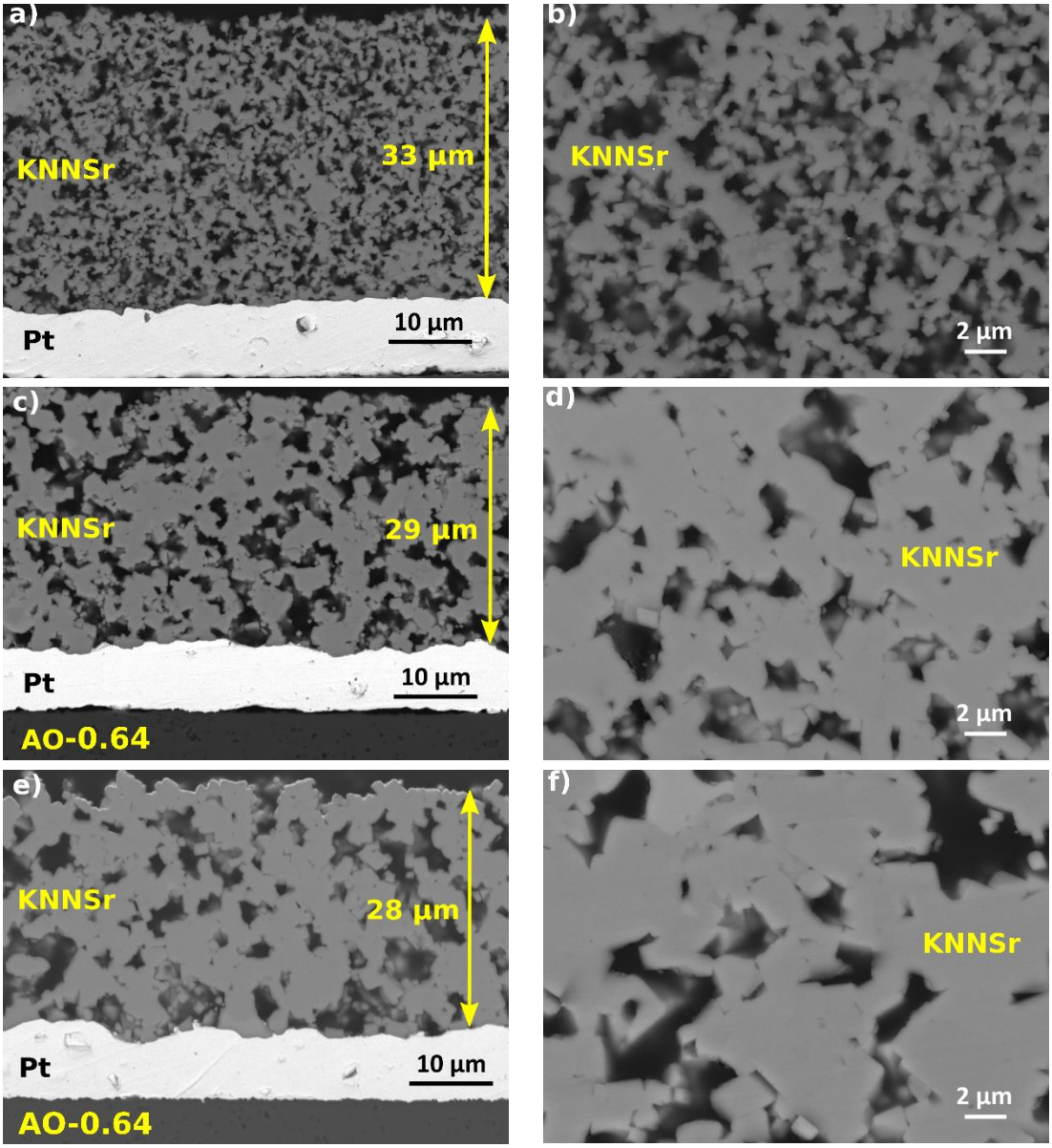

Figure 4.24: Polished cross-section SEM images of KNNSr thick films sintered in oxygen for 2 hours a), b) 1090-O, c), d) 1100-O and e), f) 1110-O. KNNSr: $(K_{0.5}Na_{0.5})_{0.99}Sr_{0.005}NbO_3$, Pt: platinum, AO-0.64: alumina substrate.

The shrinkage, relative density and median pore area of the samples are listed in Table 4.3. We observed that regardless of the sintering atmosphere the thickness of the KNNSr thick films decreased with the increasing sintering temperature and correspondingly the shrinkage increased.

The relative densities of the thick films sintered in air and oxygen at selected temperature were similar. The relative densities increased from ~75 ± 3, to ~80 ± 3 % when the temperature increased from 1090 to 1100 °C. (Table 4.3). At 1110 °C the relative density was similar to the one of the samples sintered at 1100 °C.

Table 4.3: Shrinkage, relative density and median pore size area of 1090-O, 1100-O, 1110-O, 1090-A, 1100-A and 1110-A thick films.

Sample	Shrinkage (%)	Relative density (%)	Median pore area (μm^2)
1090-A	25 ± 12	75 ± 3	1.0
1100-A	35 ± 8	80 ± 3	4.2
1110-A	41 ± 9	81 ± 3	6.1
1090-O	27 ± 8	74 ± 3	1.3
1100-O	37 ± 10	81 ± 3	2.5
1110-O	40 ± 8	82 ± 3	6.9

From the SEM images it is evident that the evolution of the microstructure is similar upon sintering the samples in oxygen and in air. At 1090 °C we observed micrometre-sized pores randomly distributed in the microstructure (see Figure 4.26b and Figure 4.26c). The porosity was still open. After sintering at 1100 °C, the relative density increased to ~80 % accompanied by the shrinkage of the layer. The porosity was open. When the temperature increased further to 1110 °C, the relative density does not vary significantly. Even though the grain boundaries were not clearly visible, the microstructure observation suggested an increase in grain size with increasing sintering temperature.

Figure 4.25 and Figure 4.26 summarise the results obtained from the cross-section SEM images. The number of pores per area decreased (Figure 4.25), while the pore area increased with the increasing sintering temperature, regardless of the sintering atmosphere (Figure 4.26a and Figure 4.26b). Namely, the median pore area ($A_{A,50}$) increased from 1.0 μm^2 to 4.2 μm^2 for 1090-A and 1100-A, respectively, and from 1.3 μm^2 to 2.5 μm^2 for 1090-O and 1100-O, respectively (Figure 4.26c and Figure 4.26d). At 1110 °C the median pore area further enlarged to 6.1 μm^2 for 1110-A and to 6.9 μm^2 for 1110-O. 1090-O had pore areas $A_{A,10}$ and $A_{A,90}$ of 0.4 and 3.5 μm^2, respectively, while 1110-O reached $A_{A,10}$ and $A_{A,90}$ values of 1.4 and 17.3 μm^2, respectively. Similar pore areas were also measured for 1090-A and 1110-A.

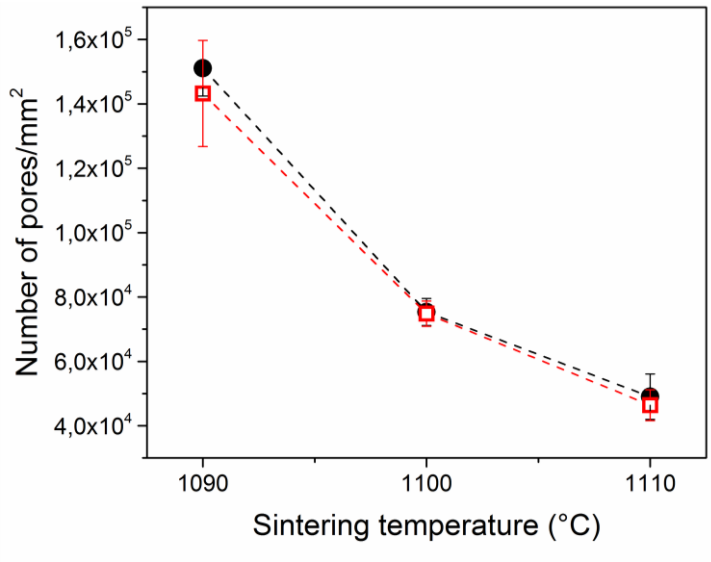

Figure 4.25: a) Number of pores per unit area for the samples: 1090-A,1100-A, 1110-A, 1090-O, 1100-O and 1110-O as a function of the sintering temperature, full circle (●) in air; hollow squares (□) in oxygen.

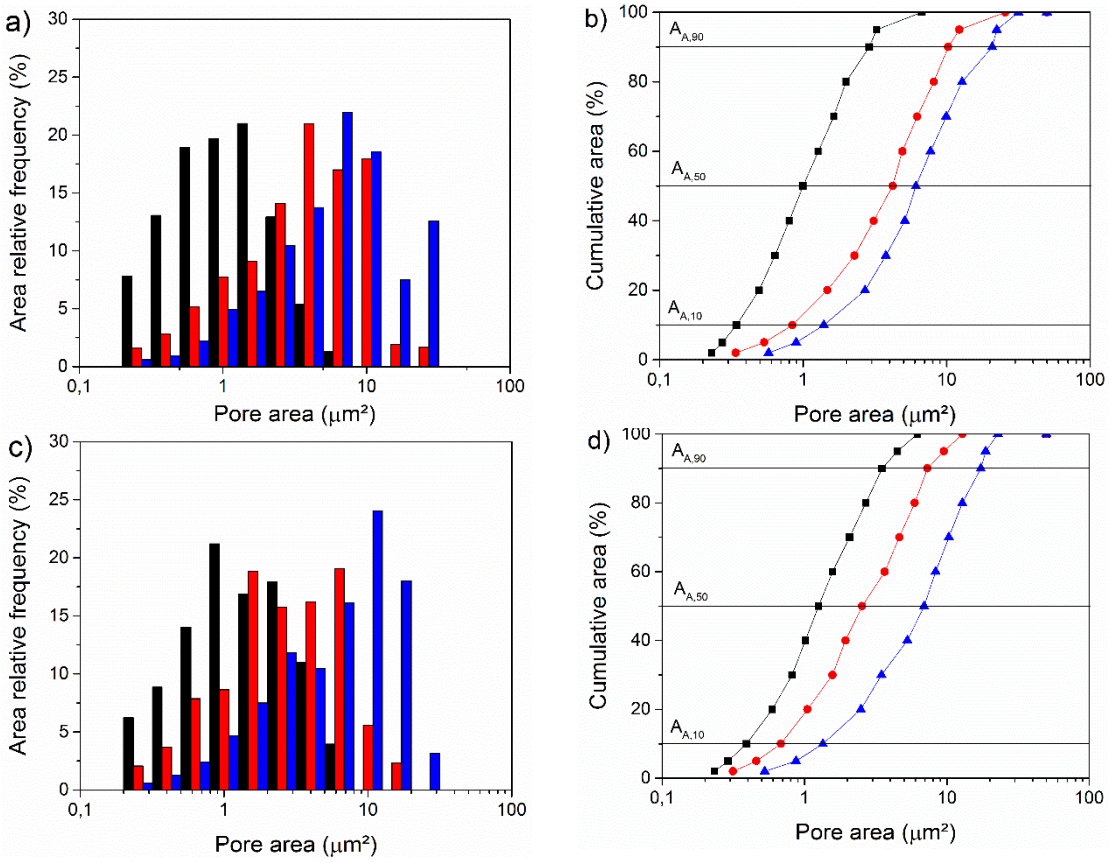

Figure 4.26: a) and b) Relative and cumulative pore area of the samples 1090-A, 1100-A and 1110-A, c) and d) relative and cumulative pore area of the samples 1090-O, 1100-O and 1110-O, for KNNSr thick films sintered at 1090 °C (■), 1100 °C (●) and 1110 °C (▲).

In comparison to the as-deposited layer, the thick films sintered at 1090 °C exhibited an increase of the relative density (calculated from SEM images) from 55 % to 75 %, while it resulted in linear shrinkages (along the thickness) of 27 ± 8 % (in oxygen) and of 25 ± 12 % (in air). The shrinkage and larger density of the thick films indicated the densification of the KNNSr thick films upon heating to 1090 °C, regardless of the atmosphere.

In alkaline niobates, the grain growth/coarsening has been frequently reported at intermediate temperatures. For example, Koruza *et al.* suggest that for $NaNbO_3$ powder compacts heated in the range 500–600 °C, the dominant material-transport mechanism was the surface diffusion [41]. This diffusion mechanisms reduces the curvature of the necks between the grains. Consequently, it lowers the driving force for sintering. They also proposed that the same material-transport mechanism may be predominant at intermediate temperature in other alkaline niobates, including stoichiometric KNN. However, the surface diffusion, which is activated at intermediate temperatures, does not cause shrinkage nor decrease the porosity of the ceramic. Thus, the shrinkage and densification of the thick films upon heating to 1090 °C indicate that at least one densifying sintering mechanism, i.e., grain-boundary diffusion and/or volume diffusion, is active in this temperature range [113]. The densifying mechanisms are presumably activated at a temperature larger than 1000 °C, since no shrinkage was observed for F-1000-A (Figure 4.22a). According to the literature the densifying mechanisms, in particular the volume diffusion, are activated at higher temperatures than the surface diffusion [156].

At a temperature of 1100 °C, the relative density of KNNSr thick films increases to 80 % and it shrank further (Table 4.3). These results indicate that at 1100 °C at least one of the material-transport mechanisms, such as grain-boundary diffusion and/or volume diffusion, participate to the densification. A further increase of the sintering temperature to 1110 °C had only a minor effect on the relative density and shrinkage of the thick films, but the pore size increased (Figure 4.26a and Figure 4.26c). The pores coalescence may be related to the mobility of the pores with the grain boundaries due to the grain growth [157].

The relative densities of the KNNSr thick films, were significantly lower compared to the bulk ceramics sintered at 1120 °C, which exhibited a relative density ≥ 94 % (Appendix D). This was true even for the KNNSr thick film sintered at 1110 °C (81 % for 1110-A and 82 % for 1110-O, Table 4.3). Even though the 1110-A and 1110-O thick films were sintered at a 10 °C lower temperature than the bulk, which may contribute to the lower relative density, we mainly related the lower density of the KNNSr thick film in comparison to the bulk to the sintering of the thick films on a rigid alumina substrate, i.e., sintering in constrained conditions [116], [158].

We concluded from the analysis of the cross-section SEM images including the relative density, shrinkage, estimated pore size, that the microstructure of the KNNSr thick films evolves similarly when sintered in air and in oxygen between 1090 and 1110 °C.

4.2.2.3 Analysis of the KNNSr thick films by XRD

The XRD patterns of air-sintered and oxygen-sintered thick films are shown in Figure 4.27 and Figure 4.28, respectively. We identified in all the patterns the diffraction peaks indexed as a perovskite phase (P, PDF: 77-0038). We also identified in some KNNSr thick films diffraction peaks indexed with platinum (Pt, PDF:04-0802), which originated from the bottom electrode. The thick films sintered in oxygen also exhibited a low-intensity diffraction peak at $2\theta \sim 29.4$ °, which was indexed as a tungsten-bronze phase (TB, PDF: 38-0297). The characteristic diffraction peaks of the tungsten-bronze phase (TB) were not observed in the air-sintered thick films.

The XRD patterns of the bulk ceramics shown for comparison in Figure 4.29, exhibited diffraction peaks that were all indexed with a perovskite phase (P, PDF: 77-0038). Note that PDF 77-0038 considers double unit-cell parameters (with 8 formula units ABO_3 per unit cell). The indexation according to PDF 77-0038 was used for the description of the Lotgering factor. When referring to lattice parameters, we used indexation according to a single perovskite unit-cell (with a number of formula unit per unit cell of 1).

The lattice parameters (Table 4.4) of the KNNSr thick films sintered at selected temperatures in air or oxygen were comparable within the experimental error. However, we note that the lattice parameters slightly, but systematically, decreased with the increasing sintering temperature. The unit-cell contraction may be related to the variation in the chemical composition of the perovskite phase. The perovskite phase composition may vary with the temperature due to the alkali losses and the formation of the TB phase. Popovic *et al.* [46] showed that the equilibrium vapour pressure of potassium over $K_{0.5}Na_{0.5}NbO_3$ (KNN) is a few times larger than that of sodium, i.e., 8 mPa as compared to 3 mPa at 990 °C. Additionally, the alkali loss increases with the increasing temperature [47], [159]. The higher vapour pressure of the potassium over KNN could lead to the deviation from the K/Na nominal stoichiometric ratio of 1 in the thick film. Moreover, the formation of the TB phase of the type $K_{5.75}Nb_{10.85}O_{30}$, which contains minor amount of sodium [48], may cause a change in the stoichiometry of the KNNSr thick film. For the oxygen-sintered samples the increase in the intensity of the TB diffraction peak at $\sim$ 29.4 ° with the increasing temperature may indicate an increase in the amount of TB phase (Figure 4.28a). Therefore, we assume that due to the alkali loss and the formation of the TB phase the K/Na ratio in the perovskite phase is lower than 1. Since the ionic radius of K^+ (0.164 nm for CN=12 [160]) is larger than that of Na^+ (0.139 nm, for CN=12 [160]), the unit cell of the perovskite contracted.

We propose that the smaller unit-cell parameter of the thick films in comparison to C-1120-O and C-1120-A, was related to the larger volatilisation of alkalis from the thick films than from the bulk. The thick films had lower relative densities, i.e., less than 90 %. We expect open porosity consisting of channels of interconnected pores and larger surface area is exposed to the atmosphere compared to the bulk ceramic with closed porosity (see Figure 4.23, Figure 4.24 and Appendix D).

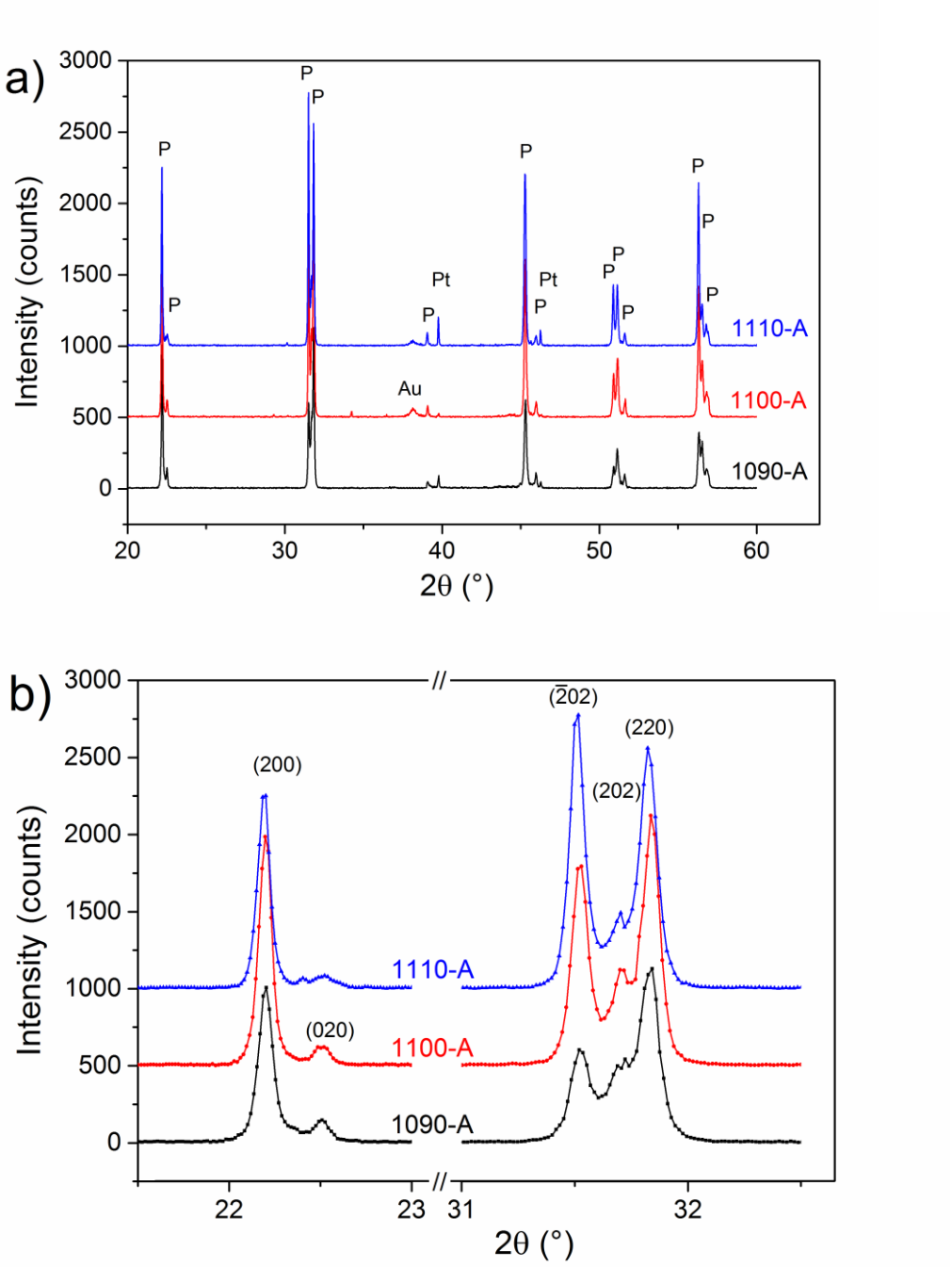

Figure 4.27: a) XRD patterns of 1090-A, 1100-A, 1110-A thick films. P: $(K_{0.65}Na_{0.35})NbO_3$ (PDF: 77-0038), Pt: platinum (PDF: 04-0802), Au: gold (PDF:01-1172), b) Enlarge view of the XRD pattern corresponding to the 21.5–23.0° and 31–32.5° 2θ ranges. (hkl) reflections are from $(K_{0.65}Na_{0.35})NbO_3$ (PDF: 77-0038).

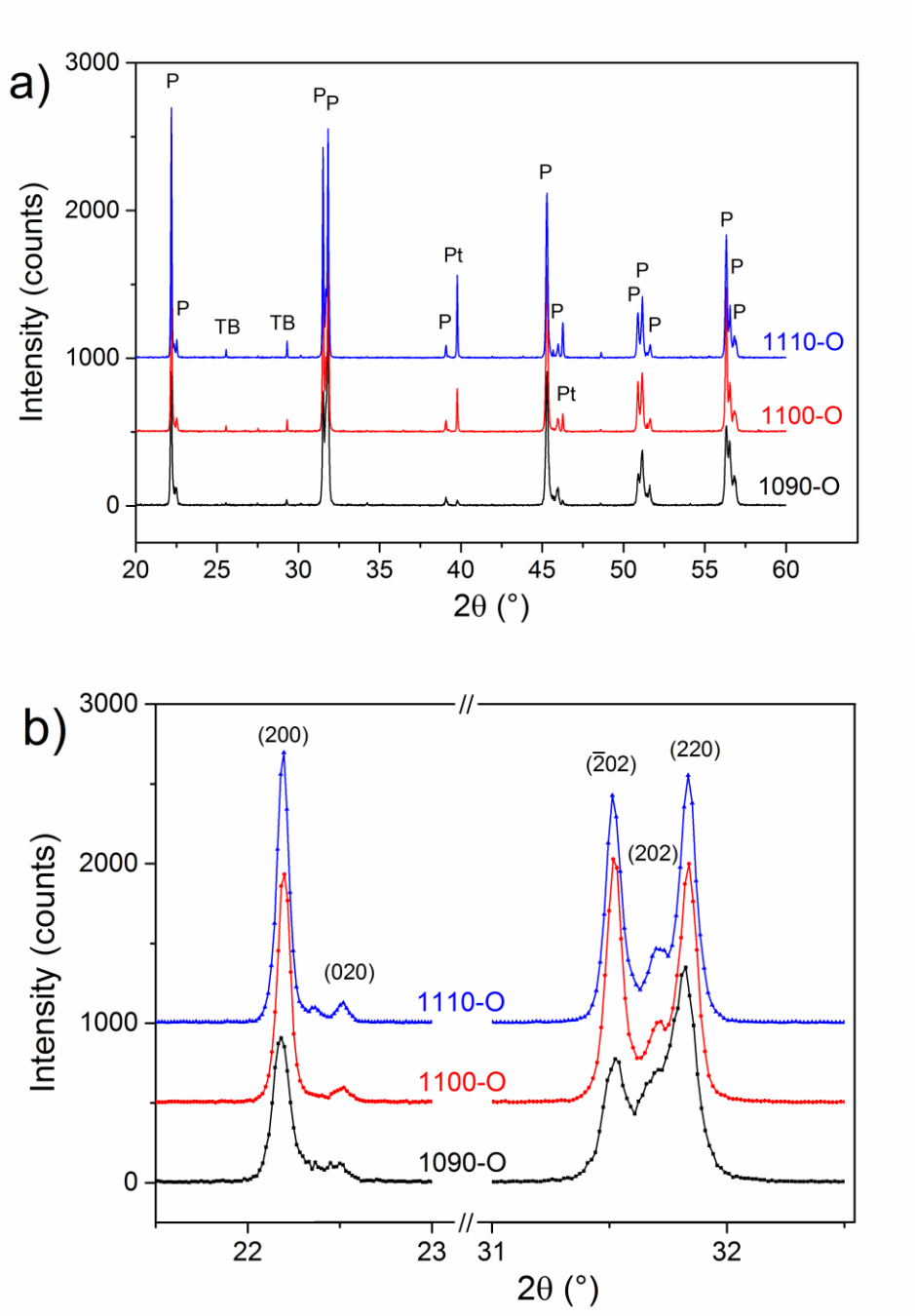

Figure 4.28: a) XRD patterns of 1090-O, 1100-O, 1110-O, thick films. P: $(K_{0.65}Na_{0.35})NbO_3$ (PDF: 77-0038), TB: $K_{5.75}Nb_{10.85}O_{30}$ (PDF:38-0297), Pt: platinum (PDF: 04-0802), b) Enlarge view of the XRD pattern corresponding to the 21.5–23.0° and 31–32.5° 2θ ranges. (hkl) reflections are from $(K_{0.65}Na_{0.35})NbO_3$ (PDF: 77-0038).

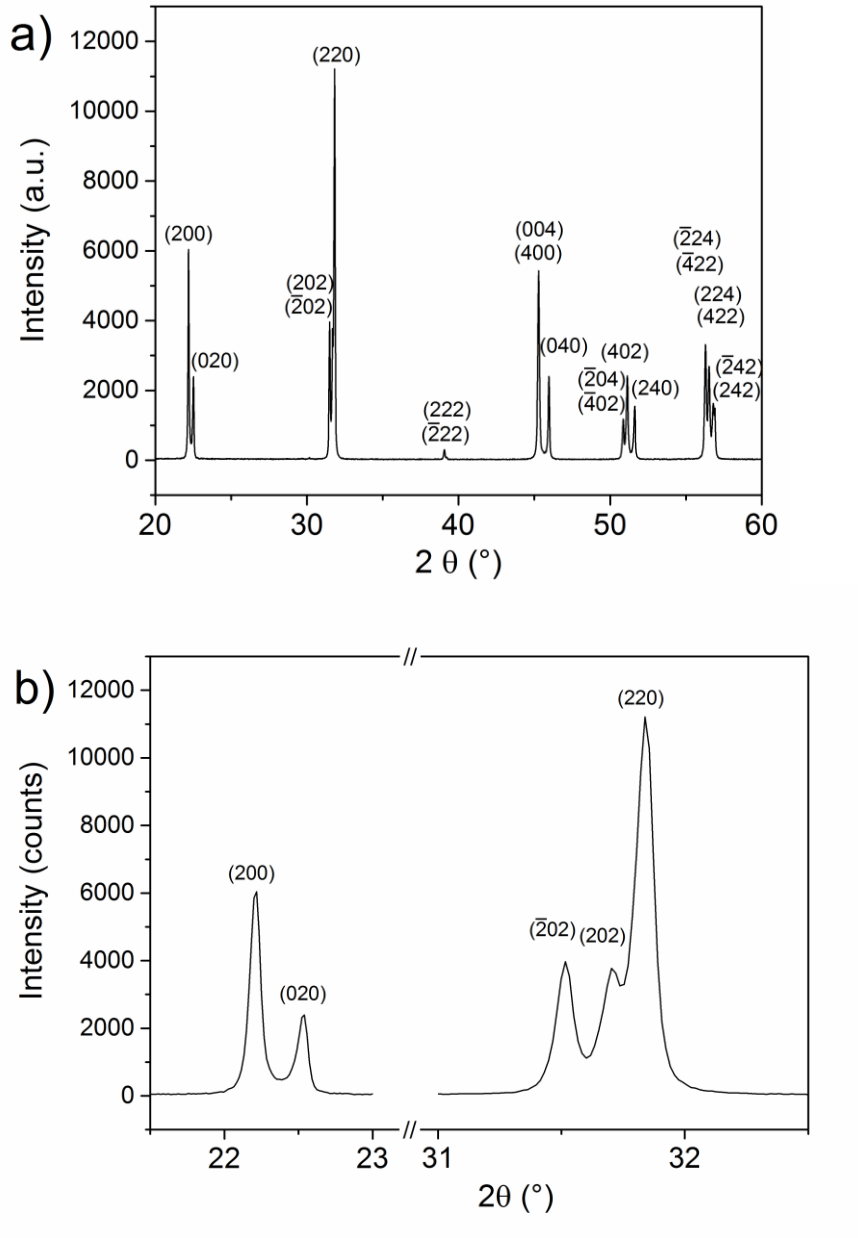

Figure 4.29: a) XRD patterns of C-1120-O bulk ceramics, b) Enlarged view of the XRD pattern corresponding to the 21.5–23° and 31–32.5° 2θ ranges. (hkl) reflections are from $(K_{0.65}Na_{0.35})NbO_3$ (PDF: 77-0038).

Table 4.4: Lattice parameters of the KNNSr thick films (1090-O, 1100-O, 1110-O, 1090-A, 1100-A and 1110-A) and bulk ceramics (C-1120-O and C-1120-A).

Sample	a (nm)	b (nm)	c (nm)	β (°)	V (nm^3)
1090-O	0.40034(9)	0.39457(6)	0.39965(7)	90.29(2)	0.06312(2)
1100-O	0.40024(9)	0.39440(7)	0.39963(9)	90.30(2)	0.06308(2)
1110-O	0.40020(9)	0.39440(7)	0.39962(8)	90.31(2)	0.06307(2)
1090-A	0.40032(9)	0.39449(9)	0.39954(9)	90.28(2)	0.06310(3)
1100-A	0.40023(9)	0.39436(5)	0.39961(9)	90.30(1)	0.06307(2)
1110-A	0.40020(1)	0.39423(7)	0.39951(9)	90.30(2)	0.06303(2)
C-1120-O	0.40035(2)	0.39449(1)	0.39983(2)	90.328(3)	0.063146(6)
C-1120-A	0.40046(3)	0.39462(2)	0.39993(3)	90.323(3)	0.063197(6)

A further comparison of the XRD patterns shows that the intensities of the diffraction peaks for the thick films do not correspond entirely with those for the bulk ceramics with identical nominal compositions. For bulk ceramics, the relative intensities of (200), (020), ($\bar{2}02$), (202) and (220) are 59, 23, 35, 33 and 100 %, respectively, (Figure 4.29b), which are close to the relative intensities of 58, 35, 34, 41, and 100 %, respectively, of the PDF: 77-0038 [139]. In the 1100-O thick films, the relative intensity of the (200), (020), ($\bar{2}02$), (202) and (220) are 89, 6, 99, 30 and 100 %, respectively. These discrepancies are also observed in the other thick films, thus the relative intensities of the (200) and ($\bar{2}02$) diffraction peaks of the thick films were larger than in the bulk ceramic XRD patterns. This suggests that the KNNSr thick films had a preferential crystallographic orientation along the [100] and [$\bar{1}01$] directions.

To evaluate the preferential crystallographic orientation of the KNNSr thick films, we calculated the Lotgering Factor (LF). The results are presented in Figure 4.30. The KNNSr thick films had the LF describing the [100] orientation (LF_{100}) in the range 0.035–0.04, except for 1110-O with a slightly higher value of 0.07. The LF describing the [$\bar{1}01$] orientation ($LF_{\bar{1}01}$), increased with the increasing sintering temperature, and it was similar for the air-sintered and the oxygen-sintered thick films at 1090 and 1100 °C. The $LF_{\bar{1}01}$for 1110-A was the largest, i.e., 0.12, while the $LF_{\bar{1}01}$ for 1110-O was comparable to 1100-O.

The crystallographic orientation in the [100] and [$\bar{1}01$] direction for screen-printed KNN thick films processed on platinised alumina substrates was reported by Pavlič *et al.* [129]. According to them, in-plane compressive stresses were developed in the KNN thick films during cooling from the sintering temperature to room temperature due to the lower linear thermal expansion coefficients of the KNN phases, i.e., 2.96, 4.35 and 7.52 × 10^{-6} K^{-1} for the cubic, tetragonal and monoclinic phase, respectively, compared to the alumina substrate (8.2 × 10^{-6} K^{-1} in the 25-800 °C range [161]). The in-plane compressive stress was also developed due to the KNN phase transitions accompanied by different unit-cell volumes of the KNN phases, i.e., linear expansion of ~0.04 % for the cubic-to-tetragonal phase transition and ~0.01 % for the tetragonal-to-monoclinic phase transition [33]. These stresses relaxed via the preferential crystallographic orientation. Namely, the [100] preferential crystallographic orientation developed in the tetragonal phase when cooling below the cubic-tetragonal phase transition at approximately 400 °C. The [$\bar{1}01$] preferential crystallographic orientation developed in the monoclinic phase when cooling below the tetragonal-to-monoclinic phase transition at approximately 200 °C. We observed that the

relative intensity of the diffraction peaks with the smallest 2θ, i.e., the larger interplanar distances within {200} and {220}, increased. Thus, the direction with the larger interplanar distances tended to orient perpendicular to the surface of the film to decrease the in-plane compressive stresses.

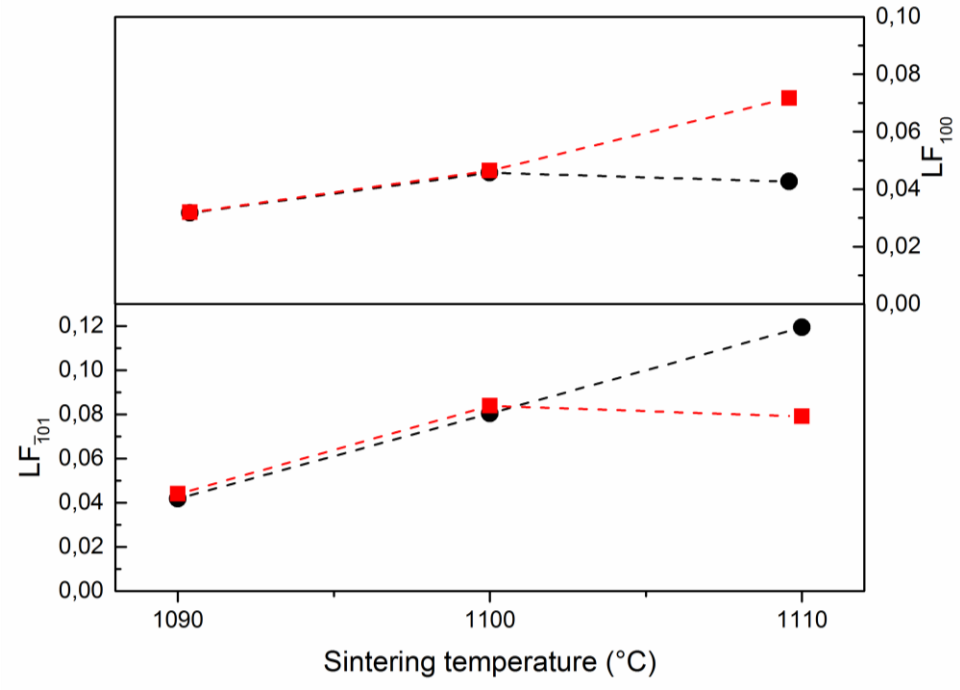

Figure 4.30: Lotgering factors LF_{100} and $LF_{\bar{1}01}$ as a function of the sintering temperature of the KNNSr thick films sintered in air (●) and oxygen (■).

The LFs for the KNN thick films reported by Pavlič *et al.* [129] were below 0.05 and thus they proposed that the grains were randomly oriented and that the preferential orientation was related to orientation within the grains. Similarly, we did not detect any grain orientation in the microstructure (Figure 4.23 and Figure 4.24).

4.2.2.4 Domain structure and local ferroelectric response of the KNNSr thick films

The domain structures and local domain switching properties of the thick films sintered at 1090, 1100 and 1110 °C in oxygen were investigated (Figure 4.31). At the three temperatures, lamellar and wedge domains were detected. The domain sizes ranged from a few hundred nanometres to a few micrometres. These domain configurations have been observed in unpoled KNN bulk ceramics where 60°, 90°, 120° and 180° domain walls were observed in KNN at room temperature [162]. Furthermore, the results of the PFM local domain switching experiments presented in Figure 4.31(d), (h) and (l) exhibited amplitude and phase hysteresis loops typical for piezoelectric/ferroelectric material. The domain-nucleation voltages $V_{DN\pm}$ were found to be similar for the samples sintered at the three temperatures, i.e., between 9 and 11 V.

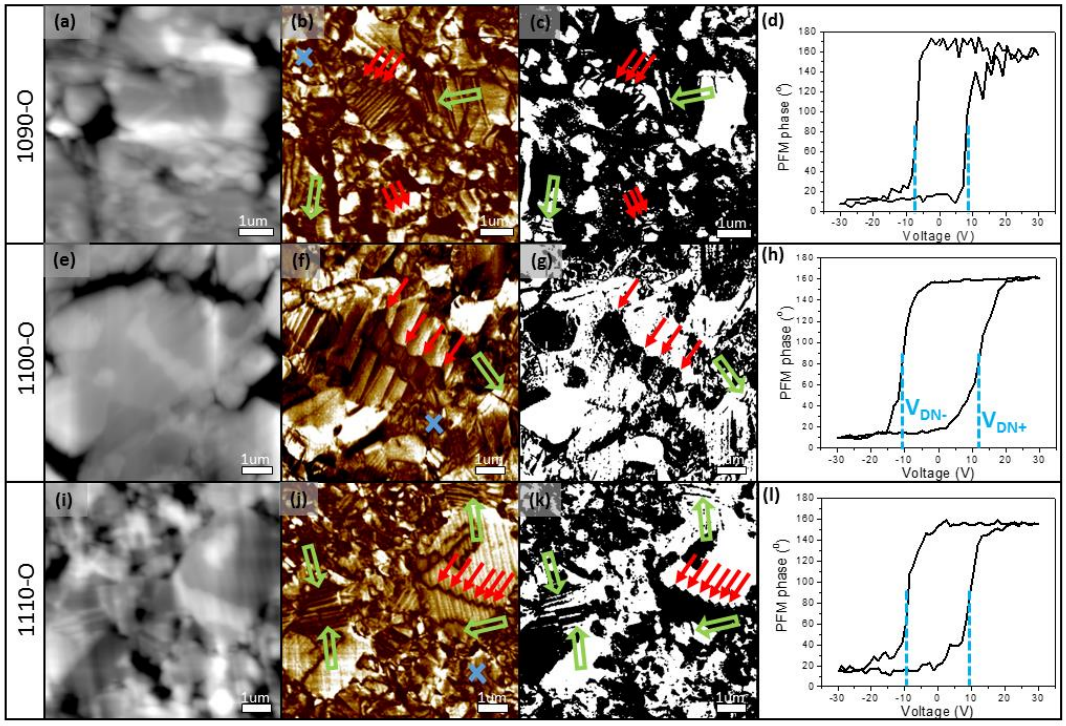

Figure 4.31: KNNSr thick films 1090-O, 1100-O and 1110-O (a), (e), (i) topography, out-of-plane PFM; (b), (f), (j) amplitude and (c), (g), (k) phase images. Some examples of lamellar (thick green open arrows) and wedge (thin red arrows) domains are marked. PFM phase local hysteresis loops of (d) 1090-O, (h) 1100-O and (l) 1110-O measured in the point market by a blue cross in PFM amplitude images. The $V_{DN\pm}$ are marked by blue dashed lines in panels (d), (h) and (l).

We also investigated the domain structure of an air-sintered sample at 1100 °C (1100-A). We observed that the domain structure of 1100-A exhibited lamellar and wedge domains and a domain-nucleation voltage ($V_{DN\pm}$) of ~14 V (Figure 4.32). These values were comparable to 1100-O; thus, we assume that there was a similar local response for air and oxygen sintered KNNSr thick films.

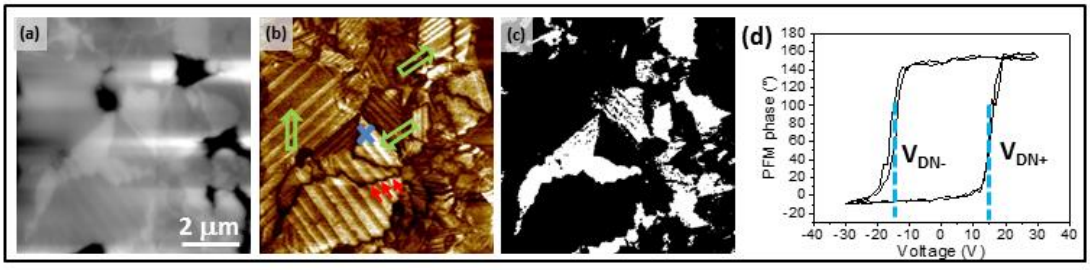

Figure 4.32: KNNSr thick films 1100-A, (a) topography, out-of-plane PFM; (b) amplitude and (c) phase images. Some examples of lamellar domains (thick green open arrows) and wedge domains (thin red arrows) are marked. (d) PFM phase local hysteresis loops measured at the point marked by a blue cross on PFM amplitude image. The $V_{DN\pm}$ are marked by blue dashed lines in panels (d).

From these results we can see that the local domain structures and local domain switching properties of the KNNSr thick film sintered in the range 1090–1110 °C are similar and independent of the sintering atmosphere.

4.2.2.5 Dielectric properties of KNNSr thick films

The dielectric measurements for bulk KNNSr ceramics were reported to depend on the relative humidity in the air [163]. Thus, the measurements of the capacitance and dielectric losses (tan δ) of KNNSr thick films, with a relative density of ~74–82 % having open porosity, were performed in vacuum to obtain reproducible values. The relative dielectric permittivity ($\varepsilon_{r,33}$) of the KNNSr thick films were calculated from the capacitance using the thickness of the films and the area of the top electrode.

The $\varepsilon_{r,33}$ and $\tan\delta$ as a function of the frequency of selected KNNSr thick films sintered at 1090, 1100 and 1110 °C in air and oxygen are presented in Figure 4.33. The $\varepsilon_{r,33}$ decreased with increasing frequency. Between 1 and 10 kHz, the $\tan\delta$ did not vary significantly for 1090-O, 1100-O, 1090-A and 1100-A, but decreased slightly with the increasing frequency for 1110-O and 1110-A. Between 10 kHz and 100 kHz, the $\tan\delta$ slightly increased with the increasing frequency for all thick films.

To better understand the effect of atmosphere and sintering temperature on the dielectric properties, we presented the $\varepsilon_{r,33}$ and $\tan\delta$ at 10 kHz, and room temperature, with their standard deviation in Figure 4.34.

The $\varepsilon_{r,33}$ of the thick films increased with the increasing sintering temperature from 1090 to 1100 °C. With a further increase of the sintering temperature to 1110 °C, the $\varepsilon_{r,33}$ slightly increased for 1110-O, but did not vary significantly for the air-sintered samples, 1110-A. The larger $\varepsilon_{r,33}$ of 1100 °C compared to the 1090 °C sintered samples are related to the larger density, i.e., 75 % to 80 %, the lower number of pores and the larger area of pores. The samples sintered at 1100 and 1110 °C had a similar relative density (~ 80 %), but at higher temperature the area of the pores increased. We assume that the denser microstructure and the smaller number of pores contribute to the increase of $\varepsilon_{r,33}$.

Regardless the sintering atmosphere the tan δ increased with the increasing sintering temperature from 1090 to 1110 °C, namely from 0.04 to 0.05 for the thick films sintered in air and from 0.03 to 0.07 for the samples sintered in oxygen at 10 kHz. The larger tan δ at 1110 °C could be related to the electrical conductivity of the samples. The alkali loss, which is more pronounced in thick films due to the large area to volume ratio and the open porosity, may results in defects such as A-site vacancies in the KNNSr thick films. The A-site vacancies can be compensated by the formation of mobile oxygen vacancies, or free carrier's holes [164]. The free carrier's holes may also result from the oxidation of the oxygen vacancies during the cooling [59]. Since the alkali loss was more pronounced at the higher temperatures (which we correlate with the decrease of the lattice parameters of the KNNSr thick films with the increasing temperature, see Table 4.4, the conductivity could be larger in KNNSr thick film sintered at 1110 °C due to the larger concentration of defects. The slight increases in the dielectric losses toward the lower frequencies in the frequency range 1-10 kHz, particularly for 1110-O (Figure 4.33b) could be an indication of the contribution from the conductivity.

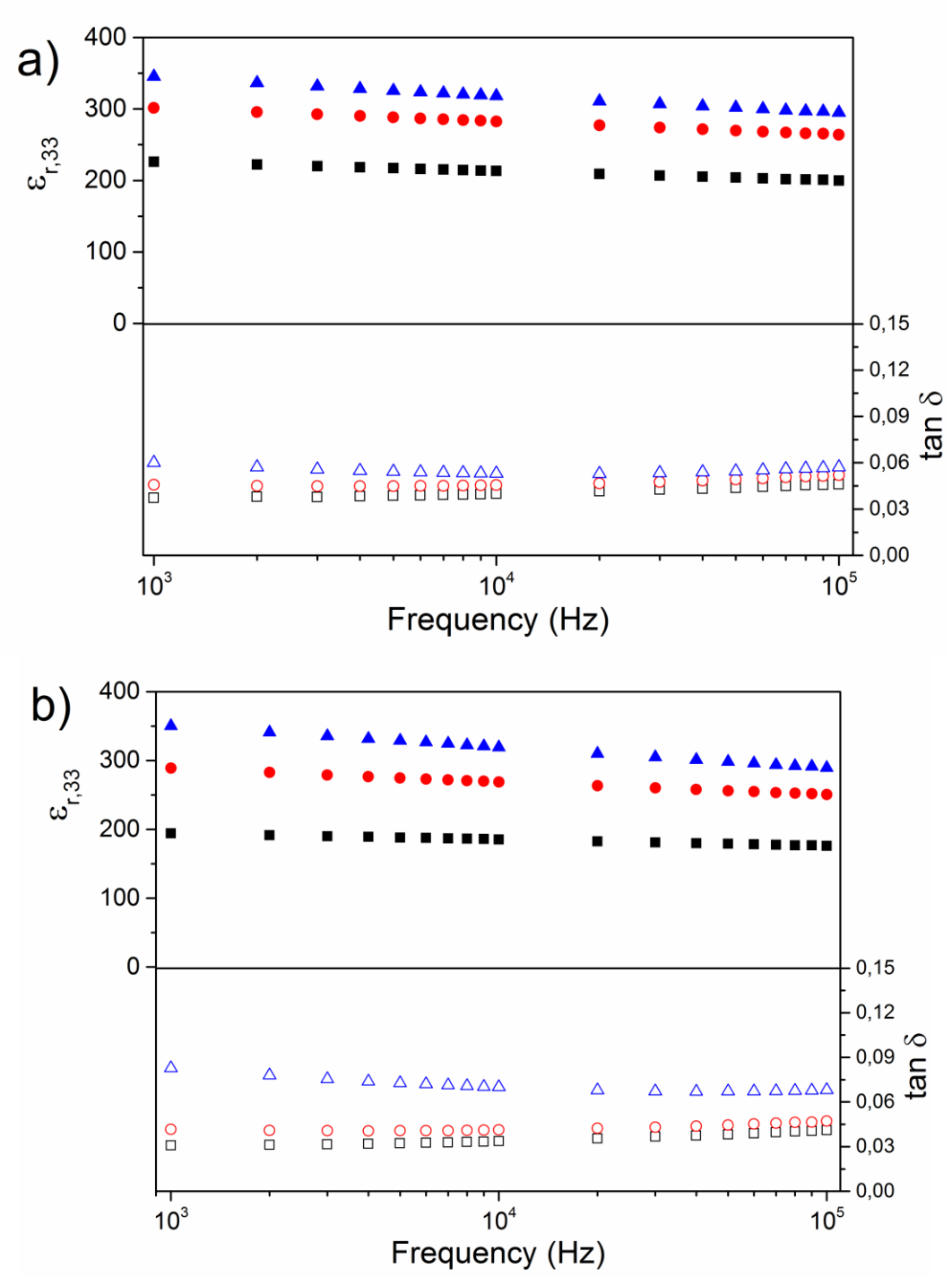

Figure 4.33: Relative dielectric permittivity ($\varepsilon_{r,33}$, solid symbol) and dielectric losses ($\tan\delta$, hollow symbol) as a function of the frequency for the KNNSr thick films sintered at 1090 (black squares), 1100 (red circles) and 1110 °C (blue triangles) in a) air and b) oxygen.

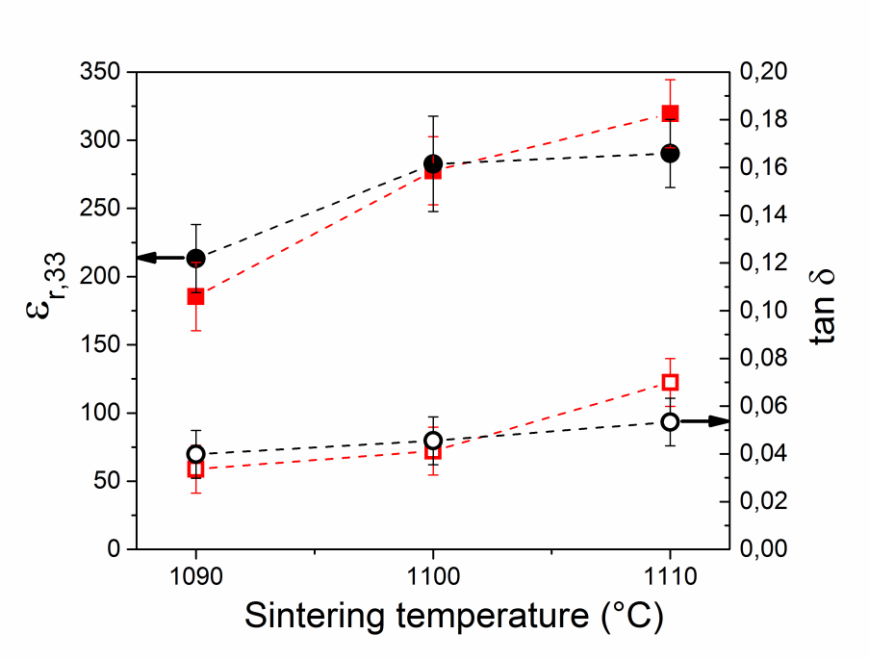

Figure 4.34: Relative dielectric permittivity ($\varepsilon_{r,33}$, full symbols) and dielectric losses ($\tan\delta$, empty symbols) of the KNNSr thick films as a function of the sintering temperature in air (black circles) and oxygen (red squares) atmospheres at 10 kHz and room temperature.

The second possibility is the contribution from the domain walls to the complex dielectric permittivity. We observed that the $\varepsilon_{r,33}$ as a function of $\log(f)$ with f being the frequency, decreased linearly for all the KNNSr thick films (Figure 4.32 and Figure 4.33). This linear relationship has been discussed for PZT in the frame of the Rayleigh law and was attributed, in part, to the contribution from irreversible domain-wall displacements [165]. A linear regression of $\varepsilon_{r,33}$ as a function of $\log(f)$ was performed for the KNNSr thick films and the calculated slopes are given in Table 4.5. The absolute values of the calculated slopes increase with an increasing sintering temperature. The two contributions from the reversible and irreversible Rayleigh parameters affect the slope. The increase in the slope could be an indication of an increased contribution from the irreversible domain-wall displacements. Since the irreversible dynamics of the domain wall is coupled to the phase angle and thus to the measured tan δ [166], [167], the domain walls' dynamics could be the reason for the increased losses measured in KNNSr sintered at a higher temperature.

Table 4.5: Calculated slopes from the linear regression of $\varepsilon_{r,33}$ as a function of $\log(f)$ in the frequency range 1 kHz to 100 kHz of 1090-O, 1100-O, 1110-O, 1090-A, 1100-A and 1110-A KNNSr thick films.

	1090-A	1100-A	1110-A	1090-O	1100-O	1110-O
Slope (s)	-5.9	-8.2	-9.6	-4.2	-8.0	-12.7

The $\varepsilon_{r,33}$ of the bulk ceramics with the same nominal composition were larger compared to the one of the thick films, i.e., 680 and 625, for C-1120-A and C-1120-O, respectively at 10 kHz in air. The $\varepsilon_{r,33}$ of the bulk ceramics were slightly larger than the $\varepsilon_{r,33}$ reported in the literature, i.e., 500 at 10 kHz. We proposed that the larger relative densities of the bulk ceramics, i.e., 93.1, 97.5 and 95.8 % for C-1120-A, C-1120-O and reported in [62], respectively, was the reason for their larger $\varepsilon_{r,33}$ in comparison to the KNNSr thick films.

The tan δ reported for the bulk ceramics [62], i.e., 0.04 at 10 kHz, was comparable to the tan δ of KNNSr thick films sintered at 1090 and 1100 °C. The reported $\varepsilon_{r,33}$ and tan δ of the EPD-derived unmodified KNN thick films were 495 and 0.08, respectively [128] and 393 and 0.07, respectively [127], at 1 MHz. The reported $\varepsilon_{r,33}$ values, although measured at a higher frequency, were larger than the one presented in Figure 4.34 at 10 kHz, which could be related to the difference in the density of the thick films and to the measurement conditions, as we reported values measured in vacuum, whereas the results in the measurement in the literature were performed in air.

Figure 4.35 presents the normalised $\varepsilon_{r,33}$ as a function of the temperature for 1090-O, 1100-O and 1110-O. Two maxima were observed, which corresponded to phase transitions, i.e., from the cubic to tetragonal phase at 386 ± 1 °C and from the tetragonal to monoclinic phase at 168 ± 5 °C. The phase-transition temperatures were a few degrees below those reported for KNNSr [62].

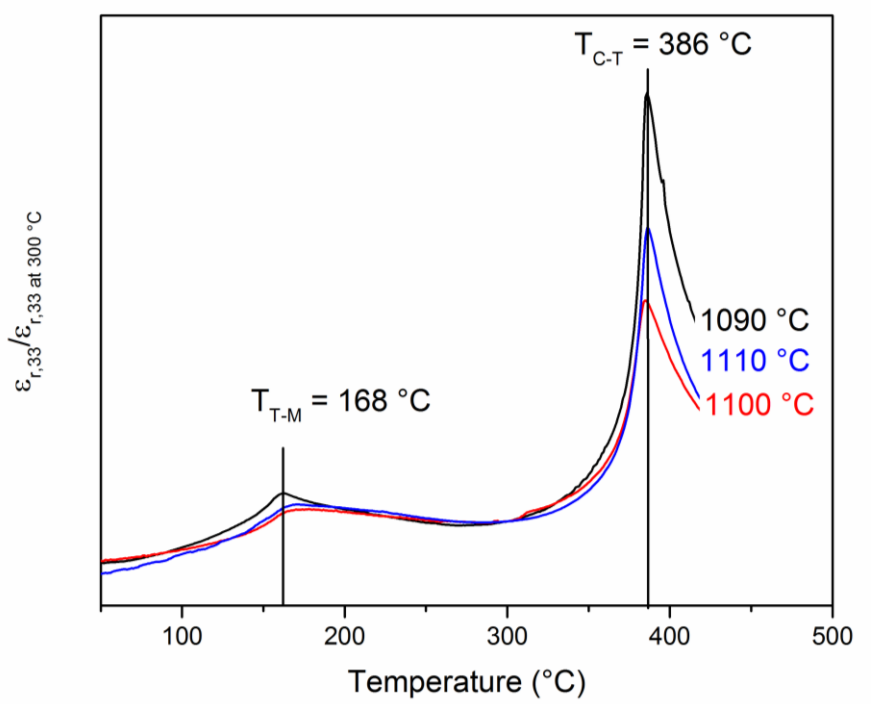

Figure 4.35: Normalised dielectric permittivity ($\varepsilon_{r,33}/\varepsilon_{r,33,300°C}$) of KNNSr thick films 1090-O, 1100-O and 1110-O as a function of the temperature measured at 1 kHz. T_{T-M}: tetragonal-to-monoclinic phase-transition temperature, T_{C-T}: cubic-to-tetragonal phase transition temperature.

4.2.2.6 Electromechanical properties

The electromechanical properties were deduced from the experimental electrical impedance by fitting these data with the theoretical electrical impedance behaviour calculated using an equivalent electrical circuit (KLM circuit, Appendix C). The experimental and theoretical complex impedances of the C-1120-O and 1100-O samples are presented in Figure 4.36 and Figure 4.37, respectively. The real part of the impedance in Figure 4.36, exhibits a unique peak, which correspond to the first antiresonance frequency of the thickness mode of the ceramic in free-mechanical conditions in air. In contrast, Figure 4.37 presents the case of a thick film deposited on a RAO substrate. In this case, we observed additional peaks around the fundamental resonance, due to the coupling of the resonances

of the thick film with the platinum electrode and the alumina substrate [168]. The KLM equivalent circuit can consider additional inert layers (Appendix C). If the acoustic properties of the alumina substrate and platinum electrode are known (the top gold electrode was neglected due to its low thickness) then the electromechanical properties of the thick film can be deduced. Using the acoustic data from the literature for the two considered inert layers, a good agreement between the theoretical and the experimental electrical impedance was obtained (Figure 4.37) to deduce the thickness mode properties of the KNNSr thick film.

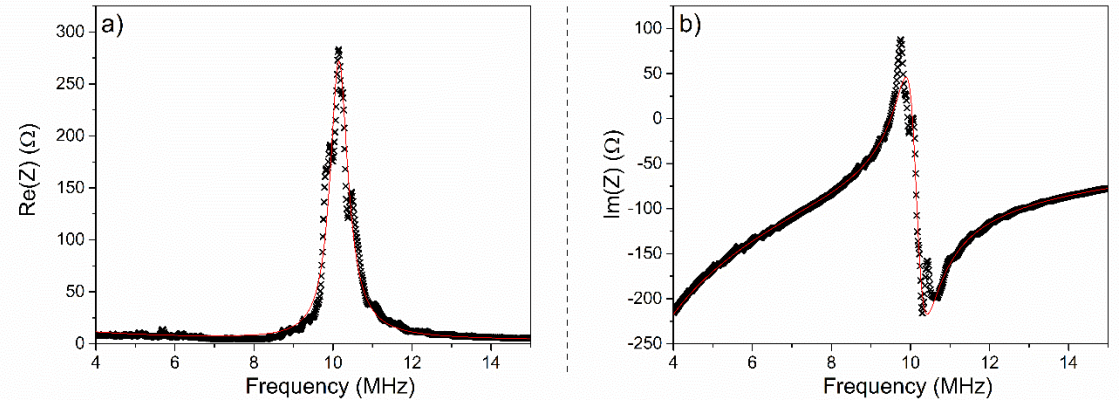

Figure 4.36: Complex electrical impedance of the KNNSr ceramic C-1120-O as a function of the frequency around the fundamental resonance a) Re(Z): real part and b) Im(Z): imaginary part. Black crosses: experimental impedance and solid red line: theoretical impedance.

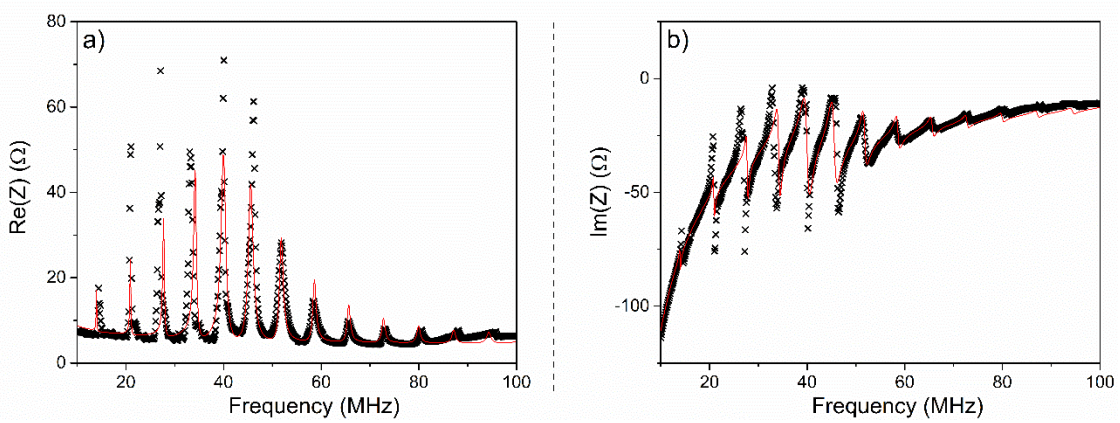

Figure 4.37: Complex electrical impedance of the KNNSr samples 1100-O as a function of the frequency around the fundamental resonance a) Re(Z): real part and b) Im(Z): imaginary part. Black crosses: experimental impedance and solid red line: theoretical impedance.

With this procedure we deduced the electromechanical properties of the thick films, which are summarised in Table 4.6. The standard deviations were calculated assuming a variation of the thick film's thicknesses of $\pm$ 1.5 μm and of thick film's density of $\pm$ 3 %.

The elastic constant at constant electric displacement (c_{33}^D) values increases with an increasing of the sintering temperature for air and oxygen sintered samples. c_{33}^D increased from 18 GPa to 76 GPa for 1090-A and 1110-A, respectively, with a sharp increase observed between 1090-A and 1100-A. KNNSr thick films sintered in oxygen showed the same trend with c_{33}^D increasing from 35 GPa to 78 GPa for 1090-O and 1110-O, respectively. With

increasing the sintering temperature from 1090 to 1110 °C, the $\varepsilon^S_{r,33}$ increased from 80 to 150 for oxygen sintered KNNSr thick films. The piezoelectric coefficient (e_{33}) increased between 1090 and 1110 °C from 1.2 to 3.7 C/m^2 in air and from 1.8 to 4.0 C/m^2 in oxygen.

Table 4.6: Thickness-mode electromechanical properties of 1090-O, 1100-O, 1110-O, 1090-A, 1100-A and 1110-A KNNSr thick films and bulk ceramics (C-1120-O, C-1120-A).

Sample name	c^D_{33} (GPa)	k_t (%)	$\varepsilon^S_{r,33}$	δ_m (%)	e_{33} (C/m^2)	f_a (MHz)
1090-O	35 ± 3	35 ± 1	90 ± 10	7 ± 1	1.8 ± 0.4	45
1100-O	75 ± 9	40 ± 1	120 ± 10	16 ± 3	3.4 ± 0.4	77
1110-O	78 ± 9	42 ± 2	140 ± 10	13 ± 2	4.0 ± 0.5	90
1090-A	18 ± 2	34 ± 1	80 ± 10	7 ± 1	1.2 ± 0.2	32
1100-A	61 ± 15	37 ± 1	140 ± 30	11 ± 2	3.0 ± 0.7	86
1110-A	76 ± 10	40 ± 3	150 ± 10	15 ± 1	3.7 ± 0.5	98
C-1120-O	186	41	300	6	9.0	10
C-1120-A	156	40	300	6	8.3	7

The increases of the c^D_{33} and $\varepsilon^S_{r,33}$ parameters that were observed when the sintering temperature increased were attributed to the denser microstructure of the thick films sintered at higher temperature. The increase of $\varepsilon^S_{r,33}$ with the sintering temperature exhibited the same trend as the one observed for the $\varepsilon_{r,33}$ measured on unpoled KNNSr thick films at lower frequency (Figure 4.33). The e_{33} further increased between 1100-A and 1110-A and between 1100-O and 1110-O, despite the change in relative density not being significant. For the thickness-mode electromechanical coupling factors (k_t) a value of 42 % was deduced for the sample 1110-O.

The mechanical loss (δ_m) increases (when accounting for the standard deviation) with the sintering temperature for thick films sintered in air and oxygen atmospheres. The anti-resonant frequency (f_a) reported in the last column of the Table 4.6, are calculated from a theoretical configuration where the piezoelectric thick film is supposed in free mechanical conditions (as for C-1120-O in Figure 4.36). In this configuration, f_a can be obtained from the relation:

$$f_a = \frac{V_L}{2\ t_M} \tag{4.5}$$

We observe that f_a increased with an increasing of the sintering temperature between 1090 and 1110 °C, this is due to the decrease of the thickness of the thick films and an increase of the longitudinal wave velocity (V_L) related to the denser microstructure (Table 4.3). Based on f_a and V_L in each KNNSr thick film, a typical wavelength λ was calculated ($\lambda = V_L/f_a = 2\ t_M$), which decreased with the sintering temperature (typically 66 μm for 1090-O and 56 μm for 1110-O). Additionally, when the temperature increased from 1090 to 1110 °C, the median pore area (Table 4.3) increased and the typical size of the pores got closer to the value of the calculated wavelength. Thus, the scattering of the ultrasound waves by the pores may lead to an increase in the acoustic attenuation [169] and thus δ_m

of the thick films. Roncari *et al.* [170] observed a similar trend in a porous piezoelectric ceramic: a narrow particle size distribution with smaller pores leads to smaller mechanical losses compared to a broad pore size distribution with the prevalence of larger pores or a narrow pore size distribution with larger pores. However, they offer a different explanation related to the interaction between the pore surface and the ferroelectric domain walls. In a porous structure it is assumed that the main role in the δ_m is played by the interaction between the waves and the scattering centres, i.e., pores [169]. Moreover, the presence of these large pores in the thick films sintered at 1110 °C could be detrimental for the fracture toughness of the KNNSr thick films [171].

The c_{33}^D, $\varepsilon_{r,33}^S$ and e_{33} coefficients of the KNNSr thick film were lower than those of their ceramic counterparts. The lower value of those parameters for the thick films was related to the lower relative densities and lower grain size of the thick films in comparison to the C-1120-O and C-1120-A bulk ceramics (see Appendix D). Despite the lower values of these parameters, the thickness-mode electromechanical coupling factor (k_t) were in the same range (40 %) due to the trade-off between the lower e_{33} and lower c_{33}^D, $\varepsilon_{r,33}^S$ in the calculation of k_t (see Appendix A).

The dielectric properties and mechanical losses of the KNNSr thick films were comparable to the $\varepsilon_{r,33}^S$ of 90 and 140 and δ_m of 15 and 9 %, respectively, reported for the thick films processed by pad and screen-printing [72]. However, the KNNSr thick films prepared by EPD had a larger thickness-mode electromechanical coupling factor compared to the 34 % and 30 % reported for the pad and screen-printed samples, respectively. The k_t values reached 40 % for thick films 1100-O, 1110-O and 1110-A (Table 4.6).

Piezoelectric coefficient ($d_{33,f}$) of the thick films ranged from 60 to 70 pC/N, being $\approx$ 63–74% of the bulk ceramic value ($d_{33}\approx$ 95 pC/N [62]). These results are in agreement with the statement of Pavlič *et al.* that in clamped KNN thick films the ratio $d_{33,f}/d_{33}$ can reach values of 72-75 %, which is larger than the achievable values in clamped PZT thick films [172].

4.2.3 Summary

The KNNSr thick films processed under optimal conditions on a RAO substrate, with an as-deposited thickness of ~40–45 μm, were porous after sintering at 1075 °C, and contained defects and/or peeled-off the substrate after sintering at 1100 and 1120 °C. The formation of defects was minimised by the use of a two-step deposition-sintering procedure. First a ~10-μm-thick layer was deposited and fired at 1000 °C. Then, on top of this layer, we deposited the second layer. The thick films processed using this procedure did not present any macroscopic defect and thus were sintered at 1090, 1100 and 1110 °C for 2 hours in air and oxygen atmospheres.

With the increasing sintering temperature from 1090 to 1110 °C, the thicknesses of the samples decreased, the pore size increased. The relative density increased with the increasing temperature from 1090 to 1100 °C, then did not increase significantly upon heating to 1110 °C. The maximum relative density was 82 %. The difficulty in densifying the thick films was attributed to coarsening of the microstructure at intermediate temperature, which reduces the driving force for sintering and to the sintering of the KNNSr layers in constrained conditions. The XRD analysis showed that the KNNSr thick films had a perovskite structure with unit-cell parameter values lower than the ones of the nominal composition, additionally we detected peaks of a secondary tungsten bronze phase

in thick films sintered in oxygen. These two features were presumably related to the volatilisation of alkalis at the sintering temperature. Thick films exhibited preferential orientations along the [100] and [-101] directions, which was caused by the thermal expansion coefficients mismatch between the substrates and the KNNSr layers. However, we did not detect any large impact of the preferential orientations on the electromechanical properties of the KNNSr thick films. The local domain structure and local domain-switching properties of the KNNSr thick films were similar, regardless of the sintering temperature and atmosphere.

The dielectric permittivity increased with increasing sintering temperature, specifically between 1090 and 1100 °C, which we related to the denser microstructure. The electromechanical properties showed similar trend to the dielectric permittivity, and thus the k_t *was in the 35–42 % range for all the thick films due to the trade-off between the* c_{33}^D, $\varepsilon_{r,33}^S$ and e_{33}. *The sintering atmosphere had a minor impact on the electromechanical properties of the KNNSr thick films.*

4.3 Towards a piezoelectric energy harvester

In this last subchapter we discuss the processing of the KNNSr bimorph structure on platinised 110-μm-thick alumina (DFAO) substrate, which offers more flexibility to the bimorph cantilever piezoelectric energy harvester (PEH). We verified that a bimorph structure can be prepared on such substrates using a specifically designed setup (Setup 2). The KNNSr thick films sintered at 1100 °C for 2 h in oxygen were identical on the top and bottom sides of the DFAO with a thickness of 40 μm and a relative density of 86 %. The electromechanical properties of the KNNSr thick film were deduced from the complex electrical impedance spectra, taking into account the additional KNNSr and platinum layers. Finally, we theoretically evaluated the effect of the porosity on the figure of merit for a PEH operating in 31 mode, with the aim to highlight the requirement for the integration of KNNSr thick films into a PEH. The purpose of this chapter is also to identify the remaining challenges related to the processing of PEHs.

4.3.1 Processing of the KNNSr bimorph structure

In the previous chapter we deposited KNNSr thick films on rigid 640-μm-thick alumina substrates (RAO) using the Setup 1. This setup enables the deposition of a layer on one side of a substrate. In order to prepare the bimorph cantilever structure, the setup should allow the deposition on both sides of a substrate and must be compatible with 110-μm-thick alumina (DFAO) substrates. To achieve these two goals, the Setup 2 was designed and fabricated.

The aim was to process KNNSr layers with Setup 2 (Figure 3.3) using the optimised processing conditions from the study performed previously with Setup 1. The deposition conditions were as follows: $h_i = 3$ mm and $D_e = 8$ mm from suspension S50 using a two-step deposition-sintering procedure with deposition times of 30 and 90 s for the first and second layer, respectively.

First, we compared the yield and thickness profiles of the KNNSr processed on RAO using Setup 1 and Setup 2. The depositions were performed from a suspension with a conductivity of 26.1 μS/cm for 30 s.

Yields of 4.1 ± 0.4 and 4.4 ± 0.5 mg/cm^2 were obtained for the deposition realised with Setup 1 and Setup 2, respectively. The thickness of ~ 20 μm and the thickness profiles were similar (Figure 4.38).

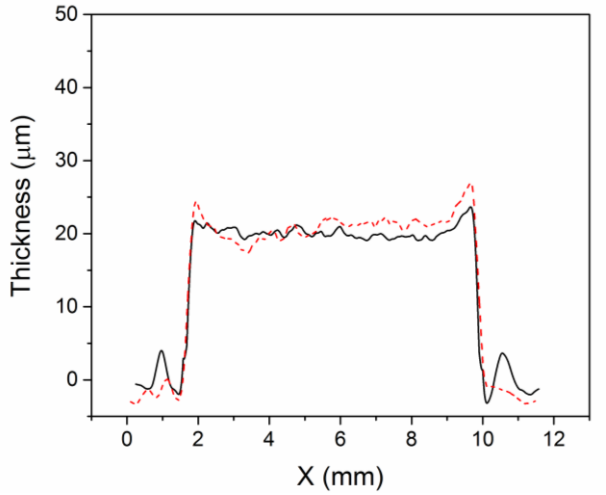

Figure 4.38: a) Thickness profiles of representative as-deposited KNNSr layers processed with Setup 1 (dashed red line) and Setup 2 (solid black line) on a RAO substrate.

After the verification that the yields and thickness profiles of the as-deposited layers obtained by the two setups were similar, we deposited KNNSr layers on DFAO substrates. We performed five depositions under the same conditions onto one side of the DFAO substrates using the Setup 2. The yield was 4.8 ± 0.4 mg/cm² and the thickness of the as-deposited layers was ~ 20 μm, which is comparable to the yield and thickness measured for the depositions performed on a RAO substrate (Figure 4.39).

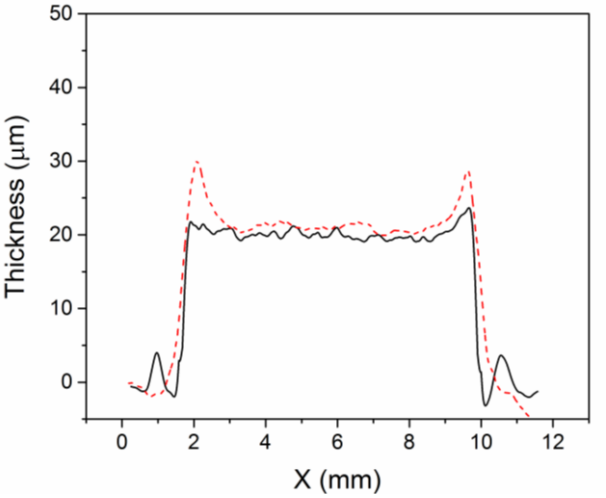

Figure 4.39: Thickness profiles of a representative as-deposited layers processed from Setup 2 on one side of DFAO (dashed red line) and RAO (solid black line) substrates.

These results validate that the yields and thickness profiles of the as-deposited layers processed with Setups 1 and Setup 2 were comparable. Moreover, the yields and thickness of the as-deposited layers processed on RAO or DFAO substrates with the Setup 2 were comparable although the edges were thicker for the KNNSr layers processed on the DFAO substrate. According to these results, Setup 2 was used in the following experiments.

KNNSr thick films were processed on one side of the DFAO substrate using Setup 2 and the two-step deposition-sintering procedure. The first layer was deposited for 30 s and fired at 1000 °C for 2 h in synthetic air. Then, the second layer was deposited for 90 s on top of the first layer. The yield and thickness of the as-deposited layers were

16.9 ± 0.5 mg/cm² and ~ 65 μm, respectively. The representative thickness profile of the as-deposited layer is presented in Figure 4.40.

In these preliminary experiments we sintered the as-deposited layer at 1100 °C for 2 h in oxygen. We observed that after the sintering the thick-film structure was bent (Figure 4.40).

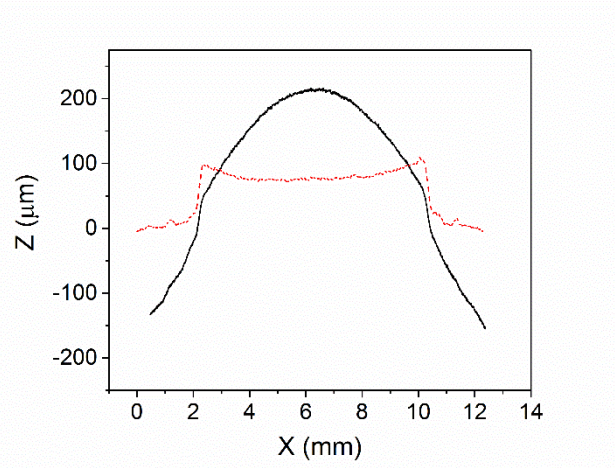

Figure 4.40: Profilometer measurements of the structure with as-deposited layer (dashed red line) and sintered (1100 °C) thick film (solid black line) processed from Setup 2 on one side of DFAO substrate. Note: the thickness is the sum of the thicknesses of the KNNSr layer and platinum bottom electrode (~6 μm).

To minimise the bending of the structure, one of the possible solutions is to deposit KNNSr layers on each side of the DFAO substrate and to sinter a symmetric structure [173]–[175]. Thus, we processed KNNSr layers on each side of a DFAO substrate. The thickness profiles of the as-deposited layers processed on DFAO substrate on side 1 (KNNSrl1) and side 2 (KNNSrl2) are presented in Figure 4.41. The thickness profiles of the layers were similar on both sides, with a mean thickness of ~ 65 μm, ARs of ~1.5 and yield of 17.5 mg/cm² for the as-deposited layers, before sintering.

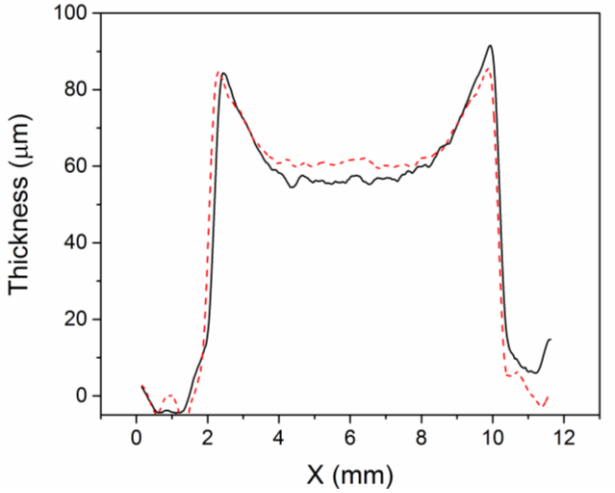

Figure 4.41: Thickness profiles of the as-deposited KNNSr layers processed with Setup 2 on each side of the DFAO substrate. The layers are referred as KNNSrl1 (dashed red line) and KNNSrl2 (solid black line).

The cross-section SEM images of the KNNSr bimorph structure on DFAO substrate sintered at 1100 °C for 2 h in oxygen (DF-1100-O) are presented in Figure 4.42. The two KNNSr thick films deposited on each side of a DFAO substrate were well adhered to the substrate. The KNNSrl1 and KNNSrl2 layers exhibited similar thickness of ~ 40 μm and similar microstructure.

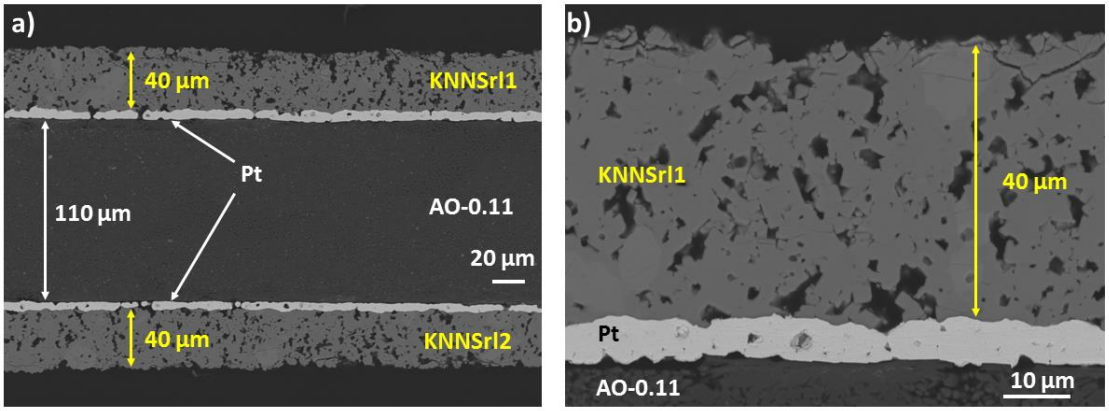

Figure 4.42: a) Polished cross-section SEM images of KNNSr bimorph structure (DF-1100-O), b) Enlarged view of the layer KNNSrl1. KNNSrl1 and KNNSrl2: KNNSr layers, AO-0.11: 110-μm-thick alumina (DFAO) substrate, Pt: platinum electrode.

The relative density of the KNNSr layers measured from the SEM images was 86 ± 4 %, which is slightly larger than the density of the KNNSr sintered on the RAO substrate under the same conditions (1100-O), i.e., 81 %. From Figure 4.43 it is evident that the pores are slightly larger in DF-1100-O with a median area of 4.0 μm^2, but the number of pores was lower, i.e., 3.3 x 10^4 pores/mm^2, in comparison to 1100-O, i.e., 7.5 x 10^4 pores/mm^2 (Figure 4.25). From the results, we concluded that both sides of the KNNSr exhibited a similar density and pore size distribution and we observed that the bending of the structure was minimised.

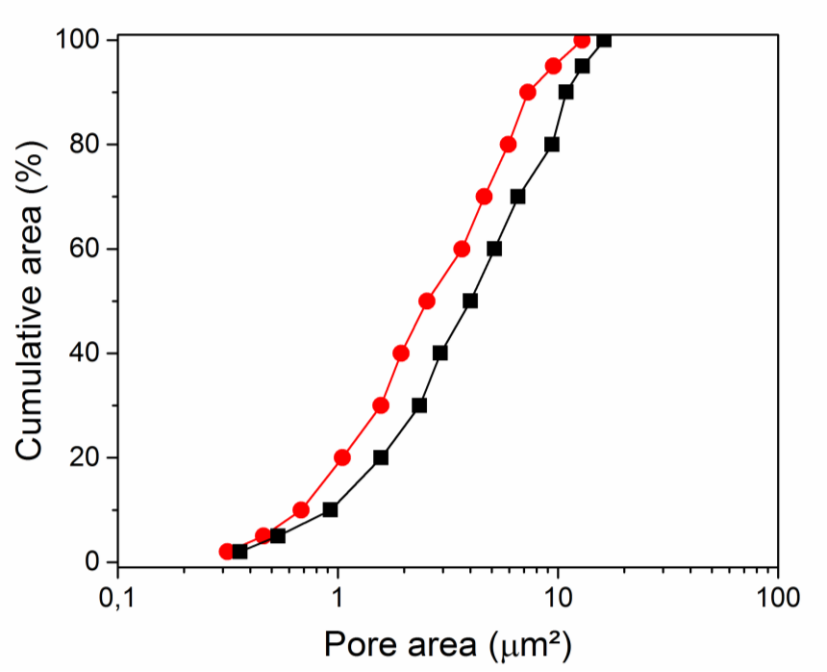

Figure 4.43: Cumulative pore area distribution of 1100-O (●) and DF-1100-O (■).

In this work we have deposited and sintered the KNNSr layers on DFAO and RAO substrates in three different cases:

1. Deposition of KNNSr on one side of RAO substrate;
2. Deposition of KNNSr on one side of DFAO substrate;
3. Deposition of KNNSr on both sides of DFAO substrate.

The first two cases illustrate asymmetric structures, whereas the third case was a symmetric structure. In the following discussion, we neglect the elastic properties of the platinum electrode and considered that the thickness of the as-deposited KNNSr layers was 44 μm for the case 1 and 65 μm for the cases 2 and 3. When the thickness of the KNNSr layer and alumina substrate are small in comparison to the lateral dimension of the sample and when the substrate remains flat during the processing, we use the thin plate approximation which hypothesises that the in-plane stresses are constant along the thickness of the layers [173] to represent the stresses state.

Figure 4.44 is a schematic representation of the behaviour of the two asymmetric structures (typically on RAO and DFAO substrates without electrodes) during the sintering. During the firing, the KNNSr layer (thickness t_L) tends to shrink whereas the dense alumina substrate (thickness t_S) does not change dimensions (Figure 4.44a).

For the KNNSr processed on the RAO substrate with an AO thickness of 0.64 mm (AO-0.64), the thickness ratio t_L/t_S is ~ 0.07. We observed that the substrate was flat after the sintering, and thus we assumed that AO-0.64 was a rigid substrate. Since the KNNSr thick film is clamped on the RAO substrate, it shrinks predominantly in the thickness direction (denoted z) and is unable to shrink along the direction r. As a result, in-plane tensile stresses are formed in the layer ($\sigma_{r,L}$) and in-plane compressive stresses in the substrate ($\sigma_{r,S}$). The in-plane tensile stresses in the KNNSr layers reduce the shrinkage rate of the layers, and thus the density of the thick film is lower compared to bulk ceramics sintered under the same conditions [115], [116].

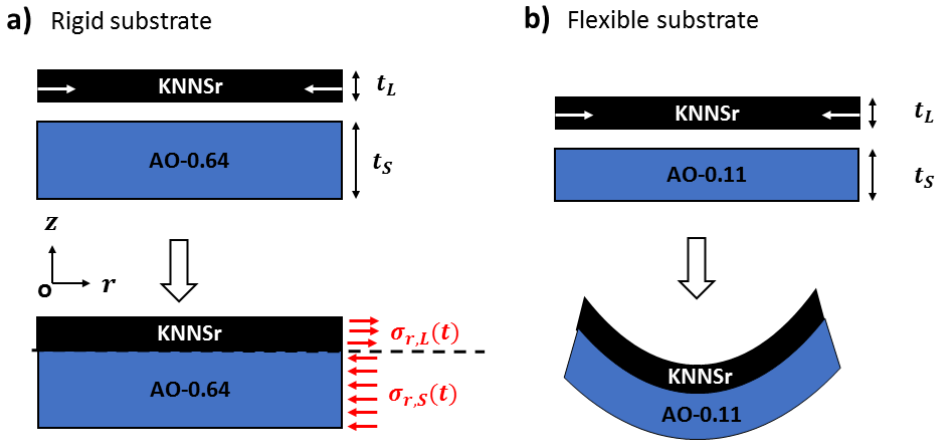

Figure 4.44: Schematic representation of the asymmetric structures during the sintering of KNNSr layers deposited on a) AO-0.64: 640- μ m-thick alumina substrate and b) AO-0.11: 110- μ m-thick alumina substrate. The white arrows represent the lateral shrinkage of the film if it was not clamped on the substrate and the red arrows represent the in-plane stresses in the clamped layer ($\sigma_{r,L}$) and substrate ($\sigma_{r,S}$).

For the asymmetric structures processed on DFAO substrates the AO thickness is 110 μm, the ratio t_L/t_S reached ~ 0.6. At a larger ratio t_L/t_S the structure bends during the sintering as the shrinking KNNSr layer exerts a higher force to bend the substrate

[176]. Indeed, we observed that the structure was bent after the sintering, thus the AO-0.11 was assumed to be a flexible substrate in this case. In the initial stage of sintering similar stresses occur in the structure as in the asymmetric structure processed on RAO substrate, i.e., in-plane tensile stresses in the substrate and in-plane compressive stresses in the substrate near the interface. However, in this case the structure can bend to relax the stresses [176]. The situation is schematically represented in Figure 4.44b. The bending of the structure during the sintering depends on several parameters, such as the thickness ratio t_L/t_S and the elastic properties of the substrate [176].

For the third case corresponding to a symmetrical structure, the structure is schematically represented in Figure 4.45. Due to the inability for the KNNSr layers to shrink laterally, we expect tensile stresses in the two KNNSr layers, and compressive stresses in the substrate. The t_L/t_S ratio was ~ 0.6 as in the case of the asymmetric structure processed on the DFAO substrate. Since we deposited layers with similar thicknesses on both sides of the substrate (Figure 4.41 and Figure 4.42), we expect similar stresses in the two KNNSr layers. Thus, both layers should exert a similar force to bend the substrate but in the opposite direction, which minimised the bending of the symmetrical structure [174], [175].

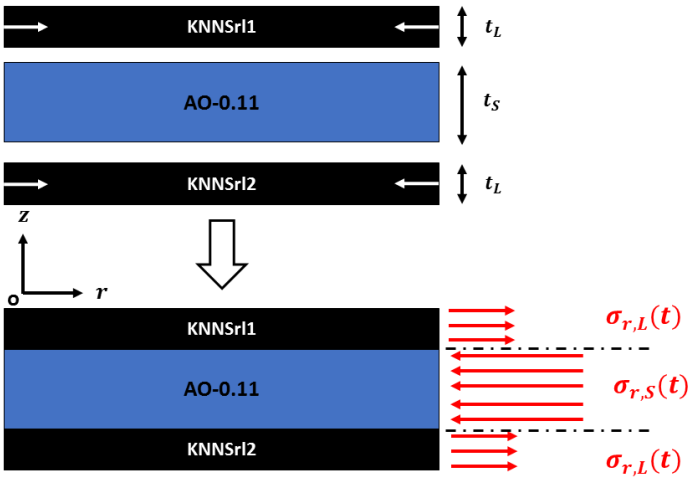

Figure 4.45: Schematic representation of the symmetric structure during the sintering. KNNSrl1 and KNNSrl2: KNNSr layers, AO-0.11: 110-μm-thick alumina substrate. The white arrows represent the lateral shrinkage of the films if it was not clamped on a rigid substrate and the red arrows represent the in-plane stresses in the layers ($\sigma_{r,L}$) and substrate ($\sigma_{r,S}$).

During the cooling from the sintering temperature to room temperature the structure is also subjected to stresses associated with the thermal-expansion-coefficient mismatch between the alumina substrate and the KNNSr thick films.

Since the thermal expansion coefficient of the alumina (8.2 x10^{-6} K^{-1}) is larger than the one for KNN, regardless of its crystal structure, i.e., 2.96, 4.35 and 7.52 × 10^{-6} K^{-1} for the monoclinic, tetragonal and cubic phase, respectively [33], the alumina tended to shrink more than the KNN. On a flat rigid substrate the KNNSr layer will be under in-plane compressive stresses, whereas the alumina substrate would be subjected to in-plane tensile stresses (Figure 4.46a). If the thicknesses of the KNNSr thick films and substrate get closer (t_L/t_S ~ 0.6 for the KNNSr processed on DFAO substrate) then the structure could bend in the opposite direction than the one observed during the sintering (Figure 4.46b). This phenomenon may reduce or even invert the direction of the bending that developed during

the sintering in the asymmetric structure processed on the DFAO substrate. For the symmetric structure, since the same stresses theoretically develop in KNNSrl1 and KNNSrl2 during this step, the bending is minimised.

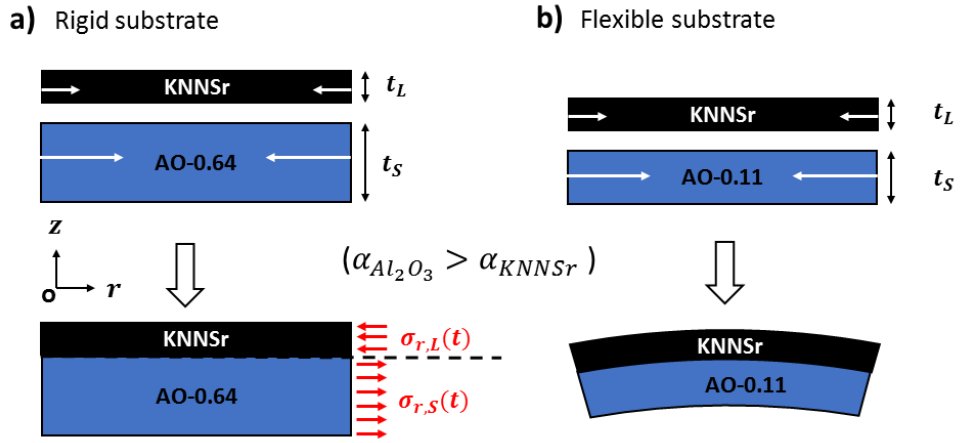

Figure 4.46: Schematic representation of the asymmetric structures during the cooling processed on a) AO-0.64: 640-μm-thick alumina substrate and b) AO-0.11: 110-μm-thick alumina substrate. The white arrows represent the lateral strains related to the linear thermal expansion coefficients ($\alpha_{Al_2O_3}$ and α_{KNNSr}) in the case where the KNNSr thick film and substrate were not clamped and the red arrows represent the in-plane stresses in the layers ($\sigma_{r,L}$) and in the substrate ($\sigma_{r,S}$).

4.3.2 Dielectric properties

The dielectric properties of DF-1100-O were measured for KNNSr1 layer and are shown in Figure 4.47. For comparison we added the dielectric properties of 1100-O to the same figure.

The relative dielectric permittivity ($\varepsilon_{r,33}$) and dielectric losses ($\tan\delta$) of DF-1100-O were 430 and 0.08 at 10 kHz and room temperature, which was higher than the values of ~270 and ~0.04 measured for 1100-O. The larger values of $\varepsilon_{r,33}$ may be related to the higher relative density measured for DF-1100-O.

The increase in $\tan\delta$ observed towards low frequencies for DF-1100-O could be an indication of the contribution of elevated conductivity. Defects such as A-site vacancies can easily form in KNNSr due to the alkali loss and can be compensated by the formation of defects such oxygen vacancies. The conductivity could be related to the larger concentration of defects. However, the thick-film structures DF-1100-O and 1100-O were sintered at the same temperature and we assume that the alkali loss was similar. Thus, the formation of defects is presumably not the only reason for the larger $\tan\delta$.

Another possibility is related to the irreversible domain-wall displacement contribution [165]. We observed a linear-logarithmic frequency dependence of permittivity of DF-1100-O similar as for 1100-O in Figure 4.33b. A linear regression of the curve revealed that the slope of the curve was -13.3 s, whereas the value for 1100-O was -8.0 s. The absolute value of the slope was larger for DF-1100-O compared to 1100-O. This larger absolute value of the slope could be related to an increased contribution from the irreversible domain-wall displacements and thus to $\tan\delta$ [166].

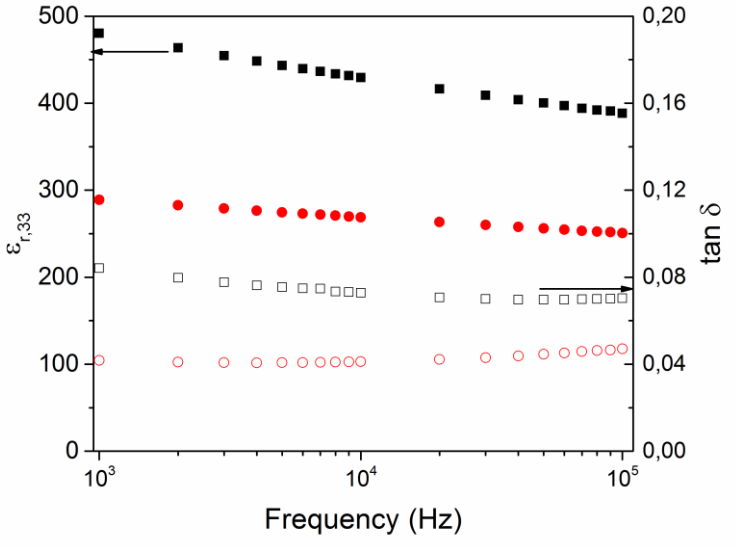

Figure 4.47: Relative dielectric permittivity (full symbols) and dielectric losses (hollow symbols) of DF-1100-O (black squares) and 1100-O (red circles).

4.3.3 Electromechanical properties

The evaluation of the electromechanical properties of one of the layers (typically KNNSrl1), requires the measurement of the complex electrical impedance of this poled layer. We observed in Figure 4.37 that the 1100-O complex electrical impedance around the fundamental resonance of the piezoelectric layers consisted of several peaks, which was attributed to the coupling of the piezoelectric layer and the substrate. For KNNSr layers deposited onto a DFAO substrate, additional layers must be accounted for, i.e., two platinum layers on each side of the AO substrate and an additional KNNSr layer (typically KNNSrl2). The use of the KLM equivalent electrical circuit scheme in its matrix notation allows the calculation of the theoretical complex impedance of this multilayer structure. Using the KLM equivalent circuit, we calculated, based on the properties of 1100-O thick films (Table 4.6), the complex electrical impedance of a 40-μm KNNSr (typically KNNSrl1) layer on a platinised AO-0.11 substrate (one side). Then we added an additional platinum layer on the rear face (DFAO) and lastly, we added a second non-piezoelectric 40-μm KNNSr layer (KNNSrl2) to the platinum on the rear face. The second KNNSr layer was considered as an inert material, i.e., an acoustic propagation line with several parameters taken as being equal to those of KNNSrl1, i.e., Z_{KNNSr}, γ_{KNNSr}. We note that the KNNSrl2 layer was not considered as poled, and thus the elastic properties of this layer may slightly differ from the elastic properties of the KNNSrl1 material. However, in the present calculation the same longitudinal wave velocity was considered in the KNNSrl1 and KNNSrl2 layers. The representation of the adapted final matrix notation for the KLM scheme (complement of Appendix C), is given in Figure 4.48.

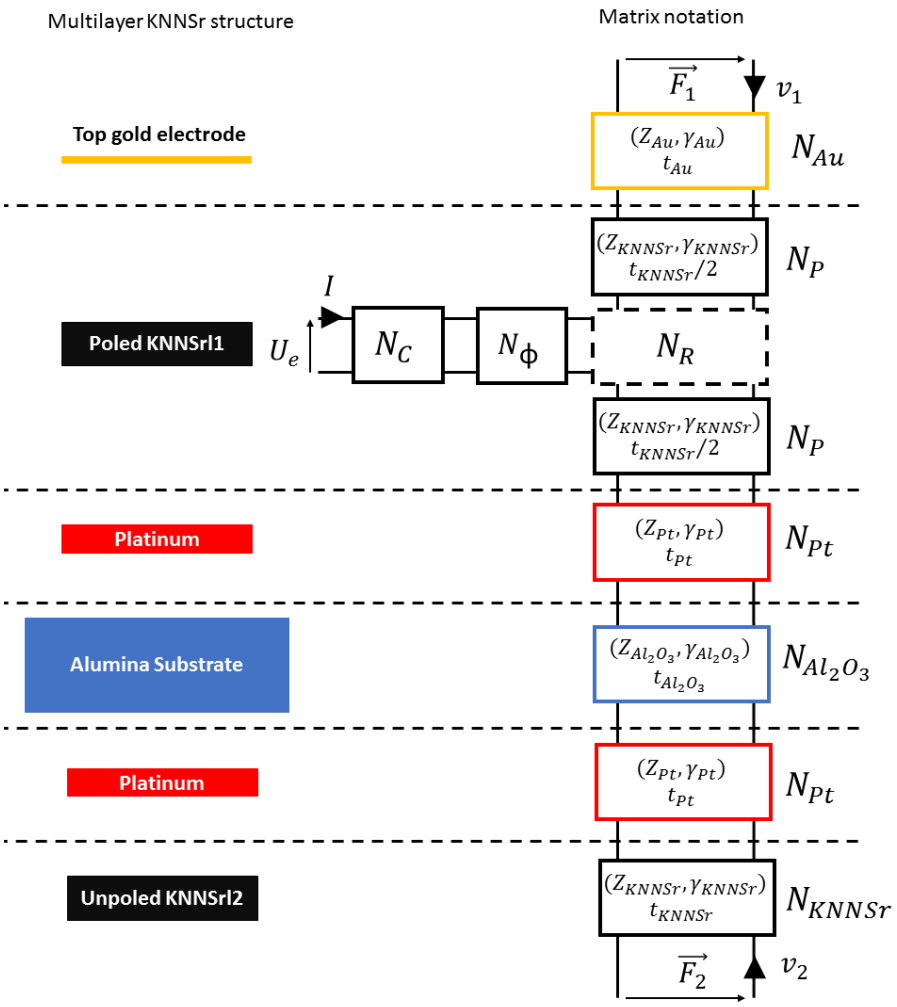

Figure 4.48: Matrix notation of the KLM model and corresponding layer applied to KNNSr bimorph processed on platinised alumina (DFAO) substrate.

The effect on the electrical impedance of successive additions of the second platinum electrode and inert KNNSr layer are presented in Figure 4.49. Figure 4.49a represents the case where one KNNSr layer was deposited onto an AO-0.11 substrate platinised only on one side, we observed four peaks in the frequency range 10–100 MHz, which was lower than the thirteen peaks observed when depositing KNNSr onto the RAO substrate (Figure 4.37). This was because the resonance frequency within the substrate ($\sim v_s/2l_s$) was larger for this case (48 MHz) than for the RAO substrate (23 MHz).

Figure 4.49b represented the same situation with the addition of the second platinum layer (the thicknesses of the two platinum electrodes were 10 μm) on the other side of the substrate, which resulted in a shift of the peaks towards the lower frequencies. This shift was clearly observed for the 2nd (from ~40 to ~35 MHz) and 3rd (from ~75 to ~60 MHz) peaks. The 4th broad peak's magnitude was larger than previously observed (at ~85 MHz).

Lastly, Figure 4.49c represents the complex electrical impedance of the entire bimorph structure. With the addition of a second KNNSr layer, we observed a split of the 2nd (~ 35 MHz) and 4th (~ 85 MHz) peaks observed in Figure 4.49b into two distinct peaks (29–38 MHz and 82–87 MHz).

With the addition of the second KNNSr layer, the theoretical impedance spectrum was significantly different from Figure 4.49b. These results reveal that the contribution of the

additional KNNSr layer play a significant role to deduce the properties of the KNNSrl1. The presence of numerous layers in the structure do not allow extracting the electromechanical performance of the KNNSrl1 layer with a good accuracy, especially if we do not precisely know the parameters of the second layer KNNSrl2.

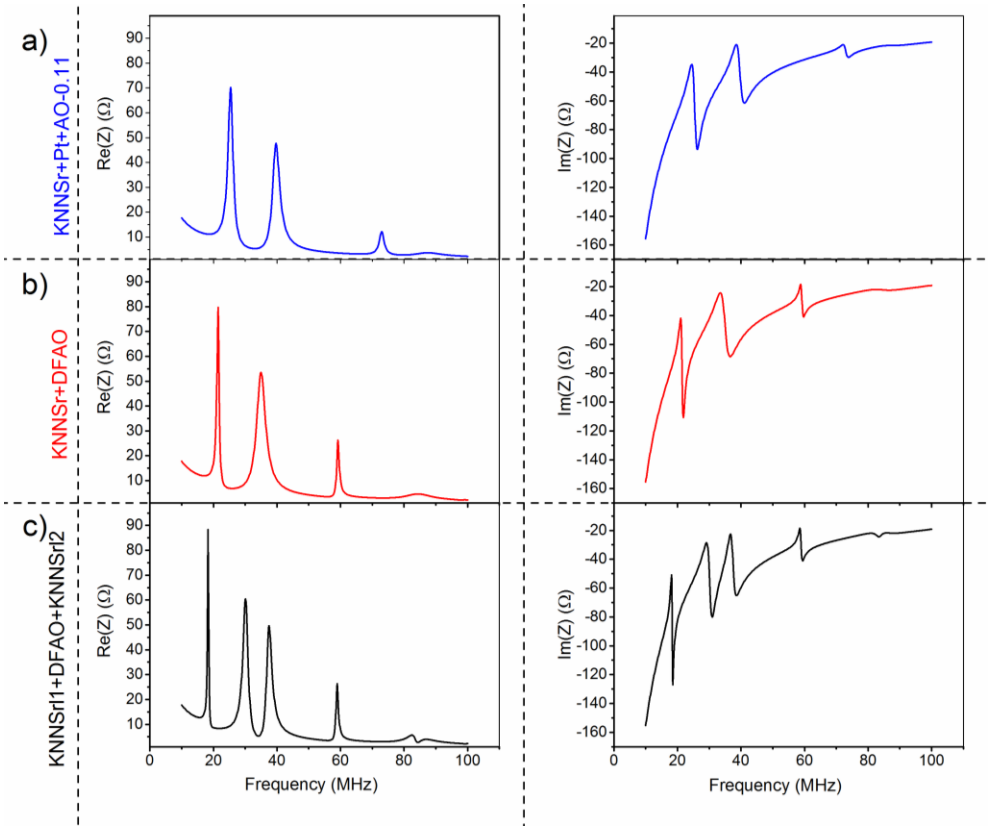

Figure 4.49: Theoretical complex electric impedance (Re(Z): real part; Im(Z): imaginary part) of a supported piezoelectric KNNSr thick film deposited onto a) alumina substrate platinised only on one side (KNNSr+Pt+AO-0.11), b) alumina substrate platinised on each side (KNNSr+DFAO) and c) complete bimorph structure (KNNSrl1+DFAO+KNNSrl2).

To avoid the issue associated with KNNSrl2, we characterised the KNNSr layer deposited only on one side of the DFAO substrate (OF-1100-O). The top electrode (2 mm diameter) had a small area compared to the bottom electrode's dimensions and a flat structure can be considered in this location. The measured and fitted electrical impedance spectra are presented in Figure 4.50. The complex electrical impedance exhibited a similar feature to the calculated complex electrical impedance presented in Figure 4.49b, except for the 4^{th} peak. By processing a KNNSr layer on one side of a DFAO substrate, and accounting for an additional platinum layer, we succeeded in extracting the electromechanical properties of the KNNSr layer.

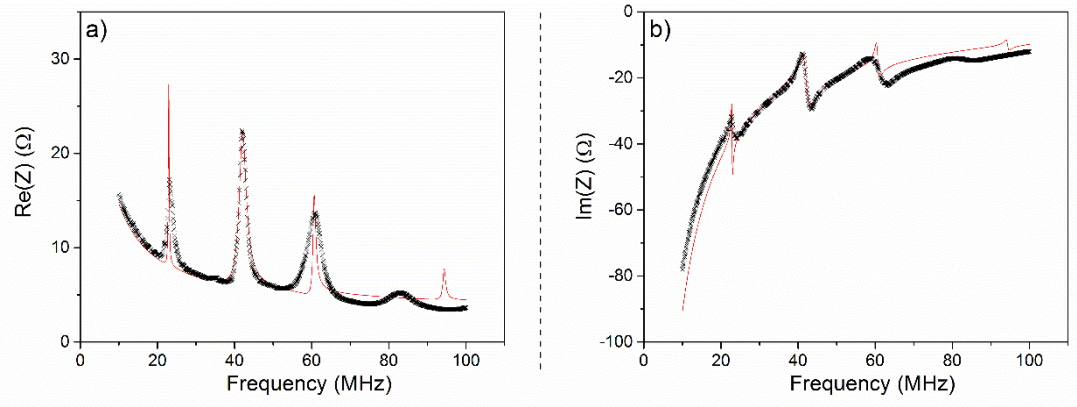

Figure 4.50: Complex electrical impedance (Z) of the KNNSr samples OF-1100-O as a function of the frequency around the fundamental resonance a) Re(Z): real part and b) Im(Z): imaginary part. Black cross: experimental impedance and solid red line: theoretical impedance.

The electromechanical properties of OF-1100-O deduced from the fit (Figure 4.50) are presented in Table 4.7 and compared with the properties of 1100-O. To calculate the standard deviations, we assume a variation in the thick film's thicknesses of ± 1.5 μm and in the thick film's density of ± 3 % similar, as described in 4.2.2.6. We observed that c_{33}^D and $\varepsilon_{r,33}^S$ of the OF-1100-O were larger than for the reference 1100-O. This agrees with the higher density of this thick film compared to the 1100-O samples. The reason for the lower value of e_{33} for OF-1100-O compared to-1100-O is not clear yet. The decrease of e_{33} and the increase c_{33}^D and $\varepsilon_{r,33}^S$ lead to a k_t value of 26 %, which is lower than for 1100-O.

Table 4.7: Electromechanical properties of KNNSr thick films on DFAO (OF-1100-O) and RAO (1100-O) substrates.

Sample	c_{33}^D (GPa)	k_t (%)	$\varepsilon_{r,33}^S$	e_{33} (C/m²)
OF-1100-O	83 ± 8	26 ± 1	170 ± 10	2.9 ± 0.3
1100-O	75 ± 9	40 ± 1	120 ± 10	3.4 ± 0.4

4.3.4 Effects of the porosity on the electromechanical properties of KNNSr for 31-mode harvester application.

In the previous parts the electromechanical performance of the KNNSr thick films was evaluated using properties of the thickness mode. This procedure was mainly chosen due to the ease in deducing the corresponding mode parameters such as k_t. Moreover, the measured k_t values allowed us to evaluate the performance of the KNNSr thick films. The thick films reported in the thesis are porous with a porosity of 15–25 %. The literature reports that this porosity content can be beneficial for the electromechanical performance in thickness mode. More precisely, the k_t value increases for PZT ceramics with a porosity content ranging from 10 to 30 % compared to the dense ceramics [177], [178] and was previously observed in PZT thick films [155]. Thus, thick films containing 10–30 % porosity have been accordingly integrated in a high-frequency ultrasonic transducer for medical imaging applications [73].

For the targeted application (bimorph cantilever energy harvester) the important parameters are the ones of the 31-mode, such as d_{31} or k_{31}. However due to the difficulty in deducing the parameters of this mode, these properties have not been measured in the present work. For example, the transverse mode was not observable from the electrical impedance measurement in the case of a thick film on a substrate. Thus, in this last section, we investigate the theoretical effect of the porosity on the FOMs of the 31-mode piezoelectric energy harvester presented in Equation (1.1) and Equation (1.2). In Equation (1.1) we neglect the dielectric losses.

To perform the calculation, we first need piezoelectric, dielectric and elastic components of the tensors. These parameters were determined from the dense ceramic C-1120-O (Appendix D). In this way, two bulk ceramic samples (C-1120-O), with rectangular and circular shapes, were used to deduce the properties of the thickness, width-extensional and radial modes. From these measurements s_{11}^E and s_{12}^E (radial mode [179]), k_t, c_{33}^D, ε_{33}^S, e_{33} (thickness mode using KLM equivalent circuit) and k'_{31}(width extensional mode) were obtained.

The determination of other effective constants to complete the database, such as the measurement of the thickness-extensional mode of the thinned ceramics [180] was not experimentally performed. Instead, the complete database was calculated using the procedure described in [181]. This database included the seven experimentally determined constants, i.e., s_{11}^E and s_{12}^E, k_t, c_{33}^D, ε_{33}^S e_{33} and k'_{31}. These constants were completed with values found in the reference [182] for unmodified KNN to restrain the search space and were only used as the initial input. The calculated database contained the parameters required for the calculation of FOM for a 31-mode PEH and are given in Appendix D.

In a second step, this database was introduced in a homogenised model to extract the effective parameters of porous piezoelectric material. The fabricated KNNSr thick films can be considered as a biphasic material with a piezoelectric dense phase that represents the matrix and the pore with air for the second phase. On a larger scale than the microstructure one, the properties of the considered composite can be characterised by a set of effective constants of an equivalent homogenised material. These constants can be obtained for different porosity contents and used to calculate the FOMs. The model used to calculate the effective constants (called the "matrix method" [183]) is based on a generalisation of the series and parallel analysis from 2-2 connectivity composites [184]. KNNSr material is represented by a unit cubic cell that contains an isolated cubic shape inhomogeneity corresponding to the pore phase. The shape of this inhomogeneity defined the spatial arrangement between the two phases, and consequently the connectivity of the composite. In our present study, only closed porosity was considered, i.e., isolated pores in a matrix phase. This configuration corresponds to 3-0 connectivity [184]. All details of the calculation are given in [177] and the input data are all the components of the elastic, dielectric and piezoelectric tensors of the two phases.

In the matrix method, the mechanical losses, i.e., $1/Q_m$ are not considered. Thus, we hypothesised that the variation of the relative value of the Q_m as a function of the porosity content was the same as the one reported for the porous PZT ceramic in reference [178]. From the variation of the parameters as a function of the porosity, we finally calculated the FOMs as a function of the relative density of porous KNNSr materials. The results for the parameters d_{31} and $\varepsilon_{r,33}^T$ and $FOM_{off-resonance}$ are presented in Figure 4.51.

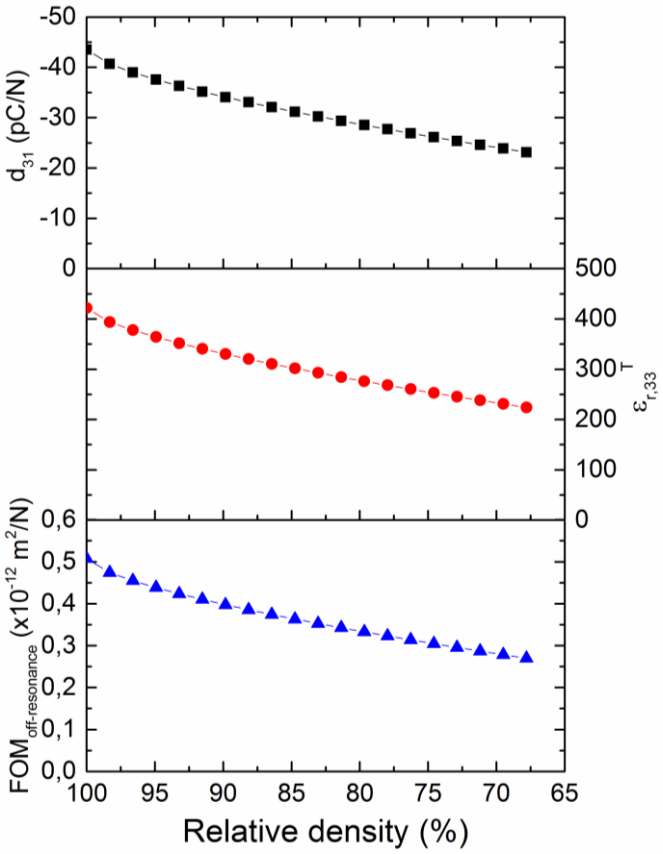

Figure 4.51: d_{31}: piezoelectric coefficient (■), $\varepsilon^{T}_{r,33}$: relative dielectric permittivity at constant stress (●) and figure of merit in off-resonance conditions (▲) of porous KNNSr materials as function of relative density with 3-0 connectivity.

We observed that the absolute values of d_{31}, $\varepsilon^{T}_{r,33}$ and $FOM_{off-resoncance}$ decreases when the relative density of the material decreases. At a relative density of 1 (fully dense ceramic) the $FOM_{off-resonance}$ exhibited a value of 0.5 x 10^{-12} m^2/N, which is close to the value of 0.6 x 10^{-12} m^2/N calculated from the values given in Table 1.1 for stoichiometric KNN when dielectric losses are not accounted. Then, we observed that the $FOM_{off-resonance}$ decreases with the decreasing relative density. At a relative density of 85 % (typical density of the KNNSr thick films) the $FOM_{off-resonance}$ decreased by 28 % of its initial value of dense KNNSr ceramic. The decrease of the FOM can be explained as follows: the ratio $d_{31}/\varepsilon^{T}_{33}$ is quasi-constant versus the porosity with a value of around - 0.012 V.m/N. Then the $FOM_{off-resoncance}$follows mainly the behaviour of d_{31}.

The literature shows that if the pores' longest dimension is aligned along a direction parallel to the main surface (lateral dimension), it is possible to increase the $FOM_{off-resonance}$ of the PEH operating in 31-mode [185]. Whereas when the porosity was aligned perpendicular to the substrate the $FOM_{off-resonance}$ in 31-mode decreased [185]. In the present results we introduced porosity without a particular alignment (cubic shape), which is more representative of the KNNSr thick films' microstructure.

Variations of Q_m, k_{31}, and $FOM_{on-resonance}$ are presented in Figure 4.52. Q_m was measured on the experimental admittance of the width extensional mode of the ceramic C-1120-O [186] to be 78 and the relative variation as a function of the porosity, as explained before, is taken from [178]. The value of k_{31}, Q_m and $FOM_{on-resonance}$ decreases with a decreasing relative density.

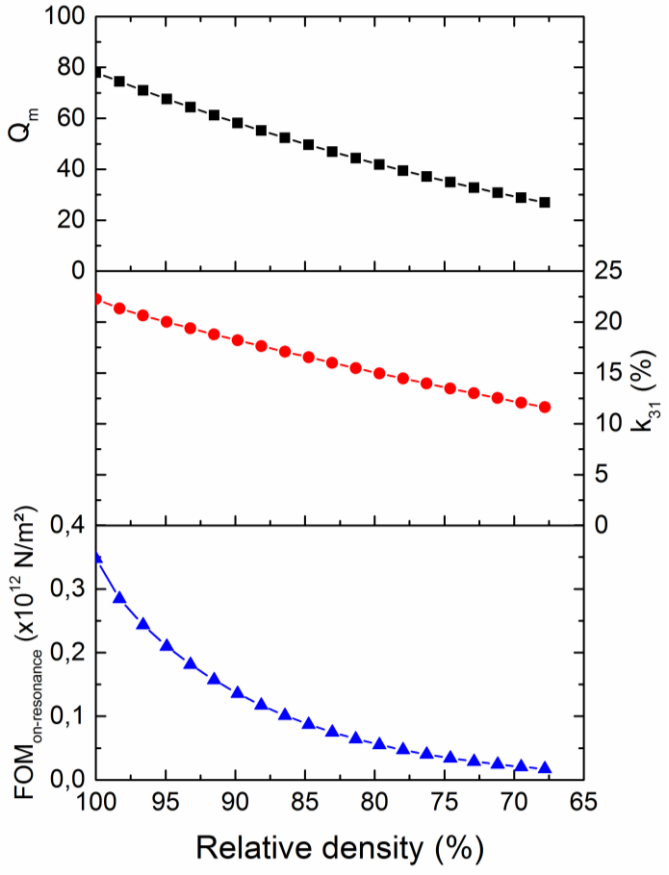

Figure 4.52: Q_m: mechanical quality factor (■), k_{31}: 31-mode electromechanical coupling factor (●) and figure of merit in on-resonance conditions (▲) of porous KNNSr materials as function of relative density with 3-0 connectivity.

k_{31} did not follow the same trend as the k_t, which exhibited a larger value when the porosity content was in the range 10–30 % [177], [178]. The parameters in the 31-mode such as d_{31} and k_{31} decreased with increasing porosity due to the interruption of the quasi-rod ceramic skeleton continuity of the medium in the lateral direction [169].

The value of $FOM_{on-resonance}$ for a relative density of 1 was ~0.35 x 10^{12} N/m², which is five times lower than the reported value in Table 1.1. The lower value is mainly attributed to the values of Q_m and k_{31}, i.e., 78 and 22 %, respectively. Whereas for the calculation of FOMs in Table 1.1, Q_m and k_{31} values of 240 and 27 % [7] were used, respectively. We observed that at a relative density of 85 % the $FOM_{on-resonance}$ had decreased by 75 % of its initial value.

These results indicate that the porosity had a more prominent effect on $FOM_{on-resonance}$ in comparison to the $FOM_{off-resonance}$. This can be explained by the fact that the variation as a function of the relative density of all the parameters in the $FOM_{on-resonance}$ participate to decrease its value, i.e., a decrease of k_{31} and Q_m at the numerator and an increase of s_{11}^E at the denominator.

These results indicated that for an energy harvester operating in 31-mode, the porosity in KNNSr notably influences its performance. The FOMs for both on- and off-resonance conditions are larger for a higher density of the ceramic. These results qualitatively agree with results reported in the literature [22].

Despite the clear trends revealed from these theoretical calculations, it is extremely demanding to predict the exact influence of the porosity on the PEH performance. In

particular because the calculated FOM took into consideration only the properties of the material. Also, we made several assumptions. First, we considered only 3-0 connectivity; however, the KNNSr thick films with relative density of ~85 % presented a network of interconnected pores corresponding to an amount of 3-3 connectivity. This second connectivity can have a different influence on the properties and then on the FOMs. The literature shows that the shape of the pores strongly influences the $FOM_{off-resoncance}$ [185] and in our case we limited the study with a cubic shape. We also assumed the same variation of Q_m as a function of porosity than that reported in [178]. But other studies show different behaviours of the mechanical losses where its variation as a function of the porosity is low and depends on the pore size distribution [170].

According to these considerations, variations of these two FOMs could be minimised with an optimisation of the connectivity, orientation and shape of the pores and pore size distribution. Moreover, these two FOMs are representative of the piezoelectric material, but not of the whole device with its electrical and mechanical environments. For example, if the bandwidth of the excitation is broad, material with a lower Q_m may be preferred [22]. Consequently, the energy output of the PEH does not necessarily follow the same trend as the two FOMs.

4.3.5 Summary

A specific deposition setup that enables the realisation of a bimorph structure on a 110-µm-thick alumina (DFAO) substrate was fabricated and validated. When sintering KNNSr layers deposited on one side of DFAO substrate, we observed a bending of the structure, related to the flexibility of the substrate and to the in-plane stresses which develop during the sintering and the cooling of the structure. We showed that in the symmetrical structure composed of KNNSr layers of similar thicknesses on each side of DFAO substrate, the bending of the structure was minimised. Using this method, the bimorph KNNSr/DFAO/KNNSr structure have been processed.

The two ~40-µm KNNSr thick films had a homogenous microstructure with a relative density of 86 ± 4 %. To characterise these piezoelectric layers in the bimorph structure, the KLM electrical equivalent circuit was adapted to take into account the extra inert layers and to deduce the electromechanical properties of one piezoelectric thick film. The KNNSr thick film had a larger relative dielectric permittivity and elastic stiffness in comparison to 1100-O, which was ascribed to the larger density.

Finally, we theoretically investigated the effect of close porosity on the 31-mode figures of merit (FOMs) of a cantilever PEH integrating KNNSr materials to evaluate the performance of thick films for the targeted applications. We observed that with introduction of 3-0 connected pores without a particular alignment, the d_{31}, $\varepsilon^T_{r,33}$, k_{31} and Q_m decrease, whereas s^E_{11} increases. These results indicated that the $FOM_{off-resonance}$ and $FOM_{on-resoncance}$ decreased by 28 and 75 % of their nominal values, respectively, with the decreasing relative density of the KNNSr from 100 % to 85 %. These conclusions are based on considering only the material properties. The results may be different when we consider the whole device with its electrical and mechanical environments.

Chapter 5

Conclusions and Outlook

Harvesting energy from ambient mechanical vibrations is a promising way to power autonomous sensors and support innovative developments in the internet of things, wireless sensor networks and implantable medical devices. The energy can be harvested with piezoelectric effects using a cantilever, i.e., piezoelectric layers integrated on one side (unimorph) or two sides (bimorph) of a substrate. This work described the processing of $(K_{0.5}Na_{0.5})_{0.99}Sr_{.005}NbO_3$ (KNNSr) lead-free thick films on alumina substrates.

In the first part, with the aim to process the layers with EPD, we stabilised submicrometre KNNSr particles in absolute ethanol using poly(acrylic acid-co-maleic acid) (PAM) and n-butylamine (BA). The suspension was stable with the ZP of the particles being –47 ± 6 mV. The conductivity of the suspension was tailored by the amount of PAM and BA and ranged from 9.2 to 29.1 μS/cm.

The particles were deposited at a constant current density of 1.56 mA/cm^2 on a rigid platinised 640-μm-thick alumina substrate. The deposited mass increased linearly with the deposition time and was inversely proportional to the conductivity of the suspensions. The deposits from the suspension with a conductivity of 9.2 μS/cm were non-homogenous, with defects after the drying, and thicker edges in comparison to the central part of the thick films. With the increasing conductivity of the suspension, the homogeneity and thickness uniformity of the layers improved. The suspensions with conductivities between 20 and 30 μS/cm were suitable for the processing of KNNSr layers by EPD.

With a finite-element analysis (FEA) we confirmed that the thickness uniformity was strongly correlated with the spatial distribution of the electric field strength close to the working electrode. More precisely, we theoretically predicted the electric field strength between the two electrodes for different combinations of the diameter of the counter electrode (D_e) and the inter-electrode distance (h_i).The most thickness-uniform as-deposited layers were obtained for h_i=3 mm and D_e=8 mm, i.e., when D_e had the same length as the square-shaped working electrode.

In the second part the as-deposited layers with a thickness of ~45 μm were sintered at 1075, 1100 and 1120 °C. The sample sintered at 1075 °C was porous, whereas the 1100 and 1120 °C sintered thick films had relative densities of 77 and 86 ± 4 %, respectively. They contained defects that prevent any functional characterisation. We minimised the formation of defects by depositing a ~ 10-μm-thick layer on a platinised alumina substrate and fired it at 1000 °C, followed by the deposition of a second layer on top of the first layer to reach a total thickness of ~ 45 μm. After drying we did not observe any macro-defects.

We studied the relationship between the sintering conditions, the microstructure, and the functional properties of the KNNSr thick films. Based on the shrinkage temperature curve, we sintered the layers in the narrow temperature range, at 1090, 1100 and 1110 °C, in air and oxygen. With an increasing sintering temperature up to 1100 °C, the relative

density increased from ~75 % to ~80 %, accompanied by pore growths, which was reflected in an increase of the relative dielectric permittivity ($\varepsilon_{r,33}$), and the elastic constant at a constant electric displacement (c_{33}^{D}). Upon heating to 1110 °C, the density did not vary significantly, but the pore size further increased, which resulted in similar values of $\varepsilon_{r,33}$ and c_{33}^{D}. The influence of the sintering atmospheres, i.e., air and oxygen, on the densification and electromechanical properties, is not significant.

We observed preferential crystallographic orientations in the [100] and [-101] directions of the monoclinic phase of the KNNSr thick films. However, we did not detect any significant impact of these orientations on the electromechanical properties of the thick films. The KNNSr thick films sintered at 1100 °C for 2 hours in oxygen had a density of ~ 81 %, a piezoelectric coefficient $d_{33,f}$ of 65 ± 5 pC/N and a thickness-mode electromechanical coupling factor of 40 %, similar to the bulk ceramics.

In the third part, a process for the fabrication of bimorph cantilever PEH was performed based on the results obtained in the two previous parts. For this purpose, we designed and fabricated a deposition setup which enabled the processing of KNNSr thick films on two sides of flexible substrates, i.e., a 110-μm-thick platinised alumina substrate. The KNNSr layer deposited on one side of the 110 μm-thick substrate, i.e., the unimorph structure, bent during the sintering at 1100 °C. We related the bending to the stresses that developed during the sintering and during the cooling of the structure from sintering to room temperature. The processing and sintering of a symmetric bimorph structure minimised the bending. The bimorph structure consisted of two similar KNNSr layers with a thickness of ~ 40 μm, a relative density of ~ 86 % and a thickness-mode electromechanical coupling factor of 26 %. These results indicated that KNN-based layers can be processed on both sides of a 110-μm-thick platinised alumina substrate by EPD and subsequent sintering. Thus, the innovative developed process enables the processing of a bimorph structure, which can be used in the preparation of piezoelectric energy harvesters.

The porosity content in the thick films impacted the performances of a 31-mode cantilever PEH. The theoretical evaluation of the introduction of randomly oriented and isolated pores in KNNSr ceramics (3-0 connectivity) showed that it decreases the electromechanical parameters d_{31}, k_{31}, Q_m, which resulted in a decrease of both the figures of merit in the on- and off-resonance conditions. We found that the FOM in the on-resonance condition was more impacted by the porosity than the one in the off-resonance conditions.

In future work the characterisation of the functional properties of the thick films in 31-mode (e_{31}, k_{31},...) and the calculation of the corresponding figures of merit of PEHs operating in this mode is required to evaluate the processed structure. These characteristics are needed to simulate the theoretical behaviour of PEHs integrating the KNN-based layers and to optimise, according to the targeted application, the geometry. The final step is the realisation of a demonstrator with an optimised predicted geometry and its characterisation in harvesting conditions.

The composition $(K_{0.5}Na_{0.5})_{0.99}Sr_{0.005}NbO_3$, used in this work was chosen as a model system, but the procedures developed within this thesis, are also convenient for other metal-oxide compositions. For an energy harvester working in on-resonance conditions the use of a piezoelectric with a larger mechanical quality factor and the 31-mode electromechanical coupling factor is beneficial. One of the possibilities is to modify the chemical composition of the KNN and/or to increase the relative density of the thick films using additives that enables sintering in the presence of a liquid phase. Both factors could improve the electromechanical properties of the piezoelectric resulting in larger power outputs of the PEH at the resonance frequency.

Appendix A

Piezoelectric and Ferroelectric Materials

A.1 Piezoelectric Materials

The direct piezoelectric effect exhibits a material that generates an electric charge proportional to the mechanical stress it is subjected to. The converse piezoelectric effect is exhibited by a material when the application of an electric field to the material proportionally strains the material.

Piezoelectric materials are anisotropic, i.e., their properties differ along different directions. The coupling between the electrical and elastic parameters of these materials is described by thermodynamic considerations, under isothermal conditions and choosing the electric field and the stress as independent parameters, the constitutive equations are given by [187], [188]:

$$\begin{cases} S_m = s^E_{mn}.T_n + d_{im}.E_i \\ D_i = d_{im}.T_m + \varepsilon^T_{ij}.E_j \end{cases} \tag{A.1}$$

where S_m is the strain second-order tensor, s^E_{mn} the elastic compliance fourth-order tensor at constant electric field, T_n the mechanical stress second-order tensor, d_{im} a piezoelectric third-order tensor, E_i the electric field vector, ε^T_{ij} the dielectric permittivity second-order tensor at constant stress and D_i the electric displacement vector. The i and j subscripts are 1, 2 or 3, whereas the m and n subscripts are between 1 and 6 and represent the indexes using Voigt notation (the correspondence is represented in Figure A.1b):

$$(11) = 1;\ (22) = 2;\ (33) = 3;\ (23) = (32) = 4;\ (13) = (31) = 5;\ (12) = (21) = 6$$

However, the components of the tensor using Voigt notation are not rigorously equal to the component using the full notation. For example, for the strain tensor S_{ij} or S_m we have:

$$\begin{cases} S_{ij} = S_m \ if\ i = j \\ 2\ S_{ij} = S_m \ if\ i \neq j \end{cases} \tag{A.2}$$

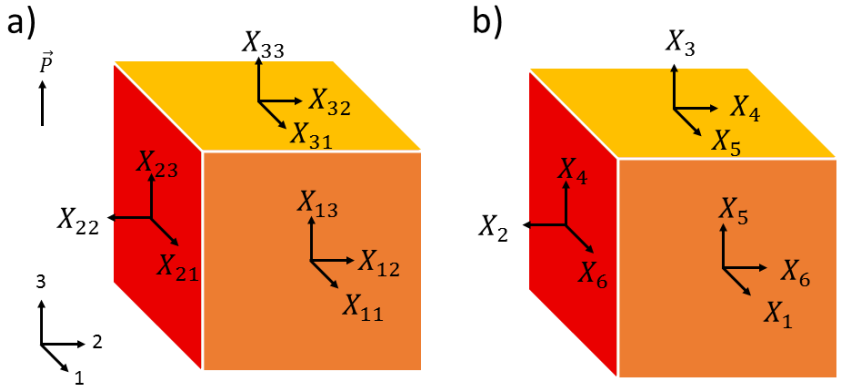

Figure A.1: Schematic representation on a cubic shape of a) index directions and b) the direction with the Voigt notations. By convention the polarisation direction ($\vec{P}$) is chosen in the direction of the axis 3. X represents the stress (T) or strain (S).

This set of equations (A.1) integrates both the direct and converse piezoelectric effects. The term $d_{im}E_i$ represents a strain induced by an electric field, i.e., the converse piezoelectric effect, whereas the term $d_{im}.T_m$ represents an electric displacement induced by a stress, i.e., the direct piezoelectric effect. According to the selected system of independent parameters (T, S, E, D), three other sets of constitutive equations are given by:

$$\begin{cases} T_m = & c^E_{mn}.S_n - e_{im}.E_i \\ D_i = & e_{im}.S_m + \varepsilon^S_{ij}.E_j \end{cases} \tag{A.3}$$

$$\begin{cases} T_m = & c^D_{mn}.S_n - h_{im}.D_i \\ E_i = - & h_{im}.S_m + \beta^S_{ij}.D_j \end{cases} \tag{A.4}$$

$$\begin{cases} S_n = & s^D_{mn}.T_n + g_{in}.D_i \\ E_i = & -g_{im}.T_m + \beta^T_{ij}.D_j \end{cases} \tag{A.5}$$

where ε^S_{ij} is the dielectric permittivity second-order tensor at constant stress, β^S_{ij} and β^T_{ij} are the reciprocals of the second-order tensors of permittivity at constant strain and stress, respectively, c^D_{mn} and c^E_{mn} are the elastic stiffness fourth-order tensor at constant electric displacement and electric field, respectively, s^D_{mn} is the elastic compliance fourth-order tensor at constant electric displacement. The e_{im}, $h_{i,m}$ and g_{im} are piezoelectric third-order tensors.

The energy conversion from electrical to mechanical or from mechanical to electrical by a piezoelectric material can be assessed using one of its electromechanical coupling factors (k). This coefficient is defined for a given resonance mode as [187]:

$$k^2 = \frac{stored\ mechanical\ energy}{supplied\ electrical\ energy} \tag{A.6}$$

Or

$$k^2 = \frac{stored\ electrical\ energy}{supplied\ mechanical\ energy} \tag{A.7}$$

k is defined for each vibration mode (k_{33}, k_{31}, k_t, k_p, ...) and depends on the material properties and material dimensions. Common resonance modes and associated electromechanical coupling factors are presented in Table A.1.

Table A.1: Resonance modes and associated electromechanical coupling factors. The blue arrows represent the vibration directions and the red arrows the polarisation direction in the piezoelectric material. Yellow areas represent the electrodes.

Vibration mode	Geometry	Electromechanical coupling factor
Thickness	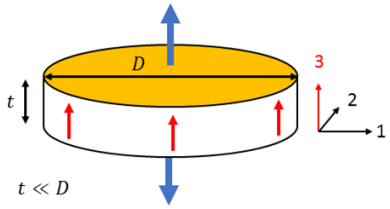	$k_t^2 = \frac{e_{33}^2}{c_{33}^D \varepsilon_{33}^S}$
Transverse	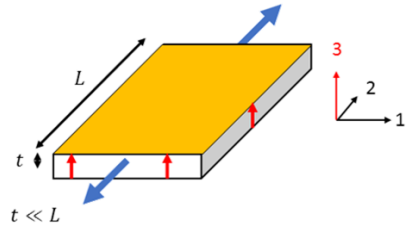	$k_{31}^2 = \frac{d_{31}^2}{s_{11}^E \varepsilon_{33}^T}$
Radial	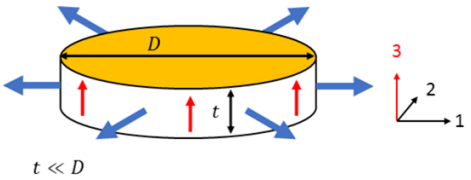	$k_p^2 = k_{31}^2 \frac{2}{1 + \frac{s_{12}^E}{s_{11}^E}}$
Longitudinal	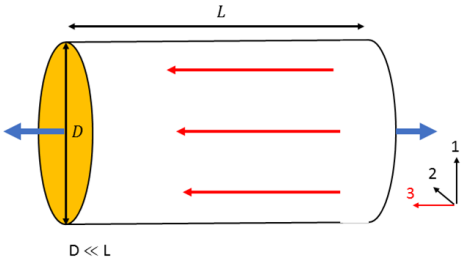	$k_{33}^2 = \frac{d_{33}^2}{s_{33}^E \varepsilon_{33}^T}$

k_t: thickness-mode electromechanical coupling factor, k_p: planar-mode electromechanical coupling factor, k_{31}: 31-mode electromechanical coupling factor, k_{33}: longitudinal-mode electromechanical coupling factor, e_{33}, d_{33}, d_{31} piezoelectric coefficients, s_{33}^E, s_{11}^E, s_{12}^E: compliances at constant electric field, c_{33}^D: elastic constant at constant electric displacement, ε_{33}^S: the dielectric permittivity at constant strain and ε_{33}^T the dielectric permittivity at constant stress.

The piezoelectric material exhibits dielectric and mechanical losses, which can be introduced by complex mechanical and dielectric parameters [189]. For the thickness mode, a complex mechanical stiffness at constant electric field:

$$\overline{c_{33}^D} = c_{33}^D(1 + j(\delta_m + k_t^2\delta_e)) \text{ with } \delta_e \ll 1 \tag{A.8}$$

and a complex dielectric permittivity at constant strain:

$$\overline{\varepsilon_{33}^S} = \varepsilon_{33}^S(1 - j\delta_e) \text{ with } \delta_e \ll 1 \tag{A.9}$$

are introduced, where δ_m and δ_e are the mechanical and dielectric losses, respectively [189]. The inverse of the mechanical losses is the mechanical quality factor (Q_m). High Q_m values are associated with low damping of the mechanical vibration. The dielectric losses are associated with the conductivity of the material and the phase lag between the polarisation and the applied electric field.

A.2 Ferroelectric Materials

Among the piezoelectric materials, ferroelectric materials exhibit a spontaneous polarisation, with at least two stable spontaneous polarisation states, which can be reversed by the application of an external electric field. Ferroelectric polycrystals contain ferroelectric domains, i.e., regions of uniform spontaneous polarisation, which minimise the sum of electrostatic, elastic, domain-wall and surface energy in the grains [190]. The application of an electric field to the ferroelectric material causes the occurrence of polarisation-electric field hysteresis loops.

By applying a large enough electric field to the ceramic, the polarisation of the domain switches towards the direction allowed by the crystal symmetry, which is as close as possible to the applied electric field direction. It results in a quick increase in charge density (see Figure A.2, segment AB). Then, along the line BC, the ferroelectric material behaves as a dielectric material, with a linear relationship between the electric field and the polarisation. Decreasing the electric field strength will decrease the polarisation due to some domain back-switching; however, the polarisation at zero electrical field still exhibits a finite value called the remanent polarisation (P_R, at point D). Reversing the electric field will cause the polarisation to decrease, reaching zero when the electric field reaches $-E_C$ (the opposite of the coercive field) at the point E. When the electric field is further decreased under E_C, it creates a new alignment of the domains in the opposite direction, until saturation is reached (point F). When the field is removed, the ferroelectric material exhibits a non-zero remanent polarisation (point G).

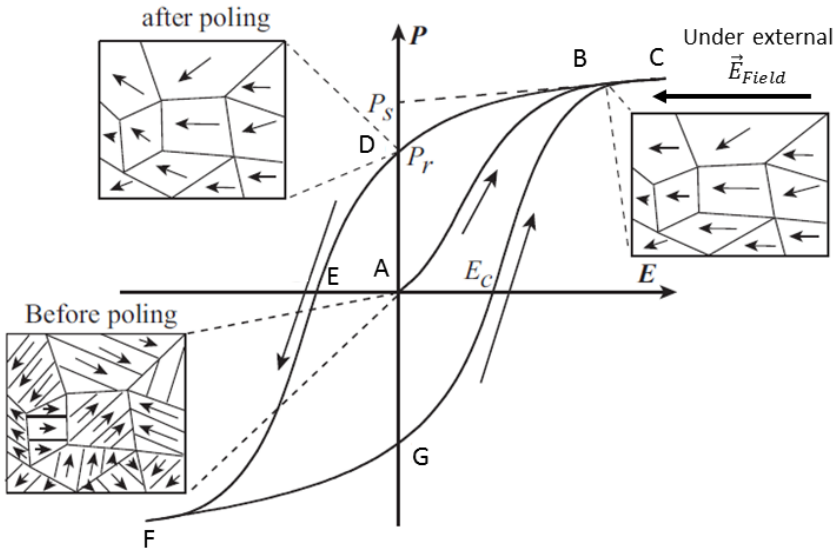

Figure A.2: a) Schematic representation of polarisation (P) electric field (E) hysteresis loop of a polycrystalline ferroelectric material (insets show the domain configurations) [191]. E_C: coercive field, P_S: polarisation at saturation and P_R: remanent polarisation.

In addition to the polarisation-electric field hysteresis, strain-electric field loops, which are also called "butterfly" loops (Figure A.3) are also observed. Here, we consider a monodomain crystal, for which the polarisation can be switched by an instantaneous 180 ° reversal. When the applied electric field is zero, the strain is taken as zero (point A). When an external electric field is applied to the crystal in the direction of the spontaneous polarisation, the strain increases through the intrinsic piezoelectric effect (line ABC). After the maximum field value is reached, reaching the maximum strain at point C, the applied electric field is reduced and the strain decreases following the line (CBA). Between the points A and D, the electric field is applied in the opposite direction to the spontaneous polarisation, and the crystal contracts through the piezoelectric effect. At the point D the electric field is strong enough to switch the polarisation direction of the domain, which becomes parallel to the field, and thus the stress becomes positive (point E). A further increase of the field in the negative direction causes an increase of the strain until the maximum field and strain are reached at the point F. Then removing the electric field causes the strain to decrease along the line FEA. If the electric field is applied again, in a positive direction, the polarisation switching would take place at the point G.

A measured hysteresis loop for the $K_{0.5}Na_{0.5}NbO_3$ ceramic is presented in Figure A.3b. The switching from one direction of the polarisation to another in a real ferroelectric is less sharp than shown in Figure A.3a, as the sample may exhibit domains with a range of coercive fields. Depending on their structure, polycrystals may also possess non-180° domain walls. The change in crystallographic orientation when the polarisation of non-180° domains is switched will cause an additional strain/stress. The situation is schematically depicted in Figure A.4 for the mobility of a 90° domain wall where the difference between the unit-cell parameter a and c and the variation in the domain structure upon applying an electric field causes an expansion of the material. The presence of those non-180° domain walls in ferroelectric polycrystals causes extrinsic contributions to the piezoelectric effect [192], i.e., contributions which are not lattice-cell dependent.

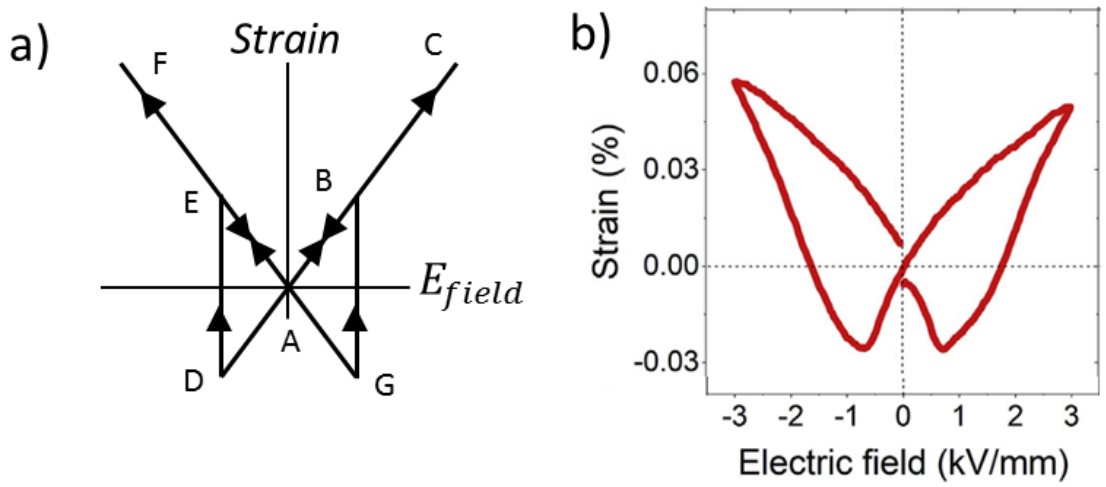

Figure A.3: a) Schematic representation of the strain-electric field hysteresis loop of a ferroelectric material containing only 180° domain walls [190], b) Measured strain-electric field hysteresis loop of $K_{0.5}Na_{0.5}NbO_3$ ceramic [193].

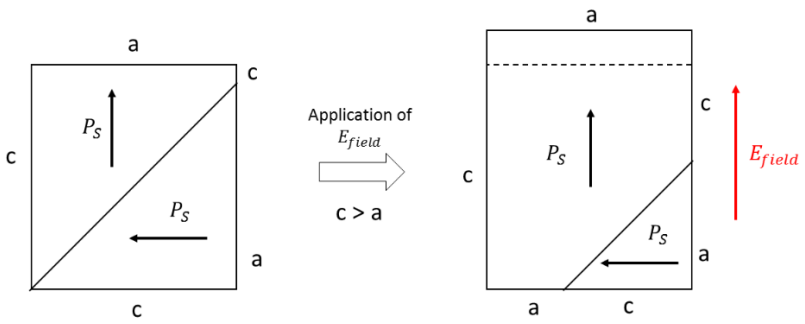

Figure A.4: Schematic representation of the dimensional change during the application of an electric field in a tetragonal structure due to the mobility of a 90° domain wall. "a" and "c" designate the unit-cell parameters of the tetragonal structure and P_S the spontaneous polarisation in each domain.

Appendix B

Electrostatic Stabilisation of Charged Particles in a Solvent

The surface of a metal-oxide (MO) particle immersed in a polar solvent can acquire charges through the ionisation of the surface groups, ion adsorption, dissolution of ionic solids and isomorphous substitution [194]. The charged MO surface attracts ions with the opposite charge (counterions) present in the solvent. The counterions are subjected to thermal motion, which tends to distribute them uniformly through the surrounding medium. The net effect of the electrostatic attraction and thermal motion is the formation of a concentration gradient of counterions forming the electrical double layer (EDL).

In close vicinity to the particles, the well adsorbed counterions form the Stern layer (in green in Figure B.1). In the Stern layer the electric potential decays linearly with the distance from the surface. In the second layer, i.e., the diffuse layer, the concentration of counterions decays gradually and the electric potential decreases exponentially with the distance from the surface towards the diffuse layer (in red in Figure B.1).

The extension of the EDL is described by the Debye length ($1/\kappa$) [81]:

$$\frac{1}{\kappa} = \sqrt{\frac{\varepsilon_r \varepsilon_0 k_B T}{{q_e}^2 \sum n_i^0 z_i^2}} \tag{B.1}$$

with ε_r and ε_0 the solvent's relative dielectric permittivity and the dielectric permittivity of the vacuum, respectively, k_B the Boltzmann constant, T the temperature, q_e the elementary charge, n_i^0 the concentration of the ions i in the suspension and z_i the valence of the ions i.

When a charged particle moves in a fluid, there is a fluid layer close to the particle surface that flows together with the particle: the hydrodynamic stationary fluid. The plane separating the hydrodynamic stationary fluid from the rest of the fluid is termed the slip plane. The electrical potential at the slip plane is defined as the zeta-potential (ZP). For non-conducting particles the ZP is given by [81]:

$$\mathrm{ZP} = f_H \frac{\eta v_e}{\varepsilon_r \varepsilon_0 E} \tag{B.2}$$

where η is the dynamic viscosity of the solvent, v_e is the electrophoretic velocity, E is the applied electric field, ε_r is the relative dielectric permittivity of the solvent, ε_0 is the dielectric permittivity of the vacuum and f_H is the Henry constant. For a particle with a radius r and the conditions $\kappa r \ll 1$ the f_H is 3/2 and when $\kappa r > 100$, f_H is 1 [81].

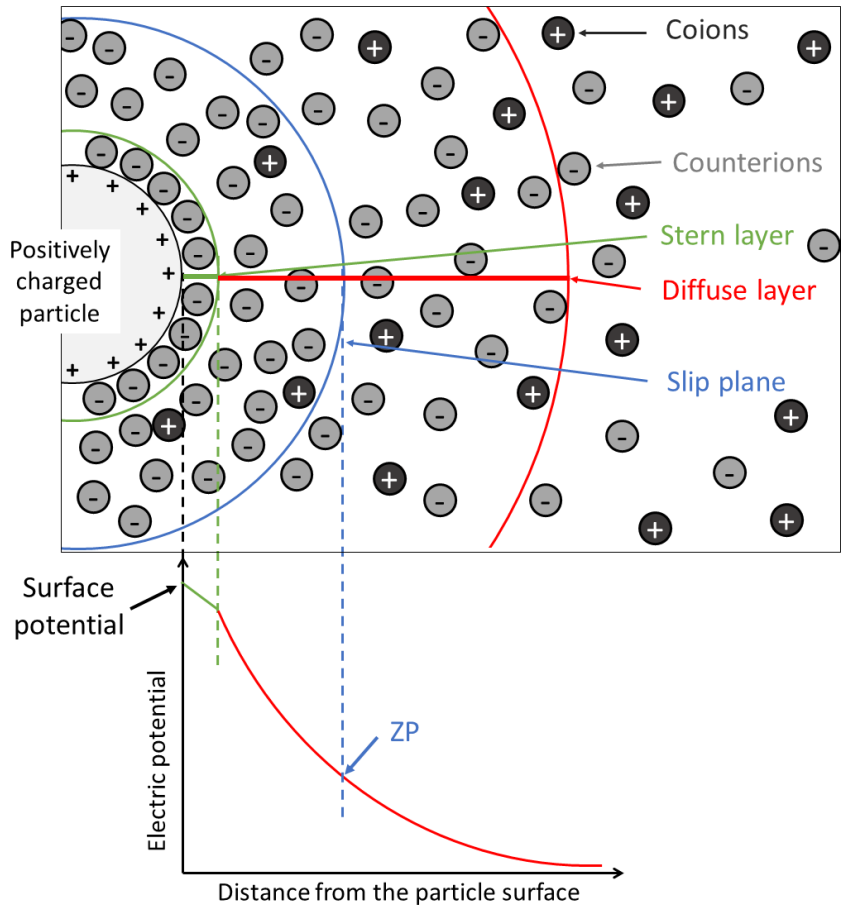

Figure B.1: Schematic illustration of the electrical double-layer structure at the solid/liquid interface of a positively charged particle.

The interactions between two particles at a distance D depend on the magnitude and range of the Van der Walls attractive potentials (V_A) and the electrostatic repulsive potentials (V_R). The interaction potential is represented in Figure B.2 [80]:

1) When particles are far apart there is no interaction between them.
2) As the particles approach one to another, there is a secondary minimum in the interaction energy versus separation distances (D). The secondary minimum is present when the magnitude and range of the electrostatic repulsion is low, and the attractive force prevails at this separation distance. The presence of a secondary minimum causes the particles to weakly agglomerate.
3) When the separation distance (D) between the particles decreases, i.e., the repulsive electrostatic force prevails over the attractive force, thus the interaction potential reaches a maximum known as the potential barrier (V_b). If this barrier is larger than 25 k_BT (thermal motion), the particles are well stabilised, no agglomeration is observed.
4) At a close distance between the particles, there is a deep primary minimum. In this primary minimum the attractive force overcomes the repulsive force, which causes a strong agglomeration of the particles.

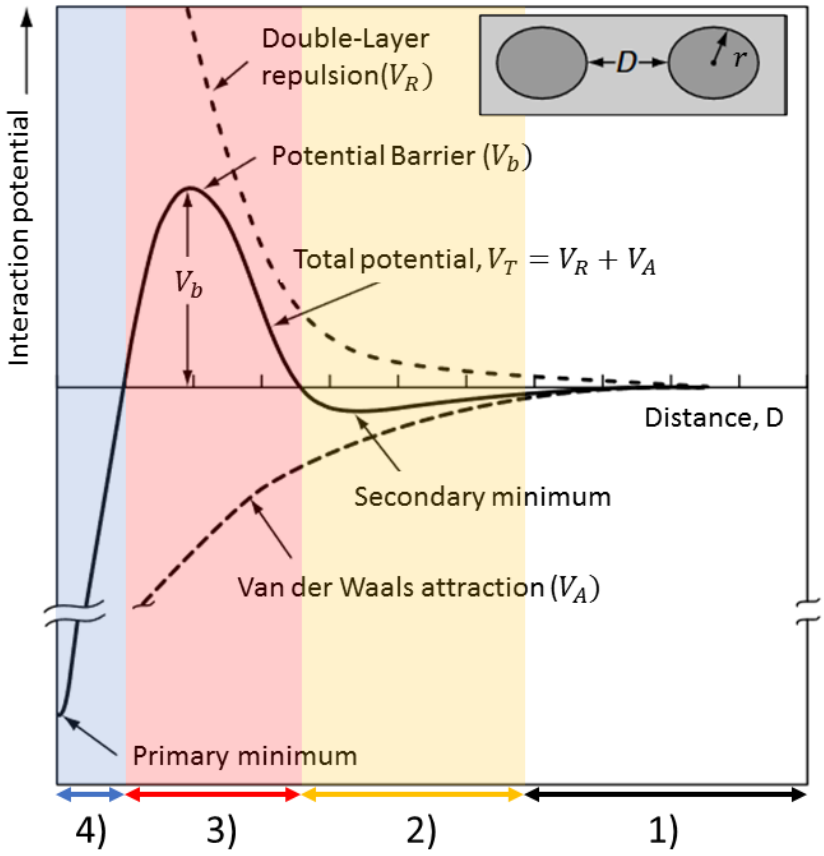

Figure B.2: Schematic representation of the interaction potential as a function of the separation (D) between two particles with radius r dispersed in a solvent [80].

Appendix C

Equivalent Electrical Circuit for Piezoelectric Thick Films Characterisation

The vibration along the thickness of a piezoelectric plate is commonly used for medical imaging, non-destructive testing, or other applications. This condition allows simplifying the corresponding models: in this case only one dimension along the vibration direction is considered and several electrical equivalent circuits were developed [195]. In this appendix, the Krimholtz-Leedom-Matthaei (KLM)model is retained and briefly described [141]. The case of the calculation of the electrical impedance of piezoelectric layers structure is highlighted for the characterisation of the electromechanical properties of a piezoelectric thick film on a substrate.

C.1 Electrical Hexapole Representation of Piezoelectric Element: KLM Model

A piezoelectric plate poled along the thickness (t_M) is considered in Figure C.1a. The lateral dimensions of the piezoelectric plate (l and w) are higher than the thickness t_M to only consider the thickness-mode vibration along axis 3 (piston mode). The two electrodes cover the surface S_{elec}.

The voltage applied to the electrodes is noted U_e, the displacement velocities, and applied forces to the front and rear faces are denoted as v_1, v_2, $\overrightarrow{F_1}$ and $\overrightarrow{F_2}$, respectively. With this hypothesis, the electric field with only a component along the axis 3 (E_3) leads to a longitudinal vibration in the 3-axis direction, and the piezoelectric constitutive equations (Appendix A) are reduced to:

$$\begin{cases} T_3 = c_{33}^E . S_3 - e_{33} . E_3 \\ D_3 = e_{33} . S_3 + \varepsilon_{33}^S . E_3 \end{cases} \tag{C.1}$$

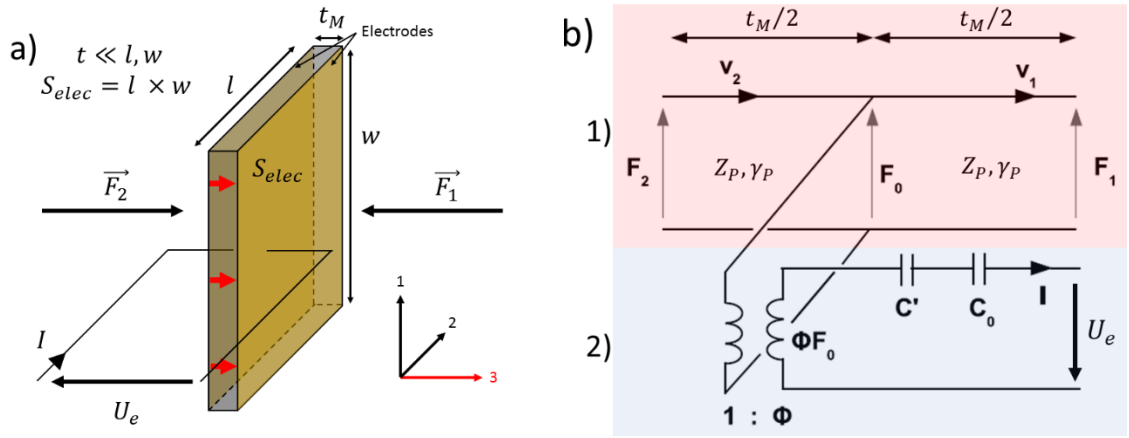

Figure C.1: a) Notation for piezoelectric plate [189] and b) Scheme of the KLM electrical equivalent circuit [141]. Red arrows represent the poling direction.

An equivalent electrical model, the KLM model (1-dimensional model, developed by Krimholtz, Leedom and Matthaei [141]) allows the calculation of different transfer functions in emission, reception and emission/reception, such as the electroacoustic response of an ultrasonic transducer. Electrical impedance as a function of the frequency is also easily calculated. In the model the piezoelectric element is described as an hexapole with two acoustical ports and one electrical port (Figure C.1b), more precisely:

1) The two propagation lines of thickness $t_M/2$ make it possible to link the acoustic ports of the rear and front faces described by the line primary parameters:
   a. Resistivity (Ω/m): R
   b. Inductance (H/m): L
   c. Capacitance (F/m): C
   d. Conductance (S/m): G

   and the secondary parameters (Z_P) and the propagation constant (γ_P) given by:

$$Z_P = \sqrt{\frac{R + j\omega L}{G + j\omega C}} \tag{C.2}$$

   and

$$\gamma_P = \sqrt{(R + j\omega L)(G + jC\omega)} \tag{C.3}$$

   with ω the pulsation.
2) An electrical port that is connected to the centre of the acoustic line by an electromechanical transformer to introduce the piezoelectric property and two capacitors in series: C_0 (static capacitance) and C' (motional capacitance). The capacitance C_0 is given by:

$$C_0 = \frac{\varepsilon_{33}^S . S_{elec}}{t_M} \tag{C.4}$$

   with ε_{33}^S the dielectric permittivity at constant strain of the piezoelectric element, and the motional capacitance C' is given by:

$$C' = -\frac{C_0}{k_t^2 \ sinc(\omega \frac{t_M}{V_L})} \tag{C.5}$$

with k_t the thickness-mode electromechanical coupling factor, and V_L the longitudinal wave velocity.
The electromechanical transformer coefficient Φ is given by:

$$\Phi = \frac{2\sin(\omega \frac{t_M}{2V_L})}{\omega C_0 Z_p} \tag{C.6}$$

Then, the voltage U_e is expressed as:

$$U_e = \frac{I}{j\omega C_0} + \frac{I}{j\omega C'} + \Phi F_0 \tag{C.7}$$

with F_0 the force in the centre of the piezoelectric material and I the electrical current.

If the piezoelectric plate resonates in air, the acoustical impedance of this media can be neglected on each side of the element and the electrical impedance of the piezoelectric plate considered in a free resonator configuration is given by [195]:

$$Z_e = \frac{U_e}{I} = \frac{1}{j\omega C_0}\left(1 - k_t^2 . \frac{tan\left(\omega \frac{t_M}{2V_L}\right)}{\omega \frac{t_M}{2V_L}}\right) \tag{C.8}$$

The maxima of the impedance, according to Equation (C.8), is observed for the anti-resonant frequency (f_a) given as:

$$f_a = \frac{V_L}{2 \ t_M} \tag{C.9}$$

and the impedance is zero for the resonant frequencies (f_r) that are obtained for the conditions:

$$k_t^2 \frac{\tan\left(\frac{\pi f_r t_M}{V_L}\right)}{\frac{\pi f_r t_M}{V_L}} = 1 \tag{C.10}$$

The determination of the resonant (f_r) and anti-resonant frequency (f_a) makes it possible to deduce the value of the thickness-mode electromechanical coupling factor by rewriting Equation (C.10), taking into account Equation (C.9):

$$k_t = \sqrt{\frac{\pi f_r}{2 f_a} cotan(\frac{\pi \ f_r}{2 \ f_a})} \tag{C.11}$$

The capacitive effect, and values of the resonant and anti-resonant frequencies are highlighted on the modulus of the electrical admittance representation ($|Y_e| = 1/|Z_e|$), see Figure C.2

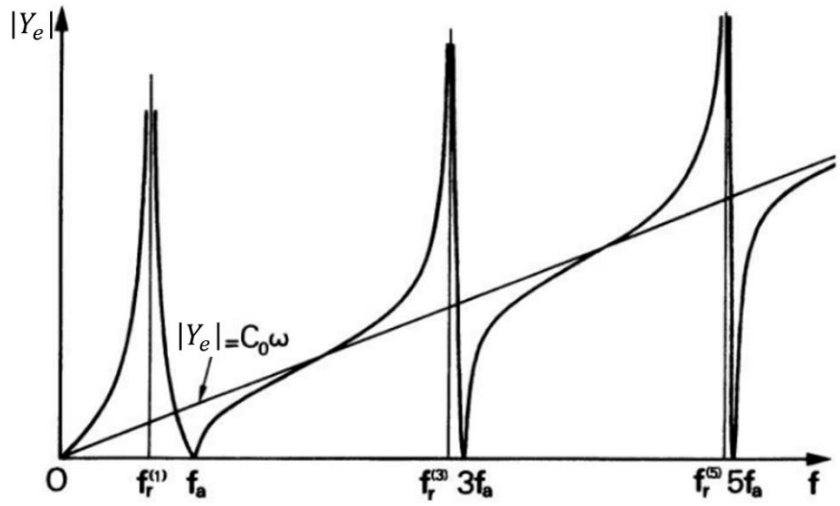

Figure C.2: Modulus of the electrical admittance ($|Y_e|$) as a function of the frequency (f) of a free piezoelectric resonator [195].

In the previous representation, losses (mechanical δ_m and dielectric δ_e) are not considered and the calculated impedance has only an imaginary part. In practice the electrical and mechanical losses limit the value of the admittance at the resonant frequencies (presented in Figure C.2) to finite values. The losses are added by integrating complex parameters in the KLM equivalent electrical circuit as [189]:

$$\overline{\varepsilon_{33}^S} = \varepsilon_{33}^S(1 - j\delta_e) \text{ with } \delta_e \ll 1 \tag{C.12}$$

$$\overline{c_{33}^D} = c_{33}^D(1 + j(\delta_m + k_t^2\delta_e)) \text{ with } \delta_e \ll 1 \tag{C.13}$$

When losses are accounted for, it is possible to calculate both the imaginary and the real part of the impedance of a piezoelectric resonator.

C.2 Multilayer Structure

In the case of a piezoelectric thick film that is surrounded by electrodes and substrate, the 1D model assumptions are still valid, but the analytical formula for the electrical impedance given in (C.8) has to be modified to take into account the impedances of the front and rear faces. The main advantage of the KLM formalism is that it can be written in matrix notation, which will allow the calculation of each layer transfer function separately [196]. Each layer added in the front or the rear face of the piezoelectric material (electrodes and substrate in our case) is represented by propagation lines (quadrupoles) defined by the parameters (Z_i, γ_i) and the layer thickness t_i. The acoustic port of the piezoelectric element is represented by two quadrupoles representing the acoustic lines (Z_P, γ_P) and the half thickness $(t_M/2)$, and the electrical port of the piezoelectric layer is introduced by two quadrupoles:

- N_C: represents the two capacities connected in series C_0 and C' ;
- N_Φ: represents the ideal transformer.

Each transfer matrix is computed separately. Thanks to this representation the hexapole representing the piezoelectric material is reduced to quadrupoles. The global transfer matrix (M) is obtained in two steps:

1) Calculating the transfer matrix of the rear port, brought to the centre of the piezoelectric layer (N_R, containing $N_{Al_2O_3}$ for alumina substrate, N_{Pt} for platinum bottom electrode and N_P for the piezoelectric "half thickness" delay line);
2) Then the global matrix M is computed as:

$$M = N_C N_\Phi N_R N_P N_{Au} \tag{C.14}$$

with N_{Au} the transfer matrix for the gold top electrode.

The specific configuration of the KNNSr thick films deposited on 640 μm alumina (RAO) substrates is schematically presented in Figure C.3.

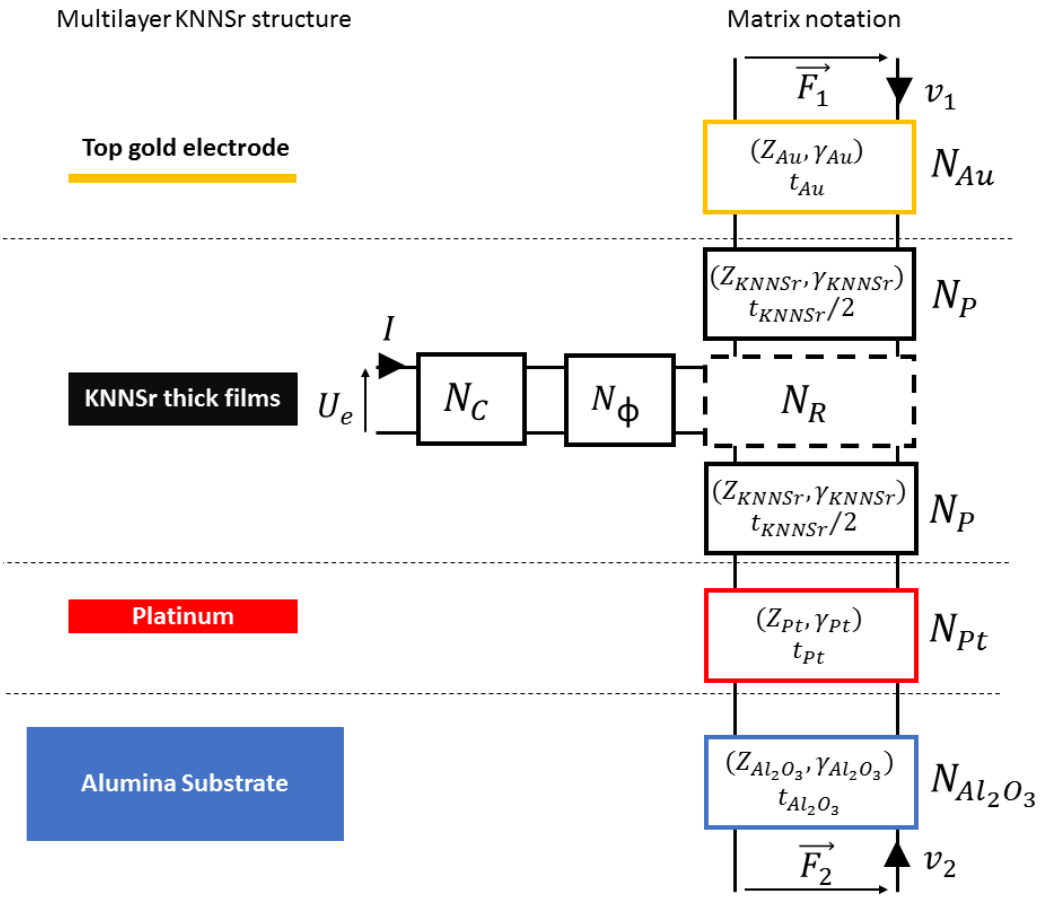

Figure C.3: Matrix notation of the KLM model applied to KNNSr films processed on platinised alumina substrates.

The matrix M makes it possible to connect the multilayer structure to an external electrical environment, such as, for example, a generator in emission conditions. An example is given in Figure C.4, with a voltage (U_g) delivered by the generator with an internal electrical impedance (Z_g). A voltage U_e is applied to the piezoelectric element and the acoustic port generates a force F_0 at the terminals of an impedance (Z_m) related to the impedance of the surrounding medium.

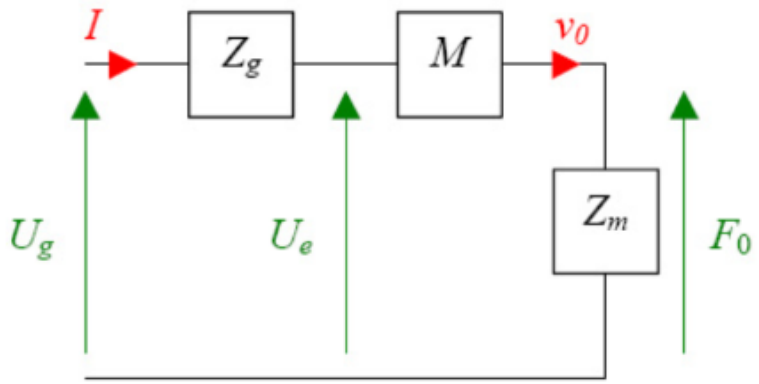

Figure C.4: Equivalent electrical circuit for a transducer in emission.

Similar conditions are defined in reception and then in emission/reception to model the behaviour of the whole ultrasonic transducer considering its electrical and mechanical environments.

For the case presented in Figure C.3, complex electrical impedance of the multilayer structure in air is calculated to characterise only the functional properties of the piezoelectric thick films.

Appendix D

KNNSr Bulk Ceramics

The polished cross-section and fracture-surface scanning electron microscopy (SEM) images of the KNNSr ceramics sintered at 1120 °C for 2 h in air (C-1120-A) and in oxygen (C-1120-O) are presented in Figure D.1. The microstructure consists of a KNNSr matrix phase and a few micrometre-sized pores. C-1120-O also exhibited a brighter phase (Figure D.1c). The EDXS analysis showed that the (Na+K)/Nb ratio in this phase was close to 0.5, which correspond to the tungsten-bronze phase with the composition $K_{5.75}Nb_{10.85}O_{30}$ [48]. The grain sizes range from ~0.5 to ~10 μm (Figure D.1b and Figure D.1d). The densities of the C-1120-O and C-1120-A, measured by Archimedes' method, were 4.4 g/cm^3 and 4.2 g/cm^3, respectively.

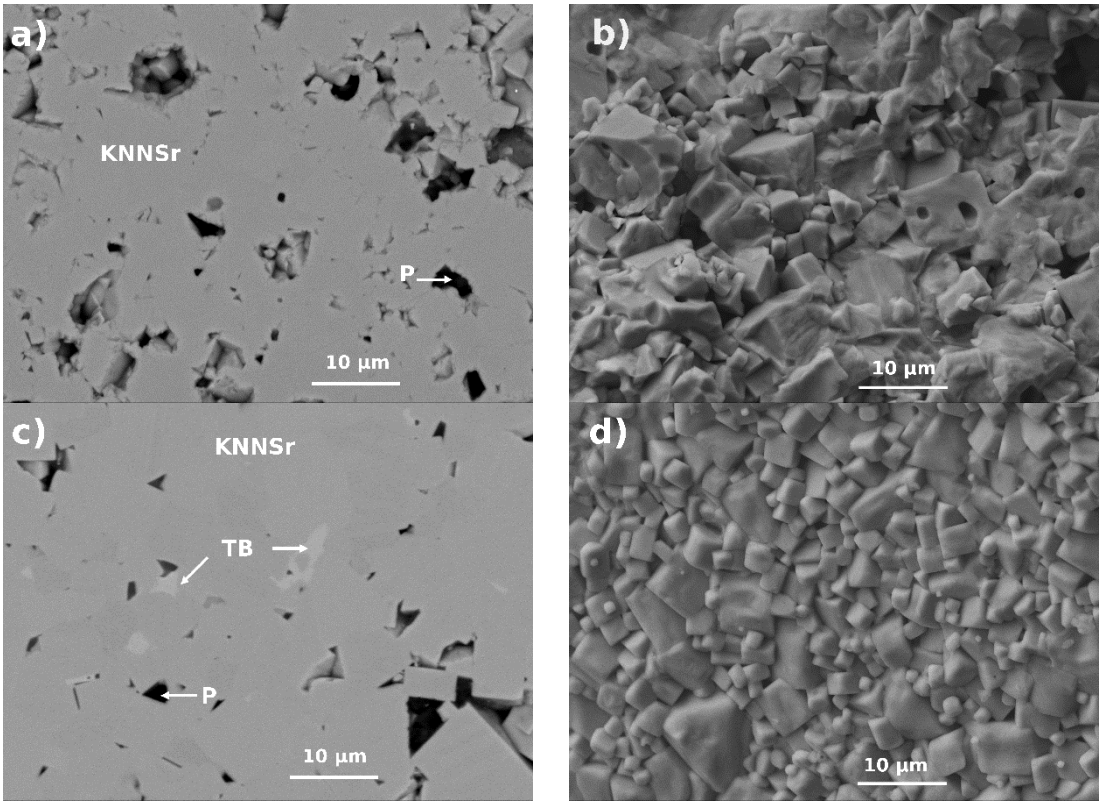

Figure D.1: Polished cross-section SEM images of a) C-1120-A and c) C-1120-O and fracture surface SEM images of b) C-1120-A and d) C-1120-O. KNNSr: $(K_{0.5}Na_{0.5})_{0.99}Sr_{0.005}NbO_3$; TB: tungsten bronze and P: pores.

The complete database (with all the components of elastic, dielectric and piezoelectric tensors) for C-1120-A is given in Table D.1. These data were obtained using samples with rectangular and circular shapes to favour one vibrational mode. Several parameters were deduced such as s_{11}^E and s_{12}^E (radial mode, circular sample), k_t, c_{33}^D, ε_{33}^S, e_{33} (thickness mode using KLM equivalent circuit, circular sample) and k'_{31} (width extensional mode, rectangular sample). The constants deduced from the measurement are marked with an asterisk in Table D.1. All the other parameters were determined using a genetic algorithm and the inter-coefficient relations between elastic, dielectric and piezoelectric parameters [181]. The experimentally determined constants were completed with initial data taken from [182] for unmodified KNN to restrain the search space of the algorithm. The chosen criterion for the algorithm allows us to optimise the consistency of the database.

Table D.1: Database for KNNSr ceramics: c_{ij}^E and c_{ij}^D (GPa), s_{ij}^E and s_{ij}^D (10^{-12} m^2/N), e_{ij} (C/m^2), h_{ij} (10^8 V/m), d_{ij} (pC/N), g_{ij} (V.m/N), $\varepsilon_{r,ij}^S$, $\varepsilon_{r,ij}^T$, β_{ij}^S (10^9 m/F) and β_{ij}^T (10^9 m/F).

(S,E)-type fundamental relations: : c_{ij}^E (GPa), e_{ij} (C/m^2), $\varepsilon_{r,ij}^S$					
c_{11}^E	c_{12}^E	c_{13}^E	c_{33}^E	c_{44}^E	c_{66}^E
142.1	68.4	65.8	131	38.3	36.9
e_{31}	$e_{33}{}^*$	e_{15}		$\varepsilon_{\mathrm{r},11}^S$	$\varepsilon_{\mathrm{r},33}^{S*}$
-2.1	8.3	10.8		508	300
(S,D)-type fundamental relations: c_{ij}^D (GPa), h_{ij}(10^8 V/m), β_{ij}^S (10^9 m/F)					
c_{11}^D	c_{12}^D	c_{13}^D	$c_{33}^{D\,*}$	c_{44}^D	c_{66}^D
143.8	70.1	58.6	156	59.4	36.9
h_{31}	h_{33}	h_{15}		β_{11}^S	β_{33}^S
-8.0	33.8	21.5		0.21	0.38
(T,E)-type fundamental relations: s_{ij}^E (10^{-12} m^2/N), d_{ij} (pC/N), $\varepsilon_{r,ij}^T$					
$s_{11}^{E\,*}$	$s_{12}^{E\,*}$	s_{13}^E	s_{33}^E	s_{44}^E	s_{66}^E
10.2	-3.3	-3.5	11.1	26.1	27.1
d_{31}	d_{33}	d_{15}		$\varepsilon_{\mathrm{r},11}^T$	$\varepsilon_{\mathrm{r},33}^T$
-47	118.4	281.9		878	450
(T,D)-type fundamental relations: s_{ij}^D (10^{-12} m^2/N), g_{ij} (V.m/N), β_{ij}^T (10^9 m/F)					
s_{11}^D	s_{12}^D	s_{13}^D	s_{33}^D	s_{44}^D	s_{66}^D
9.7	-3.9	-2.1	7.3	16.8	27.1
g_{31}	g_{33}	g_{15}		β_{11}^T	β_{33}^T
-0.013	0.030	0.036		0.13	0.24
Electromechanical coupling factors k_{ij} (%)					Density
$k_t{}^*$	k_{33}	k_{31}	k_p	$k'_{31}{}^*$	ρ^*(kg/m^3)
41	56	23	40	31	4300

*Experimentally deduced values

Appendix E

Choice of a Parameter to Assess the Uniformity of the Electric Field

We needed to choose a relevant parameter to evaluate the uniformity of the electric field strength in close vicinity to the working electrode. The electric field strength along the line A-A (see paragraph 3.4) of the electrode shows two typical configurations:
-the configuration 1 with two maxima at the edges, observed for example at $h_i = 4$ mm and $D_e = 8$ mm (Figure E.1a);
-the configuration 2 with two maxima at the edges and an additional maxima at the centre of the electrode observed for example at $h_i = 4$ mm and $D_e = 4$ mm (Figure E.1b).
The configuration 1 presented in Figure E.1a with a large region with constant electric field strength is preferred in terms of uniformity to the configuration 2 presented in Figure E.1b.

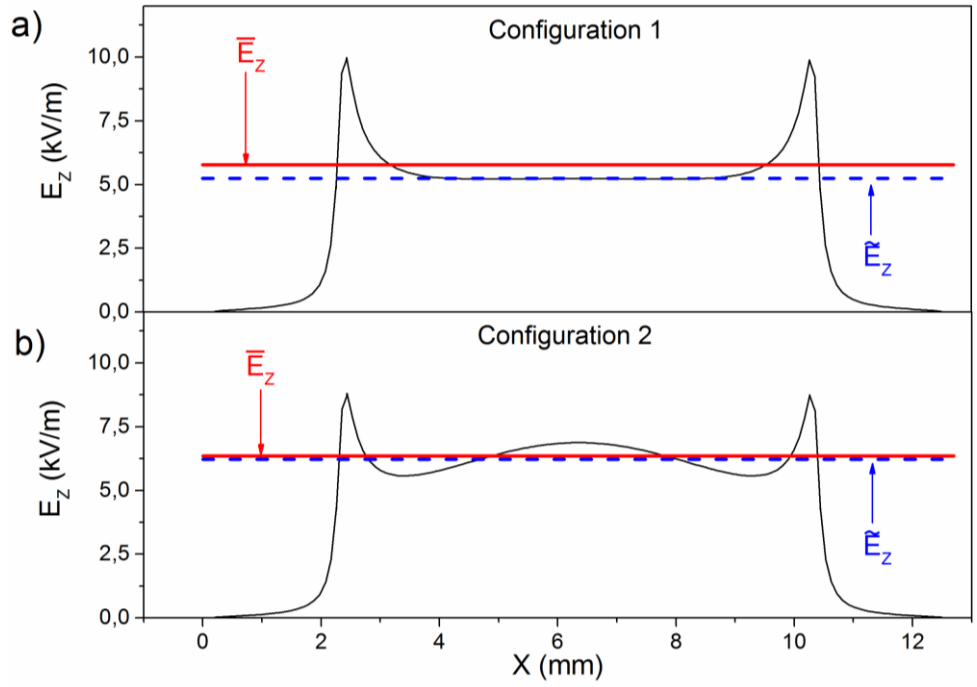

Figure E.1: Finite-element-analysis predicted electric field in close vicinity to the working electrode of the EPD setup for a) $h_i = 4$ mm, $D_e = 8$ mm (configuration 1) and b) h_i= 4 mm, $D_e = 4$ mm (configuration 2). Solid red line: average value of $E_{Z,i}$($\overline{E_Z}$) and blue dotted line: median value of $E_{Z,i}$ ($\widetilde{E_Z}$).

We selected three parameters to estimate the electric field strength's uniformity. Those three parameters were calculated using exactly the same data, i.e., the values of the $E_{Z,i}$ at the points for which X_i was on top of the working electrode, 2.35 mm $< X_i <$ 10.35 mm along the line A-A (see Figure 4.12a), representing a total of n points (~ 160 points).

1. The first parameter was an electric field aspect ratio (AR_E) calculated as:

$$\mathrm{AR}_E = \frac{\max\ (E_{Z,i})}{\min(E_{Z,i})} \tag{E.1}$$

where max($(E_{Z,i})$ and min $(E_{Z,i})$, represent the maximum and minimum values of the $E_{Z,i}$ in the dataset, respectively.

2. The second parameter was the standard deviation (SD), which was normalised by the average value of the dataset ($\overline{E_Z}$) and was calculated with the formula:

$$\mathrm{SD} = \sqrt{\frac{1}{n}\sum_{1}^{n}(E_{Z,i} - \overline{E_Z})^2}\Big/\overline{E_Z} \tag{E.2}$$

3. The third parameter was the absolute deviation (MAD), which was normalised by the median of the dataset, i.e., $\widetilde{E_{Z,i}}$, and was given by

$$\mathrm{MAD} = \text{median}\ (\left|E_{Z,i} - \widetilde{E_{Z,i}}\right|)/\widetilde{E_{Z,i}} \tag{E.3}$$

The values of these three parameters for the two configurations are given in Table E.1.

Table E.1: Aspect ratio (AR_E), normalised standard deviation (SD) and normalised median absolute deviation (MAD) for the configuration 1 (h_i = 4 mm, D_e = 8 mm) and configuration 2 (h_i = 4 mm, D_e = 4 mm).

	AR_E	SD (%)	MAD (%)
configuration 1	1.92	19.9	0.6
configuration 2	1.58	11.3	7.9

The values of AR_E were 1.92 and 1.58 for the configurations 1 and 2, respectively. The lower calculated value for the second configuration showed that AR_E was not a good criterion to describe the electric field strength's uniformity when configuration 1 and configuration 2 are compared. However, the use of AR was appropriate to address the uniformity of the electric field strength only in the configuration 1 with the maximum values at the edges and a minimum value in its centre.

For the SD parameter, the tendency was the same as AR, where the lowest value (11.3 %) was obtained for the configuration 2. This result was mainly due to the smaller distribution of $E_{Z,i}$ around the average $\overline{E_Z}$ value (solid red line in Figure E.1).

Finally, the calculated MAD values are more representative of the electric field uniformity with a significant lower value for the configuration 1 (0.6 %) compared to the configuration 2 (7.9 %). The median value integrated in the MAD definition represented an intermediate parameter that was close to the constant electric field strength value in the central part of the electrode for the configuration 1 (dashed blue in Figure E.1). The MAD parameter was retained in the whole thesis since it best describes the statistical dispersion of the electric field strength and quantifies its uniformity.

Appendix F

Deposition Yields: Comparison on Various Substrates

In the two-step deposition-sintering procedure, we deposited the first KNNSr layer on RAO substrate, meaning on the platinum electrode. The second layer was deposited on top of the first layer, i.e., on the fired KNNSr layer.

For the electrophoretic deposition, the use of electrodes with various materials and surface morphologies could result in different yields [86], [87]. Thus, we measured the yields after deposition of the KNNSr layer in the same conditions on two substrates, namely RAO with platinum electrode and on F-1000-A, which consist of a KNNSr-covered platinum electrode.

The depositions were performed from the same suspension with a conductivity of 29.2 μS/cm at a constant current density (1.56 mA/cm^2) onto the RAO substrate and F-1000-A.

The results of 5 depositions for 30 s onto the RAO substrate gave a yield of 3.0 $\pm$ 0.2 mg/(cm^2) and 5 depositions onto F-1000-A for 30 s gave a yield of 3.1 $\pm$ 0.2 mg/(cm^2).

These results indicated that similar yields were observed when depositing the KNNSr on the RAO substrate and F-1000-A for a selected deposition condition.

References

[1] K. A. Cook-Chennault, N. Thambi and A. M. Sastry, "Powering MEMS portable devices—a review of non-regenerative and regenerative power supply systems with special emphasis on piezoelectric energy harvesting systems," *Smart Materials and Structures*, vol. 17, no. 4, p. 043001, 2008.

[2] A. Toprak and O. Tigli, "Piezoelectric energy harvesting: state-of-the-art and challenges," *Applied Physics Reviews*, vol. 1, no. 3, p. 031104, 2014.

[3] H. Li, C. Tian and Z. D. Deng, "Energy harvesting from low frequency applications using piezoelectric materials," *Applied Physics Reviews*, vol. 1, no. 4, p. 041301, 2014.

[4] P. Cahill, B. Hazra, R. Karoumi, A. Mathewson and V. Pakrashi, "Vibration energy harvesting based monitoring of an operational bridge undergoing forced vibration and train passage," *Mechanical Systems and Signal Processing*, vol. 106, pp. 265–283, 2018.

[5] L. Dong, X. Han, Z. Xu, A. B. Closson, Y. Liu, C. Wen, X. Liu, G. P. Escobar, M. Oglesby, M. Feldman, Z. Chen and J. X. J. Zhang, "Flexible porous piezoelectric cantilever on a pacemaker lead for compact energy harvesting," *Advanced Materials Technologies*, vol. 4, no. 1, p. 1800148, 2019.

[6] H. Liu, J. Zhong, C. Lee, S.-W. Lee and L. Lin, "A comprehensive review on piezoelectric energy harvesting technology: materials, mechanisms, and applications," *Applied Physics Reviews*, vol. 5, no. 4, p. 041306, 2018.

[7] B. Jaffe, W. R. Cook Jr. and H. Jaffe, Piezoelectric Ceramics. London: Academic Press, 1971.

[8] A. Erturk and D. J. Inman, Piezoelectric Energy Harvesting. John Wiley & Sons, 2011.

[9] R. M. Ferdous, A. W. Reza and M. F. Siddiqui, "Renewable energy harvesting for wireless sensors using passive RFID tag technology: A review," *Renewable and Sustainable Energy Reviews*, vol. 58, pp. 1114–1128, 2016.

[10] G. Ferin, T. Hoang, C. Bantignies, H. Le Khanh, E. Flesch and A. Nguyen-Dinh, "Powering autonomous wireless sensors with miniaturized piezoelectric based energy harvesting devices for NDT applications," in *2015 IEEE International Ultrasonic Symposium (IUS)*, 2015, pp. 1–4.

[11] S. B. Kim, J. H. Park, S. H. Kim, H. Ahn, H. C. Wikle and D. J. Kim, "Modeling and evaluation of d_{33} mode piezoelectric energy harvesters," *Journal of Micromechanics and Microengineering*, vol. 22, no. 10, p. 105013, 2012.

[12] L. Wang, L. Zhao, Z. Jiang, G. Luo, P. Yang, X. Han, X. Li and R. Maeda, "High accuracy comsol simulation method of bimorph cantilever for piezoelectric vibration energy harvesting," *AIP Advances*, vol. 9, no. 9, p. 095067, 2019.

[13] I. Coondoo, N. Panwar, H. Maiwa and A. L. Kholkin, "Improved piezoelectric and energy harvesting characteristics in lead-free Fe_2O_3 modified KNN ceramics," *Journal of Electroceramics*, vol. 34, pp. 255–261, 2015.

[14] I.-T. Seo, C.-H. Choi, D. Song, M.-S. Jang, B.-Y. Kim, S. Nahm, Y.-S. Kim, T.-H. Sung and H.-C. Song, "Piezoelectric properties of lead-free piezoelectric ceramics and their energy harvester characteristics," *Journal of the American Ceramic Society*, vol. 96, no. 4, pp. 1024–1028, 2013.

[15] S. Priya, "Criterion for material selection in design of bulk piezoelectric energy harvesters," *IEEE transactions on ultrasonics, ferroelectrics, and frequency control*, vol. 57, no. 12, pp. 2610–2612, 2010.

[16] "Ferroperm website." https://www.meggittferroperm.com.

[17] A. Triplett and D. D. Quinn, "The effect of non-linear piezoelectric coupling on vibration-based energy harvesting," *Journal of Intelligent Material Systems and Structures*, vol. 20, no. 16, pp. 1959–1967, 2009.

[18] S. Leadenham and A. Erturk, "Unified nonlinear electroelastic dynamics of a bimorph piezoelectric cantilever for energy harvesting, sensing, and actuation," *Nonlinear Dynamics*, vol. 79, pp. 1727–1743, 2015.

[19] M. T. Todaro, F. Guido, V. Mastronardi, D. Desmaele, G. Epifani, L. Algieri and M. De Vittorio, "Piezoelectric MEMS vibrational energy harvesters: advances and outlook," *Microelectronic Engineering*, vol. 183–184, pp. 23–36, 2017.

[20] C. B. Williams and R. B. Yates, "Analysis of a micro-electric generator for microsystems," in *Proceedings of the International Solid-State Sensors and Actuators Conference-TRANSDUCERS'95*, 1995, pp. 369–372.

[21] S. Roundy, P. K. Wright and J. Rabaey, "A study of low level vibrations as a power source for wireless sensor nodes," *Computer Communications*, vol. 26, no. 11, pp. 1131–1144, 2003.

[22] J. Roscow, Y. Zhang, J. Taylor and C. R. Bowen, "Porous ferroelectrics for energy harvesting applications," *The European Physical Journal Special Topics*, vol. 224, pp. 2949–2966, 2015.

[23] J. Rödel, W. Jo, K. T. P. Seifert, E.-M. Anton, T. Granzow and D. Damjanovic, "Perspective on the development of lead-free piezoceramics," *Journal of the American Ceramic Society*, vol. 92, no. 6, pp. 1153–1177, 2009.

[24] J. Rödel, K. G. Webber, R. Dittmer, W. Jo, M. Kimura and D. Damjanovic, "Transferring lead-free piezoelectric ceramics into application," *Journal of the European Ceramic Society*, vol. 35, no. 6, pp. 1659–1681, 2015.

[25] G. Shirane, R. Newnham and R. Pepinsky, "Dielectric properties and phase transitions of $NaNbO_3$ and $(Na,K)NbO_3$," *Physical Review*, vol. 96, no. 3, pp. 581–588, 1954.

[26] M. Ahtee and A. M. Glazer, "Phase transitions in sodium niobate-potassium niobate solid solutions," *Ferroelectrics*, vol. 7, no. 1, pp. 93–95, 1974.

[27] R. E. Jaeger and L. Egerton, "Hot pressing of potassium-sodium niobates," *Journal of the American Ceramic Society*, vol. 45, no. 5, pp. 209–213, 1962.

[28] L. Egerton and D. M. Dillon, "Piezoelectric and dielectric properties of ceramics in the system potassium-sodium niobate," *Journal of the American Ceramic Society*, vol. 42, no. 9, pp. 438–442, 1959.

[29] G. H. Haertling, "Properties of hot-pressed ferroelectric alkali niobate ceramics," *Journal of the American Ceramic Society*, vol. 50, no. 6, pp. 329–330, 1967.

[30] H. Birol, D. Damjanovic and N. Setter, "Preparation and characterization of $(K_{0.5}Na_{0.5})NbO_3$ ceramics," *Journal of the European Ceramic Society*, vol. 26, no. 6, pp. 861–866, 2006.

[31] K. Wang and J. F. Li, "Analysis of crystallographic evolution in $(Na,K)NbO_3$-based lead-free piezoceramics by x-ray diffraction," *Applied Physics Letters*, vol. 91, no. 26, p. 262902, 2007.

[32] J. Tellier, B. Malič, B. Dkhil, D. Jenko, J. Cilensek and M. Kosec, "Crystal structure and phase transitions of sodium potassium niobate perovskites," *Solid State Sciences*, vol. 11, no. 2, pp. 320–324, 2009.

[33] B. Malič, H. Razpotnik, J. Koruza, S. Kokalj, J. Cilenšek and M. Kosec, "Linear thermal expansion of lead-free piezoelectric $K_{0.5}Na_{0.5}NbO_3$ ceramics in a wide temperature range," *Journal of the American Ceramic Society*, vol. 94, no. 8, pp. 2273–2275, 2011.

[34] M. Feizpour, T. Ebadzadeh and D. Jenko, "Synthesis and characterization of lead-free piezoelectric $(K_{0.50}Na_{0.50})NbO_3$ powder produced at lower calcination temperatures: a comparative study with a calcination temperature of 850 °C," *Journal of the European Ceramic Society*, vol. 36, no. 7, pp. 1595–1603, 2016.

[35] J. Hreščak, A. Bencan, T. Rojac and B. Malič, "The influence of different niobium pentoxide precursors on the solid-state synthesis of potassium sodium niobate," *Journal of the European Ceramic Society*, vol. 33, no. 15–16, pp. 3065–3075, 2013.

[36] B. Malic, D. Jenko, J. Holc, M. Hrovat and M. Kosec, "Synthesis of sodium potassium niobate: a diffusion couples study," *Journal of the American Ceramic Society*, vol. 91, no. 6, pp. 1916–1922, 2008.

[37] B. Malič, D. Kuščer, M. Vrabelj and J. Koruza, "Review of methods for powder-based processing," in *Magnetic, Ferroelectric, and Multiferroic Metal Oxides*, Elsevier, 2018, pp. 95–120.

[38] A. B. Haugen, F. Madaro, L. Bjørkeng, T. Grande and M. Einarsrud, "Sintering of sub-micron $K_{0.5}Na_{0.5}NbO_3$ powders fabricated by spray pyrolysis," *Journal of the European Ceramic Society*, vol. 35, no. 5, pp. 1449–1457, 2015.

[39] M. Bah, F. Giovannelli, F. Schoenstein, G. Feuillard, E. Le Clezio and I. Monot-Laffez, "Synthesis, microstructure and electromechanical properties of undoped $(K_{0.5}Na_{0.5})NbO_3$," *Advances in Applied Ceramics*, vol. 114, no. 4, pp. 211–219, 2015.

[40] Y. Zhen and J.-F. Li, "Normal sintering of $(K,Na)NbO_3$-based ceramics: influence of sintering temperature on densification, microstructure, and electrical properties," *Journal of the American Ceramic Society*, vol. 89, no. 12, pp. 3669–3675, 2006.

[41] J. Koruza and B. Malič, "Initial stage sintering mechanism of $NaNbO_3$ and implications regarding the densification of alkaline niobates," *Journal of the European Ceramic Society*, vol. 34, no. 8, pp. 1971–1979, 2014.

[42] M. Kosec and D. Kolar, "On activated sintering and electrical properties of $NaKNbO_3$," *Materials Research Bulletin*, vol. 10, no. 5, pp. 335–339, 1975.

[43] D. Jenko, A. Benčan, B. Malič, J. Holc and M. Kosec, "Electron microscopy studies of potassium sodium niobate ceramics," *Microscopy and Microanalysis*, vol. 11, no. 6, pp. 572–580, 2005.

[44] J. Acker, H. Kungl and M. J. Hoffmann, "Influence of alkaline and niobium excess on sintering and microstructure of sodium-potassium niobate $(K_{0.5}Na_{0.5})NbO_3$," *Journal of the American Ceramic Society*, vol. 93, no. 5, pp. 1270–1281, 2010.

[45] N. M. Hagh, B. Jadidian and A. Safari, "Property-processing relationship in lead-free (K, Na, Li) NbO_3-solid solution system," *Journal of Electroceramics*, vol. 18, no. 3–4, pp. 339–346, 2007.

[46] A. Popovič, L. Bencze, J. Koruza and B. Malič, "Vapour pressure and mixing thermodynamic properties of the $KNbO_3$–$NaNbO_3$ system," *RSC Adv.*, vol. 5, no. 93, pp. 76249–76256, 2015.

[47] Y. Wang, D. Damjanovic, N. Klein and N. Setter, "High-temperature instability of Li- and Ta-modified (K,Na)NbO_3 piezoceramics," *Journal of the American Ceramic Society*, vol. 91, no. 6, pp. 1962–1970, 2008.

[48] J. Hreščak, G. Dražić, M. Deluca, I. Arčon, A. Kodre, M. Dapiaggi, T. Rojac, B. Malič and A. Bencan, "Donor doping of $K_{0.5}Na_{0.5}NbO_3$ ceramics with strontium and its implications to grain size, phase composition and crystal structure," *Journal of the European Ceramic Society*, vol. 37, no. 5, pp. 2073–2082, 2017.

[49] J. F. Li, Y. Zhen, B. P. Zhang, L. M. Zhang and K. Wang, "Normal sintering of (K, Na)NbO_3-based lead-free piezoelectric ceramics," *Ceramics International*, vol. 34, no. 4, pp. 783–786, 2008.

[50] X. Vendrell, J. E. García, F. Rubio-Marcos, D. A. Ochoa, L. Mestres and J. F. Fernández, "Exploring different sintering atmospheres to reduce nonlinear response of modified KNN piezoceramics," *Journal of the European Ceramic Society*, vol. 33, no. 4, pp. 825–831, 2013.

[51] J. G. Fisher and S.-J. L. Kang, "Microstructural changes in $(K_{0.5}Na_{0.5})NbO_3$ ceramics sintered in various atmospheres," *Journal of the European Ceramic Society*, vol. 29, no. 12, pp. 2581–2588, 2009.

[52] R. Zuo, J. Rödel, R. Chen and L. Li, "Sintering and electrical properties of lead-free $Na_{0.5}K_{0.5}NbO_3$ piezoelectric ceramics," *Journal of the American Ceramic Society*, vol. 89, no. 6, pp. 2010–2015, 2006.

[53] J. Ma, H. Li, H. Wang, C. Lin, X. Wu, T. Lin, X. Zheng and X. Yu, "Composition, microstructure and electrical properties of $K_{0.5}Na_{0.5}NbO_3$ ceramics fabricated by cold sintering assisted sintering," *Journal of the European Ceramic Society*, vol. 39, no. 4, pp. 986–993, 2019.

[54] C.-W. Ahn, C.-S. Park, C.-H. Choi, S. Nahm, M.-J. Yoo, H.-G. Lee and S. Priya, "Sintering behavior of lead-free (K,Na)NbO_3 -based piezoelectric ceramics," *Journal of the American Ceramic Society*, vol. 92, no. 9, pp. 2033–2038, 2009.

[55] J. G. Fisher, S. Choi and S. L. Kang, "Influence of sintering atmosphere on abnormal grain growth behaviour in potassium sodium niobate ceramics sintered at low temperature," *Journal of the Korean Ceramic Society*, vol. 48, no. 6, pp. 641–647, 2011.

[56] M. Bah, "Synthèse et propriétés fonctionnelles de céramiques et monocristaux piézoélectriques sans plomb (K,Na)NbO_3, Doctoral dissertation," Univeristé de Tours, Tours, France, 2014.

[57] J. G. Fisher, D. Rout, K.-S. Moon and S.-J. L. Kang, "High-temperature X-ray diffraction and Raman spectroscopy study of $(K_{0.5}Na_{0.5})NbO_3$ ceramics sintered in oxidizing and reducing atmospheres," *Materials Chemistry and Physics*, vol. 120, no. 2–3, pp. 263–271, 2010.

[58] D. Kuscer, A. Kocjan, M. Majcen, A. Meden, K. Radan, J. Kovač and B. Malič, "Evolution of phase composition and microstructure of sodium potassium niobate–based ceramic during pressure-less spark plasma sintering and post-annealing," *Ceramics International*, vol. 45, no. 8, pp. 10429–10437, 2019.

[59] F. Hussain, I. Sterianou, A. Khesro, D. C. Sinclair and I. M. Reaney, "p -Type/ n -type behaviour and functional properties of $K_xNa_{(1-x)}NbO_3$ ($0.49 \leq x \leq 0.51$) sintered in air and N_2," *Journal of the European Ceramic Society*, vol. 38, no. 9, pp. 3118–3126, 2018.

[60] C. Long, T. Li, H. Fan, Y. Wu, L. Zhou, Y. Li, L. Xiao and Y. Li, "Li-substituted $K_{0.5}Na_{0.5}NbO_3$-based piezoelectric ceramics: Crystal structures and the effect of atmosphere on electrical properties," *Journal of Alloys and Compounds*, vol. 658, pp. 839–847, 2016.

[61] K. Kobayashi, Y. Doshida, Y. Mizuno and C. A. Randall, "A route forwards to narrow the performance gap between PZT and lead-free piezoelectric ceramic with low oxygen partial pressure processed $(Na_{0.5}K_{0.5})NbO_3$," *Journal of the American Ceramic Society*, vol. 95, no. 9, pp. 2928–2933, 2012.

[62] B. Malič, J. Bernard, J. Holc, D. Jenko and M. Kosec, "Alkaline-earth doping in (K,Na)NbO_3 based piezoceramics," *Journal of the European Ceramic Society*, vol. 25, no. 12, pp. 2707–2711, 2005.

[63] J. Hreščak, "Synthesis and characterization of undoped and strontium-doped potassium sodium niobate ceramics, Doctoral dissertation," Jožef Stefan Postgraduate School, Ljubljana, Slovenia, 2016.

[64] B. Malič, J. Bernard, J. Holc and M. Kosec, "Strontium doped $K_{0.5}Na_{0.5}NbO_3$ based piezoceramics," *Ferroelectrics*, vol. 314, no. 1, pp. 149–156, 2005.

[65] R. A. Dorey, Ceramic thick films for MEMS and microdevices. Oxford: William Andrew Publishing, 2011.

[66] M. Kosec, D. Kuscer and J. Holc, "Processing of ferroelectric ceramic thick films," in *Multifunctional Polycrystalline Ferroelectric Materials*, Springer, 2011, pp. 39–61.

[67] J. A. Lewis, "Colloidal processing of ceramics," *Journal of the American Ceramic Society*, vol. 83, no. 10, pp. 2341–2359, 2000.

[68] M. Cannio, S. Novak, L. Besra and A. R. Boccaccini, "Electrophoretic Deposition," in *Ceramics and Composites Processing Methods*, N. P. Bansal and A. R. Boccaccini, Eds. John Wiley & Sons, 2012, pp. 517–549.

[69] H.-W. Lin, C.-P. Chang, W.-H. Hwu and M.-D. Ger, "The rheological behaviors of screen-printing pastes," *Journal of Materials Processing Technology*, vol. 197, no. 1–3, pp. 284–291, 2008.

[70] B. Ferrari and R. Moreno, "The conductivity of aqueous Al_2O_3 slips for electrophoretic deposition," *Materials Letters*, vol. 28, no. 4–6, pp. 353–355, 1996.

[71] A. Lei, R. Xu, A. Thyssen, A. C. Stoot, T. L. Christiansen, K. Hansen, R. Lou-Møller, E. V. Thomsen and K. Birkelund, "MEMS-based thick film PZT vibrational energy harvester," in *2011 IEEE 24th International Conference on Micro Electro Mechanical Systems*, 2011, pp. 125–128.

[72] F. Levassort, J.-M. Gregoire, M. Lethiecq, K. Astafiev, L. Nielsen, R. Lou-Moeller and W. W. Wolny, "High frequency single element transducer based on pad-printed lead-free piezoelectric thick films," in *2011 IEEE International Ultrasonics Symposium Proceedings*, 2011, pp. 848–851.

[73] A.-P. Abellard, D. Kuscer, J.-M. Grégoire, M. Lethiecq, B. Malič and F. Levassort, "Lead zirconate titanate-based thick films for high-frequency focused ultrasound transducers prepared by electrophoretic deposition," *IEEE Transactions on Ultrasonics, Ferroelectrics, and Frequency Control*, vol. 61, no. 3, pp. 547–556, 2014.

[74] L. Besra and M. Liu, "A review on fundamentals and applications of electrophoretic deposition (EPD)," *Progress in Materials Science*, vol. 52, no. 1, pp. 1–61, 2007.

[75] O. O. Van der Biest and L. J. Vandeperre, "Electrophoretic deposition of materials," *Annual Review of Materials Science*, vol. 29, pp. 327–352, 1999.

[76] H. C. Hamaker, "Formation of a deposit by electrophoresis," *Transactions of the Faraday Society*, vol. 35, pp. 279–287, 1940.

[77] L. Besra, T. Uchikoshi, T. S. Suzuki and Y. Sakka, "Bubble-free aqueous electrophoretic deposition (EPD) by pulse-potential application," *Journal of the American Ceramic Society*, vol. 91, no. 10, pp. 3154–3159, 2008.

[78] J. H. Dickerson and A. R. Boccaccini, Eds., Electrophoretic deposition of nanomaterials. New York, NY: Springer, 2012.

[79] I. Zhitomirsky, "Cathodic electrodeposition of ceramic and organoceramic materials. Fundamental aspects," *Advances in Colloid and Interface Science*, vol. 97, no. 1–3, pp. 279–317, 2002.

[80] J. S. Reed, Principles of Ceramics Processing. Wiley, 1995.

[81] R. J. Hunter, Zeta Potential in Colloid Science: Principles and Applications. Academic Press, 1981.

[82] A. M. Popa, J. Vleugels, J. Vermant and O. Van der Biest, "Influence of ammonium salt of poly-methacrylic acid and butylamine addition on the viscosity and electrophoretic deposition behavior of ethanol-based powder suspensions," *Colloids and Surfaces A: Physicochemical and Engineering Aspects*, vol. 267, no. 1–3, pp. 74–78, 2005.

[83] A. M. Popa, J. Vleugels, J. Vermant and O. Van der Biest, "Influence of surfactant addition sequence on the suspension properties and electrophoretic deposition behaviour of alumina and zirconia," *Journal of the European Ceramic Society*, vol. 26, no. 6, pp. 933–939, 2006.

[84] D. Kuscer and M. Kosec, "0.65Pb($Mg_{1/3}Nb_{2/3}$)O_3–0.35$PbTiO_3$ thick films prepared by electrophoretic deposition from an ethanol-based suspension," *Journal of the European Ceramic Society*, vol. 30, no. 6, pp. 1437–1444, 2010.

[85] A.-P. Abellard, D. Kuscer, M. Lethiecq, B. Malič and F. Levassort, "Processing and electromechanical properties of lead zirconate titanate thick films by electrophoretic deposition," *Advances in Applied Ceramics*, vol. 114, no. 4, pp. 198–204, 2015.

[86] S. Chibowski, E. O. Mazur and J. Patkowski, "Influence of the ionic strength on the adsorption properties of the system dispersed aluminium oxide–polyacrylic acid," *Materials Chemistry and Physics*, vol. 93, no. 2–3, pp. 262–271, 2005.

[87] H. Guldberg-Pedersen and L. Bergström, "Stabilizing ceramic suspensions using anionic polyelectrolytes: Adsorption kinetics and interparticle forces," *Acta Materialia*, vol. 48, no. 18–19, pp. 4563–4570, 2000.

[88] H. Y. T. Chen, W. C. J. Wei, K. C. Hsu and C. S. Chen, "Adsorption of PAA on the α-Al_2O_3 Surface," *Journal of the American Ceramic Society*, vol. 90, no. 6, pp. 1709–1716, 2007.

[89] Y. Hirata, J. Kamikakimoto, A. Nishimoto and Y. Ishihara, "Interaction between α-alumina surface and polyacrylic acid," *Journal of the Ceramic Society of Japan*, vol. 100, no. 1157, pp. 7–12, 1992.

[90] D. Kuscer, T. Bakarič, B. Kozlevčar and M. Kosec, "Interactions between lead–zirconate titanate, polyacrylic acid, and polyvinyl butyral in ethanol and their influence on electrophoretic deposition behavior," *The Journal of Physical Chemistry B*, vol. 117, no. 6, pp. 1651–1659, 2013.

[91] J. Zhao, X. Wang, Z. Gui and L. Li, "Dispersion of barium titanate with poly(acrylic acid-co-maleic acid) in aqueous media," *Ceramics International*, vol. 30, no. 7, pp. 1985–1988, 2004.

[92] J. Zhao, X. Wang and L. Li, "Electrophoretic deposition of $BaTiO_3$ films from aqueous suspensions," *Materials Chemistry and Physics*, vol. 99, no. 2–3, pp. 350–353, 2006.

[93] N. Traiphol, R. Suntako and K. Chanthornthip, "Roles of polymeric dispersant charge density on lead zirconate titanate aqueous processing," *Ceramics International*, vol. 36, no. 7, pp. 2147–2153, 2010.

[94] S. Dor, S. Rühle, A. Ofir, M. Adler, L. Grinis and A. Zaban, "The influence of suspension composition and deposition mode on the electrophoretic deposition of TiO_2 nanoparticle agglomerates," *Colloids and Surfaces A: Physicochemical and Engineering Aspects*, vol. 342, no. 1–3, pp. 70–75, 2009.

[95] J. Ma and W. Cheng, "Deposition and packing study of sub-micron PZT ceramics using electrophoretic deposition," *Materials Letters*, vol. 56, no. 5, pp. 721–727, 2002.

[96] J. Ma, C. Wang and K. W. Peng, "Electrophoretic deposition of porous hydroxyapatite scaffold," *Biomaterials*, vol. 24, no. 20, pp. 3505–3510, 2003.

[97] B. Ferrari and R. Moreno, "Electrophoretic deposition of aqueous alumina slips," *Journal of the European Ceramic Society*, vol. 17, no. 4, pp. 549–556, 1997.

[98] B. Ferrari and R. Moreno, "EPD kinetics: a review," *Journal of the European Ceramic Society*, vol. 30, no. 5, pp. 1069–1078, 2010.

[99] P. Sarkar and P. S. Nicholson, "Electrophoretic deposition (EPD): mechanisms, kinetics, and application to ceramics," *Journal of the American Ceramic Society*, vol. 79, no. 8, pp. 1987–2002, 1996.

[100] P. Sarkar, D. De and H. Rho, "Synthesis and microstructural manipulation of ceramics by electrophoretic deposition," *Journal of Materials Science*, vol. 39, pp. 819–823, 2004.

[101] B. Ferrari, R. Moreno, P. Sarkar and P. S. Nicholson, "Electrophoretic deposition of MgO from organic suspensions," *Journal of the European Ceramic Society*, vol. 20, no. 2, pp. 99–106, 2000.

[102] S. Y. Ng and A. R. Boccaccini, "Lead zirconate titanate films on metallic substrates by electrophoretic deposition," *Materials Science and Engineering: B*, vol. 116, no. 2, pp. 208–214, 2005.

[103] H. Negishi, K. Yamaji, N. Sakai, T. Horita, H. Yanagishita and H. Yokokawa, "Electrophoretic deposition of YSZ powders for solid oxide fuel cells," *Journal of Materials Science*, vol. 39, pp. 833–838, 2004.

[104] D. Kuscer, M. S. Bernardo, M. S. Zarnik and B. Malič, "Patterning of lead-zirconate-titanate thick-film structures by electrophoretic deposition from ethanol-based dispersions," *Journal of the European Ceramic Society*, vol. 36, no. 2, pp. 291–297, 2016.

[105] H. Hadraba, D. Drdlik, Z. Chlup, K. Maca, I. Dlouhy and J. Cihlar, "Laminated alumina/zirconia ceramic composites prepared by electrophoretic deposition," *Journal of the European Ceramic Society*, vol. 32, no. 9, pp. 2053–2056, 2012.

[106] C. Ji, W. Lan and P. Xiao, "Fabrication of yttria-stabilized zirconia coatings using electrophoretic deposition: packing mechanism during deposition," *Journal of the American Ceramic Society*, vol. 91, no. 4, pp. 1102–1109, 2008.

[107] B. Giera, L. A. Zepeda-Ruiz, A. J. Pascall and T. H. Weisgraber, "Mesoscale particle-based model of electrophoretic deposition," *Langmuir*, vol. 33, no. 2, pp. 652–661, 2017.

[108] M. S. Bernardo, B. Malič and D. Kuscer, "PZT-based thick films prepared by electrophoretic deposition from suspensions with different alcohol-based solvents," *Journal of The Electrochemical Society*, vol. 162, no. 11, pp. D3040–D3048, 2015.

[109] K. T. Sullivan, J. D. Kuntz and A. E. Gash, "Electrophoretic deposition and mechanistic studies of nano-Al/CuO thermites," *Journal of Applied Physics*, vol. 112, no. 2, p. 024316, 2012.

[110] A. J. Pascall, K. T. Sullivan and J. D. Kuntz, "Morphology of electrophoretically deposited films on electrode strips," *The Journal of Physical Chemistry B*, vol. 117, no. 6, pp. 1702–1707, 2013.

[111] L. Stappers, L. Zhang, O. Van der Biest and J. Fransaer, "The effect of electrolyte conductivity on electrophoretic deposition," *Journal of Colloid and Interface Science*, vol. 328, no. 2, pp. 436–446, 2008.

[112] D. A. Kurnosov, A. S. Baturin, A. S. Bugaev, K. N. Nikolski, R. G. Tchesov and E. P. Sheshin, "Influence of the interelectrode distance in electrophoretic cold cathode fabrication on the emission uniformity," *Applied Surface Science*, vol. 215, no. 1–4, pp. 232–236, 2003.

[113] S.-J. L. Kang, Sintering: Densification, Grain Growth, and Microstructure. Elsevier, 2005.

[114] T. Rabe, W. A. Schiller, T. Hochheimer, C. Modes and A. Kipka, "Zero shrinkage of LTCC by self-constrained sintering," *International Journal of Applied Ceramic Technology*, vol. 2, no. 5, pp. 374–382, 2005.

[115] R. K. Bordia and R. Raj, "Sintering behavior of ceramic films constrained by a rigid substrate," *Journal of the American Ceramic Society*, vol. 68, no. 6, pp. 287–292, 1985.

[116] G. W. Scherer and T. Garino, "Viscous sintering on a rigid substrate," *Journal of the American Ceramic Society*, vol. 68, no. 4, pp. 216–220, 1985.

[117] T. J. Garino and H. K. Bowen, "Deposition and sintering of particle films on a rigid substrate," *Journal of the American Ceramic Society*, vol. 70, no. 11, pp. C-315-C–317, 1987.

[118] T. J. Garino and H. K. Bowen, "Kinetics of constrained-film sintering," *Journal of the American Ceramic Society*, vol. 73, no. 2, pp. 251–257, 1990.

[119] O. Guillon, E. Aulbach, J. Rödel and R. K. Bordia, "Constrained sintering of alumina thin films: comparison between experiment and modeling," *Journal of the American Ceramic Society*, vol. 90, no. 6, pp. 1733–1737, 2007.

[120] L. Amaral, C. Jamin, A. M. R. Senos, P. M. Vilarinho and O. Guillon, "Constrained sintering of $BaLa_4Ti_4O_{15}$ thick films: pore and grain anisotropy," *Journal of the European Ceramic Society*, vol. 33, no. 10, pp. 1801–1808, 2013.

[121] O. Guillon, L. Weiler and J. Rödel, "Anisotropic microstructural development during the constrained sintering of dip-coated alumina thin films," *Journal of the American Ceramic Society*, vol. 90, no. 5, pp. 1394–1400, 2007.

[122] M. Tillman, J. A. Yeomans and R. A. Dorey, "The effect of a constraint on the sintering and stress development in alumina thick films," *Ceramics International*, vol. 40, no. 7, Part A, pp. 9715–9721, 2014.

[123] A. Jagota and C. Y. Hui, "Mechanics of sintering thin films — II. Cracking due to self-stress," *Mechanics of Materials*, vol. 11, no. 3, pp. 221–234, 1991.

[124] C. L. Martin, H. Camacho-Montes, L. Olmos, D. Bouvard and R. K. Bordia, "Evolution of defects during sintering: discrete element simulations," *Journal of the American Ceramic Society*, vol. 92, no. 7, pp. 1435–1441, 2009.

[125] F. Li, J. Pan and A. Cocks, "Defect healing and cracking in ceramic films during constrained sintering," *Journal of the American Ceramic Society*, vol. 95, no. 12, pp. 3743–3749, 2012.

[126] M. Kosec, J. Holc, B. Malič and V. Bobnar, "Processing of high performance lead lanthanum zirconate titanate thick films," *Journal of the European Ceramic Society*, vol. 19, no. 6–7, pp. 949–954, 1999.

[127] M. Dolhen, A. Mahajan, R. Pinho, M. E. Costa, G. Trolliard and P. M. Vilarinho, "Sodium potassium niobate ($K_{0.5}Na_{0.5}NbO_3$, KNN) thick films by electrophoretic deposition," *RSC Advances*, vol. 5, no. 6, pp. 4698–4706, 2015.

[128] A. Mahajan, R. Pinho, M. Dolhen, M. E. Costa and P. M. Vilarinho, "Unleashing the full sustainable potential of thick films of lead-free potassium sodium niobate ($K_{0.5}Na_{0.5}NbO_3$) by aqueous electrophoretic deposition," *Langmuir*, vol. 32, no. 21, pp. 5241–5249, 2016.

[129] J. Pavlič, B. Malič and T. Rojac, "Microstructural, structural, dielectric and piezoelectric properties of potassium sodium niobate thick films," *Journal of the European Ceramic Society*, vol. 34, no. 2, pp. 285–295, 2014.

[130] K. Hansen, K. Astafiev and T. Zawada, "Lead-free piezoelectric thick films based on potassium sodium niobate solutions," in *2009 IEEE International Ultrasonics Symposium*, 2009, pp. 1738–1741.

[131] G. Ye, J. Wade-Zhu, J. Zou, T. Zhang, T. W. Button and J. Binner, "Microstructures, piezoelectric properties and energy harvesting performance of undoped $(K_{0.5}Na_{0.5})NbO_3$ lead-free ceramics fabricated via two-step sintering," *Journal of the European Ceramic Society*, vol. 40, no. 8, pp. 2977–2988, 2020.

[132] Y. Su, X. Chen, Z. Yu, H. Lian, D. Zheng and J. Peng, "Comparative study on microstructure and electrical properties of $(K_{0.5}Na_{0.5})NbO_3$ lead-free ceramics prepared via two different sintering methods," *Journal of Materials Science*, vol. 52, pp. 2934–2943, 2017.

[133] Y. Tsujiura, E. Suwa, F. Kurokawa, H. Hida, K. Suenaga, K. Shibata and I. Kanno, "Lead-free piezoelectric MEMS energy harvesters of $(K,Na)NbO_3$ thin films on stainless steel cantilevers," *Japanese Journal of Applied Physics*, vol. 52, no. 9S1, p. 09KD13, 2013.

[134] S. S. Won, J. Lee, V. Venugopal, D. J. Kim, J. Lee, I. W. Kim, A. I. Kingon and S. H. Kim, "Lead-free Mn-doped $(K_{0.5},Na_{0.5})NbO_3$ piezoelectric thin films for MEMS-based vibrational energy harvester applications," *Applied Physics Letters*, vol. 108, no. 23, p. 232908, 2016.

[135] L. Van Minh, M. Hara, F. Horikiri, K. Shibata, T. Mishima and H. Kuwano, "Bulk micromachined energy harvesters employing $(K,Na)NbO_3$ thin film," *Journal of Micromechanics and Microengineering*, vol. 23, no. 3, p. 035029, 2013.

[136] R. Xu, A. Lei, C. Dahl-Petersen, K. Hansen, M. Guizzetti, K. Birkelund, E. V. Thomsen and O. Hansen, "Screen printed PZT/PZT thick film bimorph MEMS cantilever device for vibration energy harvesting," *Sensors and Actuators A: Physical*, vol. 188, pp. 383–388, 2012.

[137] D. Zhu, P. Glenne-Jones, N. White, N. Harris, J. Tudor, R. Torah, A. Almusallam and S. Beeby, "Screen printed piezoelectric films for energy harvesting," *Advances in Applied Ceramics*, vol. 112, no. 2, pp. 79–84, 2013.

[138] J. Hreščak, B. Malič, J. Cilenšek and A. Benčan, "Solid-state synthesis of undoped and Sr-doped $K_{0.5}Na_{0.5}NbO_3$," *Journal of Thermal Analysis and Calorimetry*, vol. 127, pp. 129–136, 2017.

[139] "International Centre for Diffraction Data, Powder Diffraction File. PDF-ICDD, PCPDFW in version2.2, Newtown Square, PA, 2002." 2002.

[140] F. K. Lotgering, "Topotactical reactions with ferrimagnetic oxides having hexagonal crystal structures—I," *Journal of Inorganic and Nuclear Chemistry*, vol. 9, no. 2, pp. 113–123, 1959.

[141] R. Krimholtz, D. A. Leedom and G. L. Matthaei, "New equivalent circuits for elementary piezoelectric transducers," *Electronics Letters*, vol. 6, no. 13, pp. 398–399, 1970.

[142] P. Tran-Huu-Hue, F. Levassort, F. Vander Meulen, J. Holc, M. Kosec and M. Lethiecq, "Preparation and electromechanical properties of PZT/PGO thick films on alumina substrate," *Journal of the European Ceramic Society*, vol. 21, no. 10–11, pp. 1445–1449, 2001.

[143] A. R. Selfridge, "Approximate material properties in isotropic materials," *IEEE Transactions on Sonics and Ultrasonics*, vol. 32, no. 3, pp. 381–394, 1985.

[144] D. J. Griffiths, Introduction to Electrodynamics, Fourth Ed. Pearson, 2013.

[145] B. Malic, D. Jenko, J. Bernard, J. Cilensek and M. Kosec, "Synthesis and sintering of (K,Na)NbO_3 based ceramics," in *Proceedings of the 2002 Materials Research Society (MRS)*, 2002, vol. 755.

[146] W. M. Haynes, D. R. Lide and T. J. Bruno, Eds., CRC Handbook of Chemistry and Physics, 97th Edition. CRC Press, 2016.

[147] F. Boulogne, F. Giorgiutti-Dauphiné and L. Pauchard, "How to reduce the crack density in drying colloidal material?," *Oil & Gas Science and Technology – Revue d'IFP Energies nouvelles*, vol. 69, no. 3, pp. 397–404, 2014.

[148] K. B. Singh and M. S. Tirumkudulu, "Cracking in drying colloidal films," *Physical Review Letters*, vol. 98, no. 21, p. 218302, 2007.

[149] M. S. Bernardo, B. Malič and D. Kuscer, "Piezoelectric elements for multi-element linear array transducers prepared by electrophoretic deposition," *Key Engineering Materials*, vol. 654, pp. 42–46, 2015.

[150] J. J. Van Tassel and C. A. Randall, "Role of ion depletion in the electrophoretic deposition of alumina powder from ethanol with increasing quantities of HCl," *Journal of Materials Science*, vol. 41, pp. 8031–8046, 2006.

[151] M. Farrokhi-Rad and M. Ghorbani, "Electrophoretic deposition of titania nanoparticles in different alcohols: kinetics of deposition," *Journal of the American Ceramic Society*, vol. 94, no. 8, pp. 2354–2361, 2011.

[152] G. Anné, B. Neirinck, K. Vanmeensel, O. Van der Biest and J. Vleugels, "Throwing power during electrophoretic deposition," *Key Engineering Materials*, vol. 314, pp. 187–194, 2006.

[153] J.-Q. Zhao, Y.-G. Liu, M.-H. Fang, Z.-H. Huang and T.-H. Zhang, "Preparation, characterisation, and electrical properties of $(K_{0.5}Na_{0.5})NbO_3$ lead-free piezoelectric ceramics," *Journal of Electroceramics*, vol. 32, pp. 255–259, 2014.

[154] R. K. Bordia and A. Jagota, "Crack growth and damage in constrained sintering films," *Journal of the American Ceramic Society*, vol. 76, no. 10, pp. 2475–2485, 1993.

[155] D. Kuscer, F. Levassort, M. Lethiecq, A.-P. Abellard and M. Kosec, "Lead-zirconate-titanate thick films by electrophoretic deposition for high-frequency ultrasound transducers," *Journal of the American Ceramic Society*, vol. 95, no. 3, pp. 892–900, 2012.

[156] J. Acker, H. Kungl, R. Schierholz, S. Wagner, R.-A. Eichel and M. J. Hoffmann, "Microstructure of sodium-potassium niobate ceramics sintered under high alkaline vapor pressure atmosphere," *Journal of the European Ceramic Society*, vol. 34, no. 16, pp. 4213–4221, 2014.

[157] W. D. Kingery, H. K. Bowen and D. R. Uhlmann, Introduction to Ceramics. New York: Wiley, 1976.

[158] D. J. Green, O. Guillon and J. Rödel, "Constrained sintering: a delicate balance of scales," *Journal of the European Ceramic Society*, vol. 28, no. 7, pp. 1451–1466, 2008.

[159] L. Zheng and J. Wang, "Nonstoichiometric (K, Na)NbO_3 ceramics: densification and electrical properties," *Journal of Electroceramics*, vol. 32, pp. 192–198, 2014.

[160] R. D. Shannon, "Revised effective ionic radii and systematic studies of interatomic distances in halides and chalcogenides," *Acta Crystallographica Section A*, vol. 32, pp. 751–767, 1976.

[161] "Kyocera website." https://global.kyocera.com/prdct/fc/list/material/alumina/alumina.html.

[162] Y. Qin, J. Zhang, W. Yao, C. Wang and S. Zhang, "Domain structure of potassium-sodium niobate ceramics before and after poling," *Journal of the American Ceramic Society*, vol. 98, no. 3, pp. 1027–1033, 2015.

[163] A. A. Esin, D. O. Alikin, A. P. Turygin, A. S. Abramov, J. Hreščak, J. Walker, T. Rojac, A. Bencan, B. Malič, A. L. Kholkin and V. Y. Shur, "Dielectric relaxation and charged domain walls in (K,Na)NbO_3-based ferroelectric ceramics," *Journal of Applied Physics*, vol. 121, no. 7, p. 074101, 2017.

[164] M. A. Rafiq, M. E. Costa, A. Tkach and P. M. Vilarinho, "Impedance analysis and conduction mechanisms of lead free potassium sodium niobate (KNN) single crystals and polycrystals: a comparison study," *Crystal Growth & Design*, vol. 15, no. 3, pp. 1289–1294, 2015.

[165] D. V. Taylor and D. Damjanovic, "Evidence of domain wall contribution to the dielectric permittivity in PZT thin films at sub-switching fields," *Journal of Applied Physics*, vol. 82, no. 4, pp. 1973–1975, 1997.

[166] D. Damjanovic, "Stress and frequency dependence of the direct piezoelectric effect in ferroelectric ceramics," *Journal of Applied Physics*, vol. 82, no. 4, pp. 1788–1797, 1997.

[167] M. I. Morozov and D. Damjanovic, "Hardening-softening transition in Fe-doped Pb(Zr,Ti)O_3 ceramics and evolution of the third harmonic of the polarization response," *Journal of Applied Physics*, vol. 104, no. 3, p. 034107, 2008.

[168] M. Lukacs, T. Olding, M. Sayer, R. Tasker and S. Sherrit, "Thickness mode material constants of a supported piezoelectric film," *Journal of Applied Physics*, vol. 85, no. 5, pp. 2835–2843, 1999.

[169] E. I. Petrova, M. A. Lugovaya, I. A. Shvetsov, N. A. Shvetsova, A. N. Reznichenko and A. N. Rybyanets, "Porous and composite materials based on lead-free ferroelectric ceramics for ultrasonic transducers applications," in *Advanced Materials: Proceedings of the International Conference on "Physics and Mechanics of New Materials and Their Applications 2017,"* Spinger, 2018, pp. 49–63.

[170] E. Roncari, C. Galassi, F. Craciun, C. Capiani and A. Piancastelli, "A microstructural study of porous piezoelectric ceramics obtained by different methods," *Journal of the European Ceramic Society*, vol. 21, no. 3, pp. 409–417, 2001.

[171] E. D. Yilmaz, H. E. Mgbemere, H. Özcoban, R. P. Fernandes and G. A. Schneider, "Investigation of fracture toughness of modified $(K_xNa_{1-x})NbO_3$ lead-free piezoelectric ceramics," *Journal of the European Ceramic Society*, vol. 32, no. 12, pp. 3339–3344, 2012.

[172] J. Pavlič, B. Malič and T. Rojac, "Small reduction of the piezoelectric d_{33} response in potassium sodium niobate thick films," *Journal of the American Ceramic Society*, vol. 97, no. 5, pp. 1497–1503, 2014.

[173] J.-B. Ollagnier, D. J. Green, O. Guillon and J. Rödel, "Constrained sintering of a glass ceramic composite: II. symmetric laminate," *Journal of the American Ceramic Society*, vol. 92, no. 12, pp. 2900–2906, 2009.

[174] D. Ravi and D. J. Green, "Sintering stresses and distortion produced by density differences in bi-layer structures," *Journal of the European Ceramic Society*, vol. 26, no. 1–2, pp. 17–25, 2006.

[175] E. Olevsky, T. T. Molla, H. L. Frandsen, R. Bjørk, V. Esposito, D. W. Ni, A. Ilyina and N. Pryds, "Sintering of multilayered porous structures: part I-constitutive models," *Journal of the American Ceramic Society*, vol. 96, no. 8, pp. 2657–2665, 2013.

[176] J.-B. Ollagnier, O. Guillon and J. Rödel, "Constrained sintering of a glass ceramic composite: I. asymmetric laminate," *Journal of the American Ceramic Society*, vol. 93, no. 1, pp. 74–81, 2010.

[177] F. Levassort, J. Holc, E. Ringgaard, T. Bove, M. Kosec and M. Lethiecq, "Fabrication, modelling and use of porous ceramics for ultrasonic transducer applications," *Journal of Electroceramics*, vol. 19, pp. 125–137, 2007.

[178] A. N. Rybyanets, "Porous piezoceramics: theory, technology, and properties," *IEEE Transactions on Ultrasonics, Ferroelectrics, and Frequency Control*, vol. 58, no. 7, pp. 1492–1507, 2011.

[179] A. H. Meitzler, H. M. O'Bryan and H. F. Tiersten, "Definition and measurement of radial mode coupling factors in piezoelectric ceramic materials with large variations in poisson's ratio," *IEEE Transactions on Sonics and Ultrasonics*, vol. 20, no. 3, pp. 233–239, 1973.

[180] T. Hoang, G. Poulin-Vittrant, G. Ferin, F. Levassort, C. Bantignies, A. Nguyen-Dinh and M. Bavencoffe, "Parametric study of a thin piezoelectric cantilever for energy harvesting applications," *Advances in Applied Ceramics*, vol. 117, no. 4, pp. 231–236, 2018.

[181] R. Rouffaud, P. Marchet, A.-C. Hladky-Hennion, C. Bantignies, M. Pham-Thi and F. Levassort, "Complete electroelastic set for the (YXt)-45° cut of a $KNbO_3$ single crystal," *Journal of Applied Physics*, vol. 116, no. 19, p. 194106, 2014.

[182] S. Zhang, R. Xia, T. R. Shrout, G. Zang and J. Wang, "Characterization of lead free $(K_{0.5}Na_{0.5})NbO_3$–$LiSbO_3$ piezoceramic," *Solid State Communications*, vol. 141, no. 12, pp. 675–679, 2007.

[183] F. Levassort, M. Lethiecq, D. Certon and F. Patat, "A matrix method for modeling electroelastic moduli of 0-3 piezo-composites," *IEEE Transactions on Ultrasonics, Ferroelectrics and Frequency Control*, vol. 44, no. 2, pp. 445–452, 1997.

[184] R. E. Newnham, D. P. Skinner and L. E. Cross, "Connectivity and piezoelectric-pyroelectric composites," *Materials Research Bulletin*, vol. 13, no. 5, pp. 525–536, 1978.

[185] Y. Zhang, M. Xie, J. Roscow, Y. Bao, K. Zhou, D. Zhang and C. R. Bowen, "Enhanced pyroelectric and piezoelectric properties of PZT with aligned porosity for energy harvesting applications," *Journal of Materials Chemistry A*, vol. 5, no. 14, pp. 6569–6580, 2017.

[186] G. Liu, S. Zhang, W. Jiang and W. Cao, "Losses in ferroelectric materials," *Materials Science and Engineering: R: Reports*, vol. 89, pp. 1–48, 2015.

[187] T. Ikeda, Fundamentals of Piezoelectricity. New York: Oxford University Press, 1990.

[188] D. Royer and E. Dieulesaint, "Elastic Waves in Solids I: Free and Guided Propagation." Springer, 2000.

[189] M. Lethiecq, F. Patat, L. Pourcelot and L. P. Tran-Huu-Hue, "Measurement of losses in five piezoelectric ceramics between 2 and 50 MHz," *IEEE Transactions on Ultrasonics, Ferroelectrics and Frequency Control*, vol. 40, no. 3, pp. 232–237, 1993.

[190] D. Damjanovic, "Ferroelectric, dielectric and piezoelectric properties of ferroelectric thin films and ceramics," *Reports on Progress in Physics*, vol. 61, no. 9, pp. 1267–1324, 1998.

[191] L. Jin, F. Li and S. Zhang, "Decoding the fingerprint of ferroelectric loops: comprehension of the material properties and structures," *Journal of the American Ceramic Society*, vol. 97, no. 1, pp. 1–27, 2014.

[192] D. A. Ochoa, G. Esteves, T. Iamsasri, F. Rubio-Marcos, J. F. Fernández, J. E. García and J. L. Jones, "Extensive domain wall contribution to strain in a $(K,Na)NbO_3$-based lead-free piezoceramics quantified from high energy X-ray diffraction," *Journal of the European Ceramic Society*, vol. 36, no. 10, pp. 2489–2494, 2016.

[193] H. C. Thong, C. Zhao, Z. X. Zhu, X. Chen, J. F. Li and K. Wang, "The impact of chemical heterogeneity in lead-free $(K, Na)NbO_3$ piezoelectric perovskite: Ferroelectric phase coexistence," *Acta Materialia*, vol. 166, pp. 551–559, 2019.

[194] T. Cosgrove, Colloid Science: Principles, Methods and Applications. Oxford, UK ; Ames, Iowa: Blackwell Pub, 2005.

[195] D. Royer and E. Dieulesaint, "Elastic Waves in Solids II: Generation, Acousto-optic Interaction, Applications." Springer, 2000.

[196] S. J. H. van Kervel and J. M. Thijssen, "A calculation scheme for the optimum design of ultrasonic transducers," *Ultrasonics*, vol. 21, no. 3, pp. 134–140, 1983.

Bibliography

Publications Related to the Thesis

Journal Articles

H. Mercier, F. Levassort, H. Uršič, D. Kuscer, "Microstructure evolution and electromechanical properties of (K,Na)NbO_3 - based thick films," J. Am. Ceram. Soc., Online, 2020.

H. Mercier, B. Malič, H. Uršič, J. Hreščak, F. Levassort, D. Kuscer, "Electrophoretic deposition and properties of strontium-doped sodium potassium niobate thick films", J. Eur. Ceram. Soc., vol. 37, pp 5305–5313, 2017.

H. Mercier, B. Malič, H. Uršič, D. Kuscer, F. Levassort, "Processing and sintering of sodium-potasium niobate-based thick films", J. Microelectron. Electron. Components Mater, vol. 47, pp 179–185, 2017.

Published Scientific Conference Paper

C. Bantignies, T. Hoang, H. Mercier, F. Levassort, D. Kuscer, B. Malič, "Lead-free sodium potassium niobate based piezoelectric thick film bimorph structure for energy harvesting," in IEEE International Ultrasonic Symposium (IUS 2018) Kobe, Japan, 2018, pp. 1-4.

H. Mercier, B. Malič, H. Uršič, J. Hreščak, F. Levassort, D. Kuscer, "Processing of strontium-modified sodium potassium niobate layers obtained by electrophoretic deposition," in conference proceedings of the 52nd International Conference on Microelectronics, Devices and Materials (MIDEM), Ankaran, Slovenia, 2016, pp. 1-4.

Published Scientific Conference Contribution Abstract

C. Bantignies, T. Hoang, H. Mercier, D. Kuscer, B. Malič, F. Levassort, A. Nguyendinh, "Lead-free sodium potassium niobate based piezoelectric thick film bimorph structure for energy harvesting," in joint 2019 ISAF-ICE-EMF-IWPM-PFM meeting, IEEE International Symposium on Applications of Ferroelectrics (ISAF), Lausanne, Switzerland, 2019.

D. Kuscer, H. Mercier, B. Malič, F. Levassort, "Sodium potassium niobate-based thick films for piezoelectric energy harvester applications," in Electrochemistry from knowledge to innovation, the 69th Annual Meeting of the International Society of Electrochemistry, Bologna, Italy, 2018.

H. Mercier, B. Malič, H. Uršič, T. Hoang, M. Bavencoffe, F. Levassort, D. Kuscer, "Electromechanical performances of sodium-potassium niobate-based thick films for energy harvesting applications," in 54th International Conference on Microelectronics, Devices and Materials (MIDEM), Ljubljana, Slovenia, 2018.

H. Mercier, D. Kuscer, B. Malič, H. Uršič, F. Levassort. “Sintering and functional properties of sodium-potassium niobate-based thick films,” in 2018 ISAF-FMA-AMF-AMEC-PFM, ISAF International Symposium on Applications of Ferroelectrics, Hiroshima, Japan, 2018.

H. Mercier, B. Malič, J. Hreščak, H. Uršič, F. Levassort, D. Kuscer. “Processing of strontium doped sodium potassium niobate thick films obtained by electrophoretic deposition,” in Piezo 2017: *Electroceramics* for End Users IX, Cercedilla, Spain, 2017.

H. Mercier, B. Malič, J. Hreščak, B. Kmet, F. Levassort, D. Kuscer, “Strontium-doped KNN thick films by electrophoretic deposition,” in Shaping VI: 6th International Conference on Shaping of Advanced Ceramic, Montpellier, France, 2016.

H. Mercier, B. Malič, J. Hreščak, B .Kmet, M. Santo-Zarnik, F. Levassort, D. Kuscer, “Effect of deposition conditions on the thickness uniformity of KNN-based thick films by electrophoretic deposition,” in 10th Young researchers' day, Ljubljana, Slovenia, 2016.

Biography

Hugo Mercier was born on 14 August 1992 in Quimper, France. In 2015, he obtained a Master's degree in material sciences and engineering from the Institut National des Sciences Appliquées (INSA) de Rennes, France and Master's degree in material and solid-sate chemistry from the Université de Rennes 2, France.
Since 2015, he had been a PhD student on a codirected thesis between the Université de Tours, France, and the Jožef Stefan Institute in Ljubljana, Slovenia. His research focuses on the processing of piezoelectric energy harvesters integrating lead-free thick films processed by electrophoretic deposition and piezoelectric materials characterisation